On the Design of Electric Traction Machines

Design and Analysis of an Interior Permanent Magnet Synchronous Machine for Heavy Commercial Vehicles

RASMUS ANDERSSON
FACULTY OF ENGINEERING | LUND UNIVERSITY

On the Design of Electric Traction Machines

On the Design of Electric Traction Machines

Design and Analysis of an Interior Permanent Magnet Synchronous Machine for Heavy Commercial Vehicles

by Rasmus Andersson

LUND
UNIVERSITY

Thesis for the degree of Doctor of Philosophy
Thesis advisors: Prof. Mats Alaküla, Assoc. Prof. Avo Reinap
Faculty opponent: Dr. Rafal Wrobel

To be presented, with the permission of the Faculty of Engineering of Lund University, for public criticism in the M:B lecture hall, Mechanical Engineering Building, Ole Römers väg 1, on Friday, the 25th of January 2019 at 10:15 a.m.

Organization	Document name
LUND UNIVERSITY Division of Industrial Electrical Engineering and Automation P.O. Box 118, SE–221 00 Lund, Sweden www.iea.lth.se	**DOCTORAL DISSERTATION** Date of disputation 2019-01-25 Sponsoring organization Volvo Group
Author(s) Rasmus Andersson	

Title and subtitle

On the Design of Electric Traction Machines
Design and Analysis of an Interior Permanent Magnet Synchronous Machine for Heavy Commercial Vehicles

Abstract

Recent years have proven the benefits of electrifying the road bound vehicle fleet. With new components entering, the general understanding as well as the components as such needs to be improved. Focus in the thesis is on the design of an electric machine based on specifications of requirements for a commercial heavy vehicle such as a truck or a bus. One strict requirement is that the machine has to fit in the vehicle without compromising the performance. Besides limitations on the size, this affects the power density and hence efficiency and cooling. Another characteristic of a traction machine is the difference between peak operation and average or continuous loading. Within the automotive sector, cost is also an important factor.

Prior to the design work, pre-studies are used to acquire good understanding of the intended applications. The result is a space claim of ∅220 mm times 400 mm and a peak power of 180 kW. By designing the machine with a top speed of almost five times that of a conventional heavy duty engine, the required power levels are reached with less torque. As torque is proportional to size, the power demand is reached with a smaller and hence also less expensive machine. The design work is done in a two dimensional finite element environment partly developed at the division at Lund University. Main focus is on the limited space claim and requested peak power. Cooling is done with oil directed to the active parts of the machine. Prototype testing proves the machine to be capable of propelling a heavy commercial vehicle. Some in depth studies are also done on torque ripple in the skewed machine and on mapping of the losses.

The thesis presents the thorough work on setting the requirements, designing, prototyping and testing an interior permanent magnet machine intended for propulsion of heavy commercial vehicles. Improvements implemented in the design tool is verified with measurements. A deeper study on the torque output from the skewed machine shows a load dependant influence with larger impact in the field weakening region. It is also found larger than expected from the analytical expression in relevant text books. The losses are mapped with main focus on the speed dependant parts. A review of how manufacturing processes and machine controls affect the iron losses is presented. The iron loss model is adapted based on test results. Losses in the windings and in the rotor are included in the study as well.

Key words

Design of electrical machines, IPMSM, Electric propulsion, Thermal model, Skewing, Torque ripple analysis, Mechanical losses, Iron losses, Loss analysis, Heavy commercial vehicles

Classification system and/or index terms (if any)

Supplementary bibliographical information	Language
	English
ISSN and key title	ISBN
	978-91-88934-97-0 (print) 978-91-88934-96-3 (pdf)
Recipient's notes	Number of pages: 233 / Price
	Security classification

On the Design of Electric Traction Machines

Design and Analysis of an Interior Permanent Magnet Synchronous Machine for Heavy Commercial Vehicles

by Rasmus Andersson

LUND
UNIVERSITY

Cover illustration front: Image of the prototype stator with some artistic effects.

Faculty of Engineering
Department of Biomedical Engineering
Division of Industrial Electrical Engineering and Automation

ISBN: 978-91-88934-97-0 (print)
ISBN: 978-91-88934-96-3 (pdf)
CODEN: LUTEDX/(TEIE-1091)/1-233/(2019)

Printed in Sweden by Media-Tryck, Lund University, Lund 2019

Support your local planet
DEDICATED

Det man inte kan, det kan man lära sig
Lilla Anna

Contents

Acknowledgements v
Popular Scientific Summary vii
Populärvetenskaplig Sammanfattning ix

1 Introduction **1**
1.1 Background 2
1.2 Objectives 3
1.2.1 Purpose 3
1.2.2 Method 4
1.3 Contributions 5
1.3.1 Publications 7
1.4 Disposition of the thesis 8

2 Licentiate thesis summary **11**
2.1 Machine specifications and requirements 11
2.1.1 Concept selection 12
2.1.2 PTO gear analysis 12
2.1.3 Additional specifications 14
2.1.4 Summary of specification of requirements 14
2.2 Machine Design 15
2.2.1 Design tool 15
2.2.2 Machine Design work 17
2.2.3 Machine characteristics 23
2.3 Prototyping and Measurements 27
2.3.1 Prototype build 28
2.3.2 Measurements 29
2.4 Conclusions from the Liceniate work 37

3 Thermal Model Evaluation **41**
3.1 Permanent magnet temperature dependence 41
3.2 Iron core temperature dependence 43
3.3 Simulations 44
3.3.1 No load conditions 44
3.3.2 Loading conditions 44

3.4 Verifications of the temperature dependent model . . . 47
3.4.1 No load heat measurements . . . 48
3.4.2 Heat measurements during loading conditions . . . 52
3.5 Concluding remarks on the temperature model evaluation . . . 56

4 Skewing analysis **59**
4.1 Analytical approach . . . 59
4.2 Finite element simulations . . . 60
4.2.1 Implementation of skewing in the simulation tool . . . 60
4.2.2 Simulation result . . . 62
4.2.3 Apparent skewing factor . . . 63
4.2.4 Torque ripple reduction . . . 66
4.2.5 Linked magnetic flux with skewing . . . 68
4.3 Torque ripple measurements . . . 70
4.3.1 Test set-up . . . 71
4.3.2 Measurement results . . . 71
4.3.3 Measurements compared to simulations . . . 79
4.4 Discussion and conclusions from the skewing analysis . . . 82

5 Loss mapping **85**
5.1 Introduction . . . 85
5.2 Mechanical losses . . . 86
5.2.1 Windage losses . . . 86
5.2.2 Bearing losses . . . 89
5.2.3 Additional friction losses . . . 93
5.2.4 Resulting mechanical losses . . . 96
5.2.5 Measurements on the mechanical losses . . . 98
5.2.6 Concluding remarks on the mechanical losses . . . 103
5.3 Stator core losses . . . 106
5.3.1 Theoretical background . . . 107
5.3.2 Stator core loss model used in the machine design process . . . 109
5.3.3 Magnetic flux density patterns and flux density locus . . . 112
5.3.4 Iron losses imposed by manufacturing . . . 117
5.3.5 Measurements on the stator iron core losses . . . 121
5.3.6 Revised iron core losses based on the measurements . . . 142
5.3.7 Concluding remarks on the iron core losses . . . 144
5.4 Rotor losses . . . 145
5.5 Winding losses . . . 148
5.5.1 DC copper losses . . . 149
5.5.2 AC copper losses . . . 150
5.5.3 Copper losses from measurements . . . 156
5.6 Loss mapping summary and over all concluding remarks . . . 157

5.6.1 Total losses from simulations . . . 157
5.6.2 Efficiency measurements . . . 159
5.6.3 Summary of the loss analysis . . . 165
5.6.4 Conclusions from the loss analysis . . . 167

6 Discussion and Conclusions **169**
6.1 Conclusions . . . 169
6.2 Discussion . . . 171
6.3 Future work . . . 176

Appendices **179**

A Park Clarke transformation **181**

B Torque transducer measurement uncertainties **185**

C Proximity loss derivation **189**

D Nomenclature **193**

Acknowledgements

Finally, with the Christmas lights twinkling outside, the time has come to type the last sentences in my thesis. Next to the computer lies a booklet with Lucia songs from my kids pre-school. *"Med mycket möda och stort besvär"* it says in one of the songs. These words could easily have been used to describe parts of (what turned out to be) the last 9 years of my life. Luckily, that would not have been the whole truth. Actually not even close. Looking back, most of the time, this work has instead offered so much joy and so many cheerful moments. Every so often due to all the persons that have come to cross my path and that I have been given the honour to share the road with.

One of the persons that have been there throughout the full 9 years and more than that is my main supervisor; Mats Alaküla. As mentioned in my Licentiate thesis, the similarities to professor Dumbledore is striking. He may have lots of activities going on and he may be be hard to catch from time to time, but when he shows up, it is always with absolute commitment and loads of good ideas and encouragement. I never have such faith in myself as a researcher, as after a meeting with Mats.

Another faithful companion down the road is my co-supervisor Avo Reinap. Someone once described him as poetic when providing just the right amount of direction in a discussion. I for one would sign up on that statement at any time. No one has the ability to make you think for yourself as Avo. Add a healthy attitude towards the research community and a great sense of humour and you get an outstanding guide along the way towards enlightenment. This being said without even mentioning the magic he can do with errant Matlab code.

All the colleagues at Volvo deserve being mentioned. If it had not been for you, the work could not have been done. This goes both on the crucial turns, such as giving me the opportunity to start and the conditions to transact, as well as the seemingly minor favours such as listening to the theories on why the measurements don't match. My "sister in PhD", Zhe Huang, who has been a part of both the research group in Lund and the team in Gothenburg, has meant a lot to me. Always happy and with good insight in concluding a PhD, she has been of much help. Andreas Gillström has always been there to help with setting up the machine control and testing, as well as to discuss whatever question I come up with. Anders Hedman has once again provided invaluable proof reading and sanity checks on all (and I mean all) the pages. Any typo found in the book has been added after his scrutiny. Azra Selimovic and the entire business function made me feel welcome in my new group and bedded for the completion of my work. Here, not the least Pär Ingelström has provided a solid pool of information from which I have learned a lot.

Furthermore, the entire division in Lund should of course be acknowledged. With the risk of unintentionally leave someone out, Carina Lindström, Getachew Darge, Ulf Jeppsson,

Gunnar Lindstedt, Henriette Weibull and Ulrika Westerdahl, you have all provided excellent support. And whenever I show up in Lund, there has always been someone to discuss with and to listen to for new interesting ideas. Sebastian Hall (nowadays my Volvo colleague as well) has helped a lot with the machine testing as well as with straighten out any confusion around whatever equation that have come in my way. Francisco Marquez, who is as competent in the field of electric machines as in mingling on conferences, is always a pleasure to talk with and listen to. Gabriel, Anton, Samuel, Lars, Philip, Max and everyone else that I in my weariness might have forgot: It has always been hard to answer the question what I'm doing in Lund. I hardly know myself, yet every time I return, I have learned so much and it is all thanks to you.

The possibilities for doing all of this are to large extent thanks to the supporting functions provided by Staffan and Britt in Uppåkra. The extra service in sending the kids down the stairs during early mornings has been especially appreciated!

Obviously, my dad and especially my mum have made this possible in so many ways. Also, getting together with my siblings in the "Chaotic-gatherings" is of good help to clear the mind and provide a healthy perspective on things.

Last but definitely not the least; when the journey started 9 years ago, it was in company with a lovely girlfriend. As time has passed, the company have grown to also include two lovely kids. Truly the greatest gifts I have ever been given. *Alicia och August, ni skulle bara veta hur mycket jag älskar er och hur mycket ni betyder för mig!* And Caroline, the only person who has been looking forward to this day as much as I have; thank you for everything. Without you there would be nothing of this.

Nu Alicia, nu är min bok klar! "Boken om en motor som gör så att det blir mera vroom vroom! – Fast utan vroom!"

Rasmus Andersson
Gothenburg, December 2018

Popular Scientific Summary

The automotive industry has been dominated by internal combustion engines for more than a century. At the early days of motorized road transportation, both electric and petrol driven cars was built. However, with the easily accessible and energy dense fuel, the electric cars eventually became obsolete in favour of those driven by petrol. As the global warming has become a topic of increased concern, the locally emission free electric propulsion alternative has resurrected as a technology worth looking into.

The electric machine, being a transformer between electrical and mechanical power, has been around since the first half of the 19th century. When transforming from electric to mechanical power, the machine works as a motor. When energy is transformed the other way the machine functions as a generator. Either way, this is achieved with a magnetic field in the stator interacting with another in the rotor. Although being more efficient than a combustion engine, the waste product is still heat that needs to be dissipated. Motors have been common in e.g. manufacturing plants for a long time and the same goes for generators in different kind of electrical power plants. The nature of an electric machine is hence not only opening for the possibility of more energy efficient propulsion, but also to recover energy while braking.

As the electric traction machine is entering the vehicles again, the seemingly mature technology is faced with a number of new challenges. One of the most basic and important ones is the fact that the machine has to be able to fit in the vehicle and still provide sufficient power. This is pushing the limits of the power density and related to that, the cooling capability and efficiency. Maximum power requested from the machine is during accelerations and retardations (the machine works as a generator while breaking) or when driving uphill. This sets the peak power requirement. Since less power is needed to run a vehicle at constant speed, average power is lower than during accelerations and retardations. Average power is often referred to as continuous power. The span between peak and continuous power is therefore generally large. This differ from a typical non-automotive setting, such as in an electric power plant or in a fan. Above all of this, cost is a strictly limiting factor and must be kept low in order to obtain a viable machine.

One way to address the concerns of increased power density and reduced cost is to look into increased rotational speeds. Since power is equal to torque times rotational speed, which allows for lower torque without compromising on the power. This can be compared to riding a bicycle at different gears. At a high gear when the pedals are moving slowly, the biker has to have big muscles to convey the bike. With a lower gear, the pedals rotate faster with less muscle force. Hence a slimmer person can take over the handlebar. And as with the bikers, lower torque means a smaller machine meaning that both the power density and the material cost will benefit.

This research project is on designing an electric machine intended for heavy commercial vehicle applications such as trucks and buses. This includes studying how the machine is used in the vehicle in order to obtain the restrictions and requirements on the machine. A simulation environment is used to design the machine and a prototype is built to verify the performance. Focus throughout the project is also to gain understanding and knowledge relevant when designing a machine for these specific applications. This applies both on the vehicle side as in what happens if one of the requirements is not fulfilled and also on the machine side in terms of the impact of a specific requirement from the vehicle. Some more in depth studies are also performed. These are on various kinds of loss contributors or unwanted heat sources in the machine, along with a study on the consequences of twisting or skewing the machine slightly. This to obtain a more smooth power output from the machine.

The resulting machine has the shape of a cylinder about as wide as the short end of an A4 paper (i.e. slightly more than 20 cm), is 40 cm long and capable of providing around 100 kW continuously and up to 180 kW for shorter periods of time. This corresponds to around 240 break horse powers that can be used during accelerations and retardations and almost 140 break horse powers that can be used for as long as energy is provided. This means that the machine is capable of propelling a medium sized truck or bus. In a multiple configuration, a heavy-duty truck can be propelled.

Populärvetenskaplig Sammanfattning

När de första motordrivna fordonen började ge sig ut på vägarna i mitten av 1800-talet var det lika vanligt med elektrisk framdrivning som med förbränningsmotor. Efterhand som resorna blev längre blev fördelen med att snabbt kunna tanka bilen mer uppenbar. I början av 1900-talet, när den elektriska startmotorn dessutom gjorde bilarna mer användarvänliga, slog pendeln över till bensin- och dieselbilarnas fördel. Nu, ett sekel senare, i och med debatten kring global uppvärmning har elbilen återuppstått som ett mer miljövänligt alternativ.

Elmaskinen uppfanns i början av 1800-talet och kan ses som en omvandlare mellan mekanisk och elektrisk effekt. Tekniken bygger på att elektrisk ström i en ledare omges av ett magnetiskt fält och omvänt, att ett magnetiskt fält som passerar en ledare skapar elektrisk ström. Den mekaniska rörelsen uppstår av att magnetiska nord- och sydpoler attraherar varandra. Om en elektrisk ström skapar en mekanisk rörelse, t.ex. driver en fläkt, arbetar elmaskinen som en motor. Omvänt kan en mekanisk rörelse, t.ex. en vind som driver runt fläktbladen"i ett vindkraftverk, skapa elektrisk ström. Då kallas elmaskinen för en generator. Alla elmaskiner fungerar alltså både som motor och generator. Restprodukten från energiomvandlingen är värme som behöver kylas bort. Förutom att elmotorn är mer energieffektiv än en förbränningsmotor, kan elmotorn alltså drivas som en generator vid inbromsningar och därmed ta tillvara på en del av rörelseenergin för att ladda batterierna. På så sätt minskar fordonets totala energiförbrukning ytterligare, jämfört med om det framförs med en förbränningsmotor.

När elmaskinen nu åter ska användas för framdrivning i bilar, uppstår några nya krav. Det kanske viktigaste, men samtidigt mest självklara, är att elmaskinen måste få plats i det utrymme där den ska sitta. Den måste dessutom ha effekt nog för att kunna driva fordonet framåt, vilket skapar krav på hög effekt-täthet, d.v.s. hur mycket effekt det går att få ut per volymenhet. I samband med det krävs också hög verkningsgrad och god kylning. Högst effektuttag, då elmaskinen får arbeta som mest, uppstår vid accelerationer, i uppförsbackar och vid inbromsningar (då elmaskinen fungerar som en generator). Ju mer effekt som kan tas tillvara vid en inbromsning, desto mer kan batteriet laddas. För att köra i konstant hastighet krävs inte lika mycket effekt, vilket gör att den genomsnittliga (eller kontinuerliga) effekten ofta är klart lägre än maxeffekten. Spannet mellan kontinuerlig- och maxeffekt är därför generellt större än för historiskt vanliga tillämpningar såsom t.ex. i fläktar eller i elkraftverk. Utanpå detta finns det också ett ständigt överhängande krav på att hålla nere kostnaden.

Ett sätt att höja effekttätheten och samtidigt få ner kostnaden är att öka elmaskinens varvtal. Eftersom effekt är lika med vridmoment multiplicerat med varvtal kan vridmomentet därigenom sänkas med bibehållen effekt. Detta kan jämföras med att kunna växla på en

cykel. Med en hög växel, när pedalerna går långsamt behövs mycket muskelstyrka för att föra cykeln framåt. Genom att växla ner, kan tramporna drivas runt snabbare med mindre kraft på pedalerna och en mindre stark person kan därför ta över tramporna. På samma sätt som för cyklisten betyder ett lägre vridmoment att elmaskinen kan göras mindre. Eftersom samma effekt kan tas ut ur en mindre maskin, ökar effekttätheten samtidigt som mindre materialåtgång leder till en lägre kostnad.

Forskningsarbetet som presenteras här behandlar design av en elmaskin avsedd för framdrivning av tunga fordon, såsom lastbilar och bussar. Fokus genom arbetet är att skapa kunskap och förståelse kring vad som är viktigt för en elmaskin i dessa specifika tillämpningar. Som ett första steg genomförs studier av hur elmaskinen ska användas, dels för att få en bild av de kravspecifikationer som ställs och dels för att förstå vilka begränsningarna är. Det skapar också en viss förståelse för vilka krav som är viktiga för fordonet och vilka som mer har en karaktär av att vara önskvärda. Designarbetet av elmaskinen görs i en datasimuleringsmiljö och när önskad prestanda uppfylls, tillverkas en prototyp. Denna används för att verifiera simuleringsresultaten samt för några mer djupgående studier. Dessa behandlar förlustkällorna i en elmaskin och hur de bidrar till de totala förlusterna, samt även en analys på konsekvenserna av att implementera en liten vridning (så kallat ”skewing”) i elmaskinen. Detta är något som görs för att få ett jämnare vridmoment och därmed en mindre skakig rotation.

Resultatet av designarbetet är en 40 cm lång, cylinderformad elmaskin med ungefär samma bredd som kortsidan av ett A4-papper (dvs strax över 20 cm) och som kan leverera runt 100 kW kontinuerligt och uppemot 180 kW under kortare perioder. Detta motsvarar cirka 240 hästkrafter som kan användas vid accelerationer och inbromsningar, samt nästan 140 hästkrafter som kan användas så länge som det finns energi att tillgå. Detta innebär att den uppfyller de krav som ställs för att kunna driva en buss eller en medeltung lastbil. I en uppsättning med flera elmaskiner kan den även användas för att driva de allra tyngsta lastbilsekipagen.

Chapter 1

Introduction

As the trend towards electrification is moving rapidly within the automotive industry, so must the development of the key components. One obvious key component is the electric machine propelling the vehicle. Despite the electric machine being a seemingly mature component, the demands from the evolving market are consistently challenging the boundaries. Cost and size must be reduced while power and power density must be preserved and increased. The load profile with a large span between continuous or average power and peak operation is also different to a typical industrial application.

With the machine becoming an important component in the propulsion of vehicles, there is a need to know both sides. In one end the possibilities and limitations of an electric machine should be fully mastered. In the other, the requirements from the application have to be understood. It is important to know which of the desired properties that are dimensioning and drive the cost of the machine. At the same time, it is also important to be able to distinguish between absolute requirements and nice to have features in the vehicle. Without proper knowledge within both the relevant fields, this tend to be floating. This is something that might result in an under dimensioned or unnecessarily expensive component.

The focus of the present thesis is on the electric machine design with consideration to a hybrid electric powertrain intended for a heavy commercial vehicle such as a truck or a bus. The machine design is based on the requirements of such an application with focus on fulfilling the peak power demands and reducing the physical size. This is done in order to reduce the bill of material, but more importantly to ensure the possibility to mount the machine within the available space in the vehicle. The design procedure, machine build and initial testing is reported in a Licentiate thesis [1]. There, the focus was on a general level rather than on in depth analyses.

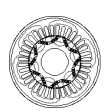

Post-licentiate work is to some extent shifting focus to a more detailed level on some important aspects. This includes: a) skewing, torque ripple and harmonics, b) power losses and loss separation and c) thermal aspects with focus on thermal dependencies. The thermal behaviour is considered in order to improve the modelling accuracy during the design process. Skewing is implemented in order to reduce noise and wear in the connecting mechanical gear transmission. The effect on the torque ripple in the machine is studied. Finally, the losses present in the machine is studied a bit deeper. The main focus here is on the speed dependant mechanical- and stator iron core losses, but attention is also directed towards the losses in the rotor and windings.

1.1 Background

At the time when the work behind this thesis was started, focus on electro-mobility was directed towards hybrid electric vehicles. This was valid for both the focus of the work, and for the entire automotive industry. As the time has progressed, the rapidly moving electro-mobility segment has shifted more towards pure electric drive-lines. This applies especially for city applications such as distribution and refuse trucks and city buses, but to some extent also for regional and long haul applications. Consequently, the focus of the work behind this thesis has turned somewhat as well. Although the component can be shared and many similarities can be seen, some details need to be addressed a bit differently.

The performance requirements set up for a hybrid electric application are in the same range as those needed to fulfil also the requirements of a fully electric powertrain. When skewing of the stator primarily is discussed and implemented, focus is on reducing the noise and wear in the gear drive connecting the machine to the conventional powertrain. A contributing factor for why skewing is implemented is also the way the machine is intended to be mounted on an already existing, high volume production transmission. Due to a limitation in torque on the shaft at which the machine is connected, the reduction in torque due to skewing is considered less significant. Regardless if skewing is implemented or not, compared to the internal combustion engine (ICE) the torque ripple of a well designed permanent magnet machine is marginal. In a fully electric application on the other hand, torque ripple should be avoided to prevent inconvenient oscillations during for example tough accelerations. On the other hand, when being the sole propulsion source, the reduction in peak torque should be valued differently compared to in a hybrid electric powertrain.

Another slight shift in focus is related to the efficiency of the machine. In a hybrid electric application, the electrification itself is providing a significant reduction in fuel consumption. The recuperated energy during decelerations makes more difference than the actual efficiency of the electric machine. As long as it is decently high, the efficiency makes less of

a difference on how often the vehicle needs to be refuelled. In a fully electric powertrain, the efficiency of the machine is more decisive for the range. An improved efficiency could mean some extra distance travelled or a reduction in system cost. This due to a possibility to slightly reduce the size of the energy storage. Consequently, as focus shift from hybrid electric to fully electric applications and the efficiency climbs on the agenda, a better understanding of the losses in the machine becomes more important.

Should the internal combustion engine be removed also in long haul applications, the speed range becomes a bit more important. Playing the second fiddle, the electric machine speed needs to relate to the optimal speed of the engine. When playing alone, running the machine at higher rotational speeds more continuously is a more likely operation point. Since constant vehicle speed requires less power compared to accelerations, the torque request at these conditions is comparably low. This way, the speed dependant, part-load operation points becomes more important to keep in mind.

1.2 Objectives

1.2.1 Purpose

The main objective is to reduce the knowledge gap between the automotive industry and one of the key powertrain components; namely the electric machine. The thesis addresses:

- Machine specification from an application and system perspective with the knowledge on machine design challenges
- A machine design process, involving model and material/production databases versus design outcomes
- Evaluation and analysis with focus on selected/important aspects on design evaluation process

This is done with focus on a machine suitable for electric propulsion of heavy commercial vehicles such as buses or trucks. One such electric machine is the permanent magnet synchronous machine. A part of the work is also to improve the simulation environment used in the design process.
The purpose of this first half of the project is also to be the base for a thesis for the degree of Technical Licentiate.

As the prototype is built and verified against the simulation results, some more detailed studies are performed. These studies are on the whereabouts of:

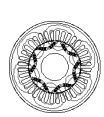

- How the operating temperature affects the performance and behaviour of a permanent magnet synchronous machine.
- How skewing affects the torque generation in an electric machine. This includes both the desired torque and the unwanted torque ripple due to cogging and harmonics in the electromagnetic torque.
- How relevant loss contributors in an electric machine are generated, distributed and modelled. This with the purpose to both obtain a more accurate prediction on the losses, but also to enlighten the difficulties in achieving just that.

The purpose of this second half of the project is also to be the base for a thesis for the degree of Doctor of Philosophy.

1.2.2 Method

In order to perform the tasks defined in the previous subsection, different relevant simulation environments are first utilized. This includes modelling and simulation in Matlab and Matlab/Simulink to generate a list of requirements on a traction machine for the intended application. The electromagnetic design of the machine is developed with a design tool [2] developed at the department of Industrial Electrical Engineering and Automation (IEA) at the Faculty of Engineering (LTH) at Lund University. This tool makes use of a two dimensional finite element (FE) modelling software controlled with a script that is generated in a Matlab environment. When the FE simulations are completed, post precessing is done in Matlab as well. Running the simulations from Matlab opens for sweeping the design parameters, allowing for a vast number of machine designs to be simulated in a semi automatic fashion.

When the machine design fulfils the defined requirements, a prototype is built and used in the analysis work. By adopting the post process environment in the design tool, deeper analyses of various kinds are made possible. This includes the response to increased temperature in the permanent magnet machine and how skewing affects the torque and torque ripple. The implemented improvements are verified with measurements on the prototype.

Loss separation is achieved with a temporary re-build of the prototype machine. The rotor with its permanent magnets is replaced by a dummy version entirely made of steel. In this way, the parts of the speed dependant losses with mechanical and aerodynamic origin are separated from the iron losses. This is otherwise difficult to achieve since the losses induced in the iron core by the permanent magnets behave similarly as those associated to friction and windage. The underlying theory behind the speed dependant losses is consulted in the subsequent analysis work. When the various loss contributors have been investigated and mapped, focus is widened to include the complete machine.

1.3 Contributions

The contributions in the present thesis, besides the personal development and experience gained by the author, are related to the development of a permanent magnet synchronous machine intended for electric propulsion of heavy commercial vehicles. With this thesis, a compilation of a number of studies is presented with the intention to be used as a guide for those working with design of electric propulsion machines. The contributions in the concerned topic are listed here:

- In combination with [1], aspects important to consider in an electric machine design process are described in detail. This includes:
  - Electromagnetic aspects related to e.g. the shape of the stator and rotor together with the selection of material.
  - Mechanical strength evaluation of the rotor in order to cope with the centrifugal forces, both within normal operating range and in over speeding events.
  - Evaluating the manufacturability of the design in order to ensure a practicable electric machine build.

  In addition to this, aspects important to consider when working on a traction machine for heavy vehicles are covered as well. This implies in particular the limited geometrical space and the interaction with the existing heavy vehicle drive train.
- In combination with [1], a documented complete sequence of specification – design – manufacturing – testing of a traction machine intended for a heavy vehicle application.
- Further evaluation of an alternative test method, so called ”dynamic testing”, to the traditional bench testing, when characterizing electric machines.
- Further development and verification of the design tool used at the department at Lund University. This includes:
  - A thermal dependency model of the magnetic properties, verified by measurements.
  - An analytical approach to take the mechanical strength of the suggested rotor design into account.
  - A well documented model on implementing skewing in the design stage of the permanent magnet synchronous machine, verified by measurements.

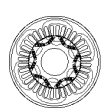

- A thorough review on how skewing affects the performance of an interior permanent magnet synchronous machine (IPMSM). The definition of the load dependant, so called ”apparent skewing factor” describes the influence on the torque output from a skewed machine. It is also stated that and explained why the torque is affected differently in different parts of the load map. The typical operating region in the *dq*-reference frame of a traction machine is compared to the apparent skewing factor in order to illustrate the impact of skewing on such a machine application. Together with a study on how the linked magnetic flux is affected, the analysis is also to some extent able to predict that skewing should impact the efficiency of the IPMSM.

- An overview of losses present in a permanent magnet synchronous machine, including loss torque from mechanical- and iron core losses, rotor losses and losses in the stator windings. The study is providing input to how the losses typically are distributed in a corresponding electric machine. The result can also be used to indicate where to put the effort when analysing the losses in a permanent magnet synchronous machine.

- A list of a number of different mechanical loss contributors that can be found in an electric traction machine. The analytical models are to some extent verified with measurements. This work can be used for estimating the order of magnitude of the mechanical losses in similar machine designs.

- An in depth review of the speed dependant losses in the stator iron core in a permanent magnet synchronous machine. The origin of the iron losses and how different manufacturing processes and machine controls can affect the iron losses are compiled and described. A detailed description on a suggested alternative way to establish the iron losses from on load machine testing is presented. An example is given on how the iron loss model can be adjusted to provide a more accurate prediction. This is based on simple roll-out tests.

- Throughout the work that provides the basis for the above mentioned contributions, a functional prototype capable of propelling a heavy commercial vehicle was delivered. The elaborated machine design has been used for various other studies on electric machines and how to utilize them in a clever manner in order to further improve the benefits of electrification of the vehicle. Examples of this are:

  - A study on the possibility to use the machine for synchronizing the gearbox during gear shifts [3].
  - A study on using the machine as a galvanically isolated rotating transformer in an on-board charging concept [4–6]. Here, the machine is rewound as a six phase machine with otherwise unchanged properties.

1.3.1 Publications

Publication part I[1]

I Andersson, R., Reinap, A., Alaküla, M. (2012), "Design and Evaluation of Electrical Machine for Parallel Hybrid Drive for Heavy Vehicles". *20th International Conference on Electrical Machines (ICEM2012)*, Marseille, France, Sept. 2-5, 2012, pp. 2622-2628.

In addition to this, the following publications are for consistency reasons intentionally left outside the scope of the present thesis. The content describes the design work on an alternative machine design with laminated stator windings and axially segmented phases.

II Andersson, R., Högmark, C., Reinap, A., Alaküla, M. (2012), "Modular Three-phase Machines with Laminated Winding for Hybrid Vehicle Applications". *International Electric Drives Production Conference and Exhibition (EDPC2012)*, Nuremberg, Germany, Oct. 16-17, 2012.

III Högmark, C., Andersson, R., Reinap, A., Alaküla, M. (2012), "Electrical Machines with Laminated Winding for Hybrid Vehicle Applications". *International Electric Drives Production Conference and Exhibition (EDPC2012)*, Nuremberg, Germany, Oct. 16-17, 2012.

IV Reinap, A., Marquez-Fernandez, F.J., Andersson, R., Högmark, C., Alaküla, M., Göransson, A. (2014), "Heat transfer analysis of a traction machine with directly cooled laminated windings". *4th International Electric Drives Production Conference and Exhibition (EDPC2014)*, Nuremberg, Germany, 30 Sept. – 1 Oct., 2014. (Awarded best conference paper.)

Publication part II[2]

V Andersson, R., Reinap, A., Alaküla, M. (2016), "Engineering considerations on skewing of an interior permanent magnet synchronous machine for parallel hybrid electric heavy vehicles". *8th IET International Conference on Power Electronics, Machines and Drives (PEMD2016)*, Glasgow, Scotland, 19-21 April, 2016.

VI Andersson, R., Hall, S. (2016), "Evaluation of a temperature model for an interior permanent magnet synchronous machine for parallel hybrid electric heavy vehicles".

[1]Publications before Technical Licentiate Degree
[2]Publications after Technical Licentiate Degree

23rd International Symposium on Power Electronics, Electrical Drives, Automation and Motion (SPEEDAM2016), Anacapri, Italy, 22-24 June, 2016

VII Andersson, R., Reinap, A. (2016), "Loss mapping of an insert permanent magnet synchronous machine for parallel hybrid electric heavy vehicles". *International Conference on Electrical Machines (ICEM 2016)*, Lausanne, Switzerland, 4-7 September, 2016.

In addition to this, the following publication is for consistency reasons intentionally left outside the scope of this thesis. The content is on characterizing and testing a permanent magnet synchronous machine while being mounted in a vehicle and connected to the drivetrain.

VIII Hall, S., Andersson, R., Alaküla, M. (2016), "A method for in-situ characterization of PMSM traction machines". *16th IEEE International Conference on Environmental and Electrical Engineering (EEEIC2016)*, Florence, Italy, 7-10 June, 2016.

1.4 Disposition of the thesis

The outline of the thesis is as follows:

Chapter 1 is the introduction of the thesis. Here the relevance of the work is highlighted. Included is also the purpose, method and contributions, along with a list of the scientific papers published throughout the work.

Chapter 2 is providing a shorter summary of the work performed within the first half of the PhD project, previously reported for the degree of Technical Licentiate [1]. This includes setting up the specification of requirements and the work on designing the machine under investigation. The purpose with including this summary is to facilitate for the reader by providing the full picture of the entire work. In addition to the material presented in the Licentiate thesis, some additional test results from complementary machine testing is presented as well. Part of the work described in Chapter 2 is based on the content presented in paper I. A more comprehensive description of the work presented in Chapter 2 is also availible in [1].

Chapter 3 presents the work done on setting up a thermal dependency in the simulation tool used. As the material data used when setting up the model is presented at room temperature, the thermal dependency needs to be considered in order to provide a more reliable result at elevated temperatures. The work is addressing the permanent magnets as well as the iron core and the copper windings. The thermal dependency is implemented in the

pre-simulation part of the design tool used. In addition to this, the testing performed to validate the model is described as well. The validation is made both at no load and on load conditions. The result is a good match between simulations and measurements in terms of temperature dependency. Part of the work described in Chapter 3 is based on the content presented in paper VI.

Chapter 4 describes the study on how the torque production is affected by skewing in the machine. Although skewing in the investigated prototype is implemented in the stator, the principle is relevant also for skewing of the rotor. Modifications in the design tool's post processing allows for studying the axial variation introduced by skewing. This despite the fact that the simulations where performed in a two dimensional finite element environment. The axial variation affects both the orientation of the slot openings along the active length and the applied current vectors. Therefore, skewing affects the torque production differently depending on the applied currents. A load dependant skewing factor is derived by comparing the torque production from simulations with and without skewing. Tests on the prototype are used to verify the simulation results on a skewed machine. Part of the work described in Chapter 4 is based on the content presented in paper V.

Chapter 5 is a compilation of losses relevant to consider when analysing an interior permanent magnet synchronous machine. This provides a useful summary of the losses present in an interior permanent magnet synchronous machine. It also illuminates the difficulties in estimating the losses in an accurate way. The mechanical losses due to windage and friction are identified and evaluated. Measurements are used to calibrate the analytic mechanical loss model. The iron losses originally derived with the prevalent three term model are revised and partly calibrated to measurements. The literature is consulted to investigate how the iron losses in a real machine can differ from the inherently simplified models. The losses in the rotor are covered briefly, while proximity losses in the copper strands are considered along with the resistive DC-losses for estimating the losses in the windings. Part of the work described in Chapter 5 is based on the content presented in paper VII.

Chapter 6 is concluding the work presented in the thesis. This is done with a discussion on the results together with a reflection on the way of working as a PhD student connected to the industry. The choice of a rare earth permanent magnet machine in a claimed environmental friendly application is discussed. Some suggestions on complementary future work are presented as well.

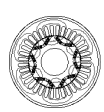

Chapter 2

Licentiate thesis summary

This chapter is a summary of the first half of the PhD work, previously presented in [1]. With a rather limited amount of set specifications, pre-studies are performed to complete the specification of requirements. This includes a concept study on where to connect the EM to the drivetrain and if applicable, with what gear ratio. Simulations on the power demand of heavy hybrid electric vehicles (HEVs) are completed. Based on these requirements, the machine is designed in a 2D finite element modelling (FEM) environment. Besides the electromagnetic characteristics, thermal and mechanical aspects as well as manufacturability are considered in the design phase. The final design is prototyped and initial testing is done to verify the simulation tool used in the design work. The content in this chapter is described in more details in [1].

2.1 Machine specifications and requirements

The machine studied in the PhD project is designed as a traction machine to be used in a heavy parallel hybrid electric vehicle. Additional powertrain components are those existing in a heavy vehicle, among others e.g. an automatic mechanically engaged transmission (AMT). Given parameters are for example the DC-voltage based on the available energy storage system (ESS) and the number of phases based on the available power electronic converter (PEC). It should also be possible to propel the vehicle in electric-only mode, hence with the internal combustion engine (ICE) turned off and disconnected. Other constrains are related to integration of the machine in the vehicle. The cooling should be accomplished with integration to other components. Possible options are oils e.g. from the gearbox, or water ethylene glycol (WEG) mixture used by the PEC. Finally, the most important and at the same time most obvious constraint is that the machine must fit in

the vehicle. This put limitations on the machine size and depending on where to mount it, also on the form factor in terms of length versus diameter.

2.1.1 Concept selection

Different machine connection points considered in the pre-study are either before, after or on the conventional AMT gearbox. The first option means mounting the EM between the clutch and the gearbox (sometimes referred to as P2). This implies a pancake shape with clear geometrical restrictions. This applies in terms of length since it affects the length of the complete power-train and also in terms of diameter to meet the SAE (Society of Automotive Engineers) standard for clutch housings [7]. Further, the rotational speed of the machine is limited to that of the ICE. Being mounted before the gearbox makes it possible to shift the torque from the EM with the AMT gearbox.

Secondly, mounting the EM after the transmission (sometimes referred to as P3 or P4) opens for a number of different locations which allows for a more flexible selection criteria in terms of physical EM size. By introducing a gear reduction, the EM speed could also be more freely selected. Since no gear shifting is possible, the EM top speed will have to match that of the vehicle. Preferably, the efficiency sweet spot shall be frequently utilized during the drive cycles. Furthermore, the torque needs to be sufficiently large to meet the desired vehicle driveability and startability.

A third option is to make use of the Power Take Off (PTO) in the AMT gearbox (a variant of what is sometimes referred to as P2.5). Thereby it is possible to shift gear for the EM. At the same time there is a high flexibility in terms of geometrical shape and if connecting the EM with a gear drive, also in rotational speed.

After immersing in the pros and cons with the different concepts, the on gearbox option is selected for the continuation of the work. Thus, the machine will be connected to the gearbox PTO. In order to obtain a compact driveline, the desired physical location for the machine is side-parallel to the gearbox. A principle sketch on the drivetrain layout is presented in Figure 2.1.

2.1.2 PTO gear analysis

Next step affecting the EM is whether to use a gear drive and if so, the gear ratio. This is evaluated with simulations in Matlab. A guidance towards the final gear ratio and corresponding machine design is obtained by evaluating a vast number of possible machines based on a number of assumptions and restrictions. Among others this includes:

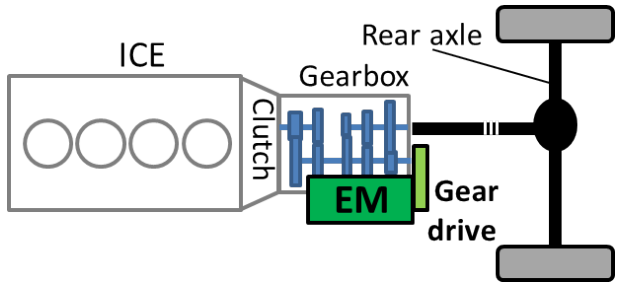

Figure 2.1: Principle sketch of a parallel hybrid electric drive train with a PTO mounted EM

- A constant torque and power contribution on the low speed side of the gear reduction (hence at the PTO of the conventional gearbox).
- A desired acceleration capability to facilitate gear shifts in the conventional gearbox.
- A range of different machine outer diameters with a defined relation to the airgap diameter.
- A restriction in the relation between machine length and airgap diameter.

In order to make a fair comparison between all machine variants, the shear stress τ is kept constant for all machines. This unit is often used for comparing machines [8, 9]. The shear stress is defined as the force F per airgap area A. Here, F is the force applied from the rotor related to the stator due to the developed torque T. This relation is shown and elaborated in (2.1) where r_A is the airgap radius and l_R is the length of the rotor, hence active machine length. By solving (2.1) for l_R which is done in (2.2), the machine length and hence volume is determined for all considered outer diameters at all considered different reduction gear ratios.

$$\tau = \frac{F}{A} = \frac{T}{r_A} \cdot \frac{1}{2\pi \cdot r_A \cdot l_R} = \frac{T}{2\pi \cdot l_R \cdot r_A^2} \tag{2.1}$$

$$l_R = \frac{T}{2\pi \cdot \tau \cdot r_A^2} \tag{2.2}$$

The selection criteria are weighted on a combination of sufficiently fast acceleration, a reasonable length versus diameter ratio and the volume of the machine. The assumption used is that a smaller machine needs less material and hence has a lower cost. All and all, it is concluded that the machine benefits from a higher PTO gear reduction ratio and a long and slender machine design.

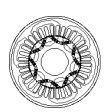

2.1.3 Additional specifications

A pre-study is also conducted looking at the power required to operate a heavy HEV. Here it is concluded that the continuous power demand is rather low, while the peak power is decisive for the potential reduction in energy consumption. In order to leave a margin for adding auxiliary loads such as electric power steering and climate control, the continuous power is set higher than indicated by the simulations. This pre-study is performed in a Matlab/Simulink environment developed for educational purposes at the department of Industrial Electrical Engineering and Automation. The simulation environment is described further in [10] and [11].

The desired concept with the electric machine mounted side-parallel to the gearbox gives a fixed space claim in terms of outer diameter and overall length. Another limitation is related to the mechanical integrity of the gearbox shaft at which the machine is connected. This gives an upper limit in the torque transmitted from the machine. The reason for this is the intention not to make any changes on the existing high volume product.

With the machine mounted in close connection to the gearbox, the transmission oil is selected as cooling media. This opens for implementing cooling directly on the active parts. That compensates for the lower specific heat compared to water or WEG [12].

With the possibility to shift EM speed in the gearbox, a burst speed demand is introduced. This is based on the requirements put on a flywheel that is supposed to be able to handle 50% over-speed in case of a faulty gear shift.

2.1.4 Summary of specification of requirements

The specifications for the machine design based on the given restrictions and the outcome from the pre-studies is summarized in Table 2.1. Here, the PTO gear ratio is stated with a target value, rahter than as the exact number. In addition to what is mentioned in previous subsections, the high peak power demand in combination with a large desired constant power speed range (CPSR) motivates for designing an interior permanent magnet synchronous machine (IPMSM) [13]. Moreover, the over-speed requirement is considered when an IPM design is selected rather than surface mounted magnets. The voltage range is imposed by the available energy storage system (ESS). The variation in range is a result of varying loading conditions and different state of charge. The available power electronic converter is setting the current limit at peak operation.

Table 2.1: Specifications of requirements

Machine type	-	3 phase IPMSM	-
Total length	l_{tot}	< 400	mm
Outer diameter	OD	< 220	mm
Continuous power	P_{cont}	80	kW
Peak power	P_{peak}	180	kW
PTO gear ratio	-	6	-
Peak torque	T_{peak}	< 250	Nm
Top speed	n_{max}	15000	rpm
Burst speed	n_{burst}	>22500	rpm
Maximum current	i_{max}	320	A_{rms}
DC-voltage range	V_{DC}	530-725	V
Coolant medium	-	Transmission oil	-

2.2 Machine Design

This sub chapter summarizes the machine design process and presents the resulting machine.

2.2.1 Design tool

The machine design work is done in a Matlab and FEMM [14] based design tool [2] developed at the department of Industrial Electrical Engineering and Automation (IEA) at the Faculty of Engineering (LTH) at Lund University. The design tool is also described and refined in [15]. The simulations are initiated in a Matlab file that generates a script executing the 2D finite element analysis (FEA) software. Geometrical symmetries are utilized to reduce the computational effort of running the FEM simulations. The fact that the process is controlled from Matlab makes it possible to sweep different design parameters. This enables for setting up a batch of simulations and let the simulation program run over night or weekends. It is also possible to implement simple analytical pre-simulation loops in the set-up file in Matlab. This could for example be a mechanical integrity check of the stator teeth or around the magnets in the rotor. By only considering machine designs viable to be built only, the computational effort can be reduced further. The post simulation analysis is also performed in Matlab which opens for further analysis of the simulation result. Being an in-house developed design tool, improving and implementing new features is a part of the process of designing a new EM.

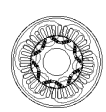

Using a 2D- rather than a 3D FE simulation environment gives a possibility to refine the mesh size to the expense of loosing one dimension. Introducing a 3rd dimension makes the computational effort increase significantly. This limits the possibility to execute simulations with a high number of mesh elements. Consequently, in order to get an acceptable simulation time the mesh elements will be larger than if simulated in a 2D environment. Small mesh size is found to be of special importance in highly saturated areas such as close to the airgap. The inherent principle of a radial flux machine makes it excessive to simulate along the axial direction. The part of the machine where the flux has an axial component is close to the machine ends and at the end windings. This due to the fringing effect at the end windings. With a reasonably long machine, these end effects are marginal and can be considered negligible [16, Ch.3.2]. The inaccuracy of a more coarse mesh size in 3D simulations is considered to be higher than if the end effects are neglected. The design parameters defined in Table 2.1 indicate a rather long and slender machine. Then the 2D simulation environment should be sufficient to give an acceptable prediction of the machine performance.

Design tool development

Besides the actual design work performed during the development of the machine design, the design tool is continuously improved in the process. For every machine design that is prototyped and tested, there is a chance to enhance and verify the design tool. The learning is achieved when comparing the simulation results to the measurements. As is concluded later on in this thesis, the conformity between simulations and measurements is satisfactory.

Alternative machine design In addition to the design work of a conventional 3-phase radial flux machine performed for this thesis, a substantially different machine design is developed as well. This design work is performed as a side project to the main scope of the thesis and is therefore only briefly mentioned here. The learning from this side project is utilised when adopting the simulation tool to analyse skewing in the 3-phase prototype. This is covered in Chapter 4.

The alternative machine design is based on the idea of having laminated windings rather than a conventionally wound stator. More information on this concept is presented in [17] and [18–20]. In order for the laminated phase windings not to intervene with each other, the phases are formed by wave windings and distributed axially. This is in contradiction to the circumferential distribution in a conventionally wound machine. Each phase is designed as a separate segment and stacked to form a multiple phase machine. Being a 3-phase machine, each phase segment is shifted 120 electrical degrees. A 3D model of the alternative machine design can be seen in Figure 2.2.

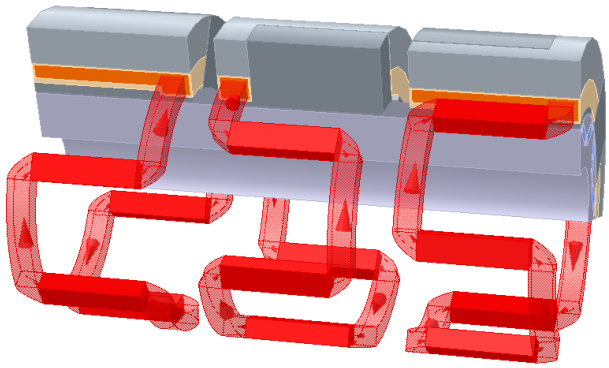

Figure 2.2: Laminated winding machine with three axially distributed phase segments

Since the twisting between phases means a variation as function of axial position, a 3D design environment ought to be used. However, with the possibility to do vast post simulation modifications, the recurrent periodicity in the machine design can be utilized. The FEM simulations are performed on one phase only and the result is multiplied and shifted with 120 and 240 degrees respectively to represent the other phases in the complete machine. A more thorough description of design tool development for this purpose is found in [19] where 3D simulations also are used to verify the 2D simulation results. Due to difficulties during manufacturing with e.g. the intended iron core material and radial distribution of the winding turns, the performance of the prototyped machine does not meet the expectations. As a consequence the measurements performed on this machine are very limited. The indications when adopting the simulation tool with the material used in the prototype are still in favour for evaluating the validity of the design tool. As this evaluation not is the main part of the content in this thesis, the results on this alternative machine design are not covered further.

2.2.2 Machine Design work

This subsection covers the most important conclusions from the machine design work. Focus is on the resulting machine characteristics based on the simulation results. Again, a more thorough review of the results is available in [1]

Electromagnetic aspects

The electromagnetic design work is conducted in the simulation tool presented in the previous subsection. Numerous machine designs are iterated with focus to fulfil the power

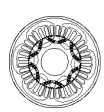

requirements within the limited available space. The design work starts with some overall simulations settling the number of poles, number of slots and airgap radius. The copper fill factor is determined based on previous experience at the department.

Parameters investigated in the rotor are e.g. magnet size, position and mutual angle as well as flux barriers to direct the Permanent Magnet (PM) flux to the stator. Also manufacturing aspects are considered, e.g. by taking the tolerances when producing the laminates and magnets into account. Magnet grade is selected to give a sufficiently large safety margin to overheating. Remanence and coercivity are also considered to give sufficient torque. Due to the higher ratings of transverse field die pressed (TP) magnets compared to axial field die pressed (AP) magnets [21, pg.879-880], TP is selected despite a higher cost. This is motivated by that the cost difference is driven by the manufacturing procedure and that manufacturing related cost is more likely to go down in the future. Since the PM raw material cost is high the consideration is to utilize the available material as much as possible. The magnet grade selected for the prototype and therefore also in the simulation environment is Vacodym 863 TP [22].

The stator design is evolved in a similar iteration process as that for the rotor. The stator tooth width and length are varied to obtain sufficiently large flux paths in the stator teeth and yoke and still have sufficiently large slots. This is needed in order to maintain a reasonable current density in the windings. Also the implementation of tapered teeth or not is analysed. Manufacturing aspects are for example the rounded base of the teeth with the copper fill factor in mind. The tooth tips are designed to facilitate the insertion of the copper wires and still hold the windings in place once mounted. Since all parameters are affecting each other, the stator and rotor design iterations are numerously repeated, consistently narrowing down the details until a sufficiently good final design is obtained. The resulting final design is presented in Figure 2.3.

The end winding configuration is selected in consultation with the prototype manufacturer with focus on minimizing the extruding end winding length. The final selection is an integer slot 1-6 configuration, conceptually presented in Figure 2.4. In addition to the total machine length, manufacturing aspects and a potentially high fill factor are considered in the selection criteria.

Mechanical aspects

The mechanical aspects considered in the design work is related to the mechanical integrity of the rotor, the stator teeth and the mechanical resonance frequency. The rotor strength is monitored with an analytical model on the mechanical stress due to centrifugal action when spinning the machine. Based on each generated geometry, the iron bridge between the magnets (within a pole) is exposed to a tensional force due to the weight of the outward

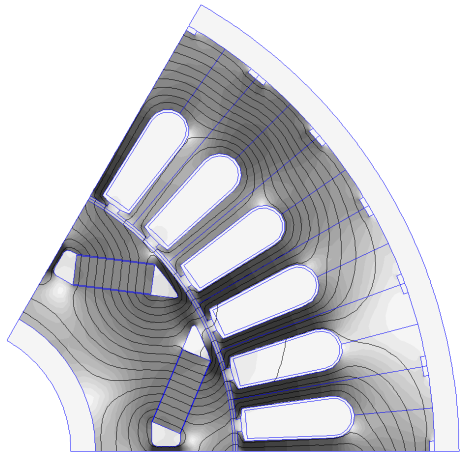

Figure 2.3: Electromagnetic design of the prototyped machine

material pulling towards the airgap. The yield strength σ_{yield} of the steel laminations is used to derive a maximum rotational speed ω_{max} at witch the rotor would burst. This is presented in (2.3) where the iron bridge width d_b, active length (or machine height) h_m and the mass m_{act} acting on the iron bridge are defined or estimated by the rotor geometry. The radius r_{act} is the distance to the centre of gravity of m_{act}. Included in m_{act} is typically the mass of the magnets and the part of the rotor between the magnets and the airgap. The epoxy used to glue the magnets is not considered but as a safety margin.

$$\omega_{max} = \sqrt{\frac{\sigma_{yield} \cdot d_b \cdot h_m}{m_{act} \cdot r_{act}}} \tag{2.3}$$

In order to obtain a safety margin in the result, all estimations are made conservatively, e.g. by considering worst case in terms of stress concentrations and tolerances from the manufacturing. Also the fatigue from multiple repetitions is included in the investigation. Those designs not fulfilling the over-speed requirement are disregarded from further analysis.

To avoid problems with mechanical resonance in the slender machine design, the critical frequency ω_{crit} is monitored as well. The distance l_b between the bearings and rotor mass m_r together with Young's modulus for steel E_{Fe} and the area moment of inertia M_{Area} for the shaft are used to derive the resonance speed according to (2.4) [23, pg.341-342]. Here, λ_{I} and λ_{II} are the relative distance from center of gravity (CoG) to each of the two bearings respectively. That is $\lambda_{\mathrm{I}} + \lambda_{\mathrm{II}} = 1$.

$$\omega_{crit} = \sqrt{\frac{3 \cdot E_{Fe} \cdot I}{m_r \cdot \lambda_{\mathrm{I}}^2 \cdot \lambda_{\mathrm{II}}^2 l_b^3}} \tag{2.4}$$

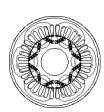

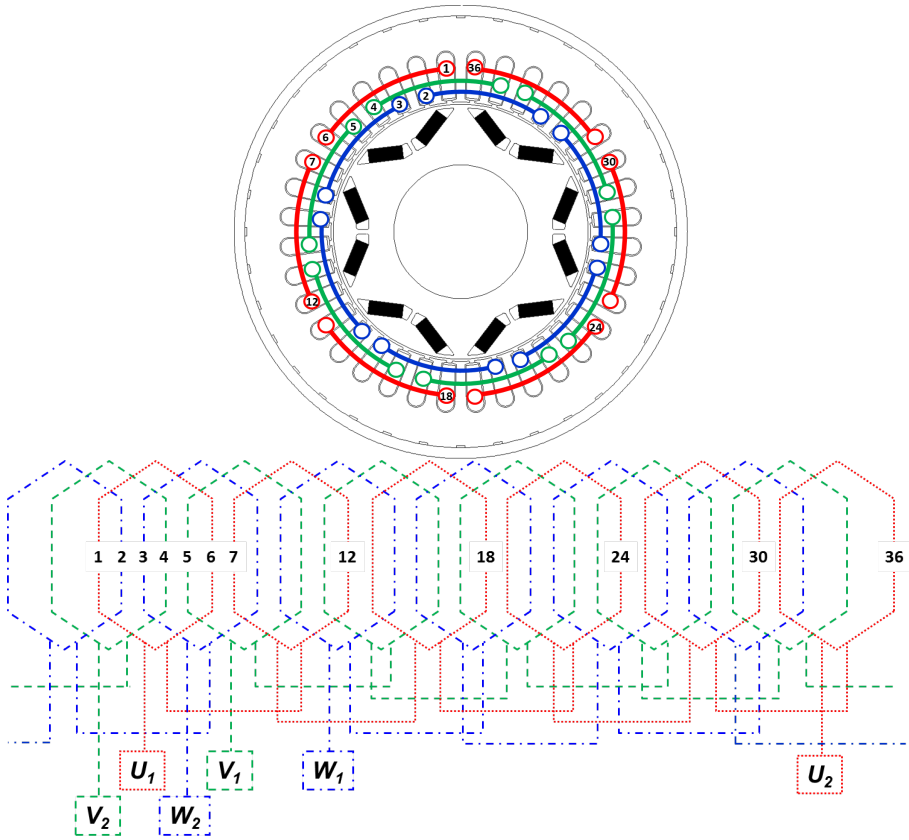

Figure 2.4: Principle sketches of the selected integer slot 1-6 winding configuration used in the prototype

Compared to the more realistic case with a distributed mass, the expression in (2.4) adds a conservativeness to the result. Assuming a worst case where the CoG is half-way down the rotor shaft (hence $\lambda_{\mathrm{I}} = \lambda_{\mathrm{II}} = 1/2$) and the bearings mounted on each end of the machine (hence l_b =400 mm), the natural frequency is considerably higher than the operating speeds considered here.

The mechanical aspects considered in the stator is the integrity of the stator teeth. In consultation with the experience from the prototype manufacturer, a restriction in the relation between the stator tooth length and width is introduced. This to make sure that the teeth will not become too long and slender and thereby introduce a potential failure point. The stator designs with too long teeth compared to width are disregarded as non-viable designs.

Thermal aspects

The thermal aspects considered during the design phase are based on output from the FEA-software. Current density in the stator slot giving the winding losses along with assumed heat generation from the magnetic flux density in the stator core are the assumed heat sources. No losses and hence no heat generation is considered in the rotor during the design phase. In the 2D simulation environment almost all heat is assumed to be dissipated through the stator envelope surface towards the housing. A small amount of heat is assumed to leave through natural convection towards the rotor shaft. Assumed thermal conductivities for the different parts of the machine are used to obtain estimations of the magnet temperature and hot spot temperature in the windings. Although the underlying assumptions are a bit coarse, the result is still considered to provide a first indication on the temperatures to be expected inside the machine. The result from the 2D heat finite element analysis is presented in Figure 2.5 along with some definitions and designations.

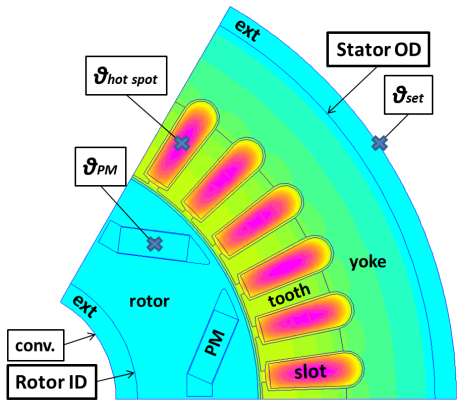

Figure 2.5: Thermal FEA elements and boundaries

With oil cooling being a requirement of specification, the possibility to implement cooling directly on the active parts is utilized. This means that the lower thermal conductivity compared to that of water or WEG is compensated by the possibility to direct the coolant closer to the heat sources.

Cooling is implemented in two partly independent circuits. One is with oil directed into the machine at the stator back halfway down the machine length. A circumferential grove on the inside of the housing directs the oil around the complete machine. Groves in the stator back, formed from the cutting process of the stator laminations directs the oil towards both machine ends. Here the oil trickles out on the end windings and down to an oil sump on the bottom of each end of the machine.

In the second cooling circuit, oil is fed into a small reservoir at the non-driving end (NDE)

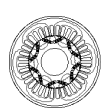

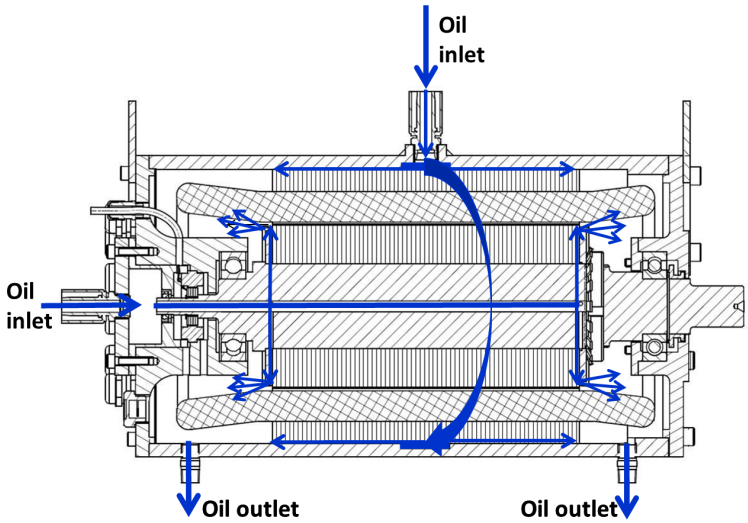

Figure 2.6: Principle sketch of the two oil circuits used to cool the prototype machine

of the machine. From here it is directed into the hollow shaft and further out towards the air-gap diameter on each side of the active rotor length. As the machine rotates, this oil is sprayed onto the end windings. This concept is based on previous design work at Lund University [15]. Since oil passes through the rotor on its way to the end windings, this circuit will also provide some cooling to the heat sensitive rotor magnets. This can be compared with the set-up in the 2D heat simulations in Figure 2.5 where neither heat generation nor heat dissipation in the rotor is included. The oil is then collected at the bottom of the machine, sharing the same sump as the oil from the first circuit. The two intervened cooling circuits can be seen in the principle sketch presented in Figure 2.6.

The idea is to feed the two oil circuits from the same oil pump and let the pressure drop along each path decide the distribution. The oil sump on each side of the machine could have been connected inside the housing, but for the prototype this is instead done in the drain piping. In the prototype, a suction pump is used to drain the oil from the motor. The intention to evaluate the cooling circuit more thoroughly has not been embodied during the execution of the PhD work.

The last aspect in the thermal analysis during the design phase is the temperature dependence of the machine. This is covered more thoroughly later on in Chapter 3.

Skewing

Skewing is implemented in the machine as a way to minimize torque ripple. This is considered important as the machine is connected to a reduction gear, with potentially high noise and wear if the torque ripple is too high. During the design phase, skewing is introduced mainly based on that the peak torque of the machine exceeded that from the requirements. A more thorough investigation on the impact of implementing skewing is presented in Chapter 4.

2.2.3 Machine characteristics

The performance of the numerous machine designs is studied and compared through the simulation results from the design tool. Typical properties of interest are the magnetic flux linkage, torque, power and efficiency. As the iteration process is converging to a design fulfilling the specification of requirements including the manufacturability aspects, the design is frozen. The main characteristics of the final design are presented here and summarized in section 2.4.

Magnetic flux linkage

The magnetic flux ψ linking with the stator windings is presented as function of i_d and i_q in Figure 2.7. Here, the upper half of the typical ellipse shaped iso-flux lines can be seen with the demagnetization point around 325 A in negative d-direction. The linked magnetic flux at origin comes from the permanent magnets. The derivation of the dq components from the three phases in the machine is described in Appendix A.

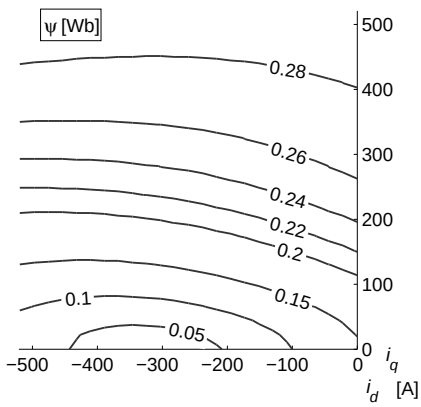

Figure 2.7: Magnetic flux linkage as function of i_d and i_q

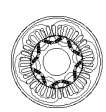

Torque as function of i_d and i_q

Torque and induced voltage at 6000 rpm (approximately base speed) are plotted as functions of i_d and i_q in Figure 2.8. Since the induced voltage is a function of the magnetic flux linkage, the elliptical shape seen in Figure 2.7 is repeated here. As the speed increases, the voltage ellipses in Figure 2.8 are decreased towards their epicentre. Hence the higher the speed, the smaller the surface in which a current vector can be applied. This means that no load operation with i_d and i_q being controlled to zero, will eventually end up as an invalid current combination at a certain speed.

The torque curves are reflecting the IPMSM design with a significant amount of reluctance torque. The torque is increased with increased field weakening current and preserved i_q. The simulated torque takes no consideration to torque losses due to the losses in the iron core and should correspondingly be slightly higher than in reality.

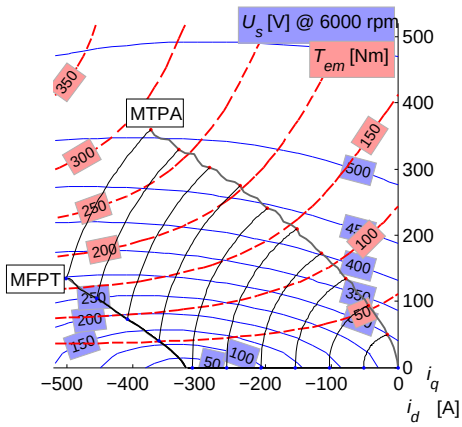

Figure 2.8: Torque and induced voltage at 6000 rpm as functions of i_d and i_q along with the MTPA- and MFPT curves and constant current curves

Included in Figure 2.8 is also a graphical presentation of the machine control. Below base speed where the available voltage not is a limitation, the current is controlled utilizing maximum torque per ampere (MTPA). This is based on keeping the winding losses at a minimum. Depending on the torque request, the current is controlled to the corresponding location along the MTPA curve. As the speed pushes the induced voltage closer to the voltage supplied from the drive, field weakening needs to commence. If the torque should be preserved, field weakening is done by increasing the current vector length and angle. This way, the requested iso-torque line can be followed as the current vector gets closer to the d-axis. If the current vector instead needs to be kept constant, the torque is reduced as the current vector starts to follow an arc (with centre at the origin) towards the d-axis. When the speed eventually becomes too high and the voltage ellipses too small, the current

is instead following the minimum flux per torque-curve (MFPT). This means maximum possible torque within the surface limited by the diminishing voltage ellipse. Since the work is focusing on machine design rather than control, no more effort is put on optimizing the control method. An alternative approach could in that case have been to include more losses than the those in the windings. Below base speed, the difference is not expected to be that significant.

Torque and power speed maps

The current combinations defined by the MTPA- the MFPT- and the constant current curves in Figure 2.8 are used to generate a torque-speed and a power-speed diagram. These are jointly plotted in Figure 2.9. Hence, each line in the torque and power maps corresponds to an arc with constant current amplitude in Figure 2.8. When the speed gets to high, some of the current vectors reach the MFPT that causes the amplitude to go down. The torque and power curves indicate that the final design will be capable of reaching the desired peak torque and power from the requirements.

Another thing noticed is that the lowest power curve does not reach maximum speed. This curve corresponds to the lowest constant current semicircle in Figure 2.8. This is a consequence of the current vector being too short for being able to reach the region of possible current combinations as the speed exceeds approximately 12500 rpm. On the other end, the three torque and power curves at the top (corresponding to the three largest current vector semicircles in Figure 2.8) are converging as the speed is increased. This corresponds to reaching the MFPT-curve. The surface enclosed by the voltage ellipse has become too small.

Power factor

The power factor or $\cos\phi$ of the electric machine is presented in Figure 2.10. This reflects the angle ϕ between the voltage and current and hence the relation between active and imaginary power. The power factor is affecting the efficiency in the PEC with higher losses for a reduced $\cos\phi$.

The significant reluctance torque in the machine can be seen on the reduction in power factor with increased torque below base speed. Above base speed, the power factor increases as the angle between voltage and current decreases. At high speed and low torque, the current vector starts to lead the voltage vector and as the angle increases, the power factor drops again.

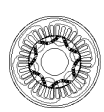

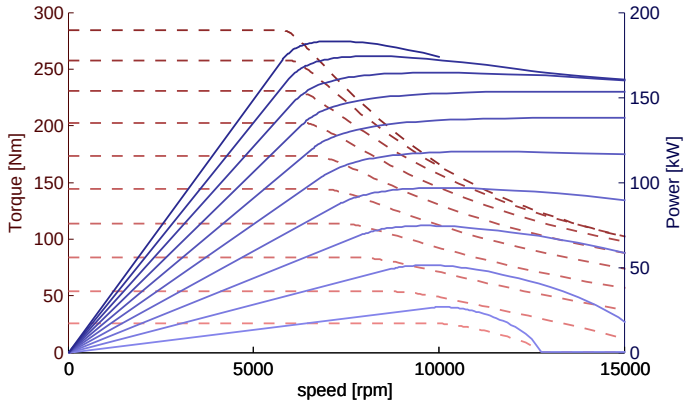

Figure 2.9: Torque and power as functions of speed utilizing MTPA for ten different current vectors in accordance with Figure 2.8

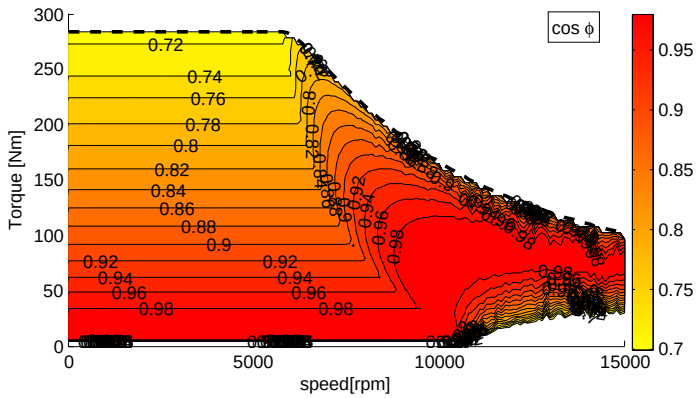

Figure 2.10: The $\cos\phi$ power factor in the machine according to simulations

Power losses and efficiency

The power losses are during the design phase estimated based on the current density in the windings and the flux density in the stator teeth and yoke. This means DC-losses in the windings with the end winding length estimated based on the distance between the relevant slots. The iron losses are derived with consideration to eddy current, hysteresis and anomalous losses due to the fundamental frequency in the stator teeth and yoke. Mechanical losses and losses in the rotor are disregarded at this stage. The result is presented as copper losses P_{Cu} and iron losses P_{Fe} in Figure 2.11.

A more thorough description on how the copper and iron losses are derived is given later in Section 5.3 and 5.5 in Chapter 5. There the loss analysis is also elaborated with consideration

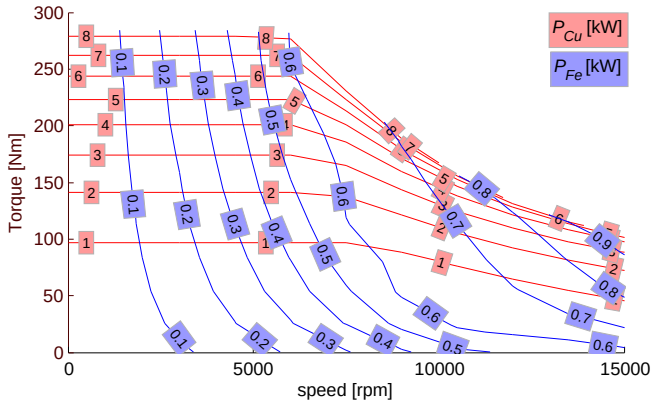

Figure 2.11: Copper losses P_{Cu} and stator iron core losses P_{Fe} according to simulations during the design phase

to more aspects and additional loss contributors.

The losses in Figure 2.11 are recalculated to the efficiency map presented in Figure 2.12. As mentioned previously this efficiency map is derived with consideration to DC-losses in the windings and iron losses in the stator due to flux varying with the fundamental frequency. The available DC-voltage in the simulation post processor is set to 600 V with no voltage margin in the control. If the voltage instead would have been set to the lower end of the range defined in Table 2.1, the overall efficiency would have been reduced slightly. The PM and winding temperatures are set according to the temperatures obtained from the 2D heat flow simulations presented earlier in Figure 2.5. This means around 100°C at the magnets and around 130°C as winding temperature. These temperatures are also affecting the resulting efficiency map slightly. The copper temperature affects due to the temperature dependency on the resistivity and the magnet temperature by a reduced PM flux that leads to higher currents for the same torque.

2.3 Prototyping and Measurements

With the simulation results indicating a viable machine design, a prototype is constructed and manufactured. This section summarizes the prototype build along with measurements performed to evaluate the simulation results from the design work.

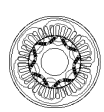

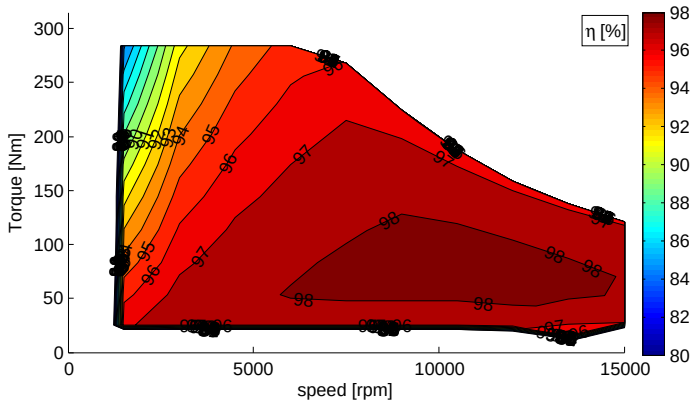

Figure 2.12: Efficiency, η as function of torque and speed from simulations on a warm machine

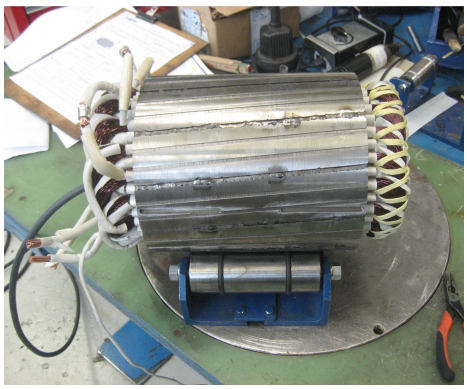

(**a**) Stator assembly

(**b**) Rotor assembly

Figure 2.13: Stator and rotor assemblies during the EM prototype build

2.3.1 Prototype build

The prototype build is a valuable part of the learning process. To leave the simulation environment and participate in the machine build adds another dimension to the understanding on what can and can not be embodied during the machine build. Furthermore, the focus on the details is changed as it is no longer possible to zoom in to tweak on those final parameters. Instead, it can very well be the manufacturing tolerances that dictate the level of meticulousness. The stator and rotor assembly during the EM build can be seen in Figure 2.13. Looking closely on the stator stack, the skewing can be seen on the slightly diagonally grooves. These groves are forming the stator back oil cooling channels.

A set of PT100 RTD temperature sensors are mounted in the machine. Approximate sensor

locations are presented in Figure 2.14 with short descriptions summarized in Table 2.2.

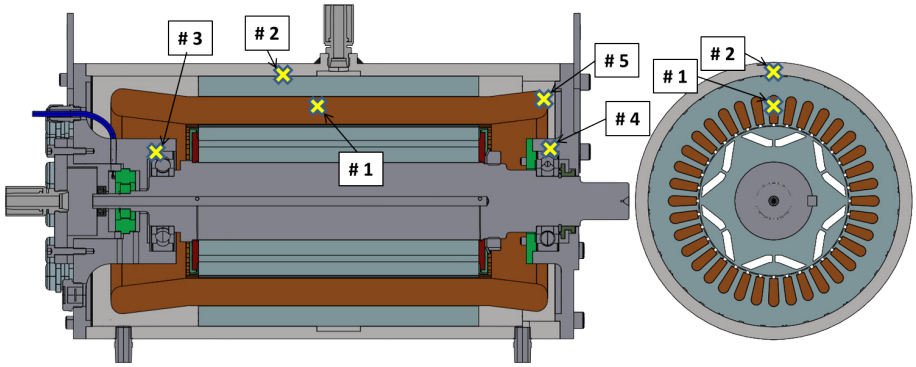

Figure 2.14: Temperature sensor positions in the prototype machine

2.3.2 Measurements

Measurements are performed on the prototype to learn the machine and to verify the simulation results. The experience gained by working with the machine in a lab instead of just in a simulation environment is highly valuable. Not to mention the effort needed to figure out why the test results differ from the expectations created by the simulations.

The most relevant tests from the licentiate thesis work are presented here, while a more thorough presentation with e.g. the different test set-ups can be found in [1]. In addition

Table 2.2: Temperature sensors in the prototype machine

Sensor no.	Designation	Description
#1	S_{HS}	Located at the expected hot spot, in the middle of a slot in one of the phases (phase A)
#2	S_{SB}	Located at the stator back outside the slot containing sensor #1
#3	S_{NDE}	Located at the bearing on the non-driving end
#4	S_{DE}	Located at the bearing on the driving end
#5	S_{EW}	Located on the outside of the end windings from the slot containing sensor #1

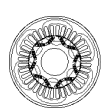

to the tests performed within the licentiate work, some test results from complementary testing done later on are presented here as well. Tests performed as a part of the deeper analysis are instead presented in each relevant chapter.

Torque measurements

The torque produced by the machine is tested in a dynamic load test set-up. The test procedure uses the system moment of inertia J, consisting of the rotor in combination with a flywheel mounted on the shaft, together with acceleration to obtain the torque. This in accordance with Newtons law of acceleration as presented for rotational conditions in (2.5). This means that no brake is needed to keep the rotor speed constant. Instead it is sufficient to securely anchor the machine in a test foundation. This is done to prevent the test object from moving during the high mechanical dynamics. The test object mounted in a cradle with a flywheel on the shaft can be seen in Figure 2.15.

$$T = J \cdot \frac{d\omega_m}{dt} \tag{2.5}$$

As the machine accelerates, sensors and a data acquisition system receive measurements of the rotor position, the phase voltages and the phase currents. The signals are logged with a sample frequency of around 10 kHz in order to handle the fast dynamics during the testing. A post-processing algorithm uses the voltage equations of the PMSM to calculate the linked magnetic flux and the torque characteristics of the machine. Since the test method is relying

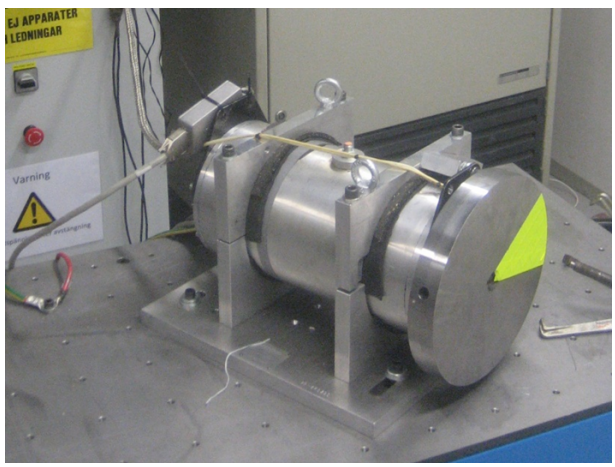

Figure 2.15: Machine mounted on the test foundation with a flywheel on the shaft for the dynamic testing

on accelerations, it is not possible to obtain test results when the torque producing q-current is set to zero. The theory behind the dynamic testing and the validity of the test method can be studied further in [24–27].

The machine is accelerated with currents in the dq-reference frame to obtain a torque map as function of i_d and i_q. The resulting measured torque is presented together with simulations with similar PM temperature in Figure 2.16. The limitation in current is due to the drive controlling the machine during the test. The limitation in current as well as in available DC-voltage prevents the machine from being tested at any higher power levels.

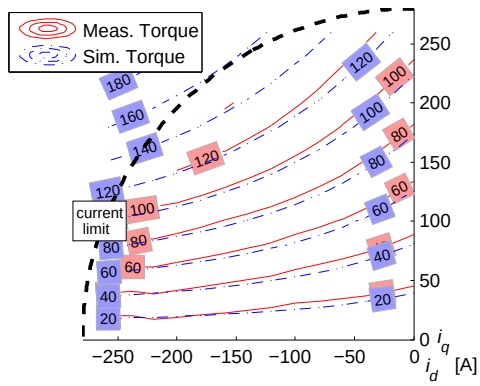

Figure 2.16: Torque as function of i_d and i_q from measurements with dynamic testing compared to simulations at corresponding temperatures

Top speed during the test depends on the location in the current map. Current combinations closer to the de-magnetization point along the d-axis allow for higher speed without reaching voltage limitation (as discussed previously around Figure 2.8). Maximum speed during the test is limited by the voltage margin or to 16000 rpm, whichever comes first. This means that the test results in the lower left side of the torque map in Figure 2.16 are derived from accelerations reaching 16000 rpm. In order to slow down the accelerations in those points where a higher torque is obtained, two different flywheels are used during the test. One smaller for the high speed test points and one larger for those with high torque. The mechanical damping introduced by the larger flywheel is also simplifying the data collection and thereby increasing the accuracy.

Although not presented here, the dynamic testing can be used to obtain the flux linkage as well. This is done by measuring the phase voltages to derive u_d and u_q and determine the derivative as function of rotational speed.

Complementary tests in a conventional test bench confirms the simulations up to peak rated current. This is presented for 1000 rpm in Figure 2.17. Torque is recorded with a HBM

T12/1kNm torque transducer with the higher accuracy option [28]. Current is recorded with the internal current sensors in the drive. DC-voltage from the battery simulator is set to 650 V. In order not to reach voltage limitation anywhere in in the load map, the test speed is limited to maximum 4000 rpm.

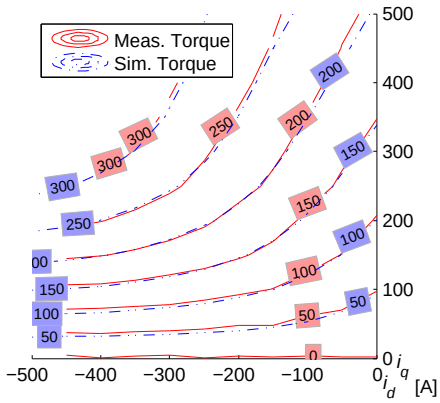

Figure 2.17: Torque as function of i_d and i_q from measurements at 1000 rpm in a conventional test bench compared to simulations at corresponding temperatures

The conformity between simulations and measurements is considered good irrespective of the test method. Largest deviation in the torque map is noticed close to the q-axis. The zoomed in perspective in Figure 2.16 makes it more pronounced there, although it is present also in Figure 2.17. The fact that a larger deviation is seen when the field weakening currents are small indicates that the deviation origins from how the permanent magnet flux linkage to the stator is modelled in the simulations. This is verified when looking more on the measured magnetic flux linkage. The deviation seen could be related to the tolerances on the dimensions introduced in the manufacturing as well as to how different materials are represented in the simulations. The ideal case in simulations where no loss torque is considered should also have an impact, although not sufficient to solely explain the difference. The deeper analysis done on this in [1] concludes one part coming from not considering the end windings in the 2D simulations. Overall conclusion is still that the torque from simulations follows the test results with acceptable accuracy.

System testing

Some limited system tests are performed with the machine mounted at its intended position on the side of an AMT gearbox. This is done to test how the machine performs in a slightly more realistic environment. The test set-up is presented in Figure 2.18. Although tested to a limited extent due to problems with the test rig, it is shown that the machine can fit on

the side of the transmission and deliver power to the powertrain. Hence, it could do so also in a vehicle. Cooling is obtained by sharing the same oil as that used in the the gearbox. Oil temperature measured in the gearbox oil sump is 80°C. This is passed through a small oil cooler before entering the machine.

Figure 2.18: The prototype machine mounted at the side of the AMT-gearbox in the system test rig

Some test data from the system testing can be seen in Figure 2.19. The last 15 minutes are shown, after several hours at similar loading. Here, power is derived from voltage times current in the dq-reference frame and speed is obtained from the resolver. Since the machine shaft is connected to the PTO gear drive, no torque can be recorded. Instead the torque is estimated based on the torque equation, hence from currents and flux linkage.

It should also be noted that the machine is controlled with manually set current references rather than torque control. This is due to problems with internal communication delays between the control layer and the drive. This was discovered after the closure of the testing activities. The consequence of the manual current entries is no optimal MTPA, but rather approximate distribution between i_d and i_q. The installed electrical power supply as well as the possibility to mechanically brake the machine is sufficient to test the machine at peak power. This is unfortunately not done due to the issues with setting up the test rig. The temperature readings at the bottom of Figure 2.19 indicates that the power could have been increased without running the machine too hot. How much is hard to say based on the uncertainties in the test set-up. Continuous operation is instead settled with complementary testing, presented in the next subsection.

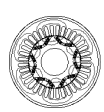

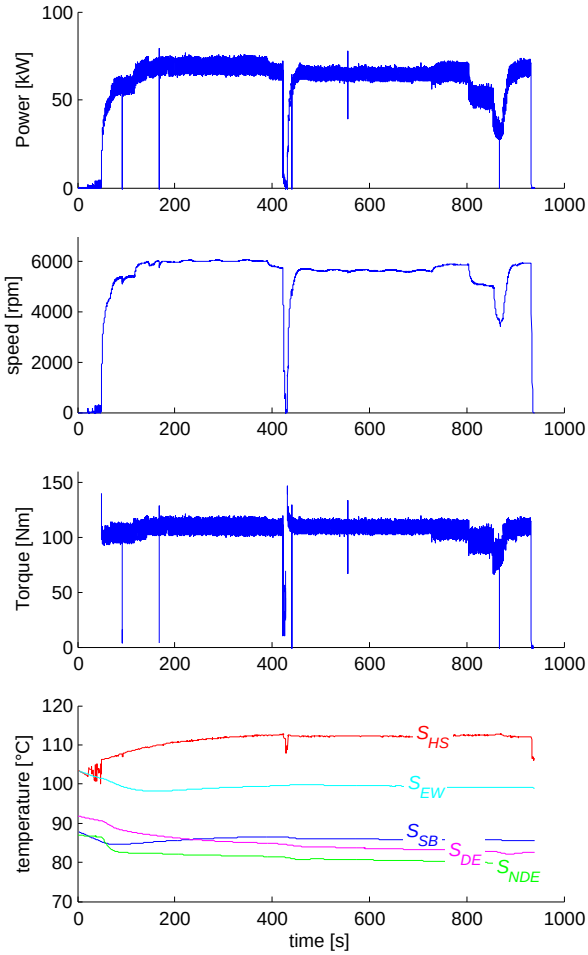

Figure 2.19: Electric power, EM speed, EM torque and temperature readings from the EM during one test sequence of the system testing

As a consequence of the problems in the test rig, the machine is unintentionally tested for its over-speed capability. During one of the tests, the time delay in the internal communication leads to loosing the control of the machine. As this happens, the machine is accelerated to a speed higher than the required burst speed (defined in the specifications of requirements in Table 2.1). After this event, the machine is sent to the machine manufacturer for a thorough health check showing that the machine is undamaged. Tests performed before and after the event do not indicate any difference either. Hence the machine is proved to survive the over speed requirement without damage.

Additional testing done on the machine when mounted in the system test set-up is utiliza-

tion of the EM for aiding synchronization of the gearbox during gear-shifts. This is studied separately in a master thesis project and presented in [3]. The outcome is that a considerably higher deceleration rate is reached compared to the conventional counter shaft brake. The requirement on the counter shaft brake is to handle up to 2000 rpm/s. When using the EM instead, a deceleration rate of more than 3300 rpm/s can be reached.

Continuous operation

The machine is tested for continuous operation in complementary tests in a conventional test bench set-up (test 1) as well as a back to back test set-up (test 2). In both cases torque is recorded with a HBM T12/1kNm torque transducer [28]. In test 1, a torque transducer with the higher accuracy option is used. The temperature is monitored with the internal PT100 temperature sensor S_{HS} mounted in one of the slots. The back to back set up means that two machines with similar performance are connected mechanically and that the braking machine is feeding power back to the DC-side. This way the electric power source only has to cover the losses present in the system. The second machine used as brake in the test has higher peak torque, but lower peak power and top speed. In addition to this, resonance phenomena on the intermediate shaft limit the maximum test speed even further. Maximum test speed is also limited in the conventional test bench, this time by the rig motor.

Similar preconditions are used in both test cases. The differences between the tests are 650 Vdc in test 1 compared to 600 Vdc in test 2. The machine is in both tests controlled with MTPA using a SKAI 2 inverter from Semicron [29]. Oil cooling is implemented with an ATF transmission oil[1] in a similar manner in both test cases. The oil cooling flow rate is approximately 10 l/min with around 60°C inlet coolant temperature. A dual stage oil pump is used to feed oil into the machine as well as to drain it. Pumping power during continuous operation is in the range of 70-80 W. At the test start up with oil at room temperature, a pumping power of up to approximately 280 W is noticed at the most. Some limited test cases with a slightly thicker (higher viscosity) transmission oil[2] requires around 120 W pumping power at normal operating temperature. For test 1, the maximum winding temperature of 130°C is kept in all points. In test 2, the winding temperature is allowed to reach almost 140°C at some test points. Ambient temperature during both tests is approximately 30°C.

Each test point is kept for about one hour of operation after stable temperature (within ±1°C) is reached. The magnet temperature is estimated immediately after completing each test point to ensure equal conditions. This is done by measuring the induced voltage with disabled drive. Resulting magnet temperature during continuous operation is around

[1]Volvo Group STD 1273,42, pn: 85120037
[2]Volvo Group STD 1273,07, pn: 85111057

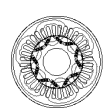

100°C. The resulting continuous torque and power from test 1 and test 2 are presented in Figure 2.20. As can be seen, continuous torque is around 180 Nm and continuous power is around 100 kW. Since a slightly higher winding temperature is allowed during test 2, the continuous operation points are slightly higher as well. Included in the graph are also torque and power curves from the simulations with 10 A/mm² and 30 A/mm². This is at the simulations roughly considered as continuous and peak operation.

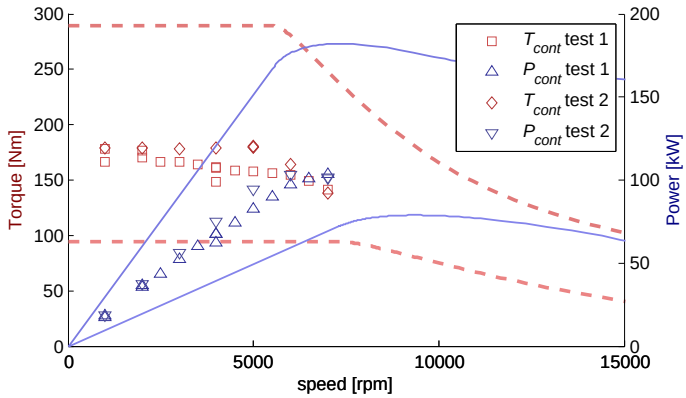

Figure 2.20: Measured continuous torque and power in two different test cells with similar preconditions together with simulations at 10 A/mm² and 30 A/mm²

In addition to the continuous operation tests described above, some limited tests are done with modified cooling. With preserved total flow rate, the coolant is distributed to either of the two cooling circuits, described earlier in Figure 2.6. For the case with all coolant directed to the stator back, similar performance is reached for the same winding temperature. The permanent magnet temperature is however elevated with 20-30°C. In the other case, with no oil on the stator back, the torque needs to be lowered with around 20-25% to maintain the winding temperature. In this case the magnet temperature is back at the same level as when operating with cooling in both circuits. Further investigations on modifying the cooling set-up is not done within the work in this thesis. It should however be possible to optimize the cooling further by adjusting and tuning the coolant distribution. If not on the capability to remove heat more efficiently, it should atleast be possible to optimize in the pressure drop and energy consumption in the cooling circuit.

Tests performed with the cooling turned off results in around 80 Nm with preserved winding temperature at 1000 rpm. With no cooling in the rotor, the magnet temperature is again increased to around 120-130°C. A very rough estimation reveals that around $\frac{180^2-80^2}{180^2} \cdot 100\% \approx 80\%$ of the losses are dissipated with the cooling system. This based on the assumption that the torque is proportional to current and that the current squared is proportional to the losses at the fairly low speed.

Peak operation

The peak performance is also tested during the complementary testing. This is done in the same back to back test set-up as for the continuous performance test described above. This means a limitation in top speed of 8000 rpm. The currents are applied up to the limit of the drive (Semicron SKAI 2 [29]), or to when the second machine (in the back to back set-up) is reaching its power limit. This means around 320 A_{rms} up to 4000 rpm after which the power is limited to below 150 kW. The potential full peak power indicated by the simulations is therefore not tested. The result is presented in Figure 2.21. Here the 10 lines of torque and power corresponds to the same currents as those used for the simulations presented in Figure 2.9. That is, the current vector length of the applied current is constant along each of the curves in Figure 2.21.

When comparing to the simulation results in Figure 2.9, it is concluded that the the expected peak torque is reached. The limitations in the test rig prevent testing at the expected peak power of 180 kW. The deviant torque and power readings between 7-8000 rpm are caused by a faulty torque reading in one of the test points.

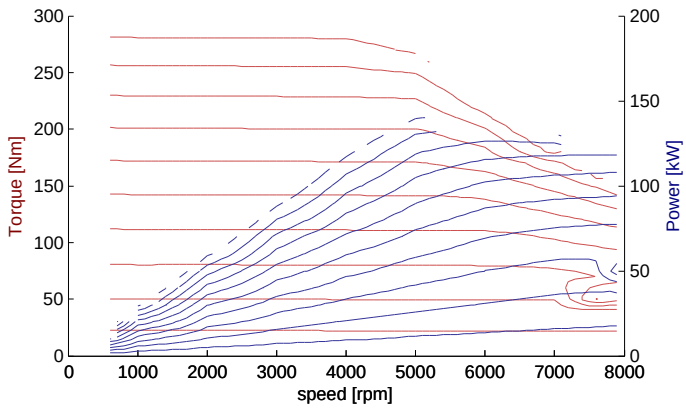

Figure 2.21: Measured peak operation, limited in power by the test set-up

2.4 Conclusions from the Liceniate work

The two main objectives with the licentiate project are to design an electric machine suitable to propel a heavy hybrid electric vehicle and in doing so, gain knowledge and understanding in the electric machine design process. Both of these are fulfilled. The prototyped machine is meeting the requirements in terms of speed, torque and as far as it has been tested also

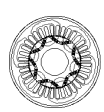

in power. The conformity between simulations and measurements motivates for using the simulation results to estimate the machine performance where tests not are performed.

Cooling is obtained with oil from the adjacent gearbox. Two different types of oil with different viscosity have been used throughout the test, with no noticeable difference in cooling capability or shaft torque. The higher viscosity however requires higher power from the cooling pump. In addition to this, the maximum coolant flow is limited by the possibility to drain the machine from oil. Both of these issues can on the other hand be optimized in a better way when designing the housing. The installation in the system test rig is also demonstrating the capability to install the machine in the intended position in a vehicle.

A side effect of the work is also improved credibility for the simulation environment developed at the department at Lund University. A more thorough review of the test results compared to simulations reveals some deviation in absolute value in for example the magnetic flux linkage. The overall conclusion is still that the simulation environment is capable to predict the machine performance with satisfying accuracy.

The second objective of the work, to gain knowledge in machine design is obtained by starting from setting the specifications based on the requirements imposed by the application. This gives a good understanding in how different preconditions can result in completely different design specifications. This is complemented by the understanding in how different design parameters affect the result, as the specifications are transformed into a machine design in the simulation environment. Another level is reached as the theoretical work in a simulation environment is complemented with practical experience. This is the case both in terms of preparing and testing the machine in different test set-ups, but also in participating in the prototype build. This is partly since it adds experience to which the theory can be connected to and partly in terms of investigating any unexpected mismatch between simulations and testing. That can be related to both a faulty assumption in the simulation set-up, as well as errors imposed by the test set-up or measurement equipment.

The main parameters for the machine designed throughout the licentiate project are presented in Table 2.3. Except for peak power, all values are acquired from measurements on the prototype machine.

Table 2.3: Machine performance and design parameters from measurements on the prototype machine

Machine topology		IPMSM	
Performance			
Peak torque	T_{peak}	300	Nm
Continuous torque	T_{cont}	180	Nm
Peak power (simulated)	$P_{peak\ sim}$	180	kW
Continuous power	P_{cont}	100	kW
Peak operation current	i_{max}	320	A_{rms}
Base speed	n_{base}	5300-5700	rpm
Top speed	n_{max}	15000	rpm
Burst speed	n_{burst}	>22500	rpm
Cooling			
Coolant medium		Oil	
Coolant inlet temp.		60-70	°C
Coolant flow rate		10	l/min
Dimensions			
Total (active) diameter	$\varnothing$	210 (200)	mm
Total (active) length	l	400 (210)	mm
Total (active) weight	m	62 (43)	kg
where of magnets/copper/iron		2 / 9 / 32	kg
No. of slots	N_s	36	
No. of poles	N_p	6	
Windings			
Winding type		Distributed	
No. of turns per coil		4	
No. of turns per phase		24	

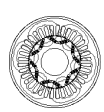

Chapter 3

Thermal Model Evaluation

This chapter describes the work done on thermal influence on the machine performance. Focus is on improving the simulation tool used within this project and at Lund University. This is done by studying the PM temperature influence on the remanence and coercivity and the resulting reduction in magnetic flux linkage and EM performance. A brief study of the temperature influence on the iron core is also performed. The temperature model is implemented in the simulation environment and validated by measurements.

3.1 Permanent magnet temperature dependence

The data sheet of the magnets holds information on the field strength in terms of the remanence B_r and coercivity H_c at room temperature (20°C). The relation between the remanence and coercivity can be expressed in BH-curves as shown in Figure 3.1. The coercivity is divided into intrinsic H_{cI} and normal H_{cB} field strength. The intrinsic coercivity expresses the field strength internally in the magnets and is hardly affected by external fields before reaching demagnetization. Once demagnetization is reached the magnet is permanently weakened. The normal coercivity along with the remanence gives information on how the magnet behaves in a magnetic circuit, such as an electric machine. The operating point when exposed to external field follows the normal curve in Figure 3.1. The relation between B_r and H_{cB} is defined by the permeability μ according to (3.1).

$$B = \mu \cdot H = \mu_r \cdot \mu_0 \cdot H \tag{3.1}$$

Here, μ_r and μ_0 are the relative permeability of the magnet material and the permeability of free space, respectively. The relation between B_r and H_{cB} means that μ can be seen as the slope of the normal BH-curves in Figure 3.1.

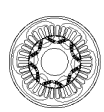

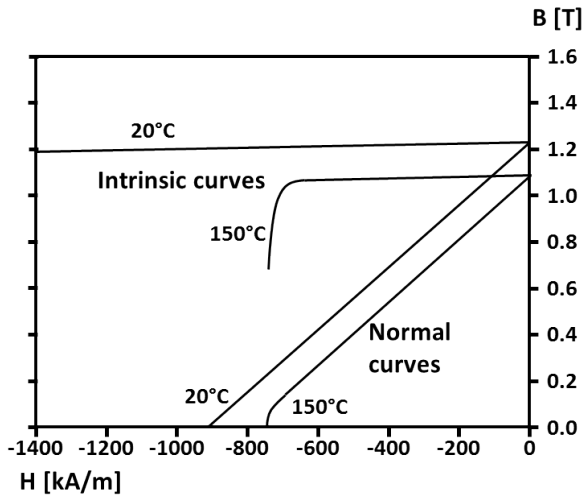

Figure 3.1: Typical magnet characteristics with intrinsic and normal BH-curves for 20°C and 150°C

The remanence and coercivity are affected by temperature. This can be described by the reversible temperature coefficients ($RTCs$) for the magnet grade. The $RTCs$ represent the relative change in magnitude as function of PM temperature difference $\Delta\vartheta$ to room temperature (20°C) and are expressed in [%/°C]. $RTC\,(H_{cI})$ defines the sensitivity of demagnetization with increasing temperature. Demagnetization occurs when the operating point passes the knee point in the BH-curve. As the temperature increases, the knee moves closer to origin. How much is determined by $RTC\,(H_{cI})$. In Figure 3.1 the knee can be seen at approximately -750 kA/m in the 150°C curves. $RTC\,(B_r)$ defines the change in remanence. Since the permeability μ hardly is affected by the temperature increase, the slope can be considered constant regardless of (normal) operating temperature. This means that in the normal operating range, $RTC\,(B_r)$ can be applied on B_r according to (3.2) and as well as on H_{cB} according to (3.3). Typical values for $RTC\,(B_r)$ and $RTC\,(H_{cB})$ in Neodymium-Iron-Boron, or NdFeB magnets are in the range of -0.11%/°C and -0.60%/°C, respectively [9, pg.42], although the exact numbers depends on the magnet grade. This means that increased temperature leads to a reduction in remanence and coercivity due to the negative signs on the RTC coefficients.

$$B_r = B_r\,(20°C) \cdot \left(1 + \frac{RTC\,(B_r) \cdot \Delta\vartheta}{100\%}\right) \tag{3.2}$$

$$H_{cB} = H_{cB}\,(20°C) \cdot \left(1 + \frac{RTC\,(B_r) \cdot \Delta\vartheta}{100\%}\right) \tag{3.3}$$

3.2 Iron core temperature dependence

The temperature dependence of the electric steel is considered as well. According to [30, Ch.6.1.10] and [31,32], the relative permeability μ_{Fe} of iron increases slightly with increased temperature at low field strength. This is investigated analytically based on the simplification presented in Figure 3.2. Here it should be noted that the different areas defined in the figure are the width of each sub region multiplied by active machine length. The relation

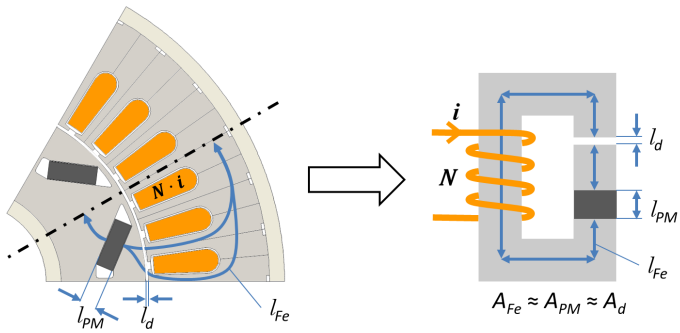

Figure 3.2: Simplification of the magnetic circuit in the electric machine with definitions of the lengths (l_{Fe}, l_d and l_{PM}) and areas (A_{Fe}, A_d and A_{PM}) for the flux paths together with the current (i) and number of turns (N) in the coil

between the induced current i in the N number of turns and the magnetic flux density B in the iron (B_{Fe}), airgap (B_d) and magnets (B_{PM}) can be calculated according to (3.4). Here the permeability is denoted by μ and the flux density from the permanent magnet by B_{0PM}. The flux density inside the magnet is hence a combination of the internal permanent magnet flux (B_{0PM}) and the external flux from the magnetic coil that is passing through the magnet (B_{PM}).

$$\begin{aligned} N \cdot i =& H_{Fe} \cdot l_{Fe} + H_d \cdot l_d + H_{PM} \cdot l_{PM} = \\ & \frac{B_{Fe}}{\mu_0 \cdot \mu_{Fe}} \cdot l_{Fe} + \frac{B_d}{\mu_0} \cdot l_d + \frac{B_{PM} - B_{0PM}}{\mu_0 \cdot \mu_{PM}} \cdot l_{PM} \end{aligned} \tag{3.4}$$

By introducing the simplification stated in (3.5), the total flux in the magnetic circuit is calculated according to (3.6).

$$A_{Fe} \approx A_d \approx A_{PM} \Rightarrow B_{Fe} \approx B_d \approx B_{PM} \approx B \tag{3.5}$$

$$B = \frac{\mu_0 \cdot N \cdot i + \dfrac{B_{0PM} \cdot l_{PM}}{\mu_{PM}}}{\dfrac{l_{Fe}}{\mu_{Fe}} + l_d + \dfrac{l_{PM}}{\mu_{PM}}} \tag{3.6}$$

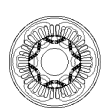

The influence of the relative permeability of iron in the magnetic circuit can then be investigated with (3.6). With zero applied current together with relevant numbers on all parameters in (3.6) it is clear that a change in relative permeability of iron has a marginal influence only. It is concluded that a duplication of the permeability results in less than 1% difference in the resulting flux density. Although the simplifications done when assuming equal cross section areas and a uniform flux density is rather coarse, the result should be valid also for a more correct representation of the actual design.

The analytical result is also backed up with FE-simulations, where an exaggeratedly modified permeability still only gives a marginal difference in the result. The conclusion from investigating the temperature dependence of the iron permeability is that the influence is negligible when investigating the machine performance. It is therefore not considered when setting up the FE-simulations.

3.3 Simulations

The influence of increased PM temperature $\Delta\vartheta$ in the machine model is investigated by modifying the remanence and the coercivity according to (3.2) and (3.3) respectively. Since the permeability does not vary with temperature, both B_r and H_{cB} are changed equally much. This is also why $RTC\left(B_r\right)$ is used on both parameters. The value for $RTC\left(B_r\right)$ for the magnet grade used in the prototype is obtained from the magnet supplier data sheet. Implementation is done in the pre-simulation stage in the simulation tool described earlier in Chapter 2.2.1. The modified remanence and coercivity are used as input when defining the magnet material in the simulation model. The temperature defined prior the FE-simulations is also used to estimate the temperature and hence resistance in the copper windings in the post simulation analysis.

3.3.1 No load conditions

The resulting reduction in flux linkage due to increased temperature at no load is presented in Figure 3.3. As can be seen, the flux linkage is reduced with almost 10% at 100°C compared to room temperature – a temperature difference $\Delta\vartheta$ of 80°C.

3.3.2 Loading conditions

The temperature dependence at loading conditions is studied by looking at the magnetic flux linkage ψ in d- and q-direction as well as the torque as functions of i_d and i_q for different temperatures. Since the magnetic flux linkage in d-direction according to its definition

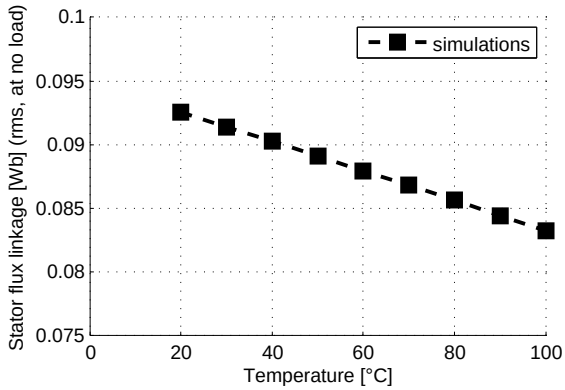

Figure 3.3: Stator phase flux linkage (rms) as a function of magnet temperature at no load

is aligned with the PM flux, a clearly noticeable temperature dependency is observed. This can be seen in Figure 3.4a where ψ_d is plotted for 20°C, 60°C and 100°C. The magnetic flux linking in q-direction, plotted in Figure 3.4b is as expected less affected by the temperature variation. The difference that still can be seen should be related to cross saturation effects. The linked magnetic flux in d-direction at origin corresponds to the stator flux linkage presented as rms-values at no load in Figure 3.3. The difference in amplitude between the figures is due to the power invariant transformation (see Appendix A) of the flux in Figure 3.4. This introduces a factor $\sqrt{\frac{3}{2}} \cdot \sqrt{2} = \sqrt{3}$ between the rms values in Figure 3.3 and the values at origin in 3.4, at corresponding temperatures. Induced voltage at each temperature can simply be obtained by multiplying the rms value of the stator flux linkage by the number of pole pairs (in this case 3) and rotational speed ω_m in radians per second.

The torque as function of i_d and i_q is presented in Figure 3.5. Here it is noticed that the torque is more influenced by the increased temperature in the upper part of the graph. The torque also shows larger temperature dependency closer to the q-axis while the torque production closer to the d-axis is less affected by the temperature. This is related to that i_q produce electromagnetic torque with the permanent magnet flux, while current in d-direction instead generates reluctance torque. As discussed earlier, the magnetic properties in the iron core is hardly affected by the temperature and hence nor is the reluctance torque.

The torque and flux maps plotted as functions of temperatures in Figure 3.5 and Figure 3.4 are used to obtain torque-speed- and power-speed characteristics with MTPA and MFPT (as described previously in Chapter 2) as functions of temperature. This is plotted at 20°C and 100°C in Figure 3.6. Here the temperature influence on the machine can be seen by approximately 5% lower torque below base speed. The reason for a lower decrease in torque

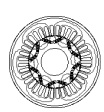

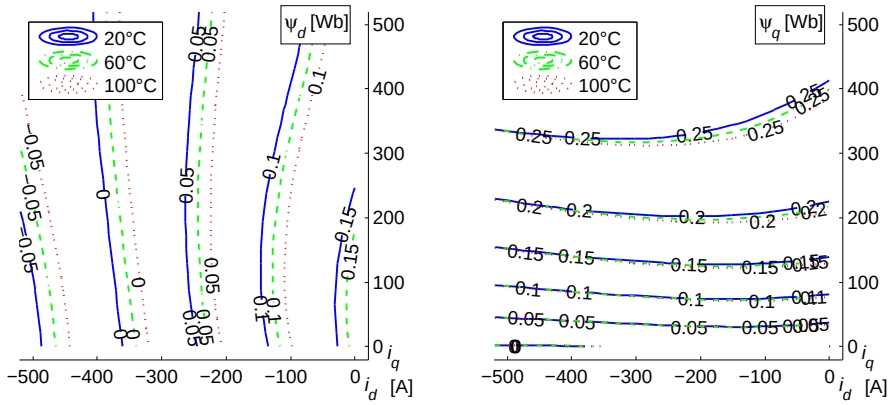

(a) ψ_d (b) ψ_q

Figure 3.4: Simulated linked magnetic flux ψ in d- (left) and q-direction (right) as functions of i_d and i_q at 20°C, 60°C and 100°C

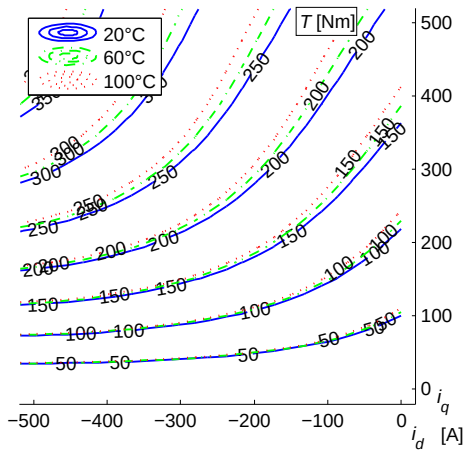

Figure 3.5: Simulated torque as function of i_d and i_q at 20°C, 60°C and 100°C

compared to in PM flux linkage (in Figure 3.3) is due to the presence of reluctance torque.

At peak operation (30 A/mm^2), the torque (and power) is decreased also above base speed. When reaching top speed the reduction is around 10%. However, at partial load (e.g. 10 A/mm^2), the torque and power above base speed are instead increased with higher temperature. The increased temperature makes the magnets slightly weaker which moves the epicentre of the flux ellipses (in Figure 2.8) slightly to the right (closer to origin) in the dq-map. Therefore the speed range in which the continuous current vector can be used is

extended. The consequence is a redistribution in how much of the current that is needed to counteract the permanent magnet flux. As the field weakening current is reduced, the torque and thereby power can be increased.

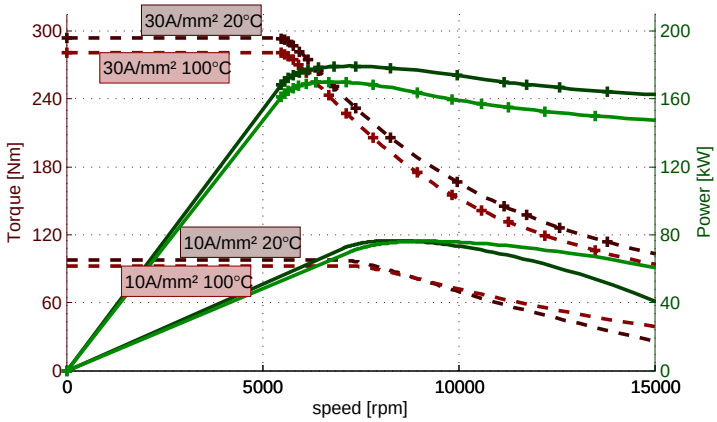

Figure 3.6: Influence of PM temperature on machine characteristics for 20°C and 100°C

The torque-speed and power-speed characteristics presented for 20°C and 100°C in Figure 3.6 are each derived with their own optimal MTPA curve. This is usually not the case when implementing the control in an actual drive. That would have required a good model for estimating the magnet temperature implemented in the drive in order to know which data tables or current controller to use in each operating point. The impact on the torque and power as functions of speed if controlled with the same MTPA-settings (based on one for example just 100°C) but different magnet temperatures is not investigated here.

3.4 Verifications of the temperature dependent model

The temperature dependence implemented in the simulation model is verified with measurements. No load tests are performed in a heat cabinet by measuring the induced voltage at different temperatures. This gives the magnetic flux density from the permanent magnets at different temperatures and hence the temperature dependence of the magnets in the prototype.
The rapid test procedure of the dynamic testing method is opening for the possibility to also test the temperature dependence at loading conditions.

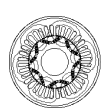

3.4.1 No load heat measurements

The no load heat test is performed within the Licentiate work. The results are presented here to provide a more comprehensive overview.

No load heat test set up

The magnetic flux linkage as function of PM temperature is investigated by preheating the electric machine in a heat cabinet. The heat cabinet temperature is gradually increased up to just below 100°C and then decreased back to ambient. This sequence is repeated twice, giving in total 69 test points at different temperatures and rotational speeds. After at least three hours at each temperature, thermal equilibrium is assumed to be reached in the machine. This assumption is used to establish the PM temperature by reading the internal PT100 temperature sensors in the stator and at the bearings (see Table 2.2 and Figure 2.14). The temperature is established by reading the resistance in the sensors with a Fluke 88V multimeter.

The induced back Emf-voltage (electro-motive force) on each phase is measured with a Yokogawa DL708E oscilloscope with plug-in input module 701853HR. This is repeated at a number of different rotating speeds up to around 2000 rpm, equivalent to around 100 electrical hertz. The raw data from the oscilloscope is post-processed to give the rms voltage as well as the frequency. The frequency and voltage are used to calculate the magnetic flux linkage.

In order to gain access to the machine, the heat cabinet is opened during each set of voltage measurements. A hand held drilling machine with a custom made quick coupling is used to rotate the machine. This makes it possible to rotate the machine without removing it from the heat cabinet as this would give time for the machine to cool down. A picture of the test set-up with the machine attached to the oscilloscope can be seen in Figure 3.7 where the quick coupling is seen in the inset picture.

The temperatures are read before and after each voltage measurement. This is done to make sure that the PM temperature can be considered constant even if the heat cabinet is opened during the measurements. Each set of measurements is completed within approximately ten minutes. During the first temperature reading, before the voltage measurements, the mutual difference in temperature between all five temperature sensors is less than 0.5°C throughout all measurements in the entire experiment. This indicates that the PM temperature also can be considered to be in the same range. Hence, the assumed thermal equilibrium is accomplished.

The temperature difference before and after each set of measurements varies partly depend-

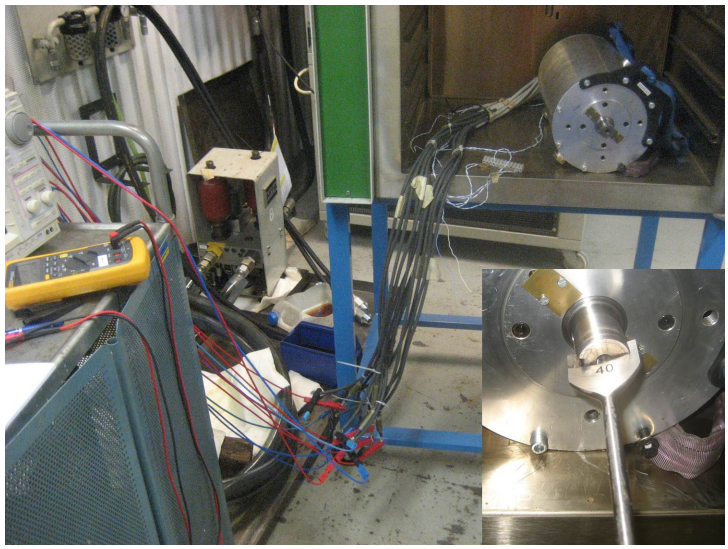

Figure 3.7: Test set-up for no load temperature dependence measurements with the custom made quick coupling in the inset picture

ing on the sensor position and partly on the different temperatures. This correlates to a higher delta temperature to ambient, which results in a faster temperature decrease. It is also noticed that the temperature sensors at the bearings (#3 and #4 in Table 2.2 and Figure 2.14) are deviating slightly more during each test than the sensors buried inside the machine (#1 in the slot and #2 at the stator back). Since the magnets are also buried, the PM temperature should coincide better with sensors #1 and #2 rather than #3 and #4. The fact that the heat cabinet is opened on the driving end (DE) of the machine is also noticed in the temperature readings. The difference before and after each measurement is slightly larger for the sensor at that end (#4) compared to the one on the non-driving end (#3).

For the temperature sensors in the slot and at the stator back (#1 and #2), the largest difference before and after a measurement is 0.5°C. The largest temperature decrease for a single temperature sensor during a measurement is less than 3°C, noticed in the sensor at the driving end bearings (#4). Both these cases are observed during the 95°C measurement, hence with a large delta temperature to ambient. The conclusion is that these results support the assumption that the PM temperature can be considered constant throughout each set of measurements.

No load heat test results

The induced voltages at all phases (ΦA, ΦB and ΦC) during one of the test points are plotted in Figure 3.8. With similar curve shapes and peak values, the balance between phases can be said to be good. The harmonic content is low due to the implemented skewing. The frequency is established by identifying the zero crossings in each phase. Magnetic flux linkage is then obtained by dividing the rms values of the induced voltage with the frequency.

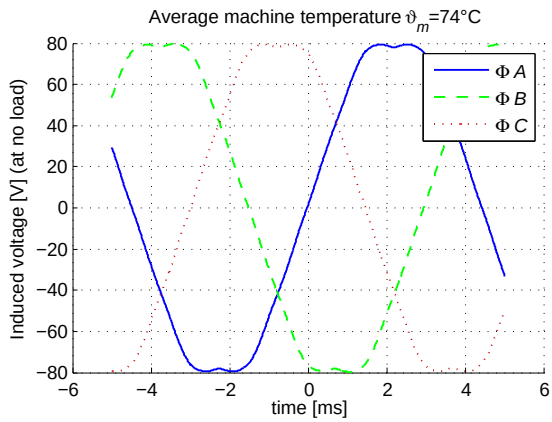

Figure 3.8: Induced voltage in all phases at 2000 rpm and 74°C

Magnetic flux linkage is plotted as function of speed and temperature in Figure 3.9. Here it can be confirmed that the linked magnetic flux is independent of speed. Higher temperature however results in a lower stator flux linkage.

The reduction in stator flux linkage due to increased temperature is clear in Figure 3.10 where the flux linkage is presented as function of temperature for each phase. As can be seen, all phases are close together, again indicating a good balance between the phases.

In Figure 3.11 the simulation results are included. The results differ around 4% at room temperature and around 3% at 100°C. This deviation between simulations and measurements is potentially caused by small deviations in the magnet size and position compared to the simulations. Another reason could by the inherited simplifications made when modelling a 3-dimensional component using a 2D FE-simulation model. Furthermore, uncertainties from when the test data is acquired and processed could potentially have an influence on the result. This is both in terms of accuracy of the test equipment and in how the rms voltage is derived from the oscilloscope readings. The conclusion from the measurements is that the temperature dependency model implemented in the simulations is adequate at no load.

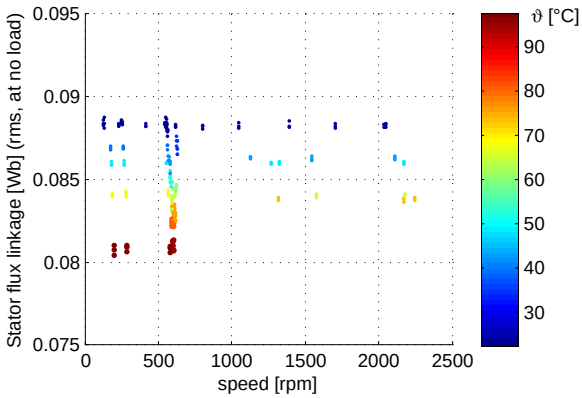

Figure 3.9: Magnetic flux linkage (rms) as function of speed and temperature (ϑ) at no load with contribution from all stator phase windings

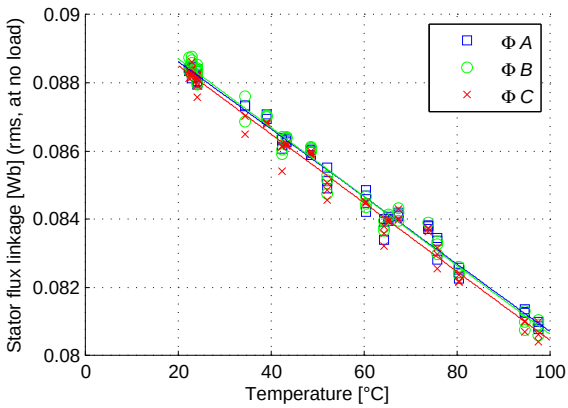

Figure 3.10: Magnetic flux linkage (rms) as function of temperature for all stator phase windings

Induced voltage at each temperature can be obtained from Figure 3.11 by multiplying the rms value of the stator flux linkage by the number of pole pairs (in this case 3) and rotational speed ω_m in rad/s. Conversely, an estimation of the magnet temperature can be obtained by measuring the induced voltage and divide with number of pole pairs and rotational speed. If the voltage is measured phase to phase, a factor $\sqrt{3}$ should be included as well. This makes it possible to estimate the magnet temperature based on induced voltage measurements at no load.

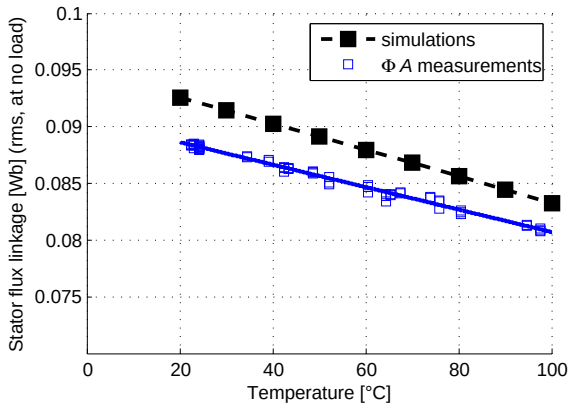

Figure 3.11: Stator phase flux linkage (rms) from simulations and measurements on phase A (ΦA) as functions of machine temperature

3.4.2 Heat measurements during loading conditions

Testing a machine during loading conditions at a constant temperature is not trivial. If connected in a conventional test bench with constant speed, heating of the test object can become complicated. Also the duration of the test needs to be short in order for the test object not to heat up too much. This is something that would lead to distortion in the measurements.

Instead, testing of the temperature dependency during on load conditions is done with the dynamic test method, described briefly in Section 2.3.2 and with more details in [24–27]. The short time to complete the load map means that a constant temperature can be assumed throughout the test. The dissipated heat from the stator windings to the magnets is marginal. Furthermore, since the device under test has no mechanical connection to a brake machine, the entire test object can be mounted in an insulated box. Thereby, a better control of the ambient temperature can be provided.

On load heat test set-up

Prerequisites for the dynamic load testing are means to measure currents and voltages along with a firm foundation that keeps the test object from moving. Hall sensors (type: LEM LA 205-S) are used to measure the currents and voltage probes (type: LEM LV25-p) are used to obtain the voltage. The PWM switching is handled by integrating the measured voltage over one switching period. The rotor position is monitored by the resolver in the

test object. A labview CompactRIO[1] system is used for machine control and data acquisition. The CompactRIO consists of a field-programmable gate array (FPGA), a real-time processor and an interface for a host computer. The FPGA part is used to control the current and the data acquisition, while the test control sequence is implemented on the real-time processor. [33] A thermally insulated box is built around the test object. This to keep control of the ambient temperature during the test. A thermostat connected to a heat gun is used to preserve a temperature approximately equal to that evaluated in the machine. The temperature during the test is monitored with the internal temperature sensors in the machine in a similar manner as for the no load tests. Figure 3.12 shows the machine when mounted inside the heat box with the heat gun fitted in the lid. Currents are applied in the

Figure 3.12: Machine mounted inside the heat box for the dynamic on-load tests

dq-reference frame to generate flux and torque maps. Limitations in the test equipment prevents the machine from being tested with currents higher than approximately 120 A. The test data points are interpolated in the post process. This will give similar maps as those presented for the simulations in Figure 3.4 and Figure 3.5.

On load heat test results

Figure 3.13 shows the linked magnetic flux as functions of i_d and i_q. In addition to the test results, the simulations are re-plotted with the same scale on the axis and at the same temperatures. Looking at the measured linked magnetic flux ψ_d^{meas} in the d-direction in Figure 3.13a, the reduction in linked flux due to increased temperature is evident. This is expected as the increased permanent magnet temperature decreases the remanence and coercivity. A comparison between the measured (Figure 3.13a) and simulated (Figure 3.13b) linked magnetic d-flux shows that the simulations yield a higher flux than the measure-

[1]http://www.ni.com/en-us/shop/compactrio.html, Accessed on 2018-12-02

ments. This is in line with the no load test results presented in Figure 3.11, where a deviation also is observed. The deviation in ψ_d was observed also during the licentiate work [1] as well as in similar analyses performed on other machine designs [27]. It is therefore likely to be related to the simulations. One explanation could be related to end winding effects as they are excluded in the 2D FEM simulations. Another could be related to how the highly saturated regions around the magnets are modelled. This would have an impact on the amount of permanent magnet flux linking with the stator windings. The complete reason for the divergence is considered to be outside the scope of this study is therefore not fully established. Considering the change of flux linkage due to temperature, the simulations and measurements match well; the linked magnetic flux decreases almost 0.01 Wb when the temperature rises from 40°C to 100°C.

Figure 3.13c and Figure 3.13d show the linked magnetic flux in q-direction from measurements (ψ_q^{meas}) and simulations (ψ_q^{sim}). As expected, the temperature has a marginal effect on the results here. The attenuated permanent magnet flux has no direct effect on the flux linking in the q-direction. When comparing ψ_q from the tests more thoroughly to the simulation results, a difference is noticed in the trend as the field weakening current is increased. In contrast to the simulation results, an increased field weakening current leads to a decrease in the q-flux for the same q-current in the tests. When instead looking at the larger flux map in Figure 3.4b, it can be observed that the q-flux eventually reduces with increased field weakening current. It is only at lower currents, covered by the test, that the opposite trend is seen. This could mean that the trend due to increased field weakening seen in Figure 3.13d is a result of errors introduced when interpolating the simulation results. As the behaviour due to temperature agrees and as the difference with increased field weakening current is present at all temperatures, no more effort is put on investigating this minor difference in the q-flux.

Figure 3.14 shows torque at different temperatures as a function of i_d and i_q. Since the linked magnetic flux in d-direction decreases when the temperature increases, the torque is decreased as well. When the distribution of current shifts towards a larger portion in negative d-direction, the torque is influenced less by the temperature variation. This is as previously mentioned due to the increasing part of reluctance torque. Since the iron core is not affected by the elevated temperature, neither is the reluctance torque. As expected from the discrepancy in ψ_d, the experiments show a lower torque than the simulations. This is especially noticeable in the upper right corner of the dq-map where there is no reluctance torque. Since all torque here is produced by the permanent magnet flux only, the difference in torque between simulations and measurements follows that between ψ_d^{sim} and ψ_d^{meas}.

A final comparison is done in Figure 3.15. Here the flux linkage in the origin during the dynamic load tests is estimated from the d-flux at i_d =0 A and i_q =10 A. The inherent method with which the data is collected during the dynamic tests out-rules origin as a possible test point. This is because no acceleration will occur at zero current. Based on the

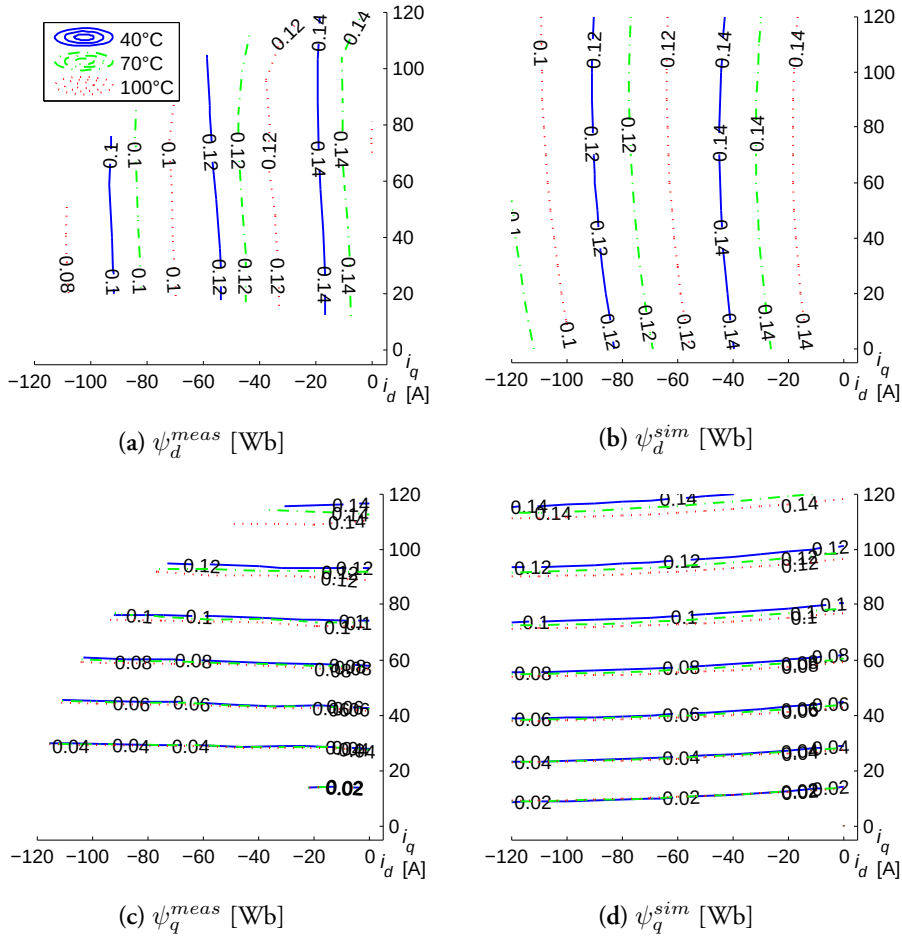

(a) ψ_d^{meas} [Wb]

(b) ψ_d^{sim} [Wb]

(c) ψ_q^{meas} [Wb]

(d) ψ_q^{sim} [Wb]

Figure 3.13: Linked magnetic flux ψ in d- (upper) and q-direction (lower) from measurements (left) and simulations (right) as functions of i_d and i_q for 40°C, 70°C and 100°C including the current limitation during testing

d-flux in Figure 3.13a, it is assumed that the linked magnetic flux is approximately the same in origin as when a small i_q (10 A) is applied. The q-flux should per definition be equal to zero when i_q is zero. In order to get phase rms quantities instead of vector quantities, the magnetic flux linkage at (or rather close to) origin in Figure 3.13a is divided with a factor $\sqrt{3}$ as discussed previously in Section 3.3. As can be seen in Figure 3.15, the trend already seen in simulations and during the no load test is repeated again for the dynamic load tests. This adds validity to the dynamic test results.

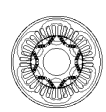

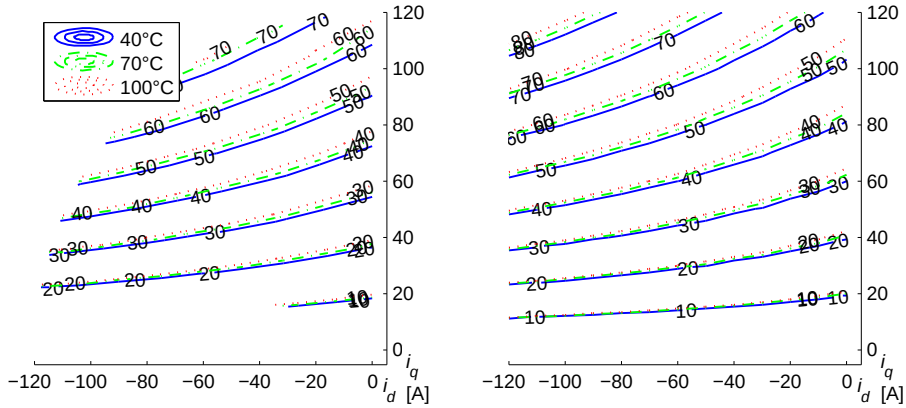

(a) Measured torque [Nm] (b) Simulated torque [Nm]

Figure 3.14: Torque from measurements (left) and simulations (right) as functions of i_d and i_q for 40°C, 70°C and 100°C including the current limitation during testing

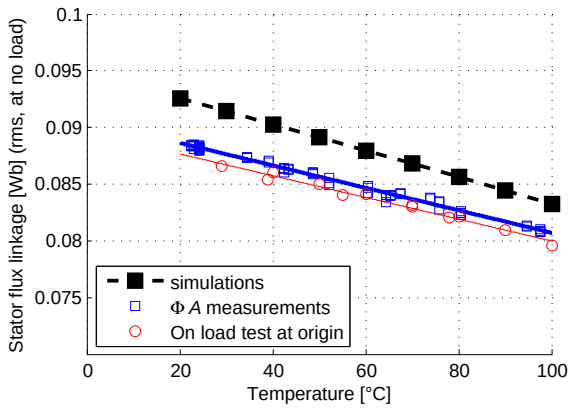

Figure 3.15: Stator phase winding flux linkage (rms) from simulations, no load measurements on phase A (ΦA) and on-load test at (near) origin as functions of machine temperature

3.5 Concluding remarks on the temperature model evaluation

The analytical expressions (3.2) and (3.3) are implemented as a part of the pre-simulation code for the simulation tool. By including the operating temperature of the machine when setting up the simulations, the remanence and coercivity of the magnet material are correspondingly adopted to that temperature. This means that the permanent magnet material parameters, when defined in the FE-simulation environment are reflecting magnets that are weakened by the elevated temperature. In addition to this, the defined temperature is also

used to estimate the resistivity in the copper windings. The temperature difference between the magnets and the windings are first estimated from FE heat flow simulations and verified during continuous operation testing. The resistivity is used for estimating the copper losses in the windings during the post simulation process. It should however be mentioned that the stator winding temperature in general is more dynamic than that of the magnets in the rotor. When operating an actual machine, this can be imposed in terms of the windings reaching operating temperatures while the magnets still are rather cold. Correspondingly, if the machine is at rest for a period of time, the windings might be cooled down faster if the cooling circuit still is in operation. This is however not the case for this machine as one part of the coolant (described in Figure 2.6) is directed through the rotor.

Despite the limitations in the dynamic load test set-up and therefore also in the test results, the overall conclusion is that the temperature dependence observed in the measurements agrees well with the simulations. This is valid for the no load test as well as with applied loading. This contributes to the validity of the implemented temperature dependence in the simulation model.

An offset is observed between the simulations and measurements in terms of linked flux in d-direction. As this is observed also at no load it should be related to how the permanent magnets are modelled. Possible reasons for the deviation could be related to how the permanent magnet flux links to the windings in the simulations compared to the prototype. This could be either due to a slight deviation in actual magnet size and material data compared to the PM data sheet, or possibly related to the heavily saturated iron bridges between the magnets in the rotor. Since the simulations are performed in a 2D simulation environment, potential end winding effects could also contribute to the difference. Apart from a marginal fringing effect, this should however not have any noticeable impact on the linked flux during no load.

A deviation is also observed in the q-directed linked flux when the field weakening current is increased. While the simulations suggest a slight increase in linked flux, measurements instead indicate a small reduction. Looking at the entire load map, it is however seen that the flux linking along the q-axis eventually is decreased as well. The overall trend in the simulations is similar to that in the tests. The small difference at low i_d is believed to be related to interpolation errors in the simulation results. The simulations are based on current steps larger than what is covered by the test. As the somewhat deviant trend is observed for all temperatures it should not be related to the temperature model as such. No more effort is therefore directed towards this. Instead the conclusion is that the temperature model introduced in the simulation tool is adequate to predict the machine behaviour at elevated temperatures.

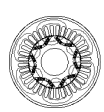

Chapter 4

Skewing analysis

This chapter covers the work done on analysing the skewing of the stator in the prototype machine. Main focus is on how the torque production and the unwanted torque variation or ripple are affected. Skewing is implemented in the stator which allows for a continuous twisting along the active machine length. This is contrary to the rotor that would have required implementation in discrete steps due to the cuboid shaped permanent magnets. Skewing is done with one slot pitch. With two slots per pole and phase the skewing angle α_{sh} becomes $\pi/6$ electrical radians. In the machine with three pole pairs this corresponds to 10 mechanical degrees. With the rather long and slender geometry this is hardly noticeable when working with the machine windings. The work presented in [34] states that the skewing angle could be chosen differently in order to optimize the influence of skewing at loaded conditions. This has however not been included in the prototyped machine design.

The simulation tool is adopted in order to study the influence of skewing in the stator or rotor even though the FEA simulations are done in a 2D simulation tool. Measurements are performed in order to verify the simulation results. A more thorough introduction to why skewing is implemented in the prototype is found in [1].

4.1 Analytical approach

The first skewing analysis is done with an analytical approach. A skewing factor, k_{sh} is calculated for the harmonic order h_a with (4.1) in accordance with, e.g., [8], [9] and [16]. Since the torque originates from the fundamental signal, the torque reduction due to skewing can be predicted by solving (4.1) for a skewing angle α_{sh} equal to $\pi/6$ and h_a equal to one and multiply it with the torque. With these numbers, the analytical and constant

skewing factor becomes k_{sh} =0.9886 $\approx$ 0.99, indicating just over 1% reduction in torque.

$$k_{sh} = \frac{sin\left(\frac{h_a \cdot \alpha_{sh}}{2}\right)}{\frac{h_a \cdot \alpha_{sh}}{2}} \tag{4.1}$$

By analysing (4.1), it is noticed that the skewing factor can be seen as the peak value of the average of an infinite number of sine waves shifted from plus to minus half the skewing angle. This is also established in [35]. As a consequence, the analytical equation is limited to no load or when the constant-torque lines are orthogonal to the current vector in a $T(i_d, i_q)$ diagram. In practice this means a surface mounted PM machine with constant iso-torque lines in parallel with the x-axis. If the iso-torque lines have a concave appearance, such as in an IPMSM, the influence of the skewing factor is increased. If the current vector has an angle different than 90° to the iso-torque lines, the influence of the skewing factor is changed further. This means that for a machine utilizing reluctance torque, the skewing factor will differ depending on the operation point. Therefore, the skewing factor as stated in (4.1) is no longer valid. Similar conclusions are also reached in e.g. [34] and [36].

4.2 Finite element simulations

As mentioned previously in 2.2.1, the electromagnetic simulations are performed in a 2D-FEM environment. Since skewing means a variation as function of axial direction, it cannot be included in 2D simulations. The modelling of skewing is instead introduced in the post simulation analysis.

4.2.1 Implementation of skewing in the simulation tool

For studying the influence of skewing, 28 load points as defined in the *dq*-reference frame in Figure 4.1 are analysed by simulations. In order to avoid extrapolation, the actual simulation load map also has an extra frame of load points surrounding the load map presented in Figure 4.1. In the subsequent analysis, the encircled load case ($i_d = -200$ A, $iq = 300$ A) is used to exemplify how skewing is implemented in the simulations.

Each load point in Figure 4.1 comprises data from a number of different rotor positions to form an electric lap. In these simulations, the electric lap is divided into steps of $\pi/30$ or 6 electric degrees. The torque ripple is studied by looking at the torque as a function of electric angle, Θ_{EL} for each of the load points. This can be seen in Figure 4.2 where the colour coding follows the colours in Figure 4.1. The encircled load case in Figure 4.1 can

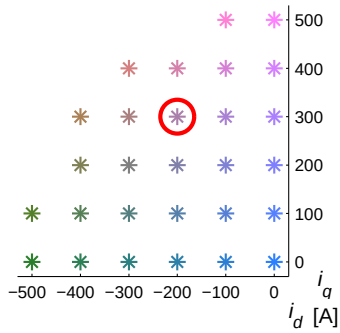

Figure 4.1: Load map in the *dq* reference frame

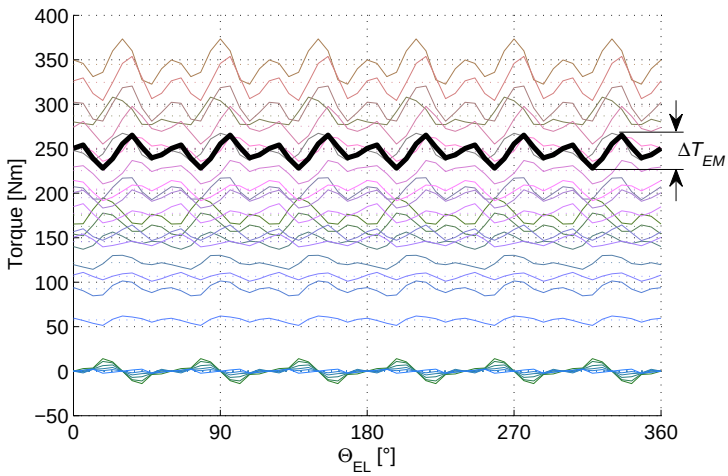

Figure 4.2: Torque as function of rotor position for 28 load cases based on simulations on an unskewed machine, with the bold line corresponds to the encircled load case in Figure 4.1

be seen as the bold line around 250Nm in Figure 4.2. Included in Figure 4.2 is also the definition of the torque ripple, ΔT_{EM}. The torque, T_{EM} and peak to peak torque ripple, ΔT_{EM} as functions of i_d and i_q is presented in Figure 4.3.

The approach to investigate the influence of skewing is to consider the machine as a continuous number of displaced machine sections. This is done not only physically along the axle, but also in terms of the applied current. The laminate in the very centre of the machine halfway down the active length is considered as reference while the last laminate on each end is twisted with plus/minus half the skewing angle respectively. The same is valid for the applied current vector. Since skewing the stator (or rotor) means a rotation of the

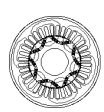

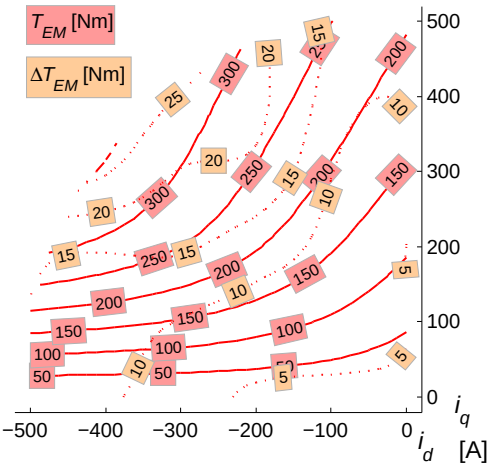

Figure 4.3: Torque (T_{EM}) and peak to peak torque ripple (ΔT_{EM}) as functions of i_d and i_q from simulations on an un-skewed machine

incoming permanent magnet flux from the rotor along the stator length, the *d*-axis direction is twisted as well. This makes the applied current vector appear as distributed along the axial stator length. Consequently, a considered reference current vector, applied halfway down the active machine length is shifted by plus/minus half the skewing angle as it moves toward each end of the machine. The result is that the applied current vector forms an arc in the *dq*-reference frame. This can be seen in Figure 4.4 where the encircled load case in Figure 4.1 ($i_d = -200$ A, $iq = 300$ A) is used to show how the current vector is distributed from the non-driving end (NDE) via the midpoint of the machine to the driving end (DE). The torque contribution from each fraction of the distributed current vectors is interpolated from the torque map in Figure 4.3.

The resulting torque contribution from the distributed currents is plotted as a function of rotor position for half an electric lap in Figure 4.5. The figure should be interpreted as a visualization of how the torque varies as a function of the machine length. The original, un-skewed torque is plotted in black. The resulting simulated torque from the skewed machine is obtained by averaging the torque from one side of the machine to the other. The resulting torque is plotted in red. By replacing the original torque with the skewed torque in the entire load map, the resulting torque from a skewed machine is obtained.

4.2.2 Simulation result

When post processed with consideration to skewing, torque vs. rotor position curves for the 28 load cases defined in Figure 4.1 become as presented in Figure 4.6. Again the torque

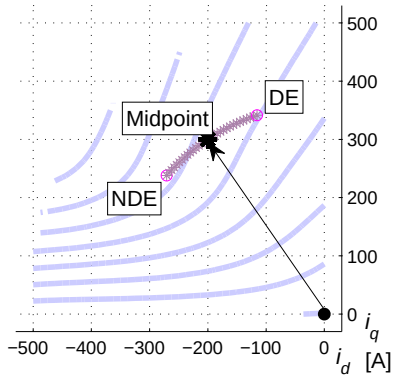

Figure 4.4: Distributed current in the *dq*-reference frame due to skewing together with iso-torque lines from simulations

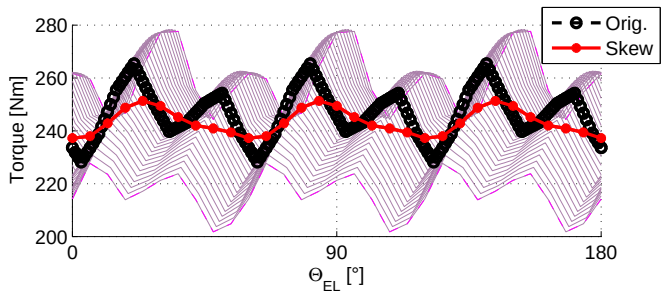

Figure 4.5: Visualization of the torque as function of rotor position from simulations for the distributed current (in Figure 4.4) together with the un-skewed original torque and resulting averaged torque from a skewed machine

obtained with $i_d = -200$ A and $iq = 300$ A is presented with a thicker line. The torque fluctuation seen at 0 Nm is a result of the five current combinations when $i_q = 0$ A and $i_d \neq 0$ A. With no current applied, the torque ripple is virtually gone. As expected, the peak to peak torque ripple is reduced considerably. This is also seen when T_{EM} and ΔT_{EM} are plotted as functions of i_d and i_q in Figure 4.7 and compared to the result of the un-skewed machine in Figure 4.3.

4.2.3 Apparent skewing factor

In order to further analyse the influence of skewing on the torque production, a load dependant, apparent skewing factor, k_{sh}^{ap} is derived from the simulation results with and without skewing implemented. The simulated torque post processed with the distributed current vectors in Figure 4.4, $T(skew)$ is compared to the un-skewed torque $T(no\ skew)$

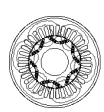

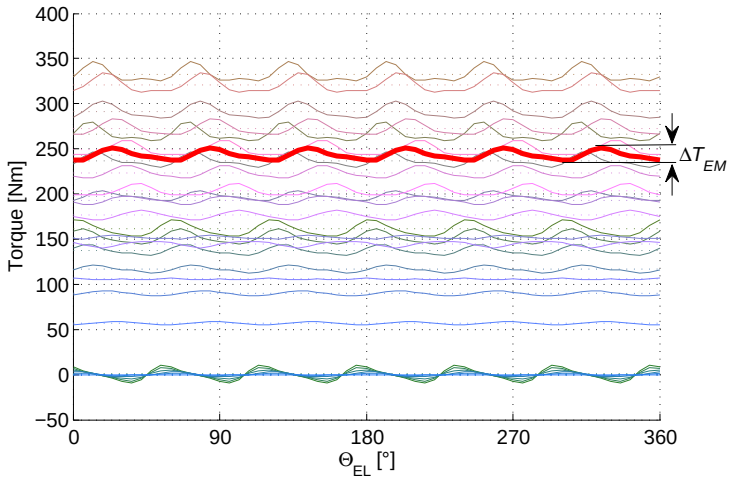

Figure 4.6: Torque as function of rotor position from simulations for 28 load cases with skewing

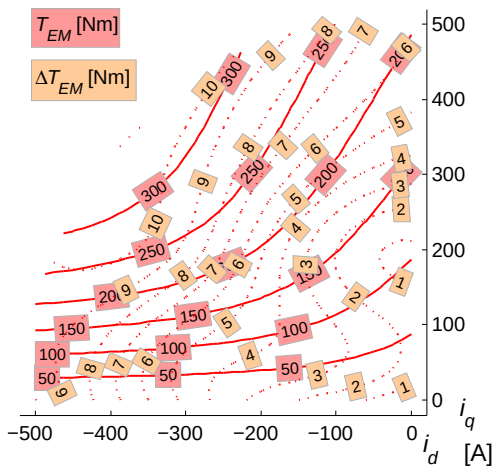

Figure 4.7: Torque (T_{EM}) and peak to peak torque ripple (ΔT_{EM}) as functions of i_d and i_q from simulations with skewing

according to (4.2). This apparent skewing factor, presented in Figure 4.8 has no real practical use but is presented to emphasize the difference with the analytical skewing factor from (4.1). Instead of being constant at almost 0.99, the skewing factor is a function of loading.

$$k_{sh}^{ap} = \frac{T\,(skew)}{T\,(no\ skew)} \tag{4.2}$$

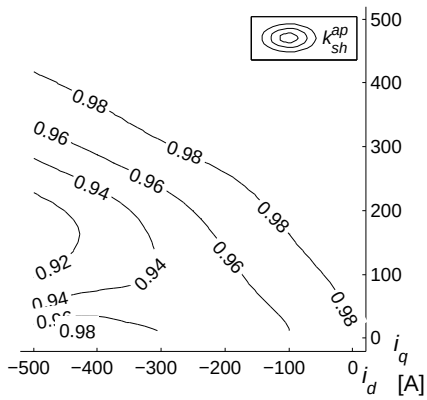

Figure 4.8: Apparent skewing factor, k_{sh}^{ap} derived from simulated torque with and without skewing with distributed current vectors

In Figure 4.8, it can be noticed that the skewing factor is lower in the lower left region of the load map. Hence the skewing has higher influence on the torque in that region. This is caused by the concave trends of the iso-torque curves in a dq loadmap of an IPMSM (seen in e.g. Figure 4.4) in combination with the arc formed by the distributed current vectors in Figure 4.4.

Along the q-axis when i_d is close to zero, it can be seen that the iso-torque lines are rather sparse. This since the torque production is less sensitive to variations in the current here. Therefore the distributed current vectors appearing when skewing the machine has a minor affect on the reduction in produced torque. Consequently, the apparent skewing factor in this region is as high as the analytical expression in (4.1).

Along a 45° angle in the second (and third) quadrant of the dq-load map, the iso-torque lines bend in opposite direction than those of the arc formed by the distributed current vectors. This means that the current vectors in the outer ends of the arc end up further from the constant iso-torque line. Compared to the analytical expression in (4.1) where the result can be derived from an arc segment tangent to a straight line, this results in slightly lower skewing factor around 0.98.

Further down towards the negative d-axis, the torque is more sensitive to a difference in applied current. The iso-torque lines in e.g. Figure 4.4 are closer together. This with the orientation of the arc formed by the distributed current vectors makes the influence of skewing more considerable. As one end of the arc stretches rather deeply towards the negative d-axis, the torque contribution from that end of the machine gets lower. At the same time, the other side of the distributed current vector arc is bending away from the increased torque. Hence the lost torque in one end of the machine is not compensated by

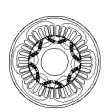

the other end to the same extent. As a result, the apparent skewing factor is getting even lower, down to just over 0.9 at the lowest.

As the load point reaches the negative d-axis, the torque distribution along the distributed current arc gets more evenly distributed again. This makes the apparent skewing factor recover slightly again. Since the torque produced in this part of the load map is rather low, the torque reduction in absolute values is rather low anyway. The reduction in absolute torque is presented in Figure 4.9.

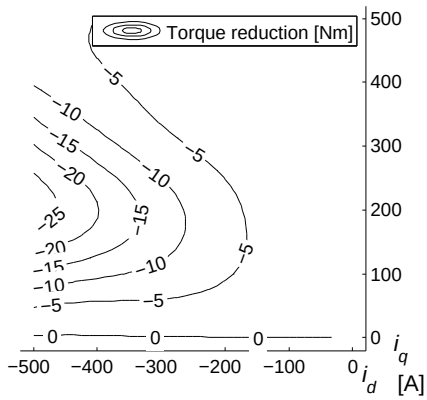

Figure 4.9: Torque reduction due to skewing as function of i_d and i_q

Based on this analysis it can be concluded that the apparent skewing factor is load dependant rather than constant. By adding the MTPA and MFPT curves (introduced earlier in Figure 2.8 when discussing the machine control in Section 2.2.3) it can also be studied how the load dependant apparent skewing factor influences the machine when in operation. This is done for k_{sh}^{ap} in Figure 4.10 and for the reduction in absolute torque in Figure 4.11. Here, the dotted lines between the MTPA and MFPT curves correspond to dq-current vectors of 100 to 500 A. From these figures it is concluded that the region of the load map where the torque is affected the most, corresponds to the region used while the machine is in field weakening. Since a traction machine is used extensively in the constant power region above base speed, the machine is influenced more than expected from the analytical expression in (4.1).

4.2.4 Torque ripple reduction

By comparing the average torque ripple, ΔT with and without skewing in a similar manner as previously done for the torque in (4.2), the influence on the unwanted torque fluctuations can be studied. This is done according to (4.3) with the result presented in Figure 4.12. Here

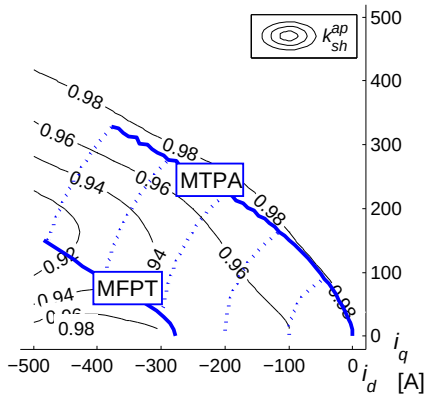

Figure 4.10: Apparent skewing factor, k_{sh}^{ap} with MTPA and MFPT curves to define the operating area for the electric machine

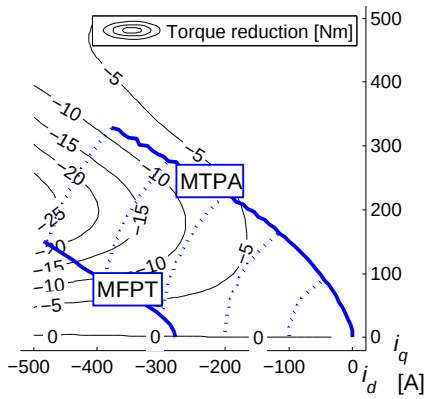

Figure 4.11: Torque reduction due to skewing with MTPA and MFPT curves to define the operating area for the electric machine

the torque ripple reduction, $\Delta T_{Reduction}$ should be seen as how much the torque ripple is decreased in percent due to skewing.

$$\Delta T_{Reduction} = \left(\frac{\Delta T\,(skew)}{\Delta T\,(no\ skew)} - 1 \right) \cdot 100\% \tag{4.3}$$

As can be seen, the torque ripple is affected differently depending on load point. Along the q-axis, the torque ripple is reduced with up to 80%. Although not visible in the figure, the torque ripple in the the origin is reduced with more than 95%. This is expected since the cogging torque theoretically should be completely removed with skewing. Therefore, with no applied currents, the torque ripple should be virtually zero in this point.

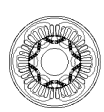

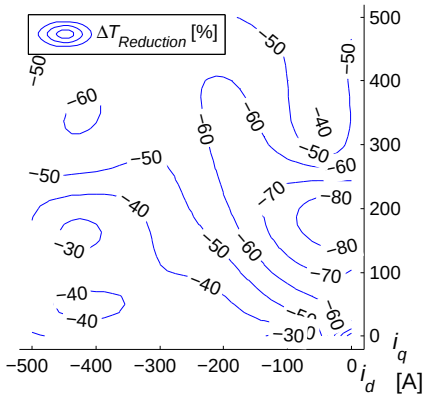

Figure 4.12: Torque ripple reduction in percent due to skewing as function of i_d and i_q

In the operating range of the machine, along an MTPA-curve ΔT is reduced with around 60%. Further down in the field weakening area the relative torque ripple reduction drops down to eventually below 40%. Hence, the benefit of introducing skewing in terms of lower torque ripple, seems to decrease in the operating area typically used by the IPMSM traction machine. A similar conclusion can also be drawn from the analytical expression in (4.1). When solved for the 6$^{\text{th}}$ harmonic the skewing factor becomes ≈0.6. Hence, the single largest torque ripple contributor is predicted to be reduced by around 40% only.

4.2.5 Linked magnetic flux with skewing

In addition to studying the torque reduction due to skewing, some attention is also directed towards the linked magnetic flux, ψ. This is presented as ψ_d and ψ_q for the direct and quadrature directions in Figure 4.13 and as ψ in absolute values in Figure 4.14. From these figures it is possible to conclude that the magnetic flux linking in the q-direction is affected more by skewing than that in the d-direction. This is expected since the effective airgap is larger in the d-direction and hence the reluctance in the q-direction is smaller compared to in the d-direction. The relative influence on the reluctance is therefore higher in the q-direction. When the current vector is distributed by the skewing (as described in Figure 4.4), a variation in the q-direction affects the linked magnetic flux more than in d-direction due to larger inductance.

A reduction factor, $k_{sh}^{|\psi|}$ (similar to the apparent skewing factor, k_{sh}^{ap} presented for the torque in Figure 4.8) for the total linked magnetic flux is derived according to (4.4) and presented in Figure 4.15.

$$k_{sh}^{|\psi|} = \frac{\psi\,(skew)}{\psi\,(no\ skew)} \tag{4.4}$$

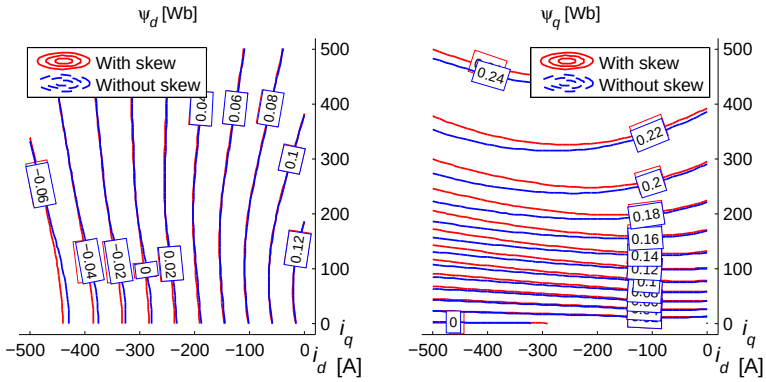

Figure 4.13: Linked magnetic flux, ψ in d- (left) and q- (right) direction as functions of i_d and i_q with and without skewing

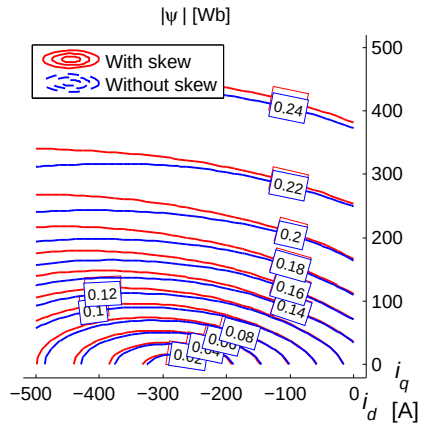

Figure 4.14: Total linked magnetic flux, $|\psi|$ with and without skewing as functions of i_d and i_q

In Figure 4.16 the two reduction factors (k_{sh}^{ap} for the torque and $k_{sh}^{|\psi|}$ for the total linked magnetic flux) are plotted together to simplify a comparison. Here it is noticed that although the overall trend agrees, the torque is affected slightly more than the linked magnetic flux when the field weakening current increases. This because the q-flux is affected more than the d-flux and that the importance of the reluctance torque is larger in that part of the load map. Since the flux in the d-direction is almost unaffected, the total magnetic flux linkage is affected less than the torque.

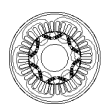

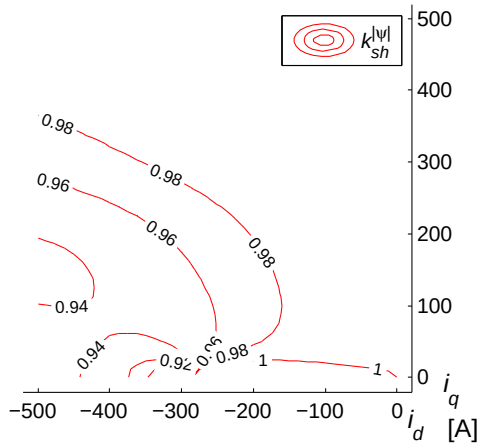

Figure 4.15: Magnetic flux linkage reduction factor, $k_{sh}^{|\psi|}$ due to skewing as function of i_d and i_q

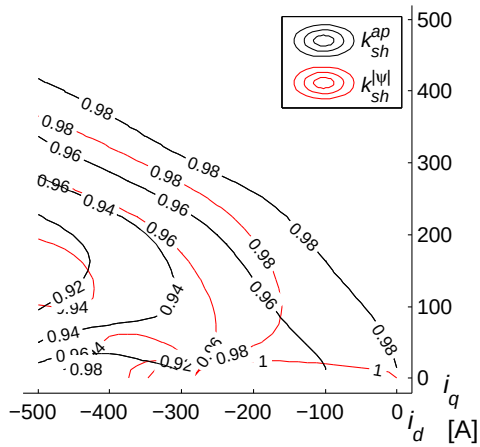

Figure 4.16: Apparent skewing factor, k_{sh}^{ap} and magnetic flux linkage reduction factor, $k_{sh}^{|\psi|}$ as functions of i_d and i_q

4.3 Torque ripple measurements

Measurements are performed in order to study the torque ripple and verify the simulation results. Since the prototype is built with a skewed stator, no comparative measurements can be done on an un-skewed machine. The test result is compared to simulations with and without consideration to skewing. This is done for skewing modelled with the distributed current vectors as described in previous sections as well as implemented with the analytical

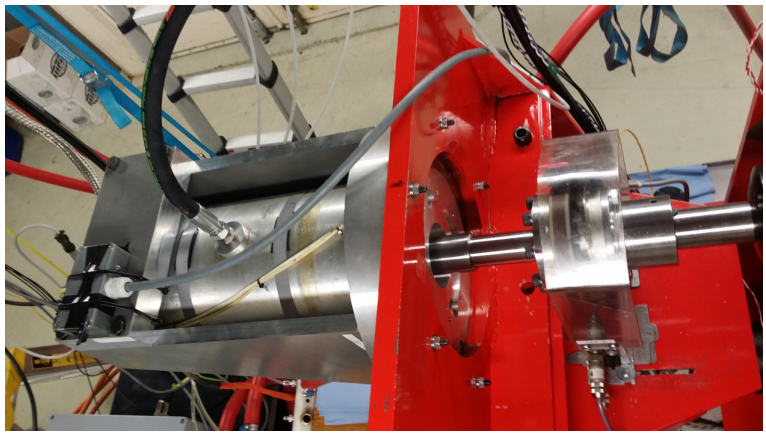

Figure 4.17: Test object mounted in the test rig

skewing factor in (4.1). The result agrees well with when the distributed current vectors are used in the model. This holds in terms of torque and torque ripple levels as well as harmonics content in the torque.

4.3.1 Test set-up

The prototype mounted in the test rig can be seen to the left in Figure 4.17. The test object is operated in current control with a Semikron SKAI 2 drive [29] utilizing PWM at a switching frequency of 8 kHz. Torque is measured with a HBM T12/1 kNm torque transducer with the Higher Accuracy option [28]. The rig dyno (a separately magnetized Siemens 1GH5 224-0NJ40-Z DC-machine controlled by a Parker DC590P inverter) is controlled in speed control with a set speed of 20 rpm. The test object is pre-heated with 60°C coolant and loaded with currents in the *dq*-reference frame as defined in Figure 4.1. Each load point is maintained for about 30 seconds, which at 20 rpm and with 3 pole pairs corresponds to 30 electrical laps. The rotor position and hence electrical angle is obtained from the resolver. The winding temperature is monitored during the entire test and the magnet temperature is monitored periodically by disabling the drive and measure the induced voltage (based on the results in Chapter 3). The magnet temperature is kept between 60°C and 70°C throughout all tests.

4.3.2 Measurement results

The torque and electric angle, Θ_{EL} are recorded as functions of time for the load cases introduced in Figure 4.1. The measured signals at $i_d = -200$ A and $i_q = 300$ A (the

encircled load case in Figure 4.1) is presented in Figure 4.18. The average torque, T_{EM} and peak to peak torque ripple ΔT_{EM} can be determined rather easily, but it is not possible to see any trends in the torque ripple. In order to do so, the data is rearranged with ascending order of the electric angle, Θ_{EL}. This way, the torque contribution from multiple laps are used to study the torque as function of electric angle instead of as function of time. The rearranged torque signal for $i_d = -200$ A and $i_q = 300$ A is presented for one complete electric lap in Figure 4.19.

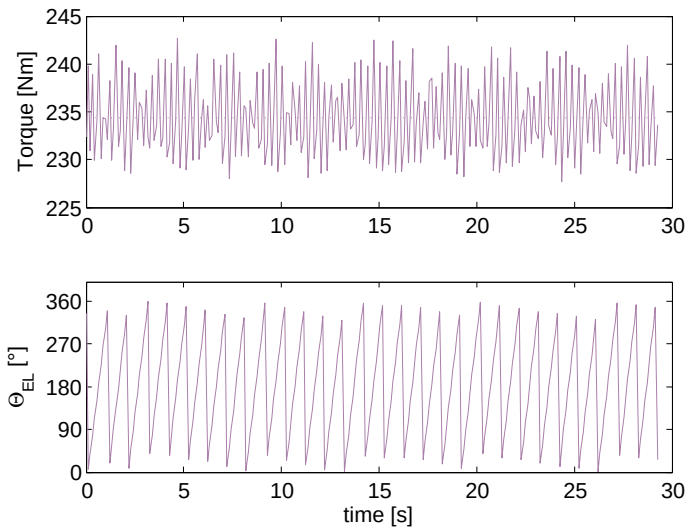

Figure 4.18: Measured torque (upper) and electric angle Θ_{EL} (lower) as functions of time for $i_d = -200$ A and $i_q = 300$ A

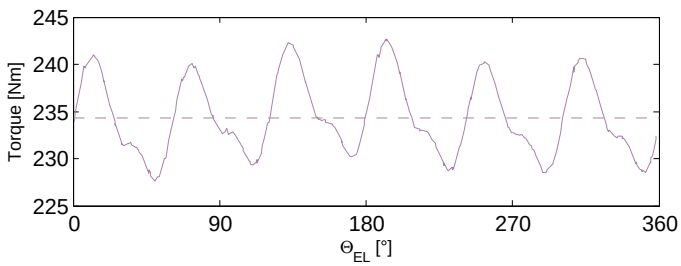

Figure 4.19: Measured torque as a function of electric angle, Θ_{EL} together with average torque (dashed line) for $i_d = -200$ A and $i_q = 300$ A

Average torque and torque ripple for all load points in the entire load map are collected in Figure 4.20. Here, each sub-plot represent a specific measurement point and is arranged ac-

cording to its applied dq-currents. Hence the sub-plots on the right hand side are with zero d-current and increasing q-current when moving upwards in the graph. Correspondingly, the sub-plots at the bottom of the figure are with no q-current and increasing d-current amplitude when moving to the left. Limitations in the dq-current amplitude in the drive prevent tests from being performed in the upper left corner of the load map.

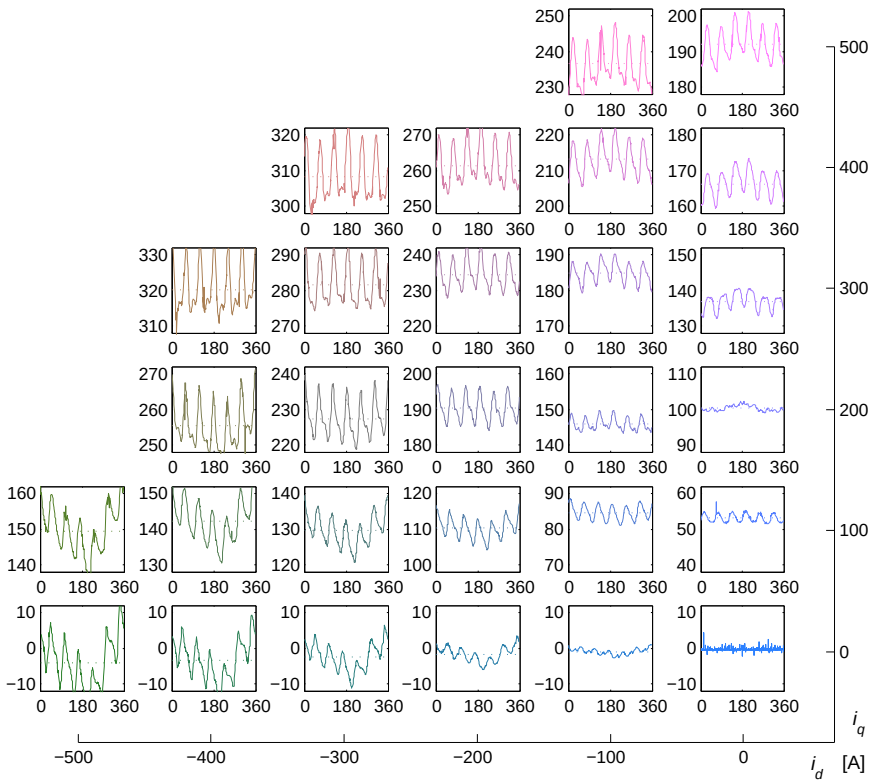

Figure 4.20: Sub plots on measured torque [Nm] on the y-axes as a function of electric angle, Θ_{EL} [0-360°] on the x-axes for 28 load cases distributed according to the location of each sub plot in the dq-current load map

In order to study the harmonic content in the torque at the different load cases, an FFT analysis is done. The result for each load case is presented with a logarithmic scale in Figure 4.21 (arranged in a similar way as in Figure 4.20). As can be seen, dominating harmonics are the 6^{th} and the 12^{th}. This corresponds to the space harmonics of order 5 and 7 (for the 6^{th}) and order 11 and 13 (for the 12^{th}) when considering the three phase system [37, pg.113-115]. Since the skewing is done with one slot pitch, corresponding to one twelfth of an electric lap, the 12^{th} order harmonic is in theory cancelled. This is why the

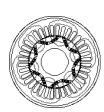

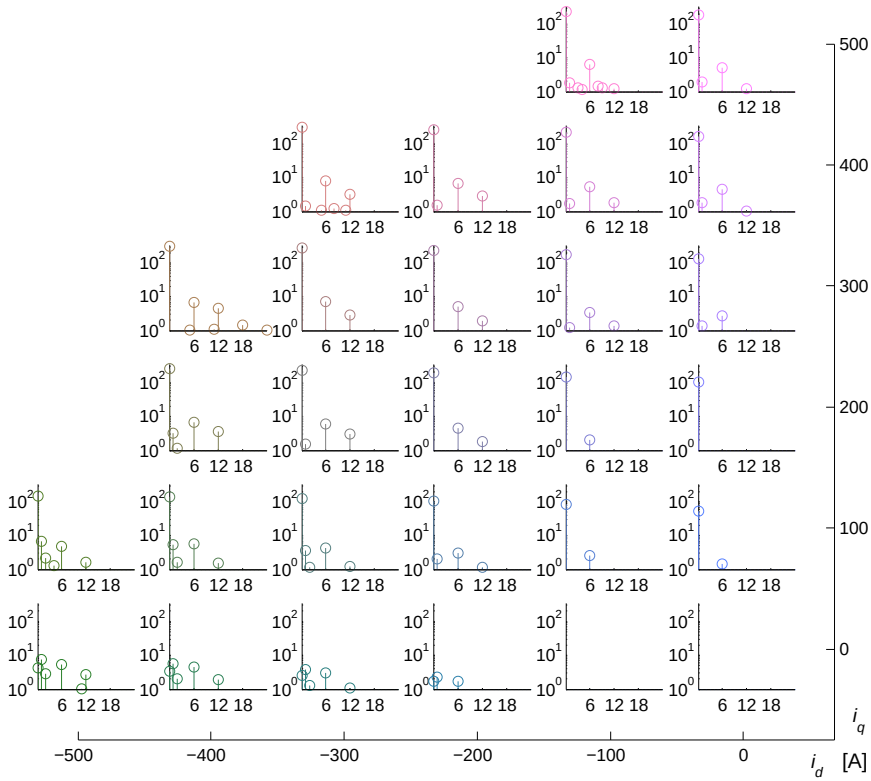

Figure 4.21: Sub plots on the amplitudes of the harmonic content in logarithmic scale on the y-axes as functions of harmonic order on the x-axes based on FFT analysis of the measured torque from 28 load cases distributed according to the location of each sub plot in the *dq*-current load map

12^{th} harmonic is removed when the analytical skewing factor for a skewing angle (α_{sh}) of 30 electrical degrees is used. In reality the 12^{th} harmonic is still present. This is explained by the different parts of the machine being saturated differently. Any blanking time from the frequency converter could also be a potential source of 6^{th} order harmonics [38]. This should however not be an issue at the low speed operation used during these tests. In addition to this, the drive used in the testing has a compensation strategy for the blanking time by adopting the pulse width to correspond to what is lost due to the dead time.

At higher loads, more harmonics can be seen when saturation effects starts to have higher influence. Finally, a first order harmonic is noticed in some of the load points. These are not expected and are discussed further in the following sub section. The measured torque and torque ripple for all test cases are collected and plotted as functions of i_d and i_q in 4.22.

Here, the torque ripple is collected as being the difference between the highest and lowest torque in each load point. Hence the first order torque ripple is included and contributes to the amplitude of the total torque ripple.

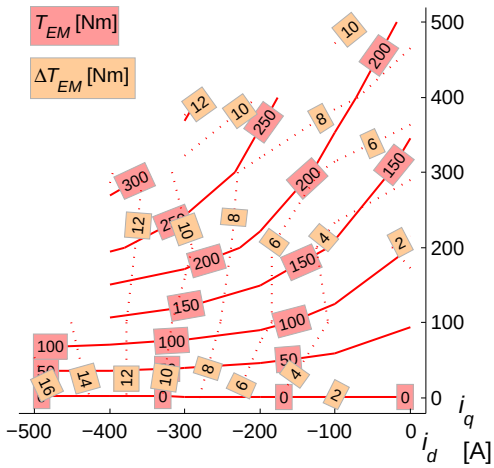

Figure 4.22: Measured torque (T_{EM}) and peak to peak torque ripple (ΔT_{EM}) including the first order torque ripple as functions of i_d and i_q from the prototype with skewed stator

Resolver eccentricity

As mentioned previously, some load cases in the test results in Figure 4.20 and 4.21 reveals an un-expected first order harmonic. This is a torque ripple that follows the electric frequency. It can also be observed that this first order torque ripple is present only in the sub plots in the lower left and upper right regions, hence along either the d- or the q-axis. In Figure 4.20 it is also noticed that there seems to be an apparent phase shift depending on whether the load point is along the negative d-axis or the q-axis. In the first case (lower left corner of Figure 4.20), the torque is higher in the beginning and end of the electric lap (0° and 360°) and lower at approximately half the lap (180°). In the upper right corner of the load map the trend of the torque is the opposite, hence lower when the electric lap starts and higher after half the turn (180°). Finally, it is observed that when the d- and q-components of the current vector are in the same magnitude, the first order torque ripple seems to fade out.

When consulting the literature, it is concluded that the first order harmonic is related to resolver eccentricity. Hence a misalignment of the resolver rotor relative to its stator. The consequence is a small difference in amplitude between the sine and cosine responses from the resolver. This leads to a fluctuation in the resolver angle reading. As a result, there will be a torque ripple with a frequency equal to the electrical frequency. This phenomenon and

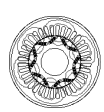

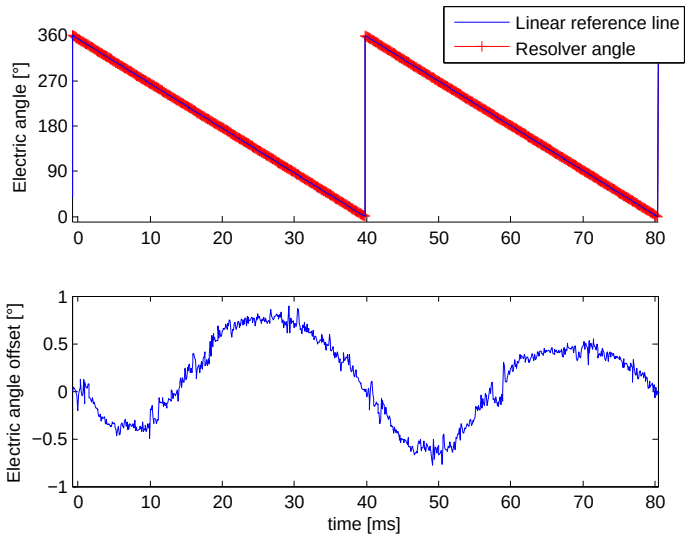

Figure 4.23: Measured resolver angle plotted with a linear reference line to simulate the actual rotor angle (upper) and electric angle offset being the resolver angle minus the linear reference angle (lower) as functions of time

how to compensate for it is handled in e.g. [39–42]. The implementation of a compensation method in the drive is not included in the work presented here.

The phenomenon with the misaligned resolver rotor on the prototype machine is investigated further by studying the sine and cosine signals. The resolver is excited by the frequency converter and rotated at no load. The resolver sine and cosine responses are sampled with an oscilloscope at 200kS (kilo-Samples) and post processed in Matlab in order to obtain the resolver angle. The result, presented in Figure 4.23 indicates that the resolver angle from the prototype machine fluctuates with an electrical angle offset of up to about $\pm 0.8°$. A similar but highly over-exaggerated sketch on how the resolver position angle fluctuation behaves compared to the actual rotor position angle can be seen in Figure 4.24. The result of this fluctuation is a small oscillation in the dq-reference frame in the frequency converter. This is noticed in the machine as a variation in angle of the applied current vector.

An attempt to replicate the effect of the eccentric resolver in simulations is done with an approach similar to when skewing is implemented (described in subsection 4.2.1). The difference is that instead of interpolating the torque in the dq-load map based on the skewing angle ($\pm 15°$), the interpolation is made based on the resolver angle offset due to the misalignment. In this way the average torque contribution from each of the two extreme cases $\pm 0.8°$ can be used to estimate an approximate amplitude of the torque ripple caused by the misaligned resolver rotor. As can be seen in Figure 4.25, the result is consistent with the

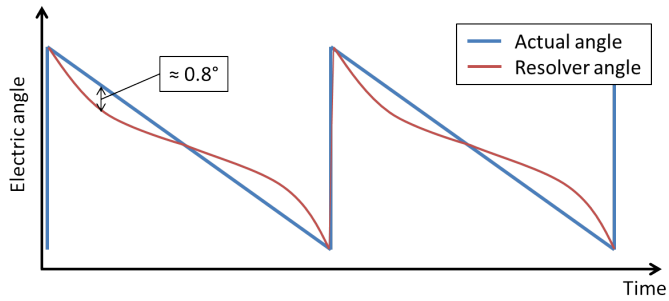

Figure 4.24: Over-exaggerated resolver angle fluctuation due to misaligned resolver rotor

trends seen in the FFT analysis in Figure 4.21.

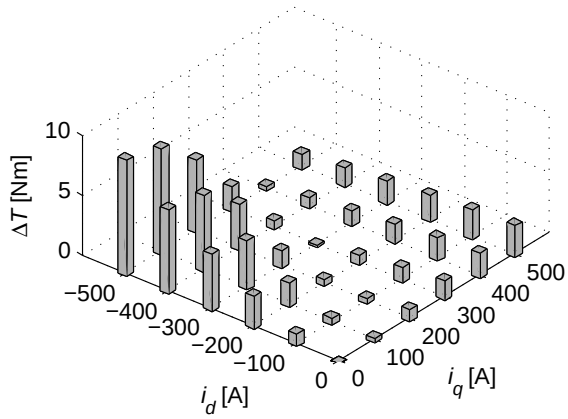

Figure 4.25: Amplitude of the first order harmonic in the torque ripple as function of i_d and i_q according to simulations with a resolver misalignment of $\pm 0.8°$

In addition to the amplitude of the first order harmonic torque ripple, the apparent phase shift at different locations in the load map can be explained by visualizing the two extreme cases $\pm 0.8°$ in a load map with torque as function of i_d and i_q such as e.g. Figure 4.7. This would look similar to the arc in Figure 4.4 but with the end points of the arc much closer together ($\pm 0.8°$ instead of $\pm 15°$). From this it can be reasoned that a current vector in the second (or third) quadrant shifted closer to the negative d-axis (hence first half of an electric lap) will result in decreased torque as long as the current vector is close to the d-axis. If the current vector instead is closer to the q-axis, the result on the torque is the opposite. In the second half of the lap, when the current vector instead is shifted slightly

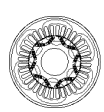

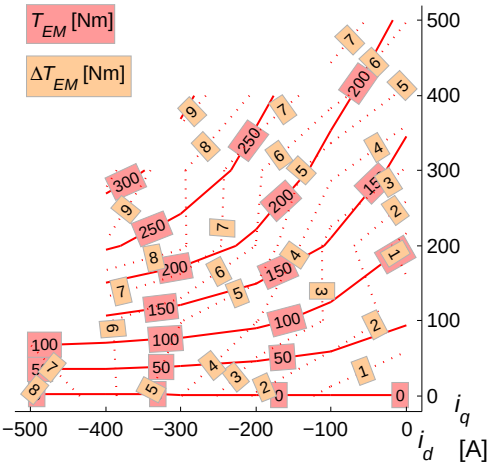

Figure 4.26: Measured torque (T_{EM}) and peak to peak torque ripple (ΔT_{EM}) without the influence of the first order torque ripple caused by the resolver eccentricity as functions of i_d and i_q from the prototype with skewed stator

towards the q-axis, the mutual relationship will be the opposite, hence increased torque close to the negative d-axis and decreased torque close to the q-axis. In between the two axes, when the d- and q-current components are in the same range and the iso-torque lines make their upward bends, the torque decreases equally much (or rather little) disregarding if the current vector is shifted positively or negatively. The result would instead be a torque ripple with twice the electric frequency. However, since the current vector oscillation has such a small amplitude, the amplitude of the resulting torque ripple in this region of the load map is so small that it is hard to detect in comparison with the higher order torque ripple from the machine.

Since the resolver eccentricity is not included in the simulations on the skewed stator, the torque ripple caused by the resolver misalignment is compensated for when post processing the test data. Instead of simply considering the difference between one maximum and one minimum over a complete electric lap (as done previously for the result in Figure 4.22), the average out of a number of local maxima and minima is regarded. Since the 6^{th} order harmonic dominates, this gives the number of local maxima and minima to consider over one electric revolution. In this way, the influence of the first order harmonic can be filtered from the test data at the post processing. The resulting torque and torque ripple with compensation for the eccentric resolver as functions of i_d and i_q are presented in Figure 4.26. For the continuing comparison between measurements and simulations, this modified torque ripple map is used. The effects of the eccentricity are not the main purpose of the experimental evaluation.

4.3.3 Measurements compared to simulations

Torque from the simulations with constant and load dependant skewing (k_{sh} and k_{sh}^{ap} respectively) as well as without skewing are plotted as functions of i_d and i_q together with the measured torque in Figure 4.27. Here it is seen that the difference between the three simulated cases is small in the upper right corner of the load map. This is expected from Figure 4.8 and solving (4.1) as the two skewing factors are basically equal in these load cases. They are also so close to 1 so the difference to the torque without skewing should be small. In the lower left region of the load map, the simulation result with load dependant skewing factor starts to deviate from the two other simulation cases. This is also expected from Figure 4.8 since the apparent skewing factor in this region drops down to just over 0.9. The mutual difference between the simulated non-skewed torque and that recalculated with the constant k_{sh} is for obvious reasons constant in the entire load map.

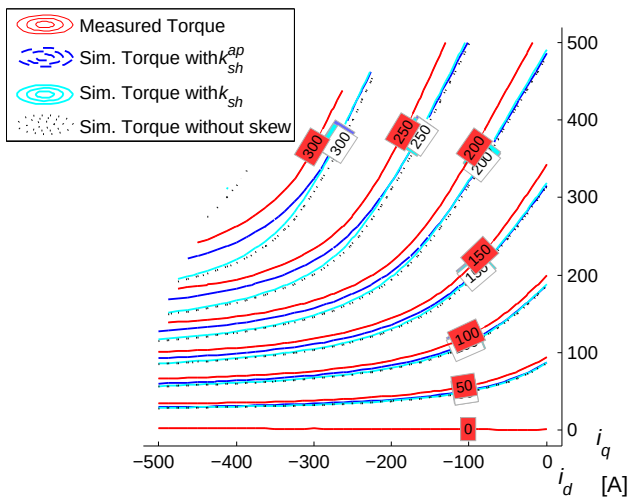

Figure 4.27: Measured torque and torque from simulations with load dependant skewing, constant skewing factor and without skewing

When comparing the simulation results with measurements it is clear that the simulations with load dependant skewing follows the measurements better than if the skewing factor is constant or if no skewing is implemented. It is also observed that there is an offset between measurements and simulations in the entire load map. When studying it closer, it is concluded that the deviation between measurements and simulations with skewing is increasing with the length of the applied *dq*-current vector. This deviation is observed also in the measurements performed in Chapter 2 as well as those performed in Chapter 3. This holds for the torque as well as the linked flux or induced voltage. As already discussed, possible reasons could be related to how the permanent magnets are modelled or how the

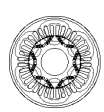

simulation model handles the highly saturated regions in the machine (typically close to the air gap and around the iron bridges between the magnets and flux barriers in the rotor). It might be that a smaller mesh size in those saturated regions or a better fitted BH-curve of the iron core could reduce the deviation between simulations and measurements slightly. This is not studied further in the analysis covering the effects of skewing on the torque production.

The amplitude of the torque ripple ΔT_{EM} from the measurements, together with simulations with k_{sh}^{ap} and without skewing is studied in Figure 4.28 (torque ripple modelled with the constant skewing factor k_{sh} is not included in this plot). As expected, the amplitude of the torque ripple is higher in the simulations without skewing. Compared to the simulations with skewing, the amplitude differ approximately with a factor of 2. The amplitude of the torque ripple from the simulations with load dependant skewing agrees well with the measurements.

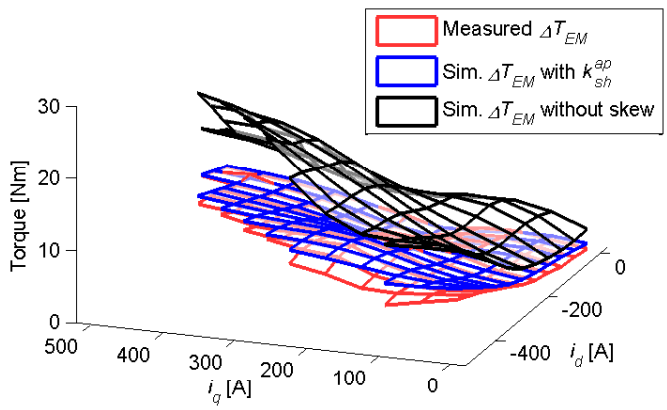

Figure 4.28: Torque ripple (ΔT_{EM}) in newton meters from measurements and simulations with and without load dependant skewing

The torque ripple is analysed a bit further by looking closer at the harmonic content for some load cases. In Figure 4.29, the harmonic content of the encircled load case in Figure 4.1 ($i_d = -200$ A and $iq = 300$ A) is plotted with logarithmic scale on the y-axis. Included in the graph is measured data as well as simulation results with load dependant skewing, constant skewing factor and without skewing. The test data in this load point does not have any visible first order harmonic from the resolver misalignment. Further on, since the load dependant skewing and the constant skewing factor are almost equal in this region of the load map (see Figure 4.8 and compare to solving (4.1)), the fundamental torque from these two simulation cases are virtually the same.

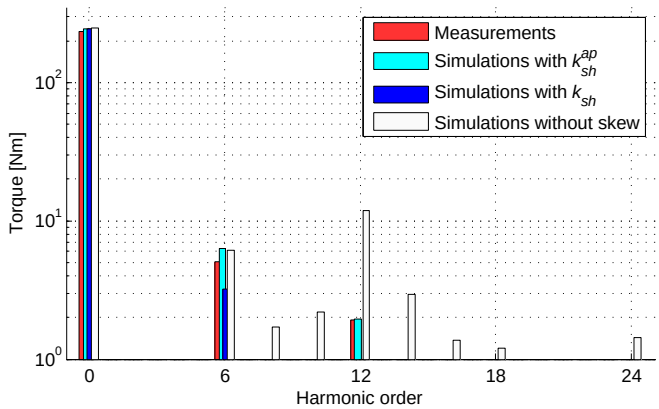

Figure 4.29: Harmonic content as a function of electric angle in the torque at $i_d = -200$ A and $iq = 300$ A from measurements and simulations with load dependant, constant and no skewing

The previously mentioned discrepancy in fundamental or average torque from measurements compared to simulations is noticed here as well. Also the 6$^{\text{th}}$ order harmonic is lower in measurements compared to simulations with load dependant skewing. The difference is around 1 Nm. Simulations with constant skewing factor instead underestimates the 6$^{\text{th}}$ order harmonic with around 2 Nm. The 12$^{\text{th}}$ harmonic which is removed completely with the constant analytical skewing factor, is almost equal when comparing measured data with the load dependant skewing simulation. Similar conclusions are drawn when studying the harmonic content at $i_d = -300$ A and $iq = 200$ A, which is done in Figure 4.30. Being located within the field weakening region, this load case is more relevant in terms where the machine is likely to operate. Here, the 1$^{\text{st}}$ harmonic from the resolver eccentricity is seen in the measured data. Further on, the difference in fundamental torque from the two versions of simulations with skewing is larger. This is expected based on the apparent skewing factor (presented in Figure 4.8) in this region of the loadmap. The fundamental torque from simulations with constant skewing factor is around 10 Nm higher than the simulation result with load dependant skewing. That is in turn around 10 Nm higher than the measurements. The trends at higher order harmonics such as the 6$^{\text{th}}$ and 12$^{\text{th}}$ are the same as in Figure 4.29. All and all, this confirms that the load dependant skewing approach is needed when analysing the influence of skewing in an IPMSM. The analytical approach in (4.1) is not sufficient when the machine is loaded.

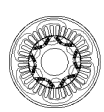

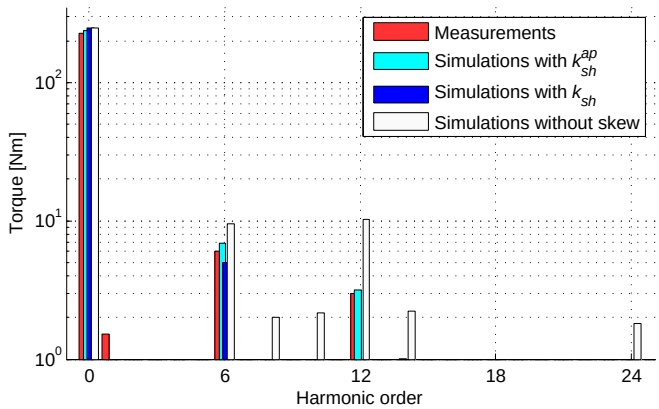

Figure 4.30: Harmonic content as a function of electric angle in the torque at $i_d = -300$ A and $iq = 200$ A from measurements and simulations with load dependant, constant and no skewing

4.4 Discussion and conclusions from the skewing analysis

As is shown throughout the chapter, implementing skewing is an efficient method to reduce the torque ripple. This is also expected both from the literature [8,9,16] and when studying the underlying physics. The drawback, also stated in the literature, is a small reduction in the torque. In addition to this, the work performed illustrates how the influence of skewing is dependant on the loading of the machine. The linked magnetic flux as well as the torque and torque ripple do behave differently due to skewing depending on the applied load. The operating area of the IPMSM traction machine utilizing reluctance torque coincides with where the torque reduction due to skewing is largest.

The validity of the simulation model is tested by comparing the simulations with measurements. The lack of a prototype without skewing limits the comparison to some extent. However, the conformity to the simulation model in terms of behaviour of the fundamental torque as well as the harmonic content, indicates that the model can be trusted. The torque ripple due to resolver eccentricity is explained using the same approach as when looking at skewing in the simulation model. Measurements on the resolver signals at no load proves that the resolver rotor indeed is slightly misaligned to its stator.

With the prerequisites for the machine (briefly introduced in Chapter 2) being exceeded in terms of peak torque, the reduced torque due to skewing should be of less importance. The benefits in terms of reduced torque ripple should instead be less noise and wear in the connecting gear reduction. However, in addition to the torque being negatively affected, so should the overall efficiency. This can be concluded with some different approaches, of

which some are used in the following reasoning.

The first approach is to consider an efficiency map where efficiency is plotted as function of torque and speed (such as Figure 2.12). Here it is elemental that the current needs to be increased in order to compensate for the reduced torque in the skewed machine. With increased current, increased losses in the windings will follow. On the other hand, with unchanged rotational speed, the reduced linked magnetic flux should imply lower flux density in the stator iron core. This leads to reduced losses due to that the flux density variation $\frac{dB}{dt}$ is reduced [43]. However, as concluded from Figure 4.16 the torque is affected slightly more than the linked magnetic flux. Consequently, the losses in the windings is likely to increase more than the reduction of losses in the iron core. In addition to this, the winding losses dominate over the iron losses in almost the entire torque speed map. As both the current and flux density have a squared relation to the losses, the proportional loss increase in the windings should be greater than the loss decrease in the core.

Another approach is to consider power in, P_{in} versus power out, P_{out} with unchanged d- and q-currents. P_{in} is affected by the voltage and the voltage is reduced due to the reduced magnetic flux linkage. P_{out} is affected by the torque and hence also reduced. However, since the torque is affected more than the magnetic flux linkage, P_{out} will be reduced more than P_{in} and hence the efficiency should be reduced. Another aspect to this could be that the harmonic content in the induced voltage is reduced and therefore potentially the iron losses as well. This is however misleading since the flux density harmonics in each laminate will be unaffected by the skewed stator. The distributed current vector should impose a small difference in iron losses in the different machine ends, but this is not believed to be decisive for the result. This potential variation in iron losses as function of machine length is however not pursued any further in the work presented here. Despite no major influence on the iron core losses, the reduced harmonic content in the magnetic flux linkage and therefore in the voltage will have a positive effect on the losses above base speed. With reduced harmonics, the voltage margin during field weakening could potentially be set smaller. Hence allowing a slightly lower current and hence losses for a given load point.

The final approach on the efficiency discussed here is starting with the applied current vector from the drive. Regardless of whether the current vector is applied with MTPA or with minimized losses in mind, the average losses in the machine and hence the efficiency should be worse as the current vector is distributed. With MTPA, this obliges a machine where the windings are the dominating loss contributor. Also in the case where the current is controlled to minimize the power factor, $\cos\phi$ the efficiency should drop. Again, the distributed current vector will cause part of the machine to deviate from the most beneficial power factor and thereby lower the efficiency. As the power factor drops, so will the active part of the electrical power going into the machine.

The outcome of this chapter is that skewing affects the torque as well as the efficiency a

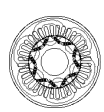

bit more than predicted by the analytical approach. Therefore it is important to reach a conclusion for each application on whether the benefits in reduced torque ripple and linked magnetic flux harmonics is worth the extra penalty. In the application aimed for in this project, the mechanical as well as acoustic aspects in the connecting gear drive could be enough to motivate for skewing. Overall this might indicate that skewing is the right way to go.

On the other end of the scale, there is the efficiency. In a hybrid application, it might not be that crucial. But if a full electric vehicle should be considered as well, it might. In such vehicles, driving range versus energy storage size is an important issue. Shifting side yet again, the full electric drivetrain might also suffer more from addition acoustic noise in the gear reduction. This leads to the ever-repeated conclusion that designing an electric machine is all about compromising.

Chapter 5

Loss mapping

5.1 Introduction

The estimation of power losses is as sophisticated as challenging independent of whether the task is carried out in a numeric field computation tool or on a test bench. In the design stage it makes more sense to keep the complexity and computational time and effort low, rather than to achieve superior accuracy. Therefore the power loss estimation is kept on a simplified level. First of all, the material modelling is rather idealized and the geometry is not as detailed as in reality. Basically the maximum flux density values are defined at fundamental frequency for a few core regions to define the power losses in these regions. Mechanical losses are neglected and winding losses are estimated by DC-conductor losses at the operation temperature. A simplifying assumption is also that the air-gap flux density in the interior permanent magnet rotor is more sinusoidal compared to surface mounted permanent magnet machines. Hence the high frequency field changes in the rotor core and magnets are ignored. Consequently the losses are underestimated in the design stage.

As the prototype is built and verifying measurements are performed, the models are gradually improved with consideration to more parameters. Mechanical losses are introduced as analytical models for windage and various types of friction contributors. The influence of manufacturing is being considered, both in how it impacts the material properties and as tolerances during the assembly.

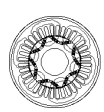

5.2 Mechanical losses

The mechanical losses that have been neglected during the design stage are introduced and accounted for in this section. The mechanical losses (P_{mech}) considered and analysed are those originating from the bearings (P_B) together with those related to the air friction or windage (P_{air}). In addition to this, some additional loss contributors are identified and accounted for. This includes friction losses from an oil seal and from carbon brushes used to connect the rotor to ground potential. The mechanical loss study is done analytically and the result is discussed in terms of uncertainties and how they affect the result. Measurements are also performed as a part of the analysis.

5.2.1 Windage losses

The air friction losses considered are those related to the air-gap together with the rotor gables. The air friction depends on the rotor speed, roughness of the surface, structure of stator core and gas properties.

Windage in the airgap

The air-gap is considered as an envelope surface meaning that the air-gap air resistance losses, P_{air}^{env} can be calculated with (5.1) [44, 45].

$$P_{air}^{env} = k_{sr} \cdot C_f^{env} \cdot \pi \cdot \rho_{air} \cdot \omega_m^3 \cdot r_A^4 \cdot l_R \tag{5.1}$$

Here, k_{sr} is a surface roughness coefficient, ρ_{air} is the density of air, ω_m is the angular mechanical velocity, r_A and l_R are rotor radius and length respectively and C_f^{env} is the viscous drag coefficient. This coefficient depends on parameters such the molecular viscosity and the eddy diffusivity of momentum which are difficult to calculate analytically [44]. Instead C_f^{env} needs to be established either experimentally or with computational fluid dynamics (CFD). According to [45] the friction coefficient can be determined with (5.2) where Re_δ is the Couette Reynolds number and Re_a is the Reynolds number for any axial airflow in the airgap. The two Reynolds numbers are described in (5.3) and (5.4).

$$C_f^{env} = \frac{0.0152}{Re_\delta^{0.24}} \left(1 + \left(\frac{8}{7}\right)^2 \cdot \left(\frac{4 \cdot Re_a}{Re_\delta}\right)^2\right)^{0.38} \tag{5.2}$$

$$Re_\delta = \frac{\rho_{air} \cdot v_1 \cdot \delta}{\nu_{air}} \tag{5.3}$$

$$Re_a = \frac{\rho_{air} \cdot v_{axial} \cdot 2 \cdot d_g}{\nu_{air}} \tag{5.4}$$

Here, v_1 is the peripheral speed of the rotor, d_g is the airgap distance, ν_{air} is the dynamic viscosity of air and v_{axial} the axial air flow in the air-gap. The dynamic viscosity as well as the density of air are functions of temperature, ϑ_K in Kelvin and can be determined with (5.5) and (5.6) [46, pg.377, 177]. Here, p is the absolute pressure in Pa and R_A is the specific gas constant of air.

$$\nu_{air} = \frac{1.458 \cdot 10^{-6} \cdot \vartheta_K^{1.5}}{\vartheta_K + 110.4} \tag{5.5}$$

$$\rho_{air} = \frac{p}{R_A \cdot \vartheta_K} \tag{5.6}$$

Assuming an air temperature of 100°C (373.15K) and atmospheric pressure, the Couette Reynolds number (Re_δ) becomes just over 4000 at 15000 rpm for the machine in question. By assuming little or no axial air flow in the air-gap, Re_a can be disregarded. This gives a simplified friction coefficient C_f^{env} according to (5.7).

$$C_f^{env} \approx \frac{0.0152}{Re_\delta^{0.24}} \tag{5.7}$$

According to [47], (5.7) is valid for Reynolds numbers from 800 to $6 \cdot 10^4$ but takes no account for Taylor vortices in the airgap. As a consequence, the analytical result is underestimating the drag losses due to windage. An alternative equation described in [47] gives C_f^{env} with consideration for Taylor vortices. This is introduced in (5.8). This equation is valid for Reynolds number from 500 to 10^4. For the machine under examination, this corresponds to a rotational speed interval from around 1860 rpm to 37000 rpm

$$C_f^{env} = 0.515 \frac{\left(\frac{d_g}{r_A}\right)^{0.3}}{Re_\delta^{0.5}} \tag{5.8}$$

Comparing the results from (5.7) and (5.8) shows that the result from (5.7) is a bit lower. This coincides with Taylor vortices being included in the latter equation. In order to obtain a more conservative result, the friction coefficient derived with (5.8) is selected in the proceeding analytical analysis. Looking at the air friction losses at the lower Reynolds number limit at which (5.8) is valid, it is concluded to be insignificantly small (below 0.5 W). Therefore, no additional consideration is given to speeds below 1860 rpm (at which the Reynolds number drops below 500). Instead, the same equation (5.8) is used all the way down to zero speed when estimating C_f^{env} .

Windage at the rotor gables

Besides the air friction on the envelope surface, the influence on the rotor gables is included when determining the total air resistance. By considering the two gables as a rotating disk,

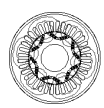

the contributing power loss, P_{air}^{gab} can be established with (5.9). Here r_{in} is inner rotor radius i.e. the radius of the shaft extending axially from the rotor. Depending on whether there is laminar flow or not and if there is a radial pumping effect or not, different viscous drag coefficients should be used. For the geometry and rotor speeds of the machine in question, C_f^{gab} is determined with (5.10) for laminar flow and radial pumping effect. Here, s is the axial distance from the rotor gable to the opposing stationary housing gable and Re_r is the tip Reynolds number according to (5.11). [47]

$$P_{air}^{gab} = \frac{1}{2} \cdot k_{sr} \cdot C_f^{gab} \cdot \rho_{air} \cdot \omega_m^3 \cdot \left(r_A^5 - r_{in}^5\right) \tag{5.9}$$

$$C_f^{gab} = \frac{3.7 \cdot \left(\frac{s}{r_{in}}\right)^{0.1}}{Re_r^{0.2}} \tag{5.10}$$

$$Re_r = \frac{\rho_{air} \cdot v_1 \cdot r_A}{\nu_{air}} \tag{5.11}$$

Resulting windage losses

The resulting losses due to air drag, or windage is obtained by solving equations (5.1) and (5.9) with relevant numbers. The result is presented in Figure 5.1. From here, it is concluded that air drag losses reach 1 W at around 2500 rpm and 80-90 W at the intended top speed. It is also noticed that around 90% of the windage comes from the air-gap and 10% from the gables. In addition to this, attempts with different temperatures and air pressure are carried out. Varying temperature from room temperature to 100°C will have marginal effect on the air resistance while doubling the air pressure results in almost 50% higher windage losses.

Another interesting aspect is related to the cooling solution. This opens a question of how any presence of oil in the airgap compartment and around the rotor gables would impact the drag losses. Introducing oil droplets in the air should, with the use of common sense, lead to increased density ρ as well as dynamic viscosity ν. Even if the magnitude is not settled, a quick sensitivity analysis is done by studying the underlying analytical equations. By studying (5.3) and (5.11) it is concluded that the Reynolds numbers are fairly unaffected as long as the dynamic viscosity and the density is increased in the same magnitude. However, since the density is also used to estimate the air friction losses in (5.1) and (5.9), the losses should increase in the same order as the density of the air/oil-droplet mixture surrounding the rotor. This requires that the equations used here are valid also when the density and dynamic viscosity are tampered with. The impact of oil droplets on the air drag losses is not further investigated within this thesis.

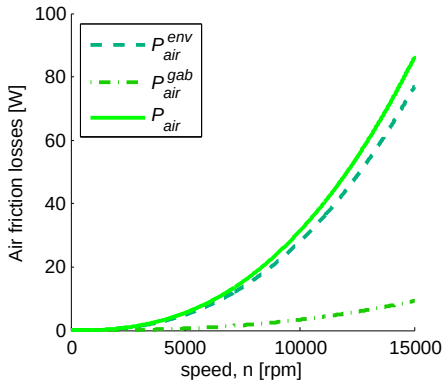

Figure 5.1: Losses due to air drag or windage as function of rotational speed at room temperature (20°C) and atmospheric pressure

5.2.2 Bearing losses

The prototype machine is equipped with two identical deep groove ball bearings[1], one on the driving end and one on the non driving end. The losses in a bearing, P_B is a result of the loss torque, T_B^{Loss} and the mechanical rotational speed according to (5.12).

$$P_B = T_B^{Loss} \cdot \omega_m \tag{5.12}$$

The loss torque, or frictional moment can often be estimated with an assumed constant friction coefficient, μ_{fb} for the selected bearing [48, Ch.6.1]. This coefficient gives an estimated T_B^{Loss} from the general expression for calculating frictional torque based on the radial force and lever length. In (5.13) the radial force is expressed as equivalent bearing force F_b and the length of the lever equals the bearing bore diameter d_B divided by two.

$$T_B^{Loss} \approx T_{B,rr} \approx \mu_{fb} \cdot F_b \cdot \frac{d_B}{2} \tag{5.13}$$

The equivalent bearing force is here considered as a combination of the static gravitational force, F_G, the dynamic centrifugal force, F_D and any potential external forces, F_E due to loads applied to the motor shaft, as expressed in (5.14).

$$F_b = f_m \cdot (F_G + F_D + F_E) \tag{5.14}$$

According to [49, pg.86], a combination of dynamic loads from e.g. unbalance and static loads due to e.g. gravity shall be added as vectors, where dynamic load vectors are rotating. This can be compensated for with a factor, f_m, being a function of the relation between

[1] SKF 6208-2RZTN9 / HC5C3WT deep grove ball bearing with ceramic balls; d_B = 40mm; Radial internal clearance C3 (15-33 µm); Dynamic load rating C = 32.5kN

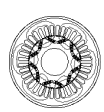

the static and dynamic contributions. Since this has only a marginal effect on the overall result, in combination with that it mainly impacts the bearing life, f_m is neglected in this analysis and set to 1.The gravitational force is based on the rotor mass, m_r and gravitational constant g according to (5.15).

$$F_G = m_r \cdot g \tag{5.15}$$

The dynamic centrifugal force is caused by any eccentricity, e_r or imbalance in the rotor. The resulting force is calculated with (5.16) [50, pg.160].

$$F_D = m_r \cdot \omega_m^2 \cdot e_r \tag{5.16}$$

As can be seen from the two force equations 5.15 and 5.16, the dynamic centrifugal force increases with increased speed, while the gravitational force is constant.

The rotor in the machine under examination is balanced to class G2.5 in accordance with [51]. With a top speed of 15000 rpm, this corresponds to a permissible residual specific imbalance of approximately 1.6 g·mm/kg, hence an eccentricity of 1.6 µm. Since the balancing is performed separately on the rotor, the eccentricity might increase slightly after assembly. The rotor could for example be affected by thermal distortion during operation. This could lead to a slight shift in the inertia centreline [52]. Another possible influence on the rotor balance in the prototype machine is the cooling system with oil present in the rotor. On the other hand, since the oil is distributed in a small channel in the centre of the shaft in combination with the much lower density compared to the rotor laminations, the overall influence should be virtually none. When delivered, a bearing has a certain radial internal clearance depending on the bore diameter and classification. Once mounted in the intended application, pre-loading is used to remove the slackness so that normal temperature operation means little or no remaining clearance [48, Ch.6.1]. The machine under examination has a wave washer to obtain correct pre-loading.

According to [49], the simplified estimation in (5.13) is valid if the bearing is loaded with approximately 10% of rated load, has good lubrication and operates in normal operating conditions. A more detailed model presented in [49] takes more aspects into account. This is presented for the total loss torque due to friction, T_B^{Loss} in (5.17).

$$T_B^{Loss} = T_{B,rr} + T_{B,sl} + T_{B,seal} + T_{B,drag} \tag{5.17}$$

Here the loss torque due to rolling resistance $T_{B,rr}$ is accompanied by loss torque due to sliding friction $T_{B,sl}$, any friction in the bearing seal $T_{B,seal}$ and drag losses T_{drag} due to e.g. splashing in case the bearing is soaked in an oil bath. The bearings used in the prototype machine under examination are equipped with so called contactless seals. This means that the distance between the rotating and stationary parts in the sealing is sufficiently small to prevent passage, but are still not in contact with each other. The result is negligible losses in the seals. In addition to this, the drag losses due to oil bath lubrication can be neglected

as well. This is possible since the bearings instead are lubricated with grease (greased for life). Hence $T_{B,seal}$ as well as $T_{B,drag}$ are set to zero in the analytical investigation. The expressions for $T_{B,rr}$ and $T_{B,sl}$ are presented in (5.18) and (5.19).

$$T_{B,rr} = r_{ish} \cdot r_{rs} \cdot G_{rr} \cdot \left(\nu_g \cdot \frac{2\pi}{60} \omega_m \right)^{0.6} \tag{5.18}$$

$$T_{B,sl} = [r_w \cdot \mu_{sc} + (1 - r_w) \cdot \mu_{FF}] \cdot G_{sl} = \mu_{sl} \cdot G_{sl} \tag{5.19}$$

Here ν_g is the operating viscosity of the grease and r_{ish} and r_{rs} are reduction factors for inlet shear heating ($_{ish}$) and kinematic replenishment or starvation ($_{rs}$) respectively. These reduction factors are dependant on e.g. bearing diameter, grease viscosity and rotational speed. Having the value 1 at zero speed, they decrease with increased speed to reflect that these phenomena diminish at higher speeds. The sliding friction coefficient, μ_{sl} in (5.19) comprises a weighting factor, r_w so that the sliding friction is higher close to stand still. Hence μ_{sc}, that depends on the additive package in the lubricant is higher than μ_{FF}, being the friction coefficient at full-film conditions. The weighting factor is dependant on bearing diameter, grease viscosity and speed and makes the sliding friction coefficient rather quickly reach the full-film condition. Finally, G_{rr} and G_{sl} are variables depending on the bearing type, diameter and applied force. For the bearing in question and no force in axial direction, G_{rr} and G_{sl} are determined with (5.20) and (5.21). Here R_1 and S_1 are constants for rolling and sliding frictional moments in ball bearings, specific for the bearing series. More detailed information on the equations and constants used to estimate the bearing losses is found in [49].

$$G_{rr} = R_1 \cdot d_m^{1.96} \cdot F_b^{0.54} \tag{5.20}$$

$$G_{sl} = S_1 \cdot d_m^{-0.26} \cdot F_b^{(5/3)} \tag{5.21}$$

Since neither the rolling, nor the sliding friction has a linear relation to the applied force, it is important to do a proper partition of the total force onto each bearing. The total force applied on a single bearing does not give the same result as applying half the force on two bearings and then sum up the total friction losses. For the sliding friction ($T_{B,sl}$), the latter case means a reduction in the total loss torque but for the rolling resistance ($T_{B,rr}$) it is the opposite. Since the rolling resistance is dominating over the sliding friction, the overall loss gets higher if half the force is distributed on two bearings compared to if the entire force is applied on a single bearing. The load distribution between the two bearings is estimated by identifying the rotor center of gravity and utilize elementary force balance. For the case any external force (F_E) is applied, this should be included in the force balance breakdown.

The losses in the bearings are highly dependant on the viscosity of the lubricant. High viscosity results in higher rolling resistance losses at low speeds. Meanwhile, since the reduction factors (r_{ish} and r_{rs}) also depend on the viscosity, the loss torque actually decreases

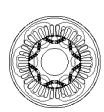

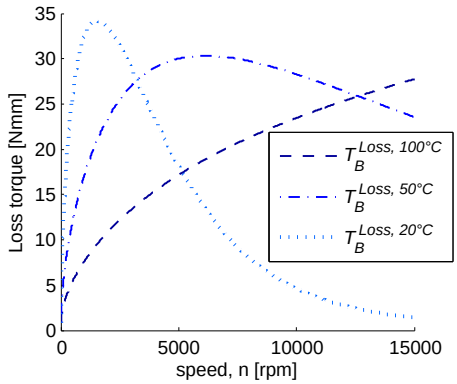

Figure 5.2: Bearing loss torque (T_B^{Loss}) in Nmm as a function of rotational speed at 20°C (room temperature), 50°C and 100°C leading to three different lubricant viscosities

at high speeds when the viscosity is high. This is due to the replenishment/starvation phenomena where some amount of the grease is splashed out from the groove when a ball passes. With high speed and high viscosity (low temperature), the next ball faces a thinner hydrodynamic film and hence lower rolling friction. With lower rotational speed, more grease will have time to replenish the groove and the rolling friction increases. The same goes for increased temperature and hence lower viscosity. More grease will have time to return to the groove to form a thicker hydrodynamic film before the next ball arrives.

With the temperature dependence of the bearing grease viscosity, operating at room temperature (20°C) means a peak in the loss torque in the bearings at around 1500 rpm. With kept temperature and further increased speed, the bearing losses go down again. This is displayed for three different temperatures leading to three different grease viscosities in Figure 5.2 (note the Nmm scale on the y-axis). The higher the temperature, the higher up in speed the loss torque peaks. At 50°C the peak is around 6000 rpm and at 100°C the peak occurs above the top speed of the EM. The corresponding graph for the bearing losses is presented in Figure 5.3. Here it can be seen that the bearing losses at room temperature (20°C) peak at around 4000 rpm.

The loss torque contributions in Nmm from rolling and sliding resistance at room temperature (20°C) are presented in Figure 5.4. As can be seen, the rolling resistance is almost completely dominant. The sliding friction is still important to represent the torque present at standstill. The weighting factor in μ_{sl} makes the sliding friction to increase close to standstill.

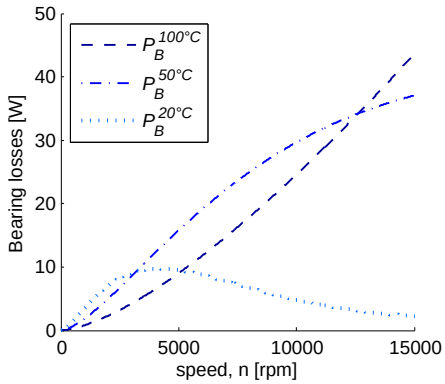

Figure 5.3: Bearing power loss (P_B) as a function of rotational speed at 20°C (room temperature), 50°C and 100°C leading to three different lubricant viscosities

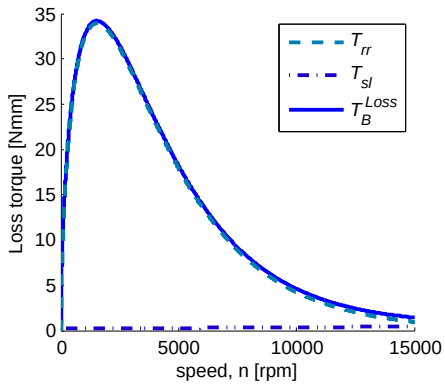

Figure 5.4: Total loss torque in Nmm from the two bearings as a function of rotational speed at room temperature (20°C)

5.2.3 Additional friction losses

In addition to the windage and bearing losses, some other mechanical losses have been identified in the machine under examination. These are introduced in the following subsection.

Friction in carbon brushes

Two carbon brushes are mounted on the shaft to provide a connection from the rotor to ground. This is to prevent problems with induced voltage in the rotor which can be present in an inverter fed PMSM [53]. It could also be that static electricity might be generated by

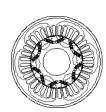

the oil flow running through the rotor.

The frictional torque due to the carbon brushes sliding on the shaft is determined by the radius of contact, $d_{brush}/2$ and force, F_{brush} together with the friction coefficient, μ_{brush} and number of brushes, N_{brusch} according to (5.22).

$$T_{brush} = N_{brush} \cdot \mu_{brush} \cdot F_{brush} \cdot \frac{d_{brush}}{2} \tag{5.22}$$

The applied force is estimated to F_{brush} ≈0.1 N and the friction coefficient is selected based on values used for slip ring units used in commutators. According to [54] it should be in the range μ_{brush} = 0.15–0.4 depending on temperature while [55] states μ_{brush} = 0.1–0.2. Reference [55] also states that the friction can be higher at no load or low load conditions. Further on, the numbers presented in the literature is for carbon to copper, while the machine under investigation has carbon to steel. Whether this makes a difference and if so, how much is been investigated here. The well known fact that static friction is higher than sliding friction [50, pg.160] is neglected as well. This would give a slightly higher friction just as the machine starts to spin. All in all, this leads to a rather large inaccuracy in the friction torque from the carbon brushes. However, since the result also depends on the radius of contact, the torque can be kept low with a limited diameter (d_{brush}) at the connection. The estimated torque based on relevant numbers in (5.22) is close to insignificant, in the range of 0.5–2 Nmm only.

A final comment on the carbon brushes is that it can be debated on whether they are necessary in the machine under investigation. The findings presented in [56] and [57] are that the bearing currents should be low in PM-machines with short axially extruding rotor under the stator end windings. In addition to this, the bearings mounted in the machine are equipped with ceramic balls. Hence the harmful electric arcing due to induced voltages from the inverter is prevented also by the non-conductive bearing connection. On the other hand, no ground connection could instead cause problems in the downstream components such as the gearbox bearings.

Friction in oil reservoir sealing

Cooling of the rotor and stator end windings is implemented with a small oil reservoir at the non-driving end of the machine. The end of the hollow rotor shaft is extruding into the oil compartment so that oil is fed into rotor and further on out to the end windings. A more detailed explanation is presented in Subsection 2.2.2 and in [1].
A seal[2] is mounted on the shaft to prevent oil from leaking the wrong way. The seal consists of a lip and a tightening spring and is defined according to [58]. Figure 5.5 shows a sketch of

[2]DIN 3760-A-12x24x7-NBR

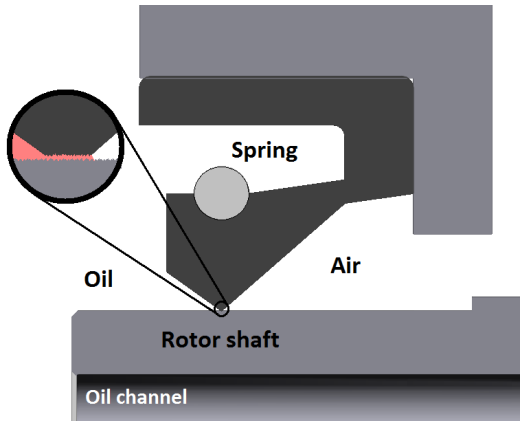

Figure 5.5: Sketch of an oil seal similar to that mounted in the machine

the sealing used in the machine. The inset magnification of the contact surface is to show the oil film that helps keeping the friction down.

In order for the seal to hold tight, a certain pressure is needed from the sealing lip onto the rotating shaft. This can be seen as a line force, or a force distributed along the diameter, here expressed as F_{seal}^{line} in [N/m]. This gives the total radially directed force, F_{seal} according to (5.23) where d_{seal} is the inner diameter of the seal.

$$F_{seal} = F_{seal}^{line} \cdot \pi \cdot d_{seal} \tag{5.23}$$

The frictional torque, T_{seal} in the seal thus becomes as in (5.24) where μ_{seal} is the friction coefficient of the seal lip to shaft contact. So, in order to determine the frictional torque, the friction coefficient and line force need to be identified.

$$T_{seal} = \mu_{seal} \cdot F_{seal} \cdot \frac{d_{seal}}{2} = \mu_{seal} \cdot F_{seal}^{line} \cdot \pi \cdot \frac{{d_{seal}}^2}{2} \tag{5.24}$$

In addition to the non-viscous dependant expression in (5.24), [59] also introduces a term depending on e.g. the speed, dynamic viscosity and temperature. The temperature dependence affects the flexibility in the sealing lip and hence the radially directed force. Especially the temperature dependance can also be seen in the frictional torque measurements performed in [60]. There, measurements are performed on a differently sized seal of the same type as the one investigated in this thesis. Although the analysis is performed on a seal with different size, the result can be used to derive the parameters needed in (5.24). This is done in (5.25) where (5.24) is solved for the friction coefficient and line force.

$$\mu_{seal} \cdot F_{seal}^{line} = \frac{2}{\pi} \cdot \frac{T_{seal}}{{d_{seal}}^2} \tag{5.25}$$

By assuming an unchanged line force and a constant friction coefficient, (5.25) can be used to derive the frictional torque from one seal based on that in the second one. This is done in (5.26), where the parameters from the different seals are denoted with $'$ and $''$ respectively.

$$T''_{seal} = T'_{seal} \cdot \left(\frac{d''_{seal}}{d'_{seal}} \right)^2 \tag{5.26}$$

Since the temperatures covered in [60] only range from 50 to 100°C, the result is linearly extrapolated down to room temperature. This way, the temperature dependence found in the measurements in [60] is taken into account. Since the speed dependency noticed in the result in [60] is less significant, this part is neglected in this simplified analysis. Based on the frictional torque and seal diameter from [60] together with the relevant diameter in the prototype machine under investigation, the frictional torque due to the seal is established. The result is a linear relation declining from 13.5 to 9 Nmm from room temperature to 100°C. Again, the static friction coefficient expected to give a higher starting torque, is neglected.

In addition to the analysis performed above, the model for bearing seals at page 109 in [49] is used to do a quick check on the validity of the result. Here, either of the RSH or RS1 seal types are judged to be most similar to that in the machine. By using the correct numbers, the resulting frictional torque becomes either 9.5 Nmm or 8 Nmm, depending which seal type that is used. Based on this, the results obtained from scaling the measurements in [60] with (5.26) are considered sufficient for the purpose of the analysis done here.

5.2.4 Resulting mechanical losses

The total mechanical loss torque T_{mech} and resulting power losses P_{mech} based on the analytical evaluations introduced above are presented at 20 and 100°C in Figures 5.6 – 5.9. As expected from the study on air friction losses (Figure 5.1), the resulting loss torque (in Figures 5.6 and 5.7) is dominated by the bearings at lower speeds. This applies especially at room temperature where the rolling friction is higher. As the speed increases, the main loss contributor shifts from being the rolling resistance to the air resistance. This due to the quadratic relation of the windage loss torque (cubic when looking at power) together with the reduction factors for shear heating (r_{ish}) and replenishment (r_{rs}) in the bearings.

When comparing the loss torque and power from the two different temperatures it can be seen that the break even point for where the power losses are higher, is at around 6000 rpm. Hence below that speed, from a mechanical loss point of view it is marginally better if the machine is operating at 100°C. Above 6000 rpm, the mechanical losses instead seem to be lower if the machine is at room temperature.

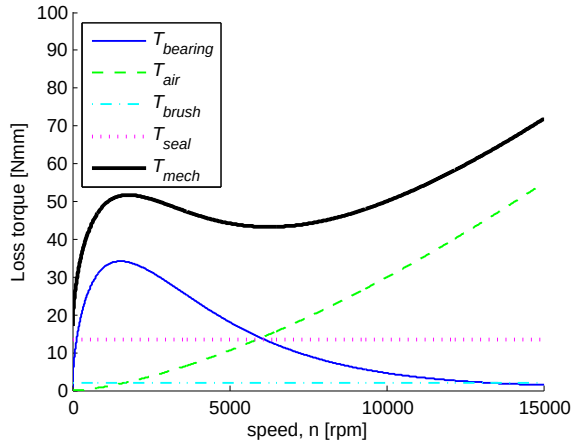

Figure 5.6: Loss torque contributions in Nmm from the bearings, windage, carbon brushes and oil seal together with the total loss torque T_{mech} as functions of rotational speed at room temperature (20°C)

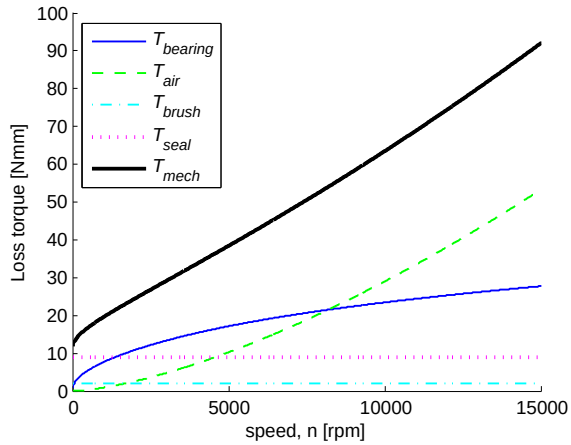

Figure 5.7: Loss torque contributions in Nmm from the bearings, windage, carbon brushes and oil seal together with the total loss torque T_{mech} as functions of rotational speed at 100°C

In order to better study the temperature behaviour, the mechanical loss torque is plotted for five different temperatures in Figure 5.10. According to this graph, the worst case in terms of mechanical losses at high speeds is 60-80°C. This is related to a combination of the rolling resistance and the reduction factors in the bearings. By looking at the power instead, it can be concluded that the torque difference at low speed is less decisive as the speed works as a leverage. Instead the lines are more bundled and start to disperse a little first at higher speeds. The power losses for the different temperatures are plotted in Figure 5.11.

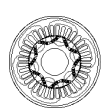

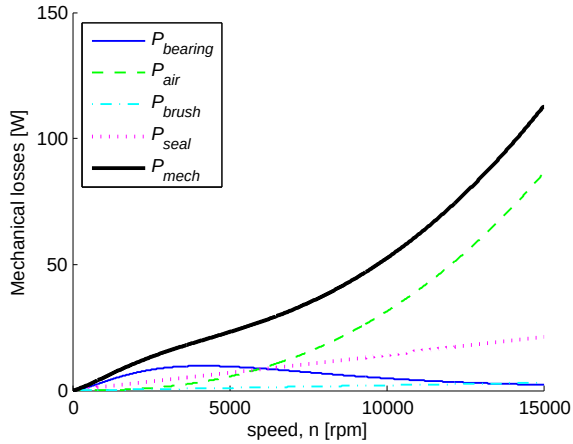

Figure 5.8: Loss contributions from the bearings, windage, carbon brushes and oil seal together with the total mechanical losses P_{mech} as functions of rotational speed at room temperature (20°C)

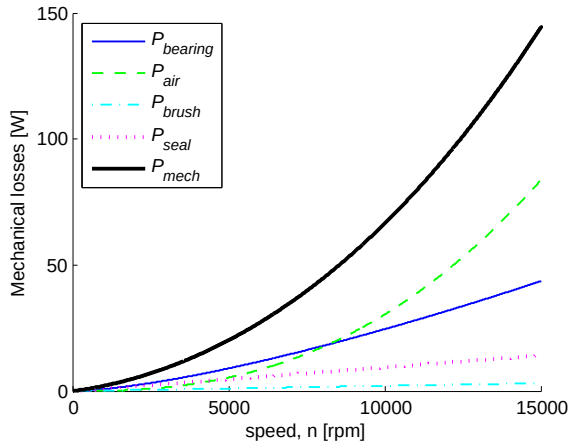

Figure 5.9: Loss contributions from the bearings, windage, carbon brushes and oil seal together with the total mechanical losses P_{mech} as functions of rotational speed at 100°C

5.2.5 Measurements on the mechanical losses

Measurements are used to verify and to some extent calibrate the analytical mechanical loss model. These tests are carried out as roll out tests where the deceleration rate is used to establish the loss torque. In addition to adding credibility to the model, the practical work is also providing a good insight in the order of the mechanical losses.

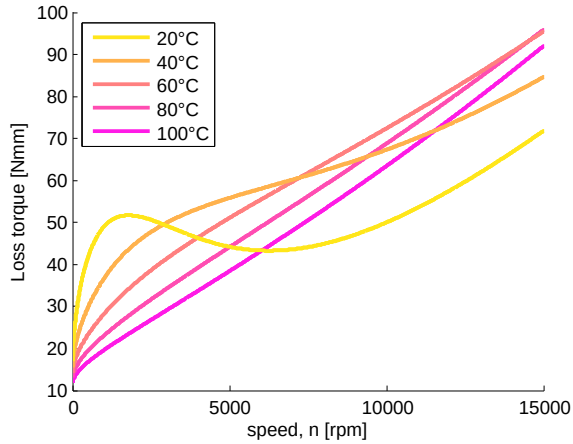

Figure 5.10: Mechanical loss torque T_{mech} in Nmm as function of rotational speed at different temperatures

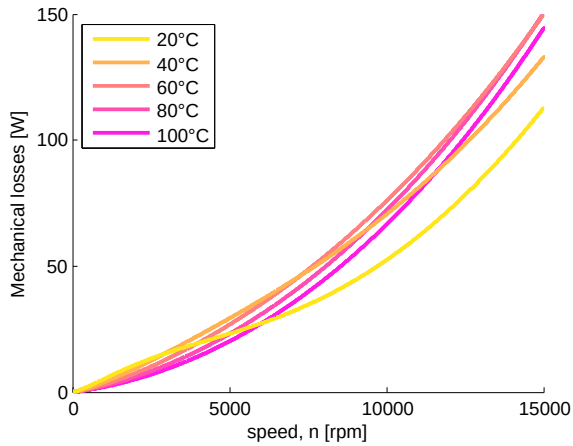

Figure 5.11: Mechanical losses P_{mech} as function of rotational speed at different temperatures

Test preparations and set-up

A dummy rotor without permanent magnets is manufactured and installed in the machine. The envelope geometry is unchanged compared to the original rotor to give similar air friction properties. For simplicity reasons, the dummy rotor is made out of solid steel. Hence the epoxy filled flux barriers around the magnets and the hollow part of the shaft are neglected as are some aluminium parts at the rotor gables. All in all, this results in a mass of 22.7 kg for the dummy rotor, compared to 21 kg for the original one. Based on

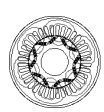

the analytical model, this 8% difference in mass is expected to give a marginal effect on the total losses. Looking at the temperature interval from room temperature up to 100°C, the difference in loss torque due to the slightly larger mass is never exceeding 1.5 Nmm. This is equivalent to about 3% difference.

Other measures for making sure that the conditions are unchanged are to use the same bearings, coal brushes and oil seal in the dummy set-up as in the original rotor. Also the resolver is kept mounted to keep track of the rotor position and hence rotational speed. This will however not have any effect on the losses since the resolver is mounted without internal bearings. Roll out tests are also performed on the original machine before the rotor is changed. After the mechanical loss tests are completed, the original rotor is re-mounted and the roll out tests are repeated again. The test results before and after the mechanical test session are compared to see that the result is unchanged. This indicates that the conditions are comparable before, during and after the measurements on the dummy rotor.

Since the dummy rotor neither has magnets nor saliency, it is not possible to accelerate it by simply applying stator currents. Instead rotation has to be made externally. This is achieved with a quick coupling on a hand held drill. Unfortunately, this means a limitation in rotational speed of just over 2000 rpm. Consequently, the air resistance is most likely negligible in the test results. Instead focus is put on the losses in the bearings and due to friction in the carbon brushes and oil seal. Once the maximum possible speed is reached, logging of the resolver signals is commenced. The mechanical loss torque T_{mech} is derived from the angular deceleration $\frac{d\omega_m}{dt}$ and the rotor moment of inertia J according to (5.27). The moment of inertia in the rotor is established both theoretically from the dimensions in CAD and from measurements performed earlier in the project. The procedure for determining the moment of inertia is described further in [26] and [24, Ch.5.2.d]. All tests are performed at a room temperature of between 20–30°C and with no oil cooling applied. Hence the temperature dependency from the viscosity has not been studied. Nor has any potential influence in air resistance from oil being present in the rotor and in connection to the airgap.

$$T_{mech} = \left| \frac{d\omega_m}{dt} \right| \cdot J \tag{5.27}$$

Test results

The test results from the roll-out tests are presented in terms of loss torque in Figure 5.12 and as power losses in Figure 5.13. The test procedure is repeated five times to check the conformity between tests. As can be seen, the non-speed dependant part of the loss torque is around 20 Nmm. It is also noticed that the loss torque seems to level at around 60–70 Nmm. This behaviour resembles that observed in Figure 5.6 where the loss torque is reaching a local maximum at around 2000 rpm. This supports the validity of the analytical

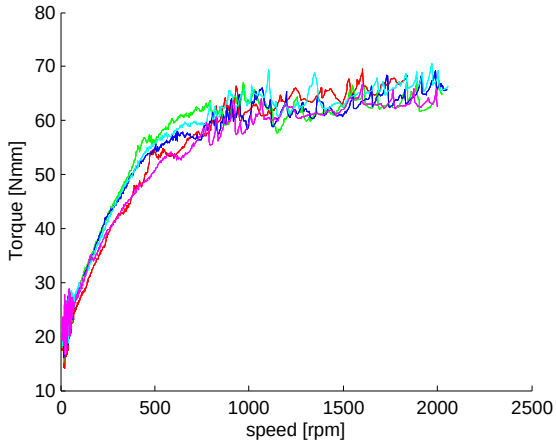

Figure 5.12: Measured mechanical loss torque in Nmm

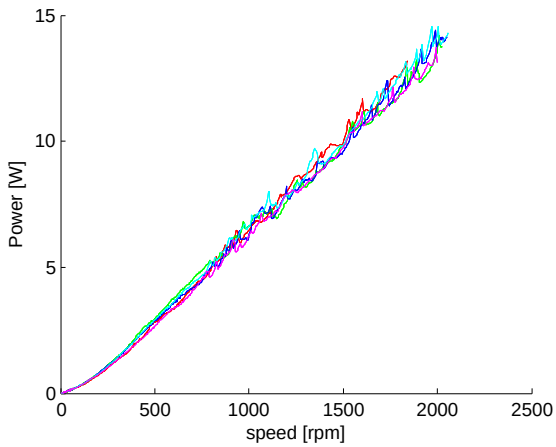

Figure 5.13: Measured mechanical power losses

model. From this, it is assumed that the analytical model should be useful for estimating the mechanical losses also at higher speeds.

Measurements compared to the analytical model

During the comparison with measurements, the rotor mass in the model is changed from 21 kg for the original rotor to 22.7 kg for the dummy rotor. When the measurements are compared to the result from the analytical model at corresponding temperature it is clear that the analytical model underestimates the losses slightly. This can be seen in Figure 5.14

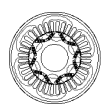

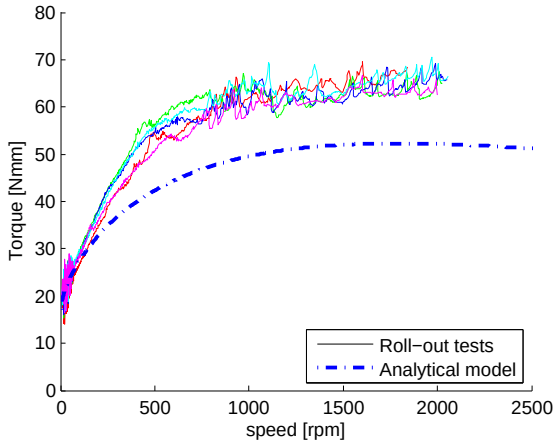

Figure 5.14: Comparison between measured and calculated mechanical loss torque

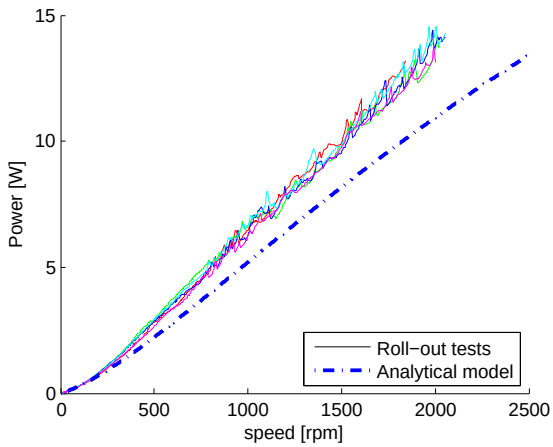

Figure 5.15: Comparison between measured and calculated mechanical power losses

where the analytical loss torque levels at a lower value and in Figure 5.15 where the slope of the power losses differ correspondingly. Still, it can be concluded that the part of the loss torque present at standstill matches very well. This indicates that the non-speed dependant loss torque is in the right order. This includes the carbon brushes and oil seal as well as the sliding part of the bearing losses. Also the shapes of the loss torque curves seem to agree well.

An attempt is made to make the analytical model match better with the measurements. Since the torque close to standstill agrees well, attention is directed towards the speed dependant parts hence rolling resistance together with the air friction. Further on, since the

air friction is expected to be very small at low rotational speeds, changes in the windage model would not affect the result to a sufficiently large extent below 2000 rpm. This leaves the rolling resistance in the bearings.

According to [48, Ch.6.1.9], new bearings have higher coefficient of friction compared to used ones. This is because worn bearings have bedded down more. Being mounted in a prototype with limited operation time, the bearings in this machine could still be considered as new. Also the dynamic load due to imbalance can be higher than predicted in the analysis. This could for example be related to the thermal distortion of the rotor mentioned earlier [52] or to elastic deformations in the bearing which should increase the eccentricity. Other things mentioned in [48, Ch.6.1.9] as affecting the rolling friction are e.g. the amount of grease in the bearings and how they are pre-loaded. In addition to this, the bearing model used in the analysis here, is valid for bearings operating in steady state conditions for several hours [49]. Hence the roll-out tests had to some extent different preconditions than what is stated for the model. Finally, the accuracy with which the rotor moment of inertia is established is having a direct relation to the test result.

In order for the analytical model to agree with measurements, a correction factor of C_F=1.4 is applied to the rolling resistance. Hence the speed dependent part of the bearing losses is increased with 40%. This gives a mechanical loss torque T_{mech} as defined in (5.28) and presented in Figure 5.16. The resulting power losses are presented in Figure 5.17. As can be seen, this makes the analytical loss model to fit very well with the measurements.

$$T_{mech} = \frac{P_{air}}{\omega_m} + C_F \cdot T_{B,rr} + T_{B,sl} + T_{brush} + T_{seal} \tag{5.28}$$

A final comparison between measurements and the corrected model going up to the EM top speed, is done for the loss torque and resulting losses in Figure 5.18 and Figure 5.19 respectively. Here it is clear that the limited top speed in the measurements creates uncertainties when validating the model. According to the model, the loss torque starts to drop just over approximately 2000 rpm, before the air friction kicks in at around 7500 rpm. For obvious reasons, this can not be observed in the test results.

5.2.6 Concluding remarks on the mechanical losses

The mechanical loss model presented previously in this section is based on analytical expressions. Hence the reliability is limited. Given this, the match with the measurements is considered to be good. Besides the simplifications introduced in the analysis, part of the difference before introducing the correction factor could, as already mentioned be due to the bearings still being in a run-in period. Also the different preconditions for the test compared to what is stated for the bearing model in [49] could have an impact. Yet another

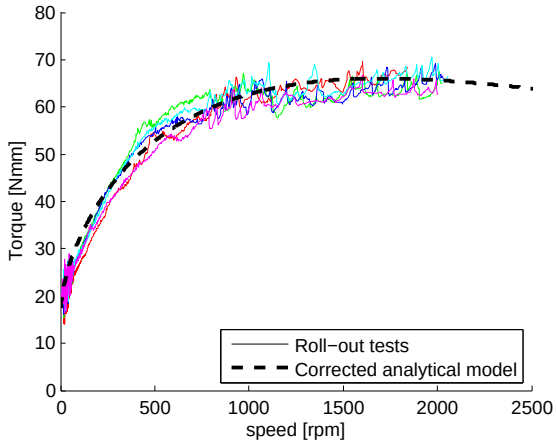

Figure 5.16: Comparison between loss torque from measurements and from the analytical model adjusted with a correction factor of C_F=1.4

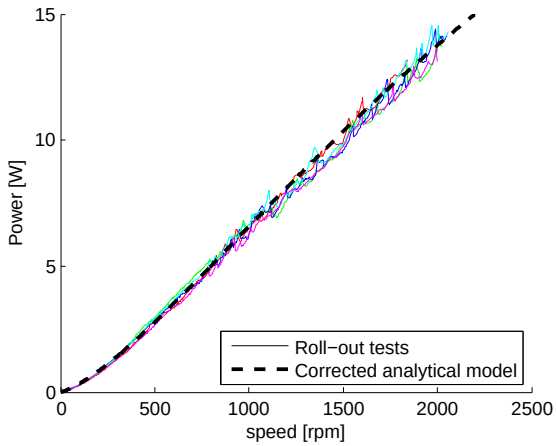

Figure 5.17: Comparison between mechanical power losses from measurements and from the analytical model adjusted with a correction factor of C_F=1.4

possible source of deviation could be related to the accuracy when determining the rotor moment of inertia.

Despite the limited test speed, the result is still considered sufficient to provide an indication of the correctness of the model. Hence that it can be used to estimate the mechanical loss torque and corresponding mechanical losses. Although the starvation and shear heating effects are probably not fully developed, the loss torque due to mechanical losses is still in the same range. Looking at the loss torque in the model (Figure 5.18) it can be noticed that

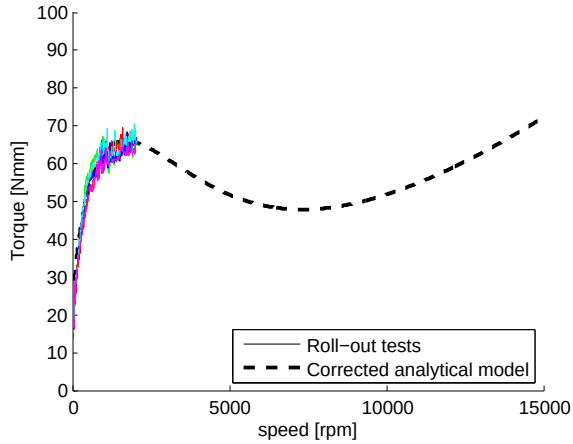

Figure 5.18: Comparison between loss torque from measurements and from the analytical model adjusted with a correction factor of C_F=1.4, going up to the EM top speed

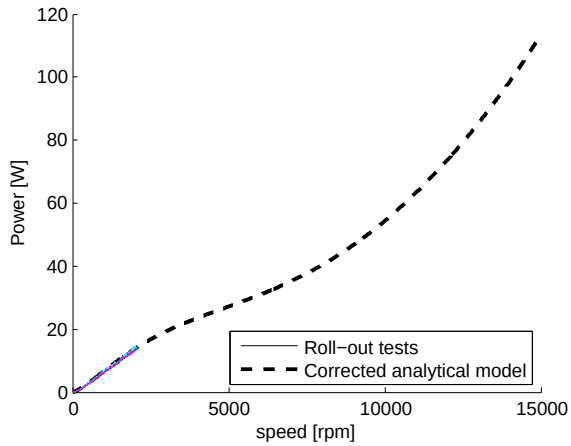

Figure 5.19: Comparison between mechanical power losses from measurements and from the analytical model adjusted with a correction factor of C_F=1.4, going up to the EM top speed

it stays within roughly 50–70 Nmm from 500 rpm up to top speed for room temperature.

The other thing hardly covered in the rather low speed measurements is the model for the air friction or windage. On one hand, this gives additional uncertainties to the over all mechanical loss model. On the other hand, the test result is instead more suitable to evaluate the other mechanical losses. This way the model can be considered to focus more on the losses in the bearings and due to friction in the oil seal and at the carbon brushes.

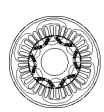

If found necessary, future work could be directed towards achieving measurements also at higher speed to better evaluate the air friction model. This has not been prioritized within this project.

Another thing that could have been pursued further in the test rig is the temperature dependency. As the measurements are done at room temperature only, the model can really only be validated at those conditions. Still, the indications from e.g. Figure 5.11 are that the model can be used also at higher temperatures. When looking at the power losses rather than the loss torque, the difference due to a varying temperature is less prominent. The difference in power losses seen in Figure 5.11 as the temperature is varied can be said to be in the same range as the the overall uncertainty in the mechanical loss model as such. Furthermore, when zooming out from the Newton-millimetres discussed here, the difference makes less impact on the permanent magnet machine. That is also clearly noticeable when working with the hardware during the roll out tests. The rotor seems to never come to a stop. As is concluded later on in the chapter, the iron losses are much more dominating. Instead of using the results as the correct answer, the mechanical loss model is used as indications on the behaviour and impact on the total loss distribution in the machine. Since the mechanical losses are unaffected by magnetic fields, the model verified at no load conditions with a dummy rotor is assumed to be valid also with magnets in the rotor and loads applied to the machine.

5.3 Stator core losses

Estimating the iron core losses accurately is both challenging and difficult [61–83]. Things that can affect the result are for example the magnetic flux frequency content and waveforms [62, 64–66, 68, 70, 80, 84, 85], magnetic property degradation when processing the material or during manufacturing [66–68, 71, 79, 81–83, 86–88], or due to general material properties [66, 79, 82]. This section gives a short introduction to various aspects affecting the iron losses. It also presents the efforts made on estimating the stator iron core losses within the scope of this thesis.

In the initial design procedure, a simplified model is used. This is to prioritize design speed over accuracy. As the prototype is built and tested, some attempts are made to explain the difference between measurements and predictions based on the originally used iron loss model. Iron core losses in the stator are estimated based on the magnetic flux density and frequency together with material parameters, where the latter generally are obtained from the material supplier. These data parameters are based on standardized tests and are not always fully representative with the reality in an electric machine [81, 83]. The power loss calculation is mainly a part of the FE-simulation post processing where the field variation is used as an input to different loss models.

5.3.1 Theoretical background

The physical explanation behind losses arising in soft magnetic materials such as electric steel, is related to a motion of the domain walls separating different magnetic domains in the material and by the large scale instability in the creation and destruction of magnetic domains. This is a consequence of a varying magnetic field. The result of these vibrations is typically acoustic noise and/or heat. With the underlying complexity and non-linear behaviour, simplified models have been constructed in order for being able to estimate the losses [63].

These simplified models are addressing the problem in the frequency domain. They are based on that the losses found in an iron core is related to magnetic flux density B and (magnetizing) frequency f as well as material parameters and geometry. The commonly used power loss model is a sum of loss separation of the so called hysteresis losses, eddy current losses and excess or anomalous losses. Steinmetz described the iron losses as a combination of hysteresis losses (p_{hy}) and eddy current losses (p_{ec}) already in 1892 [89]. This model has later been complemented and improved with a third term for the anomalous losses (p_{an}) by Bertotti in 1988 [61]. In (5.29) the three term equation of Bertotti is presented for the iron losses, p_{Fe} per mass (in [W/kg]) with coefficients for the hysteresis (c_{hy}), eddy current (c_{ec}) and anomalous (c_{an}) losses together with an exponent (e_{hy}) on the magnetic flux density in the hysteresis term. These core loss coefficients are determined by the material properties and dimensions or geometry.

$$p_{Fe} = p_{hy} + p_{ec} + p_{an} = c_{hy} \cdot B^{e_{hy}} \cdot f + c_{ec} \cdot (B \cdot f\,)^2 + c_{an} \cdot (B \cdot f\,)^{1.5} \quad (5.29)$$

The hysteresis losses, sometimes also called the static or quasi-static losses, can be described as a result of sudden changes in size and orientation of magnetic domains and domain walls as magnetisation propagates in a magnetic material. These changes are called the Barkhausen effect or Barkhausen jumps [90] and are related to that the walls separating the magnetic domains are pinned by impurities in the magnetic structure. This creates energy barriers for the magnetic field. The local eddy currents induced by these small wall jumps, dissipates a small amount of energy in terms of heat through Joule losses. A higher energy barrier means larger amount of dissipated energy. The external field has no effect on the jumps as such, but rather on the time between them. A higher field strength leads to more frequent jump [91]. With the losses being the sum from all jumps, higher field strength leads to higher losses. As the process is repeated when the magnetisation direction changes, the total hysteresis losses are also proportional to the frequency of the applied magnetic field. [63]

Hysteresis losses are often visualized as a redrawing process of a loop in a $B(H)$-curve, such as in Figure 5.20. This describes the relation between the driving magnetic field H and caused magnetic flux density B when applied with sinusoidal frequency. The enclosed area

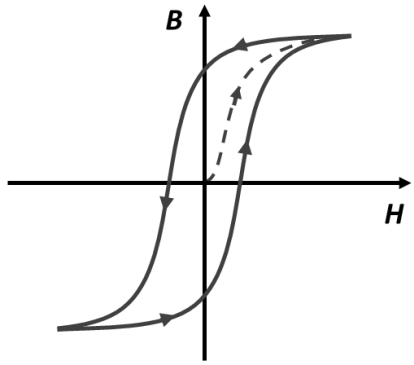

Figure 5.20: Graphical visualisation of a hysteresis loop

within the loop illustrates the magnetic energy that is irreversibly dissipated into heat due to the work on re-magnetizing the material. The stronger the applied field, the larger the area, hence higher losses. Since the energy loss (being the power loss divided by frequency) is independent of frequency, the effect is present also when applying, or slowly changing a static magnetic field. Hence the phrase "quasi-static losses".

The eddy current losses, also often referred to as classical iron losses, are a result of an electric field that is induced due to the varying magnetic field. For a conducting material, the induced electric field gives rise to internal currents running around the material circumference. This leads to heat dissipation through Joule losses. Therefore, the eddy current losses are scaled by the length of the current loop and hence is related to the actual geometry. This is the reason why a stator stack in general is built up by multiple thin laminations rather than a solid piece. As the height of the eddy current loops is limited, the losses are reduced. The eddy current losses can be estimated by solving Maxwell's equations for a homogeneous conducting medium. This gives (5.30) for sinusoidal conditions. [63]

$$p_{ec} = \frac{\pi^2 \cdot \sigma \cdot {d_{lam}}^2}{6} \left(B \cdot f\right)^2 \tag{5.30}$$

Here σ is the electrical conductivity of the material and d_{lam} is the lamination thickness. By comparing with the term for the eddy current loss in (5.29), it gets obvious how the eddy current coefficient c_{ec} is derived. From (5.30), it can also be observed that the magnetisation law of the material is not included. Hence the behaviour is the same in all materials as long as the geometry and electric conductivity are similar. In addition to this, it is also observed that the eddy losses increase with increased electric conductivity. This is why silicon steel is used in machine laminations. The conductivity drops significantly to the expense of a small reduction in magnetic permeability.

The simplifications made when deriving (5.30) introduce a limitation for when the equation is valid. When the frequency becomes too high or the laminations (hence flux path) become

too thick or if the electrical conductivity is too high, the generated eddy currents create an opposing magnetic field. This results in a relative reduction in eddy current losses compared to if calculated with (5.30). [63]

The anomalous losses or excess eddy current losses come from the smooth, large scale motion of the domain walls. The excess losses depend on the size and arrangement of the magnetic domains. With a fine domain structure the excess losses become small. In some conditions, the excess losses can be negligible if the domain width is much smaller than the lamination thickness. For non-grain oriented materials where the micro structure is less arranged, or if the micro structure is affected by e.g. residual stresses, the domain size becomes less decisive. In these cases, excess losses can occur also with small domain size. Since increased magnetisation frequency means creation of additional magnetic domains, the average domain size will go down as the frequency go up. Therefore, the excess losses increase less with increased magnetisation frequency. [63]

5.3.2 Stator core loss model used in the machine design process

In the initial design stage, speed is prioritized over accurate stator iron core loss estimations. The iron losses, P_{Fe} are derived in the post process of the electromagnetic FE-simulations (performed in FEMM [14]) by solving the three term equation introduced in (5.29) multiplied with the iron mass, m_{Fe}. This is done in (5.31).

$$P_{Fe} = p_{Fe} \cdot m_{Fe} \tag{5.31}$$

Input to the equation is simulation data from the FE-simulations together with loss parameters for the material in the selected laminations. The different loss coefficients are determined based on curve fitting the test data from the material suppliers, rather than on the theoretical expectations of the classical eddy current losses (such as in (5.30) or the mathematical description of magnetic hysteresis). The supplier test data is typically obtained from standardized Epstein frame tests [92].

The initial data for the calculations is the peak values of the flux density characteristic magnetisation waveform at predefined operation points and locations of the core. The flux density values are recorded from single points considered to provide an average or representative value of the specific region, such as a tooth ($_{th}$) or yoke ($_{yk}$). The mass is derived from the volume (based on the geometry) of each region multiplied by the density of electric steel. This means that the total losses in the stator iron core, P_{Fe} are determined with (5.32). Although this is a rather blunt way to determine the flux density, the simplification is still able to give a first indication of the resulting iron losses.

$$P_{Fe} = p_{Fe,th} \cdot m_{Fe,th} + p_{Fe,yk} \cdot m_{Fe,yk} \tag{5.32}$$

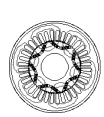

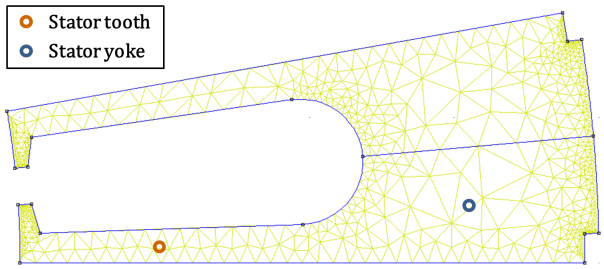

Figure 5.21: Stator core section with the points representing a tooth (th) and yoke (yk) region

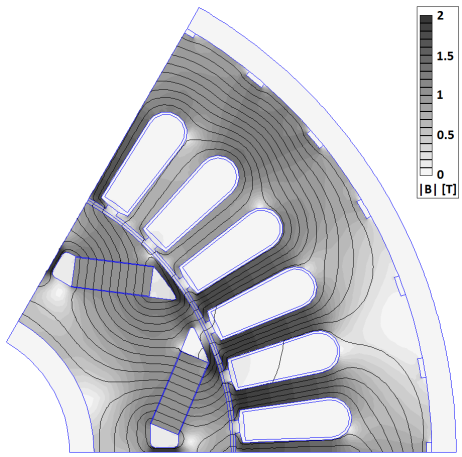

Figure 5.22: Flux density distribution at part load q-current

The natural selection points for flux density in the stator yoke and teeth are angularly and radially in the middle of each region. Since the teeth due to periodicity reasons are divided into two in the simulation model, the flux in each tooth is represented by two points. The points representing half a tooth and a section of the yoke are displayed in Figure 5.21. The flux density distribution during part load applied in q-direction only is presented in Figure 5.22. The total volume of the stator yoke is 2.03 dm^3 and for the stator teeth 0.98 dm^3. The density used for the electric steel is 7.7 kg/dm^3.

In Figure 5.23, the no load stator iron core losses, as calculated analytically, are plotted as a function of rotational speed. The different curves represent different permanent magnet temperatures in accordance to what is introduced and described previously in Chapter 3. The different temperatures result in different flux densities (B) and hence according to (5.29), different losses. The temperature dependency in the loss coefficients mentioned in [93] is however not included here.

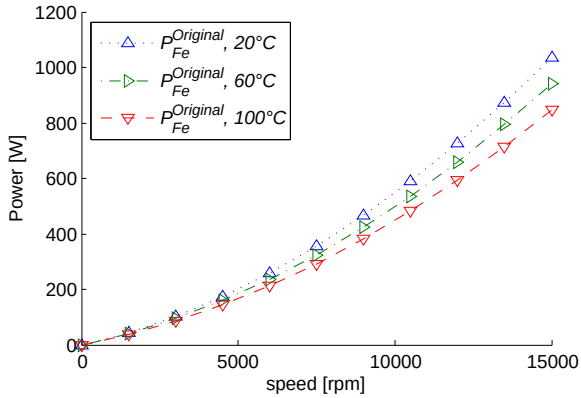

Figure 5.23: Estimated no load stator core losses as function of rotational speed

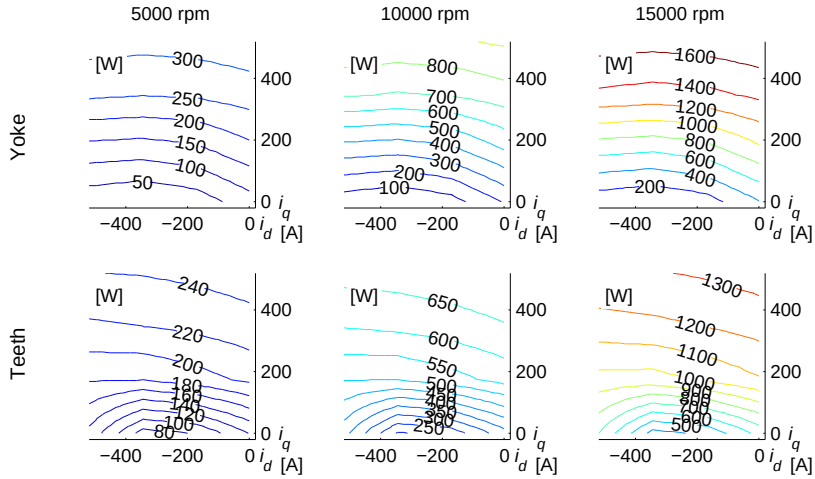

Figure 5.24: Estimated stator core losses at 5000 (left), 10000 (middle) and 15000 rpm (right) in the yoke (top) and teeth (bottom) as function of i_d and i_q

By defining an operational speed of the machine, the fundamental frequency is derived and used for further power loss estimation. In Figure 5.24, 5000, 10000 and 15000 rpm are used as examples of the power loss estimation in the stator yoke and the teeth. They are presented as functions of d- and q-currents. The losses are obviously higher at higher speeds as the frequency is higher. It is also noticed that the total losses are higher in the yoke than in the teeth. However when taking the volume of each region into account, it is concluded that the loss density is higher in the teeth than in the yoke. This due to the higher flux density in the teeth, as can be seen in Figure 5.22.

The information presented in Figure 5.24 is also used to derive an iron loss map as function

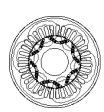

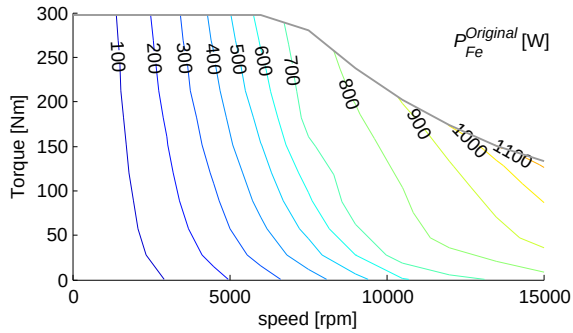

Figure 5.25: Estimated stator core losses, $P_{Fe}^{Orginal}$ as function of torque and speed utilizing MTPA

of torque and speed by implementing e.g. MTPA. This is presented as total stator (yoke and teeth) core losses in Figure 5.25.

5.3.3 Magnetic flux density patterns and flux density locus

When establishing the iron losses with (5.29) an alternating and sinusoidally shaped flux is assumed. By studying the flux density pattern in the machine more thoroughly, it is concluded that part of the stator faces flux variations in more than one dimension. This will form rotating flux variations or flux density locus. In addition to this, the flux density variation, whether it is alternating or rotating, is not purely sinusoidal.

Additional iron losses due to flux density locus

Since losses in an iron core are generated by variations in the flux, consideration needs to be done to whether the flux is varying in more than one dimension. Hence if the flux density vector just goes back and forth or if it forms an ellipse or circle. In the latter case, iron losses from the flux variation in both directions need to be considered. If not, the iron losses will be underestimated. Investigations made in e.g. [73, 84, 85] have shown that simply adding losses from the variation in two orthogonal directions instead overestimates the losses. According to [85], this is connected to saturation effects. In [84] a loss correction factor, γ is introduced to give a more accurate loss prediction. This is done by calculating the losses in the different directions with the corresponding flux densities individually and multiply the sum with the correction factor. Thus, the iron losses with rotational flux density variation, P_{Fe}^{rot} are established according to (5.33) where $P_{Fe}^{0\,\mathrm{deg}}$ and $P_{Fe}^{90\,\mathrm{deg}}$ are established with (5.29) using the major and minor flux density components respectively.

$$P_{Fe}^{rot} = \left(P_{Fe}^{0\,\mathrm{deg}}\left(B_{Maj}\right) + P_{Fe}^{90\,\mathrm{deg}}\left(B_{Min}\right) \right) \cdot \gamma\left(\lambda, B_{peak}\right) \tag{5.33}$$

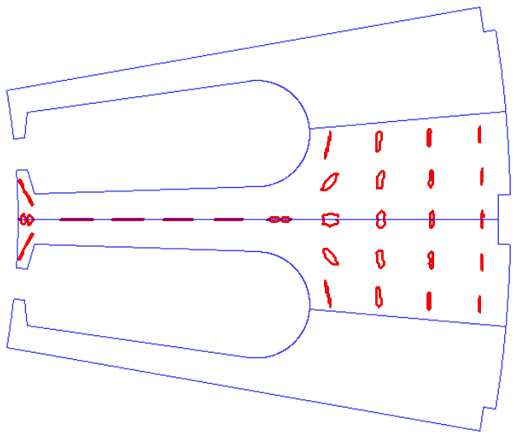

Figure 5.26: Illustration of flux density locus in the stator core with pulsating flux in the tooth and stator back and rotating flux in the transition between tooth and yoke

The loss correction factor $\gamma\left(\lambda, B_{peak}\right)$ is a function of the peak value of the flux density B_{peak} and the ratio λ between the major and minor flux components according to (5.34). The loss correction factor is determined based on experimental data in [84]. This data is also presented in a slightly different way in [85].

$$\lambda = \frac{B_{Min}}{B_{Maj}} \tag{5.34}$$

The appearance of flux density locus in the machine under investigation is studied by plotting the flux as a function of time in different locations of the stator core. The result is presented in Figure 5.26. Here it can be seen that the flux density in the tooth forms radially directed lines rather than circles or ellipses. Hence it varies in one dimension only and is obviously alternating. The orthogonally directed flux variations in the outer most part of the yoke are alternating as well. Since the laminations are made of non-oriented steel, the direction of the flux variation makes no difference. Closer towards the tooth it gets less obvious whether the flux is alternating or rotating while the flux density in the transition between a tooth and the yoke clearly rotates to form ellipses.

A rule of thumb established in [65] is that the flux should be considered as rotational if the axis ratio λ is larger than 0.4. With that, it is concluded that the flux in the yoke can be assumed to be pulsating, while the flux density variation in the yoke-tooth transition region is rotational. Hence flux density loci are present in the machine, but in a limited geometrical region only.

In an attempt to foresee the influence on the iron losses, (5.33) is employed when estimating the iron losses in the stator core. The result is compared to that of (5.29). As expected from Figure 5.26, the resulting iron losses in the tooth region is unaffected. In the yoke region,

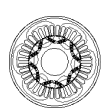

the iron losses become 7% higher when estimated with (5.33) compared to if only the major flux component is used in (5.29). When considering the entire stator with the yoke and teeth combined, the difference is 4%. This coincides with the results presented in both [65] and [85] where the loss increase due to the flux density locus is in the range of 4-6%.

The analysis performed in [73], indicates that the additional losses due to flux density loci are connected to the hysteresis. The conclusion in [73] is that the loss contribution from the rotational flux density variation has almost no significance. The marginal influence on the result is probably also a reason for why rotational losses have not become common practice to include in the iron loss analysis despite that e.g. [84] was published more than 20 years ago.

Magnetic flux density variation waveforms

One of the prerequisites for using (5.29) is a sinusoidally shaped magnetic flux density variation. This is generally not the case in large parts of the iron core in an electric machine. This is partly related to the geometry that might make the magnetic flux density vary more in a triangular or trapezoidal shape [62,64]. This results in steep $\frac{dB}{dt}$, or harmonics that need to be considered to achieve a more accurate loss prediction. Apart from the geometrical aspects, there are also harmonics in the applied magnetic field. These are caused by the non-ideal curve shapes generated by the machine control, typically originating from e.g. PWM switching [94, 95].

When looking into the physical origin of losses due to hysteresis, [62] concludes that they occur due to the average re-magnetization rate rather than the frequency. This means that if there are variations in the magnetic flux as it propagates through the iron core, these variations will give rise to additional losses. In order to include this, a modified Steinmetz equation (MSE) is developed [62]. The general idea is to establish an equivalent frequency that depends on the re-magnetization rate. This way the time derivative of the magnetic flux density is taken into account. The equivalent frequency, f_{eq} is described in (5.35) where $\Delta B = B_{max} - B_{min}$. Other parameters needed to calculate the iron losses are those originally used in the Steinmetz equation. Hence the only modification is to replace the frequency with the developed equivalent one.

$$f_{eq} = \frac{2}{\Delta B^2 \cdot \pi^2} \int_0^T \left(\frac{dB}{dt} \right)^2 dt \tag{5.35}$$

In [64] the losses are established in the time domain rather than in the frequency domain using (5.36) – (5.38) for the hysteresis, p_{hy} classical eddy current, p_{ec} and excess or anomalous losses, p_{an} respectively.

$$p_{hy} = H_{irr} \cdot \frac{dB}{dt} \tag{5.36}$$

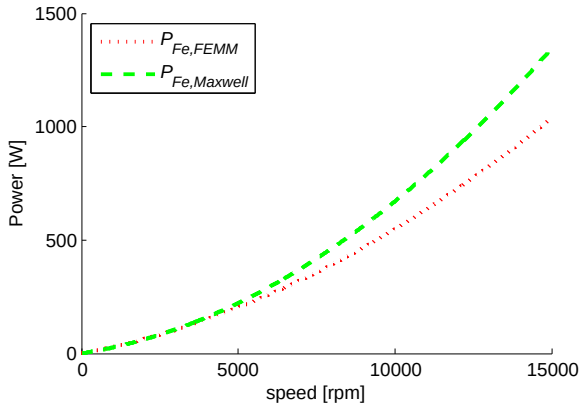

Figure 5.27: Estimated no load stator core losses based on 2D FE simulations in FEMM ($P_{Fe,FEMM}$) and Ansys Maxwell ($P_{Fe,Maxwell}$)

$$p_{ec} = \frac{1}{2\pi^2} \cdot c_{ec} \cdot \left(\frac{dB}{dt}\right)^2 \tag{5.37}$$

$$p_{an} = \frac{1}{C_{an}} \cdot c_{an} \cdot \left|\frac{dB}{dt}\right|^{1.5} \tag{5.38}$$

In (5.36) H_{irr} is the irreversible hysteresis losses. This is modelled as an ellipse, defined according to (5.39) and derived by solving the hysteresis losses in the time and frequency domain at the same sinusoidal conditions.

$$H_{irr} = \frac{1}{\pi} \cdot c_{hy} \cdot B_m \cdot \cos(\omega_e) \tag{5.39}$$

The term $\frac{1}{2\pi^2}$ in (5.37) and constant C_{an} in (5.38) are obtained in similar manner as H_{irr} for (5.36). [64]

The influence of non sinusoidal magnetic flux density waveforms on the stator core losses is studied by running 2D simulations in Ansys Maxwell [96]. This is a commercially available FE software where the iron losses are solved in accordance to (5.36)–(5.38). The resulting no load losses are presented in Figure 5.27 together with the simulation result based on the simplified stator core loss model used in the design stage (covered in subsection 5.3.2). The difference in terms of increased losses at higher speed is expected based on how the frequency waveform is represented in the different approaches. In addition to this, there is also a difference when separating the losses. The result from Ansys Maxwell predicts higher eddy current losses but smaller hysteresis losses compared to FEMM. This can be more easily observed if the result is divided with speed, hence presented as loss torque ($T_{Loss,Fe}$). This is done later on in Figure 5.36 in subsection 5.3.5. The iron loss coefficients used in the different sets of simulations are presented in Table 5.1.

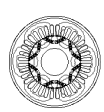

Table 5.1: Core loss coefficients

Parameter	FEMM	Maxwell
Hysteresis loss coefficient, c_{hy}	167.2	166.6
Hysteresis loss exponent, e_{hy}	1.7404	
Eddy current loss coefficient, c_{ec}	0.3622	0.366
Anomalous loss coefficient, c_{an}	0.1664	0.077

In addition to the different ways of handling the flux density waveforms, also the estimation of the magnetic flux density is recorded differently from the different FE-simulations. As already described, the iron losses based on the simulations in FEMM are derived from selected single points representing different relevant regions in the stator core (typically teeth and yoke). The peak value of the magnetic flux density in each point is used for the entire region with assumed sinusoidally shaped flux density waveforms. The iron losses based on 2D simulations in Ansys Maxwell are instead established on the change rate of the magnetic flux density ($\frac{dB}{dt}$) in each mesh element. This way, these simulations should give a better representation of the iron core losses. This holds both in terms of the form of the magnetic flux density variation and in terms of how the losses are distributed in the stator core.

Despite the differences in deriving the iron losses, the simulation results are considered comparable. The difference is just below 30% at top speed. This difference gets gradually smaller down to around 2600 rpm where the two simulation approaches predict the same losses. Below this speed, the iron losses originally estimated get larger, up to around 20% difference at standstill. The reason for the comparable results should be that the underestimation introduced by the waveform representation in the original simulations are compensated by the single point flux densities. The location of the points (defined previously in Figure 5.21) lead to an overestimation of the magnetic flux density in the corresponding region. This is why the iron losses are (marginally) higher in the original simulations at low speeds, but lower as the frequency is increased.

In [94], the presence of harmonics on the fundamental magnetic flux density is handled by introducing minor hysteresis loops. This is done with a simplified Preisach model. The classical eddy current losses are established using the same eddy current loss model, but with different frequency and amplitude in accordance with the different harmonics. It is also shown how minor hysteresis loops occur with a two-level PWM supply. To get the total losses, the individual contributors are summed up. Hence the approach is the same as the classical loss separation in e.g. (5.29), but with more hysteresis and eddy current loss contributors. The obtained loss model with minor hysteresis loops rely on experimental

knowledge on the major hysteresis loop and the value of the energy loss at the involved polarization values and frequencies. [94]

The iron loss model used in [95] takes consideration of minor hysteresis loops and eddy currents induced by low amplitude high frequency magnetic flux density variations. These are both induced by harmonics from the PWM switching. The lower the switching frequency, the higher the additional losses. Here, improvements on a model using varying iron loss coefficients depending on frequency, magnetic flux density and temperature are presented. The simulation results are obtained by adding the sum of a number of minor hysteresis loops to the hysteresis loss part. In addition to this, the eddy current losses are considered as the sum of eddy currents arising as the PWM ripple is propagated to the magnetic flux density in the iron core. The result is presented as function of switching frequency along with measurements showing how the iron losses are increased as the switching frequency is reduced with constant fundamental frequency. [95]

In [80], three iron loss models are compared. Included in the investigation are one time domain model and two frequency domain models, of which one is considered a simplified method. The loss parameters are fitted based on measurements during sinusoidal conditions. Except for the simplified method, this gives a good correlation between simulations and measurements at varying magnetic flux density and sinusoidal conditions. Further on, it is shown that the iron loss parameters fitted on sinusoidal conditions still can provide reasonable estimations on iron losses at non sinusoidal conditions. [80]

5.3.4 Iron losses imposed by manufacturing

As the laminations are being processed throughout manufacturing, the loss characteristics are affected. This includes the material structure close to the edges after cutting or punching, as well as creating unwanted axially directed conducting paths when stacking the iron core. This matter is considered in the following subsection.

Cutting or punching effects

Producing the laminations for electric machines is often done with either mechanical cutting such as stamping/punching or laser cutting. Since punching requires a rather large tooling investment, prototype machines are often produced by means of laser cutting. Several studies have been performed on how the iron losses are influenced by cutting and the resulting effects close to the edges [65, 68, 71, 81–83, 86–88, 97, 98]. The mechanical stress on the material when being cut, damages the magnetic structure. This causes the hysteresis losses to go up as the number of impurities at which the magnetic domains are pinned (described earlier in Subsection 5.3.1) is increased. How much is depending on e.g. lamin-

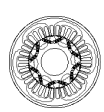

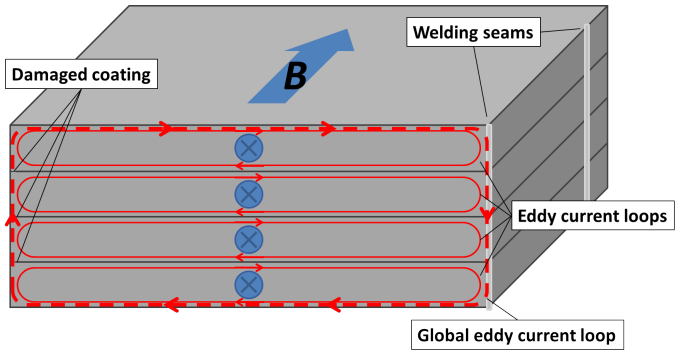

Figure 5.28: Principle sketch of a global eddy current loop due to (partial) short circuits at the lamination edges

ation thickness and grain size. The quality of the cut has effect on the result, too. A new cutting tool gives a more clean cut compared to if it is worn out and not as sharp when apporaching end of life. When testing is done in a single-sheet setup, the eddy losses are less affected by the cutting process. The assumption in [68] based on single sheet tests is that the eddy currents are not affected at all. However, if the lamination coating close to the edges is damaged, short circuit can occur between sheets that creates larger scale global eddy current loops [66,82]. A principle sketch of global eddy currents in a lamination stack is shown in Figure 5.28.

Even though the expression for c_{ec} introduced earlier in (5.30) not is valid at too large lamination thickness, it can still be used to illustrate that the global eddy current loop will generate more losses. As the the distance d_{lam} is increased, so is c_{ec} and hence the resulting losses. How much the losses are increased is more difficult to predict since it is hard to detect how many laminations that get connected. In addition to this, the electric conductivity (σ) between laminations is hard to predict or establish.

Studies presented in the literature indicate that laser cutting in general has a higher influence on the iron losses than stamping [81–83]. This is explained by the stress build up in the material by local heat from the laser. In [82], it is stated that the depth of the affected iron is in the range of up to a couple of millimetres, while [88] concludes it to range from 0.1 mm and upwards. Therefore, small machines, or machines with a higher number of slots are affected more by the cutting effect. In addition to this, laser cutting also has higher impact on the coating close to the edge compared to with stamping [82]. The affected area is clearly visible in Figure 5.29 where the edge area on both sides of a lamination sheet from the prototype design is magnified using an Alicona InfiniteFocus G4 microscope. The changing of colour close to the edges indicates that the coating on both sides are affected with a depth of around 100µm. This distance coincides with what is seen in a corresponding figure in [82]. As the coating at the lamination edges is affected, the risk of introducing

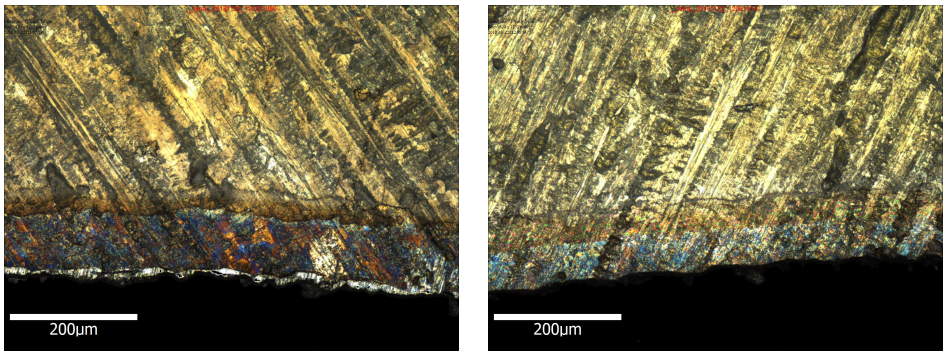

(**a**) Side A (**b**) Side B

Figure 5.29: Optical investigation of the laser cut edge area on side A (left) and side B (right) of a lamination

global eddy current loops is increased.

Another detail noticed in Figure 5.29 (a), is the metal lip next to the edge. This is what is left of the burr, after being grinded in the manufacturing process. The software in the microscope[3] estimates the height of the burr to 2–4µm. This is comparable to the coating thickness of typically approximately 1–6µm [99]. On the edge of the opposite side (side B), a rollover depth is found. With an extruding metal lip close to the edge, the risk of short circuit between the laminations is increased. This holds especially for a stator with skewing, in which there is an overlap between the stator laminations.

Suggested means to compensate for the cutting effects when modelling the losses are to change the material properties [98], or to compensate with correction factors [65]. In [65], a cutting factor is introduced to take the cutting effects on the iron losses into account. The cutting factor is based on measurements on 0.5 mm laminations with varying flux path widths. The increase in losses compared to the 30 mm wide reference from the Epstein test procedure [92] gives the correcting cutting factor. The straight forward engineering approach is to simply multiply the iron losses obtained from (5.29) with the cutting factor to get a more realistic iron loss prediction. Similar measurements are performed in [71], but on 0.3 mm laminations instead. By doing a rough estimation that the relation to lamination thickness is fairly linear, these two results are used to derive cutting factors also for other lamination thickness's. This way, correction factors for the teeth and yoke regions respectively are derived for the 0.35 mm laminations in the machine under investigation. The tooth width of in average 4.5 mm results in a correction factor of 1.45, or 45% while the yoke width of in average 16 mm gives a correction factor of 1.07, hence 7%. That is, according to this approach the iron losses in the teeth and yoke should be 45% and 7%

[3]Focus-Variation: www.alicona.com/focus-variation/ Accessed on 2018-12-02

higher than if estimated straight off with (5.29).

However, according to [66], grain size is the main influencing factor for cutting effects. Hence information on the lamination thickness only, might not be sufficient to derive reliable cutting factors. The influence due to material properties is also observed in [83]. Here, two test samples share the same lamination thickness but have different loss properties. But although there is a difference, it is not as significant as that to a sample with smaller lamination thickness. Another result presented is how different settings in the laser cutting influence the normalized specific losses.

Based on the experimental results, [83] introduces correction factors on the loss coefficients for hysteresis and eddy current losses separately. The machine geometry is divided into different regions depending on the flux path widths where the average impact due to cutting is assumed constant. The losses can then be estimated based on the previously used expression in (5.29), but with the relevant correction factors in each region. The strategy to introduce regions in the simulation model is also implemented in [68]. Here, the regions are set up based on the distance to the edges. This is done with the assumption that the closer to the edge, the more affected the material. The losses are computed in the post process with different material properties in each separate region. The conclusion after having reviewed parts of the literature is that cutting the laminations affects the iron losses. How much the losses are affected and on what part in the iron loss model, is however less unanimous.

Losses due to the machine mounting process

Welding as a mean to get the stator package to keep together can introduce more losses due to the creation of axially directed electrically conducting paths [67, 82, 83]. In [67] tests are performed on a ring sample with welding seams on both the inner and outer side. As a result, there are axially directed electrically conducting paths on both side of the magnetic flux (see Figure 5.28). This leads to global eddy current loops and high losses. The setup is however not really representative for an electric machine where welding typically is done on the outisde only. Complementary tests in the same paper with welding on the outer side only, did not result in an increase of losses. Veigel et al. [82] states that a weld connection in most cases is responsible for very high eddy current losses. However, the basis for eddy current losses is an electrically connected loop with magnetic flux running through. Hence a number of welding seams on the outside of the stator should not affect the eddy current losses on its own. In [83], the result of a number of measurements on welded iron strips is presented. Here, the conclusion is that more welding seams gives more losses. Thermal residual stresses and local eddy currents are stated as explanations. It is also concluded that welding on both sides increases the losses significantly more, which agrees with the result in [67]. This is however not a common way to build machines. Nevertheless, it could still be that welding on one side in combination with damaged coating as a result of laser

cutting enhance the risk of getting global eddy current loops (see Figure 5.28).

Another thing in the manufacturing process that can have an impact on the iron losses is stress in the material due to for example shrink fitting of the stator into its housing [79, 100, 101]. In [79] the dependency on losses due to tensile as well as compressive stress is investigated. Compressive stress can typically be a result of shrink fitting or from the stator core getting warmer than the housing so that stress is introduced by an uneven thermal expansion. Tensile stress would especially occur in the rotor laminations as a result of centrifugal forces during rotation. The result of the study in [79] is that tensile stress has a small impact on the iron losses. Compressive stress has a much higher impact on the losses, up to almost a factor of three depending on the grain size, alloying content and field strength and frequency. By performing loss separation on the measured losses, it is concluded that especially the excess losses are affected, while hysteresis losses are affected to a smaller extent and classical eddy current losses in principle are unaffected.

The results from the study performed in [100] show similar influence on the losses based on compressive stress in the same magnitude, although presented as total losses rather than separated. In this study, the result of the laboratory set-up is transferred into FEM simulations with modified permeabilities and loss properties in different parts of the machine. This is according to mechanical FE-simulations estimating the stress levels. The result indicates that the losses are affected to a noticeable extent, but despite that the permeability is affected, the flux distribution in the stator core is not. This is expected due to the impact of the air-gap in the complete magnetic circuit.

In [101], means to manipulate the coefficients to be used in (5.29) are presented. There, it is also said that the classical eddy currents are not effected by compressive stress. For the hysteresis and anomalous losses, c_{hy}, e_{hy} and c_{an} are set up as functions of mechanical stress. The paper also includes plots showing the dependency in the parameters for two lamination with different thickness. Although the thinner lamination has lower losses from the start, the influence due to mechanical stress seems comparable in terms of absolute values.

5.3.5 Measurements on the stator iron core losses

The iron losses in the machine is also investigated by measurements. These measurements are performed both with and without applied loading with varying result. No load tests are done with the machine stand alone, hence not being connected to a converter. On load tests are done with the machine connected to and controlled by the converter. This subsection sets out to describe the activities performed on this matter. The measurements of mechanical losses performed earlier in section 5.2 are used to separate the iron losses from the overall speed dependant losses.

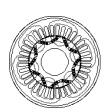

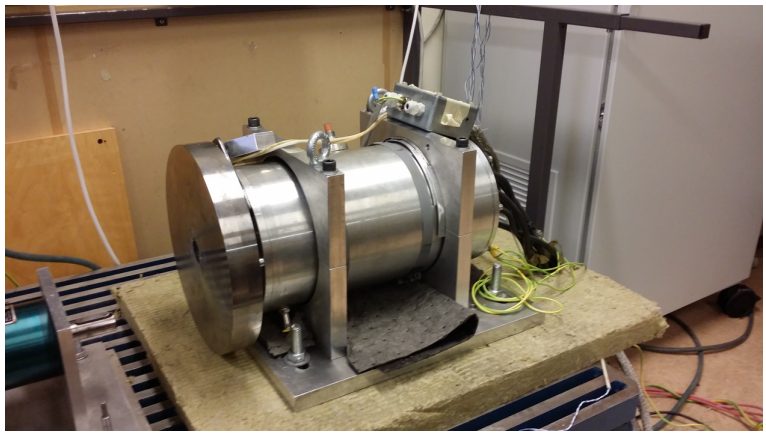

Figure 5.30: Test object mounted in its cradle with a flywheel connected to the shaft

No load loss measurements

No load loss tests are performed in two different approaches. One being with the machine connected to a conventional test bench with a torque transducer. The second approach is a roll out test in which the loss torque is derived from the deceleration and moment of inertia.

Roll out test set up and results The roll out test is set up in a similar manner as described for the mechanical losses in section 5.2.5: The logging starts as the machine starts to decelerate and the deceleration rate ($\frac{d\omega_m}{dt}$) and moment of inertia (J_{tot}) are used to establish the loss torque T_{Loss} according to (5.40).

$$T_{Loss} = \left| \frac{d\omega_m}{dt} \right| \cdot J_{tot} \tag{5.40}$$

The difference to (5.27) is that an external moment of inertia is added in the form of a flywheel mounted on the shaft. That is, J_{tot} is the combination of the rotor inertia J_{rotor} and the external inertia J_{ext} of the flywheel. The set-up can be seen in Figure 5.30 where the machine is mounted in its test frame with a flywheel connected to the shaft.

As the total moment of inertia in the system is increased, the system dynamics goes down. This is beneficial for reducing mechanical oscillations which facilitates the data collection, especially close to standstill. In addition to this, the geometrical simplicity of the flywheel makes it easier to estimate the moment of inertia. Hence the uncertainties from establishing the moment of inertia of the rotor become less decisive. A disadvantage with the external flywheel is that the conditions for the mechanical losses are changed. Based on preliminary tests with and without the flywheel mounted on the dummy rotor (handled in

subsection 5.2.5) and the magnitude of the mechanical losses compared to the iron losses, this influence is considered to be negligible. The total moment of inertia, J_{tot} of the system (rotor and flywheel together) is again established according to how it is described in [26]. This paper also confirms a maximum offset of $\pm 5\%$ and a standard deviation below 2% when determining J. Since the loss torque is a product of J and $\frac{d\omega_m}{dt}$, this offset is transferred as an uncertainty directly onto the loss torque readings.

The mechanical angular velocity, ω_m is obtained from the resolver. Since this has a comparably much higher accuracy, the uncertainty in the roll out test is considered to be a result of that in determining the moment of inertia.

The means of reaching the speed at which the test starts is also a bit different compared to the mechanical test set up. Here a motor drive, available in the lab is used to get the machine up to the max test speed. Available DC-voltage and motor drive ratings put a limit on the top speed to around 3500 rpm. In order for the motor drive not to influence the test result, a three phase circuit breaker is mounted in-between the drive and the machine. When maximum test speed is reached, the drive is disabled and the three phase breaker is opened to physically disconnect the machine phase cables from the inverter.

The test is repeated a number of times to verify the consistency. All tests are conducted at room temperature. The entire procedure is also repeated before and after the mechanical loss measurements, covered previously in subsection 5.2.5. The resulting loss torque is presented to the left in Figure 5.31. From this, the power losses are derived and presented in the right plot. When studying the power losses, an apparently squared relation to speed is observed. This goes well with the theory in subsection 5.3.1 and equation (5.29). The term representing eddy current losses, with its squared relation to frequency is reflected in the measurement results. The presence of hysteresis losses and anomalous losses is discussed later on in this subsection.

The run-through before and after the dummy rotor test is presented as test case 1 and 2 respectively in Figure 5.31. From this it is concluded that the conditions are comparable before and after the mechanical loss measurements. Hence, the conditions during the mechanical testing are likely preserved as well. The ringing observed close to stand still in the loss torque graph (to the left in Figure 5.31) is from mechanical oscillations at the end of the roll out test, just before the rotor stops.

No load test bench set up and results No load losses are also measured in a conventional test bench set up. The test object is disconnected from the drive (hence open circuited) and connected to a rig motor or dyno via a torque transducer and a belt driven speed reduction. The drag torque measured by the transducer as the machine is rotated is logged as the loss torque. The test object mounted in the test bench can be seen in Figure 5.32.

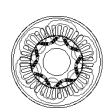

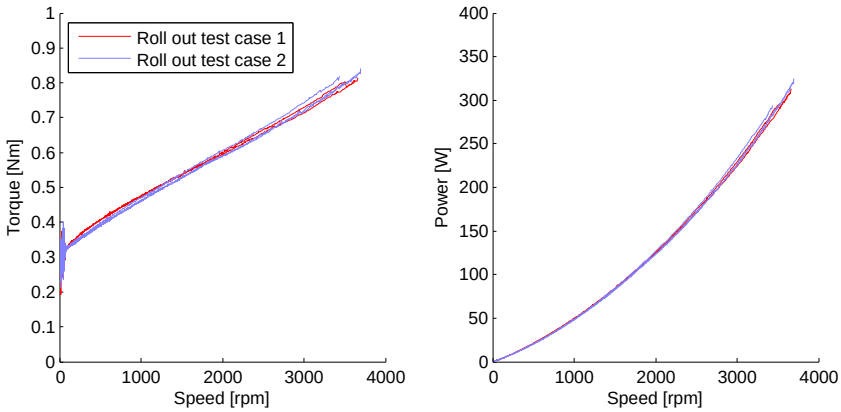

Figure 5.31: Loss torque (left) and power (right) from the roll out tests before (test case 1) and after (test case 2) the mechanical loss measurements

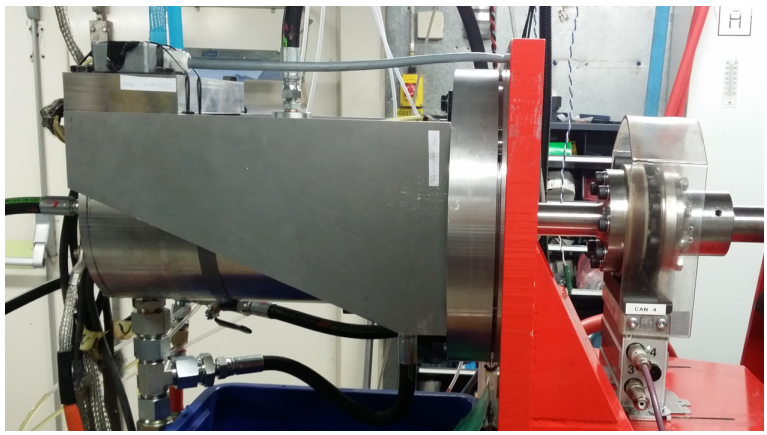

Figure 5.32: Test object mounted in the test bench mechanically connected to the torque transducer

The no load measurements are performed from 0-6500 rpm, limited by the test bench. The speed is kept constant for around 10 s at each test point while measuring the torque. This is done in order for the results not to be influenced by the dynamic effects during the speed changes. The test sequence is started at standstill and sequentially increased to the top speed in steps of 500 rpm. When maximum test speed is reached the procedure is repeated as the machine is gradually decelerated back to zero speed. This full sequence is also repeated three times for consistency. The entire test is performed once at room temperature around 25°C and once when the machine is warm with an even temperature of around 60°C in the inner parts of the machine. This is based on temperature readings from the sensors at the stator slot, stator back and NDE bearing (in accordance to Figure 2.14).

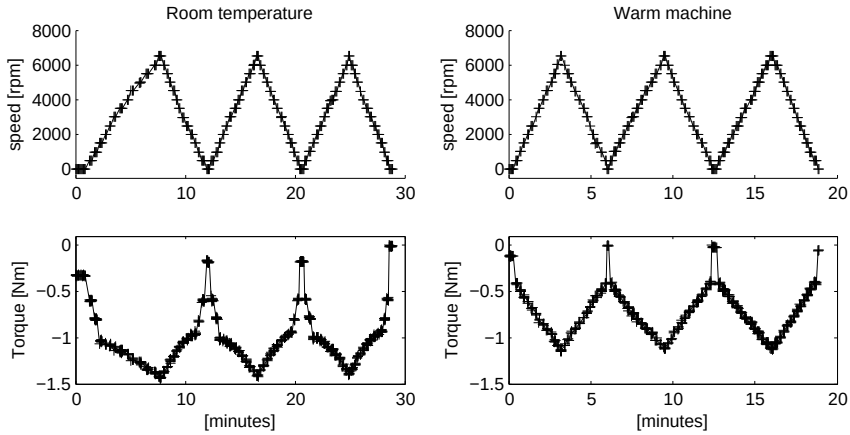

Figure 5.33: Test sequence for measuring no load losses in the conventional test bench at room temperature (left) and warm machine (right)

The shaft speed is controlled with the dyno (a separately magnetized Siemens 1GH5 224-0NJ40-Z DC-machine controlled by a Parker DC590P inverter) and the torque and speed are recorded with a HBM T12/1kNm torque transducer with the higher accuracy option [28]. The accuracy class of the transducer is 0.03%. Although this not is a number of the definitive measurement uncertainty, it gives an indication of the range in which the accuracy will end up. Since the nominal torque, T_{nom} is reaching 1000 Nm, the accuracy class in question corresponds to 0.3 Nm. Hence the torque transducer at hand is really not optimal for measuring the loss torque with expected values of around and even below 1 Nm. Due to availability reasons it is used nevertheless. Things affecting the total uncertainty (u_{tot}) are a sensitivity tolerance deviation (d_C), linear deviation and hysteresis effects (d_{lh}) together with a relative standard deviation (σ_{rel}) and temperature effects (TK_C and TK_0). In addition to this, any external parasitic loads on the torque transducer could affect the uncertainty further (u_{par}). The latter would be a result of how the torque transducer is mounted in the rig and should preferably be avoided when preparing the rig for the test. The two most decisive parts are the temperature and any parasitic loads acting on the transducer unit. This is explained more in detail in Appendix B.

The two test sequences are presented to the left and right in Figure 5.33 for room temperature and warm machine respectively. The upper graphs show shaft speed as a function of time, while the measured drag torque is presented in the lower graphs. Here it is noticed that the torque readings at stand still differ from zero. This is more obvious in the left graph, where the readings at standstill have a spread of 0 to -0.3 Nm. This could to some extent be expected from the accuracy class of the torque transducer.

Another observed phenomenon is a somewhat different curve shape on the torque readings.

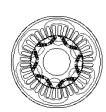

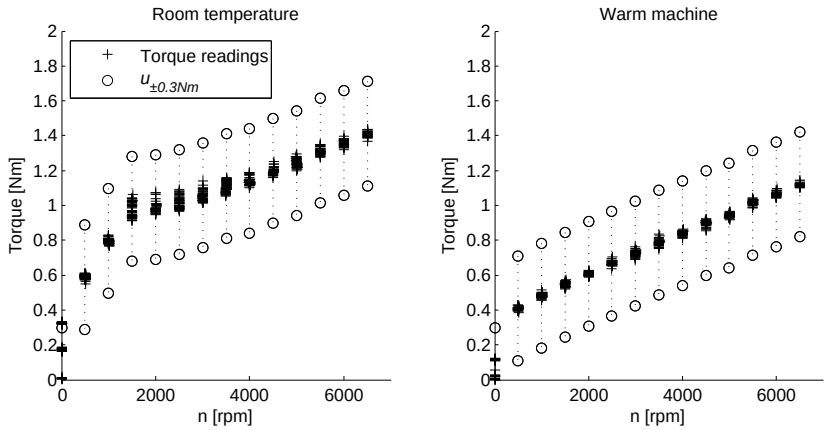

Figure 5.34: Loss torque as a function of speed from drag torque measurements at room temperature (left) and warm machine (right) in a conventional test bench including the uncertainty ($u_{\pm 0.3\mathrm{Nm}}$) indicated by the accuracy class of the torque transducer

This difference can be further studied in Figure 5.34 where the absolute values of the drag torque are presented as loss torque as a function of speed. Included in the graph is also an uncertainty, $u_{\pm 0.3\mathrm{Nm}}$ based on the torque transducer accuracy class. The knee point at 1500 rpm is not expected from the theoretical expressions of the iron losses nor from the mechanical losses. This in combination with the larger spread at standstill indicates that the unexpected behaviour could be related to an underlying tension in the transducer. The exact cause behind this is not investigated any further.

The loss torque in the warm machine behaves more as can be expected from the iron loss theory. Another observation is that although the left graph has a strange behaviour, the absolute values seem to be higher at room temperature than in the warm machine. This phenomenon is also expected and should at least partly be related to the reversible temperature coefficients of the permanent magnets. The warmer machine has a weaker flux linkage and therefore a lower magnetic flux density, B in the stator core. The difference in absolute values is however too large to be explained by the weaker magnets on its own. Additional explanations besides the torque transducer could be related to a thermal dependency of the hysteresis and eddy current parts of the losses. Again however, the difference is bigger than what can be expected when consulting the literature [93]. A final comment on the graphs in Figure 5.34 is that the uncertainty obviously is too high. Despite an excellent rated accuracy, the over-dimensioned nominal torque brings too much inaccuracy into the logged data readings. All in all, the need of a more accurate low range torque transducer questions the result from the loss torque measured in the test bench. The results should therefore be handled with care and used as indications rather than a definitive result.

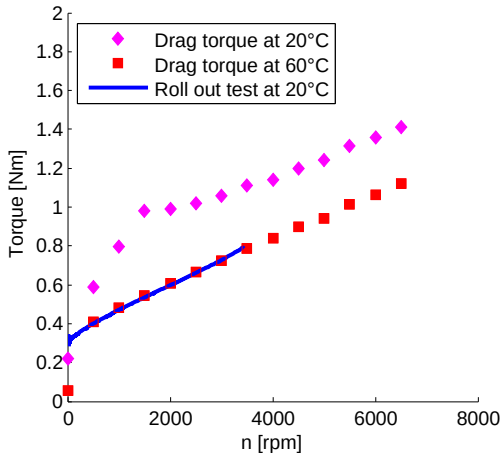

Figure 5.35: Loss torque as a function of speed from conventional test bench at two different machine temperatures and from roll out test at room temperature

Analysis of the results from the different test procedures Before starting with analysing the test results compared to the simulations, some remarks are made on the conformity between the two test procedures. To aid in this, the test results are jointly plotted in Figure 5.35. Here, each test case (two drag torque measurements in a conventional test bench set-up and one roll out test) is combined and presented as mean values respectively. The first observation is a good match in the speed dependency. This is seen on the similar inclination in the curves and is especially true when comparing the warm machine and the roll out test. Above 4000 rpm, the same goes for the room-tempered case. The divergent behaviour below 4000 rpm in this test case is believed to be caused by external tension on the torque transducer. These readings are therefore not considered in the further analysis.

The match in terms of absolute values is not as good. The difference between the two tests performed at room temperature (one of the test bench tests and the roll out test) at 4000 rpm is ≈0.3 Nm. If the roll out test results would have been extrapolated to higher speeds, this offset would have remained roughly constant. The torque readings from the warm machine follow the roll out test result very precisely. The good match in speed dependency indicates that a roll out test starting at higher speeds would have had a continued linear relationship between loss torque and speed also at higher revolutions per minute.

Based on earlier measurements on linked magnetic flux as a function of temperature (presented in Figure 3.13 in Chapter 3), the expected difference in magnetic flux density, B from the machine at 60°C compared to 25°C is in the range of 5%. This due to the reversible temperature coefficients (RTC) of the permanent magnets. With a quadratic relation to the eddy losses and close to quadratic relation to hysteresis (according to equation (5.29)),

the difference in iron losses should be in the range of 10%. Hence the curves from the warm machine and the roll out test should not match as well as they do. Given the large level of uncertainty from the test bench, this difference is not possible to detect in the measurements.

A final remark on the analysis work done on the torque transducer readings is somewhat related to the too large mutual difference between the different measurements. The zero signal offset during calibration of the torque transducer (performed 3 months after these tests, according to a planned schedule) corresponded to -0.216 Nm at 21.6°C. Hence, since measured torque is negative (see Figure 5.33) the room-tempered test bench test should perhaps be 0.2 Nm lower. Further on, assuming a 20°C temperature difference $\Delta\vartheta$ at the torque transducer (from approximately 25°C to 45°C *at the torque transducer*) results in a temperature influence on the zero signal, u_{TK0} equal to $\pm d_{TK0} \cdot T_{nom} \cdot \Delta\vartheta/10 = 0.01\% \cdot 1000 \cdot 20/10 = \pm 0.2$Nm. If this in reality would be $+0.2$ Nm, there is a chance that the room temperature readings are ≈ 0.2 Nm too large (due to the zero signal offset), while the readings from the warm machine are not (if the temperature offset counteracts with the zero signal offset). That would have brought the torque readings from the two test bench tests much closer to each other. In fact the difference could go down to the range of the previously mentioned 10% due to the 5% reduction in flux linkage in the warm machine. In addition to this, the readings would also have been much closer to the roll out test.

Nevertheless, with all the speculations the overall conclusion is still that the test bench results should be considered as information only. Further analysis is instead done with consideration to the roll out test result only. It is also assumed that these results could have been accurately extrapolated to higher rotational speeds by simply extending the linear relation.

No load test results compared to simulations A comparison between the iron losses from simulations and measurements is done in Figure 5.36. Included in the graph is the result from the roll out test together with simulations on the iron loss torque. Both $T^{sim}_{Loss,Fe}$ from the original simulations (based on data from FEMM) and $T^{sim,Maxwell}_{Loss,Fe}$ from when the simulations considering magnetic flux density change rate ($\frac{dB}{dt}$) instead of frequency are shown. In addition to this the total loss torque from simulations T^{sim}_{Loss} is included. This is the sum of the mechanical losses handled previously in section 5.2 and the iron losses used in the design stage, i.e., $T^{sim}_{Loss,Fe}$ derived from equation (5.32) as described in subsection 5.3.2. Since the roll out test on the permanently magnetized rotor has contributions from both iron- and mechanical losses, the comparison should be done with the combined total simulation result T^{sim}_{Loss}. The simulation result from the Ansys Maxwell simulations is presented as reference only. As can be seen, the difference between the two simulation

methods are marginal compared to that to the roll out test.

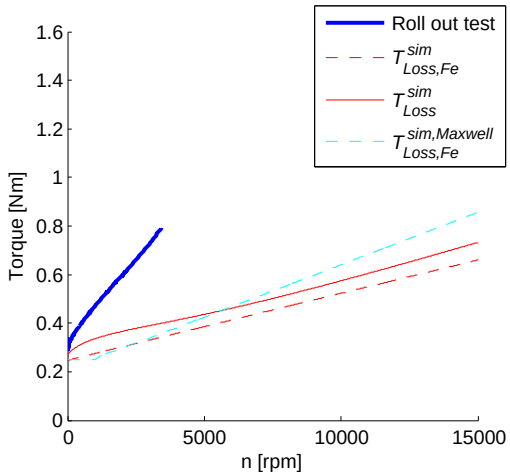

Figure 5.36: Loss torque as a function of speed from the roll out test together with iron loss torque $T^{sim}_{Loss,Fe}$ and total loss torque T^{sim}_{Loss} from the original simulations and the iron loss torque $T^{sim,Maxwell}_{Loss,Fe}$ from the Ansys Maxwell 2D simulations

Studying Figure 5.36, an obvious and in some ways rather large deviation is observed between simulations (T^{sim}_{Loss}) and measurements. Starting at stand still however, the measured and simulated readings are in the same range. By returning to the three terms in the theoretical expression (5.29) in subsection 5.3.1 some conclusions can be made. As the data studied in Figure 5.36 is presented as torque, the power losses in (5.32), originating from (5.29) need to be divided with the angular velocity ω_m. This is done in (5.41) where the constant $k_{m,Fe}$ includes the iron core mass m_{Fe} and the number of poles N_p according to 5.42.

$$T^{sim}_{Loss,Fe} = \frac{P_{Fe}}{\omega_m} = \left(c_{hy} \cdot B^{e_{hy}} + c_{ec} \cdot B^2 \cdot f + c_{an} \cdot B^{1.5} \cdot \sqrt{f} \right) \cdot k_{m,Fe} \tag{5.41}$$

$$k_{m,Fe} = \frac{m_{Fe} \cdot N_p}{4 \cdot \pi} \tag{5.42}$$

Looking at the frequency dependency, (5.41) states that the expression for iron loss torque has one constant term, one term depending linearly and one relating to the square root of the frequency. Since the value of c_{an} is rather small in combination with a diminishing significance with increased frequency, the last term is ignored in the further analysis. This gives a constant term relating to the hysteresis effects and a linear term relating to the eddy currents. From Figure 5.36 it can be concluded that this is the case also for the measurements. Despite the obvious deviation in absolute values, the loss torque has a constant

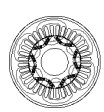

part present already at stand still and one part that increases linearly with speed, hence frequency.

So, according to theory the torque present already close to and at stand still should correspond to the static hysteresis losses (in combination with the frictional loss torque already covered in section 5.2). As the deviation in the constant term is rather small, the estimation of the hysteresis losses should be rather good. The hysteresis loss coefficient (c_{hy}) and exponent (e_{hy}) in (5.29) and (5.41) seem to be about correct. As the rotational speed is increased, the deviation between simulations and measurements gets increasingly bigger. This should then correspond to the eddy currents in (5.41) and originally in (5.29). Here it seems as the parameter c_{ec} in simulations is rather far off. The conclusion is therefore that the hysteresis losses are estimated with an acceptable accuracy, while the eddy current losses are not.

In order to further analyse these results, the findings from the literature review in subsections 5.3.3 and 5.3.4 are used. Based on this, it seems to be mainly the flux density waveforms and any presence of global eddy currents that should affect the eddy currents. Some findings are also indicating increased eddy currents locally in each sheet, but not in the magnitude found here. It is also stated that laser cutting has a potentially higher impact on the generation of losses in the iron core. Especially if the coating is damaged around the edges of the laminations, global eddy current loops could arise. Also welding as a mean of joining the stack could enhance the risk for getting global eddy current loops. For the prototype machine studied in this case, both laser cutting and welding is used in the manufacturing process.

Another way to consult the theory is by returning to the theoretical expression (5.30). Here it is clear that increased eddy current losses should be a result of either increased conductivity (σ) or a wider flux path (d), that is larger loops for the eddy currents to circulate. Since the conductivity should not be enhanced by laser cutting, the flux path thickness is the remaining component to consider. With the squared relation to d in (5.30), an increased thickness rather quickly leads to increased eddy current losses. The average conductivity (σ) in the global loop should on the other hand not be as good as within a lamination. In addition to this, according to [63], the simplifications made when deriving (5.30) makes it unsuited to use for too large flux path thicknesses. It is therefore not possible to use it straight off to try to foresee the increased eddy current losses due to short circuits or partial short circuits at the lamination edges.

In the event of any axially directed flux density components running orthogonally through the laminations, the eddy current losses would increase. The eddy current coefficient as determined in (5.30) would be higher for flux in axial, or z-direction compared to in the xy-plane along the laminations. The hysteresis losses do not have this dependency of the flux direction. The axially directed flux component could be a side effect from having a

skewed stator. Whether skewing actually introduces any axial flux density components and if so, how large they are has not been investigated any further within this project. The findings in [43] and [102] are that the iron core losses should decrease when skewing is introduced. It is however not investigated in any of these papers whether or not there are any axial flux density components in the stator core due to skewing.

Another possibility that perhaps could explain a part of the deviating results could be stray flux paths, inducing losses in other parts of the machine construction. Nevertheless, based on the reflections discussed above, it is stated as most likely that the deviation in the speed dependant part of the loss torque is related to global eddy currents (described in the principle sketch in Figure 5.28). To what extent is however not based on theory, but rather by comparing the simulation result with measurements.

Iron loss model adaptation based on the test results The final measure when analysing the no load test results is to try to adopt the simulation model to get a better agreement with measurements. A similar approach is also found in [103]. The idea is to increase the hysteresis loss coefficient c_{hy} until the simulations agree with measurements at standstill. Since the flux density is constant during this experiment, it is not possible to determine whether the exponent e_{hy} should be altered as well. It is therefore kept unchanged for the time being.

The eddy current coefficient e_{ec} is altered in a similar manner until the speed dependencies agree. As stated previously, the anomalous or excess losses are disregarded in this analysis due to a marginal effect on the result only. The small bend visible at low rotational speed that would be a an expected result from the excess losses, is present also in the mechanical loss measurements.

The result from the corrected loss model is presented as loss torque in Figure 5.37 and as power losses in Figure 5.38. These results are obtained by multiplying the hysteresis coefficient, c_{hy} with a factor of 1.1 and the eddy current coefficient, c_{ec} with a factor of 4.9 according to (5.43). The constant $k_{m,Fe}$ is again defined according to 5.42.

$$T_{Loss,Fe}^{sim} = \left(1.1 \cdot c_{hy} \cdot B^{e_{hy}} + 4.9 \cdot c_{ec} \cdot B^2 \cdot f + c_{an} \cdot B^{1.5} \cdot \sqrt{f}\right) \cdot k_{m,Fe} \quad (5.43)$$

The inset plot in Figure 5.38 is a zoomed in view with focus on the speed range of the roll out test. Here it is seen that the corrected power losses follow the test result very well.

As can be seen, the resulting corrected no load loss model (consisting of combined mechanical and iron losses) reveals a dramatic increase in losses compared to the original prediction. The behaviour of the loss torque suggests that the difference mainly originates from inaccuracy in the estimation of the eddy current losses. In combination with what is found in the literature, the deviation should to a large extent be related to global eddy currents due

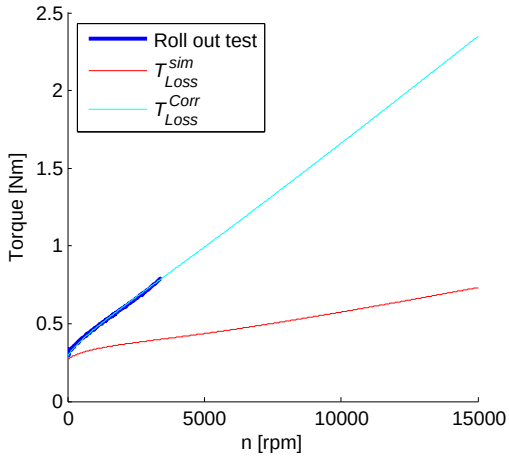

Figure 5.37: Loss torque as a function of speed from the roll out test together with original (T_{Loss}^{sim}) and corrected (T_{Loss}^{Corr}) loss torque with contributions from the mechanical losses and the iron core losses

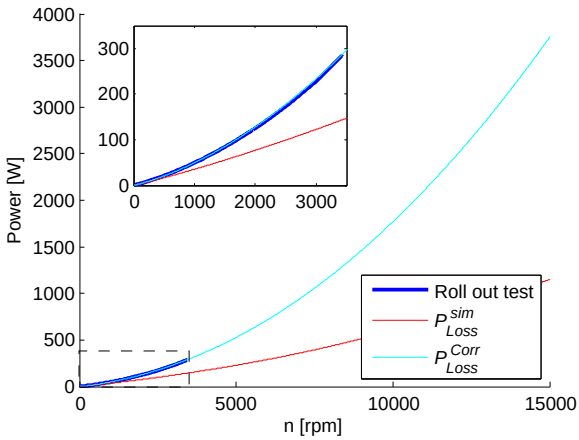

Figure 5.38: No load losses as function of speed from the roll out test together with total mechanical and iron core losses from the original (P_{Loss}^{sim}) and corrected (P_{Loss}^{Corr}) simulation model with zoomed in focus on the roll out test speed range in the inset plot

to the laser cutting. This could possibly be in combination with the welding seams on the stator back. Consequently the increased no load power losses are specified as being related to manufacturing of various origin and accounted for by a building factor. This is a similar approach as in e.g. [104].

Final remarks on the no load iron loss test As mentioned above, the results in Figurs 5.37 and 5.38 are obtained by adopting the iron loss coefficients c_{hy} and c_{ec} only, hence not the hysteresis exponent e_{hy}. One way to examine the hysteresis coefficient versus its exponent is to extract iron losses during loading conditions as that would alter the magnetic flux density. This is attempted in the following subsection. Another approach could perhaps be to do roll out tests at different magnet temperatures. This way, the reversible temperature coefficients in the magnets should have resulted in a different magnetic flux linkage and hence flux density in the stator core. This would on the other hand also require more knowledge on how the iron core is affected by increased temperature. Since this experiment has not been performed within the project, no more thoughts or considerations are made on this.

Iron losses at loading conditions

Tests are performed in an attempt to look further into how the iron losses relate to applied load and hence a varying flux density. Although the collected test data is too inconclusive to give a definitive outcome, the procedure and its results are still presented along with a discussion on the findings.

Load test bench set up The tests looking at iron losses with load applied on the machine are carried out in a back to back set up with a similarly rated machine as mechanical load. The back to back set up means that the electrical power generated when braking is fed back into the DC-side of the motoring supply. This way the electric power source only has to cover the losses in the system. A HBM T12/1kNm torque transducer with standard accuracy option [28] is mounted on the shaft connecting the two machines. The test set up limits the top speed to around 7000 rpm. This is a safety precaution due to resonance starting to occur on the intermediate shaft at higher speeds. This also indicates that there might be external dynamic loads acting on the torque transducer affecting the readings. The voltage on the DC-side is set to 600 V. The phase currents are recorded with MACC2plus sensors connected to a Yokogawa WT3000 power analyser. Specified accuracy of the sensors is 5 ppm of rated current plus 3.3 ppm of actual output. This corresponds to in total below 5 mA. Forced cooling is applied with approximately 60°C coolant inlet temperature at a total flow rate of around 9 l/min. This leads to a machine temperature measured with the internal sensors in the range 60-70°C. The sensor measuring the supposed hot spot in the windings is reaching maximum 90°C at some of the test points. Transformation from 3 phase currents to the dq-reference system is done with live math in the rig system. This means that the measured 3 phase currents are recalculated to dq quantities at each sample. Good current readings are ensured by considering the average of the data collected with a sample rate of 200kHz.

The machine is operated in current control using a SKAI 2 inverter from Semicron [29].

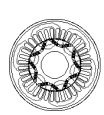

Currents are applied as a matrix in the second and third quadrant in the dq-reference frame. This means negative d-currents along with positive and negative q-currents. To limit saturation effects, the current is kept below 125 A in both d- and q-direction. The test is based on the assumption that the copper losses are unaffected by the direction of the current vector. Hence, the copper losses is constant as long as the length of the current vector is constant. In addition to this, it is assumed that the electromagnetic torque is not affected by the copper losses. This is valid as long as the machine is accurately operated in current control. Finally it is assumed that the electromagnetic torque is the same regardless of any changes in speed.

Based on the assumptions stated, the iron losses are derived by comparing the measured torque (T_{meas}) from the currents mirrored around the d-axis. Since the machine is operated in current control, the current is the same disregarding the copper losses. Any resistive voltage drop is compensated for by the current controller to keep the set current. As a result, the copper losses do not affect the current and according to the well known torque equation (5.46) for a PMSM, thus do not affect the electromagnetic torque. As the current control in the drive drifts slightly in applied currents, the torque and current is interpolated when post processing the test data. In this way the same current amplitude and angle offset in relation to the d-axle can be obtained in each of the two quadrants operated during the test.

The loss torque, T_{Loss} is obtained according to (5.44), where T^{+}_{meas} and T^{-}_{meas} are the interpolated measured torque on opposite sides of the d-axis.

$$\left|\frac{T^{+}_{meas} + T^{-}_{meas}}{2}\right| = \left|\frac{T_{em} - T_{Loss} - T_{em} - T_{Loss}}{2}\right| = T_{Loss} \tag{5.44}$$

The assumption is that the measured torque is a combination of the electromagnetic torque, T_{em} and the loss torque, T_{Loss} braking the machine due to mechanical losses and losses in the iron core. This is defined in (5.45).

$$T_{meas} = T_{em} - T_{Loss} \tag{5.45}$$

The electromagnetic torque is established from the current ($i_{d,q}$) and magnetic flux linkage ($\psi_{d,q}$) together with the number of poles (N_p) according to (5.46).

$$T_{em} = \frac{N_p}{2} \cdot \frac{3}{2} \left(i_q \cdot \psi_d - i_d \cdot \psi_q\right) \tag{5.46}$$

Here it is clear that the electromagnetic torque gets positive or negative depending on the polarity of i_q. That is, if the amplitude of i_q is constant, but the polarity is shifted, equally sized positive or negative torque is produced. It is however not necessary to solve (5.46) in this approach since the electromagnetic torque is cancelled when solving (5.44).

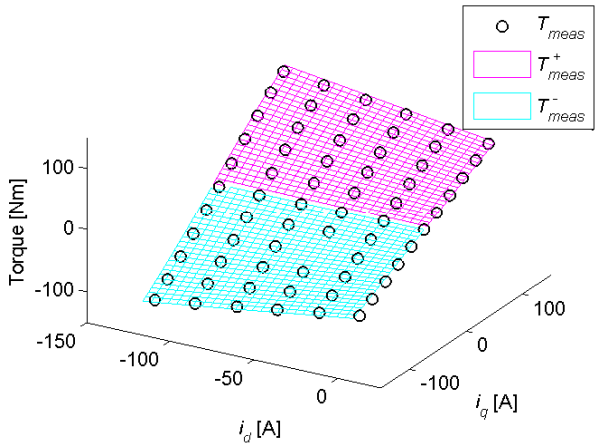

Figure 5.39: Measured and interpolated torque as functions of i_d and i_q at 2000 rpm

The test is commenced at three different speeds. This will keep track of the frequency dependency of the iron- and mechanical losses. The test data recording starts at 6000 rpm with currents in the second quadrant with positive i_q and hence positive torque. This is followed by 4000 rpm and 2000 rpm. Then the procedure is repeated in the same order in the third quadrant, hence with negative i_q and torque.

Load test result and analysis The measured torque readings (T_{meas}) at 2000 rpm are presented in Figure 5.39 along with the interpolated positive (T^+_{meas}) and negative (T^-_{meas}) torque as functions of i_d and i_q. Looking carefully in the plot it can be seen that the currents controlled by the drive do not follow the reference values perfectly. This indicates a less accurate current measurement internally in the drive unit. This should however not be an issue since the actual currents fed to the machine are measured by the external current sensors. This deviation between set and actual currents is therefore not investigated any further within this project. It should instead be considered a question for the current controller.

The interpolated positive and negative measured torque (T^+_{meas} and T^-_{meas}) are used to derive the loss torque T_{Loss} as previously defined in (5.44). The result is presented for 2000, 4000 and 6000 rpm as surfaces in Figure 5.40 and as contours in Figure 5.41.

Studying the trends in the measured loss torque, the result agrees with expectations from the theoretical expression describing the iron losses. First of all, higher rotational speed means higher iron core losses and hence higher loss torque. This is based on the increased frequency as already discussed previously in the no load subsection. As i_q is increased, the air gap flux is increased and hence presumably also the magnetic flux density (B) in the

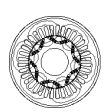

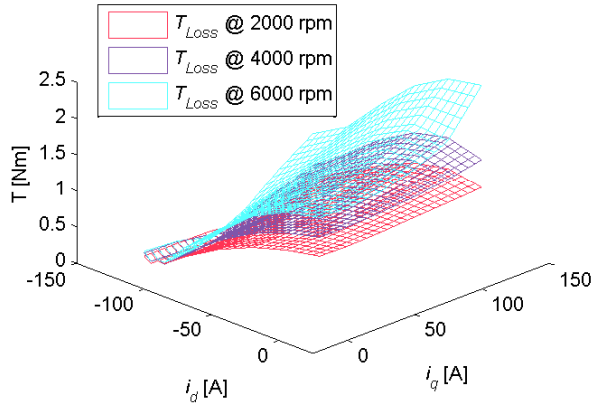

Figure 5.40: Loss torque T_{Loss} as a function of i_d and i_q at 2000 (lower surface), 4000 (middle surface) and 6000 rpm (upper surface) derived from measurements

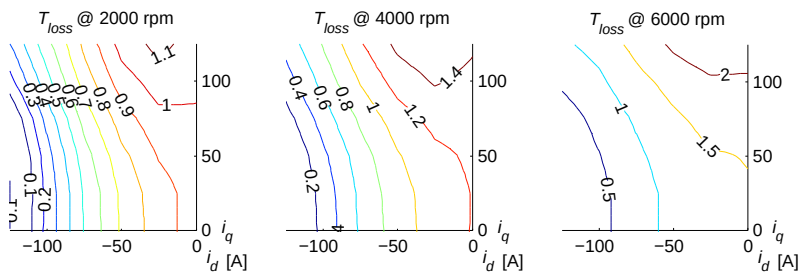

Figure 5.41: Loss torque contours at 2000 (left), 4000 (middle) and 6000 rpm (right) derived from measurements

iron core. This leads to higher losses and loss torque according to (5.29) and (5.41). This trend is observed when following the y-axis, representing i_q in the test results in Figure 5.40 and Figure 5.41.

Similarly, an increased field weakening current (negative i_d) reduces the air gap flux linking with the stator windings. With the assumption that this also means a reduction in magnetic flux density (B) in the iron core, the iron losses and loss torque should decrease as well (again according to the expressions in (5.29) or (5.41)). From Figure 5.40 and Figure 5.41, this is also the case in the measurements. With most of the contours being nearly perpendicular to the x-axis, the continuity when entering the third quadrant seems to be good as well. However, when looking more closely in the graphs, it is observed that the loss torque is reduced almost all the way down to zero as i_d is reaching approximately -120 A. This is first

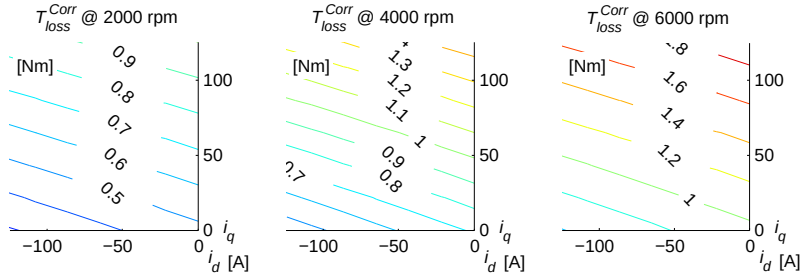

Figure 5.42: Loss torque as a function of i_d and i_q due to stator iron core losses from simulations with corrected hysteresis and eddy current coefficients at 2000 (left), 4000 (middle) and 6000 rpm (right)

of all not realistic as the mechanical losses are not affected by the field weakening current. In addition to this, the simulation result presented previously as stator yoke and teeth core losses in Figure 5.24 suggests that the losses reach their minimum when i_d is in the range of approximately -300 A. In order to facilitate the comparison with simulations, the simulation result is presented again in Figure 5.42. Here the losses in the yoke and teeth are added into total stator iron core losses and recalculated from power losses to loss torque. In addition to this, the iron core losses are estimated based on the revised or corrected hysteresis and eddy current coefficients, hence as presented in Figure 5.37 and Figure 5.38. The speeds as well as the scaling on the axis are also changed to the current levels and speeds used in the test set up. The temperature in the simulation set-up is also adjusted to match the 60°C measured during the tests.

When comparing the test results in Figure 5.41 with those from simulations in Figure 5.42 it is concluded that the absolute values do not match that well. The readings along the y-axis when i_d is zero seem to be in the right order of magnitude. Since the simulations are based on iron loss parameters calibrated with the roll out test, the simulations at no load (at origin in the plots in Figure 5.42) should be about correct. At the same time, since the drive is enabled (switching active) during this test sequence the losses can very well be higher in this test than during the roll out test. When moving along the x-axis the difference becomes much more evident. The data from measurements gets close to zero torque at i_d being approximately -120 A. When analysing the results a bit more thoroughly, it is however not possible to conclude whether it is the test results or the simulations (or both) that are incorrect.

The fact that the test data suggests reaching zero loss torque is a major reason for being suspicious about these results. In addition to this, the faster reduction in loss torque along the x-axis from the test compared to simulations is unexpected. Even if the fundamental

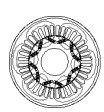

magnetic flux density is decreased, there will still be harmonics contributing to loss torque due to iron core losses. The flux density waveforms and harmonic content are studied by means of simulations in [105]. The effect of these harmonics are not included in the simulations so if anything, the loss torque from the measurements should be larger in the field weakening region. Furthermore, the field weakening should redirect some of the magnetic flux from the magnets along the airgap and tooth tips instead of through the stator teeth and yoke. Since the simplified simulation method used here only considers flux densities in the teeth and yoke (see Figure 5.21), any additional losses in the tooth tips are omitted. Operating a PMSM in field weakening at higher speeds should lead to higher eddy current losses in the core due to higher harmonic content [106]. All this being said, the location in the dq-load map at which the iron losses are at its minimum does not necessarily have to agree with the field weakening point. The minimum iron loss point could very well be shifted closer to origin, as seems to be the case in the measurements. The order of magnitude is however still not considered as realistic, leaving a question mark on the reliability of the readings.

A comparison of the loss torque with and without a connected and enabled drive with current references set to zero is presented in Figure 5.43. The difference in loss torque should

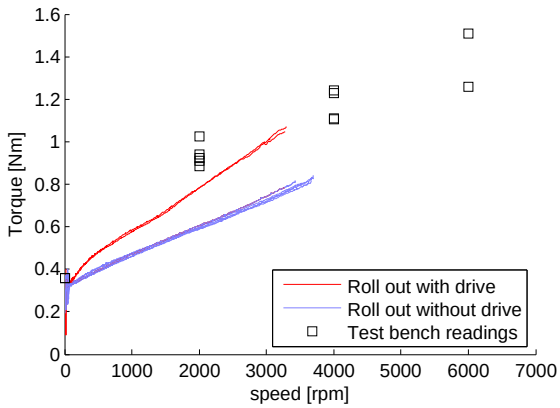

Figure 5.43: Loss torque from roll out tests with and without a drive connected and set to zero current along with torque transducer readings with a drive connected and set to zero

be a result of current ripple from the drive inducing additional losses in the stator iron core. The difference seen between the two roll out tests should therefore be an indication on the losses induced by high frequency components imposed by the drive. Included in the graph is also the torque transducer readings at measured zero current during the load test. The two test cases with the drive enabled is done at different test set-ups with different drives and DC-voltage. The mutual difference should therefore be related to both different switching frequency and applied DC-voltage. A higher DC-voltage means higher amplitude in the

current ripple and should therefore give higher losses, while the switching frequency influence the harmonic content. The stator core losses in the machine is hence to some extent affected by the drive it is connected to and the voltage level on the DC-side. Since the purpose with Figure 5.43 is to highlight that additional speed dependant losses can be induced by the drive, no deeper analysis is done on whether the results are comparable between the two drives. Instead it is again concluded that the readings from the test bench set-up are considered less reliable due to the relatively large uncertainty from the torque transducer.

Some attempts are made on compensating the on-load test results based on stated inaccuracies in the current sensors and torque transducer. Due to the relatively large degree of uncertainties in terms of the actual origin for the deviations, these results are not considered useful for continued analysis. Instead the analysis is limited to a discussion around different possible error sources, without implementing them in the test data processing. Since the torque readings on the opposite sides of the x-axis are used to derive the loss torque, the sensitivity of the torque transducer is crucial. Despite very good accuracy, the uncertainty u in the torque transducer is in the same range as the loss torque. Hence the actual version of the expression in (5.44) becomes as in (5.47) where u_p and u_n are the uncertainties of the measured positive and negative torque.

$$\left|\frac{T_{pos}+T_{neg}}{2}\right| = \left|\frac{T_{em}-T_{Loss}\pm u_p - T_{em}-T_{Loss}\pm u_n}{2}\right| = T_{Loss} \pm \frac{u_p}{2} \pm \frac{u_n}{2} \tag{5.47}$$

Things affecting the torque transducer uncertainties are as discussed previously in section 5.2 for example temperature variations, linear deviations, deviations due to different torque directions and any zero signal offset. As can be concluded from (5.47), those uncertainties acting in the same direction (having the same sign) on both positive and negative torque are transferred to and affect the resulting loss torque. Since the accuracy class indicates up to u <0.3 Nm, the influence on the result can be significant.

In addition to the torque transducer, the readings from the current sensors have a noticeable influence on the resulting loss torque. This is partly in terms of absolute values of the current vector, but even more in terms of current angle. As mentioned earlier in connection to Figure 5.39, there is an observed deviation between the current readings and the set values in the drive. Unfortunately, the internal current measurements in the drive were not recorded during the test in question. Some limited complementing tests when looking on both the current measured and communicated by the drive and the current measured by the test rig, show a deviation between these two. This deviation seems to be depending on both machine speed, current amplitude and torque direction. The exact behaviour and wherein the mismatch in current readings lies is however not pursued more within this project.

Since the transformation from measured currents in the three phases to the dq-coordinate system is also based on the rotor angle, this is yet another possible error source. The rotor angle is established by using the resolver signal. Hence the same angle readings are used both

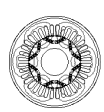

internally by the drive and for the dq-transformation of the externally measured currents. Based on the discussions previously in Chapter 4, a faulty current angle will have higher influence on the resulting torque when operating in the field weakening region. Since the result is obtained by comparing positive and negative torque, a deviation from the actual shaft torque can result in double impact on the loss torque when derived with (5.44). The machine temperature could also affect the test result. The internal temperature sensors in the machine all indicate around 5°C temperature difference between the recording of positive and negative torques. This was at the test considered small enough not to have a significant influence on the result.

The conclusion from the discussion above is that the deviating and inconclusive result to a large extent probably is a consequence from when the dq-currents are acquired. This could be either by the current sensors or from the dq-transformation, most likely in combination with a relatively high inaccuracy in the torque readings. This is based on the trend in the test result where a more unexpected behaviour is observed in the field weakening region. It is also to some extent confirmed by [107], where acquiring the torque and the power factor are judged to be the two most decisive contributors to uncertainties when performing measurements on an electric machine.

Alternative ways of determine loss torque from measurements In addition to comparing the positive and negative torque, two other methods for determining the loss torque T_{Loss} from the back to back measurements are tested as well.

The first alternative is to use the difference between electric power P_{el} and mechanical power P_{shaft} at the shaft and deduct the losses P_{Cu} in the windings. This method is therefore dependant on good knowledge of the winding resistance R_s. This is something that can be hard to obtain since both temperature and frequency affects the actual resistance. Things like harmonics content in the currents and uneven temperature distributions in the windings will hence affect the result. The loss torque is determined according to (5.48). This expression is valid for motoring. When power is generated, the signs on P_{el} and P_{shaft} should be shifted.

$$T_{Loss} = \left| \frac{P_{el} - P_{shaft} - P_{Cu}}{\omega_m} \right| \tag{5.48}$$

For the second alternative, T_{Loss} is established by comparing the measured torque T_{meas} with the electromagnetic torque T_{em}. The voltages are measured and transformed into u_d and u_q components. These are used to derive the magnetic flux ψ_d and ψ_q linking with the stator. Again the winding resistance is necessary as input for determining the linked magnetic flux. This can be seen in (5.49) and (5.50) where ω_e is the electrical angular frequency. Another complication with this method besides requiring accurate ways of acquiring the

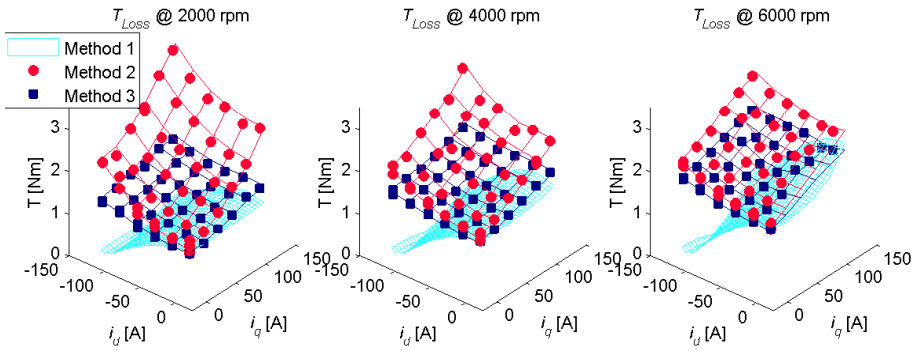

Figure 5.44: Comparison of three different means of deriving loss torque from measurements using (5.44) in Method 1, (5.48) in Method 2 and (5.51) in Method 3 at 2000 (left), 4000 (middle) and 6000 rpm (right)

resistance, is to get useful readings of the PWM-generated 3 phase voltages.

$$\psi_d = \frac{u_q - R_s \cdot i_q}{\omega_e} \tag{5.49}$$

$$\psi_q = \frac{R_s \cdot i_d - u_d}{\omega_e} \tag{5.50}$$

Once the linked magnetic flux is obtained, T_{em} is determined with the previously introduced expression in 5.46 and the loss torque with (5.45) solved for T_{Loss} according to (5.51).

$$T_{Loss} = |T_{meas} - T_{em}| \tag{5.51}$$

An advantage with both of these alternative methods is that the interpolation of the test data becomes obsolete. This is because there is no need to mirror the result around the x-axis. The loss torque as derived with (5.48) and (5.51) is presented as Method 2 and 3 respectively together with that derived by (5.44) in Figure 5.44. Here the stator resistance, R_s is estimated with consideration to the winding temperature but not the frequency. Hence DC-resistance is used rather than AC-resistance. The phase resistance is measured at room temperature. The temperature coefficient for copper together with temperature is used to estimate the resistance in each test point. The copper temperature is established by using the readings from the internal temperature sensor (sensor #1, S_{HS} in Table 2.2) mounted in the center of one of the slots.

The voltages needed in (5.49) and (5.50) are acquired by using the average of the readings sampled at 200 kHz during 1.2 s at steady state operation. That is, the dq-transformation is done on each sample in the raw data and the results averaged over 1.2 s are used as output.

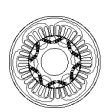

Looking in Figure 5.44 a distinguishable dispersion between the results is observed. As concluded previously, the first method (Method 1 in the plots) when using (5.44) yields unexpectedly small losses during field weakening. The data post processed with equation (5.48) (Method 2 in the plots) has a strange behaviour to speed. The test case at 2000 rpm shows higher losses than at 4000 and 6000 rpm. Looking closer, it is noticed that this is the case especially at higher currents. This opens for a possibility that the result is influenced by the estimated resistance. If the resistance would have been higher, the losses in the copper (P_{Cu}) would have been higher. Since the results in Figure 5.44 is presented as torque, higher copper losses would affect the result more at lower speeds. This is because the losses in the windings are divided by mechanical speed before presented here. An attempt to alter the resistance is done by doubling the resistance to see how it affects the result. This is presented further down in Figure 5.45 This makes the result more reasonable in terms of the speed dependence, but is still somewhat strange in other aspects.

The loss torque is still increased in the field weakening region, compared to at origin. This is something that contradicts with the expectations from the original simulations. But on the other hand, as mentioned earlier, the loss torque does not necessarily have to go down during field weakening even if the fundamental magnetic flux density does. No more effort is however put into sorting out these speculations on modifying the resistance.

The loss torque derived with (5.51) (Method 3 in the plots in Figure 5.44) shows a bit more reasonable behaviour. The torque is in the same range as with the post processing method first used and also with the simulations. The major difference is the behaviour seen in the field weakening region. Here the loss torque is increased as the airgap flux linkage is reduced. This is again contradicting with the simulations as well as the first results (Method 1). However, if field weakening leads to increased harmonics it might be leading to increased losses despite a reduction in the fundamental magnetic flux density in the iron core. A parenthesis to these results is that doubling the resistance in accordance to what was discussed when looking at the copper losses, instead makes the loss torque behave unexpectedly here. Hence altering the resistance affects the two methods (Method 2 and Method 3 in Figure 5.44) in different ways. This can be observed in Figure 5.45 where the results are obtained with twice the stator resistance. The fact that the three different methods give such diverging results combined with the known limitations in the simulation model makes it difficult to draw consistent conclusions on the load dependency of the iron losses from the measurements performed and presented here. This is especially the case when operating in the field weakening region.

5.3.6 Revised iron core losses based on the measurements

The stator iron core losses determined with (5.43) where the hysteresis and eddy current terms are revised based on the roll out test, is presented as function of torque and speed in

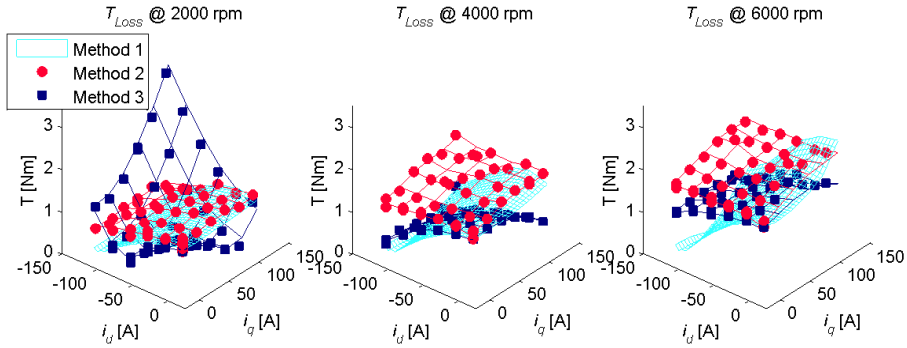

Figure 5.45: Comparison of three different means of deriving loss torque from measurements using (5.44) in Method 1, (5.48) in Method 2 and (5.51) in Method 3 at 2000 (left), 4000 (middle) and 6000 rpm (right) with modified (doubled) stator resistance

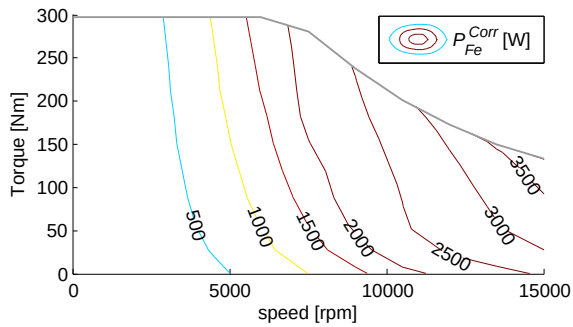

Figure 5.46: Estimated stator core power losses, P_{Fe}^{Corr} based on the corrected iron loss parameters as function of torque and speed utilizing MTPA

Figure 5.46. As previously, the result is obtained by utilizing MTPA as control strategy. The result here should be compared to that presented previously in Figure 5.25. As already noted, the losses in the iron core are significantly increased compared to the original estimations.

The iron loss parameters could perhaps be tuned further based on the result of the on-load testing. The large uncertainties following these results make this analysis less valid and is therefore not put into use. If this would not have been the case, the relation between the hysteresis coefficient (c_{hy}) and exponent (e_{hy}) could possibly be adjusted a bit more. Also the contribution from the anomalous losses in relation to the classical eddy currents should perhaps be possible to include in the post-measurement analysis. The result can then be expected to be a somewhat different relation to magnetic flux density, hence torque in Figure 5.46. Due to the difficulties in getting adequate results from the test, no effort is directed towards that at this time.

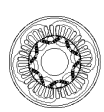

5.3.7 Concluding remarks on the iron core losses

In order to accurately predict the iron losses, a lot of information is required on the material as well as on the geometry and manufacturing technique. A lot of this information is hard to obtain even if the prototype is manufactured, not to mention during the design phase. This could for example be how the laminations are manufactured, whether the cutting tool is new or almost worn out. Or in the case of laser cutting (as in the prototype studied here) how the manufacturing settings are set and kept during production. Also any presence of global eddy current loops due to short circuits at the lamination edges is hard to detect in advance.

In addition to this, the drive used to control the machine will have an effect on the iron losses. The adaptation of the iron losses is based on the roll out test results, hence at no load and with no drive connected. It would perhaps be more just to base the iron loss parameter correction on the the roll out test with a drive connected. Or even better, based on the on-load test. All in all, the output from the simulations in terms of iron loss prediction should be considered as indications rather than facts. Hence, how a machine in a larger population statistically can be expected to behave.

It is also concluded that the rather blunt method originally used to estimate the iron losses gives a comparable result to when it is estimated based on the rate of flux density change in each element in the simulation model. This is despite a presumably more accurate consideration of the magnetic flux density variations and distribution. At least this seems to be the case for the prototype machine with laser cut laminations. The case of a more serial production like manufacturing with stamped laminations has not been investigated here. Expectations from the literature, e.g. [81–83] is however that the simulation results should be closer to the test data if measurements are done on a machine produced in serial production.

In the other end of the scale where the machine is built and tested, additional uncertainties are introduced. As the iron losses are such a small part of the measured values, even equipment with high accuracy can give scattered results. Again, statistics are important to consider. If not by performing measurements on multiple machines, this should be done at least by repeating the tests several times with as similar pre-conditions as possible. This is not always easy if the test method is time consuming.

The final concluding remark based on the aspects mentioned above, is the importance of knowing the limitations in estimating the iron losses in a PMSM. The prevalent simulation model is easy to implement rather than accurate. At the same time, there is a risk that measurements on a prototype are misleading as well. The results should instead be used as indications rather than predictions. For example to compare different designs to each other. More important than acquiring a correct prediction is to know what aspects are

acting negatively on the iron losses and how to avoid them.

5.4 Rotor losses

For the sake of a simplified design routine, the estimation of rotor core losses is neglected during the design phase. Since the rotor is rotating synchronously with the fundamental frequency in the stator, the major part of the magnetic flux in the rotor is constant. The same simplification is also applied to the permanent magnets. The magnetic flux density ripple still present comes from the space harmonics imposed by e.g. saturation effects and the interaction with the stator teeth, in combination with time harmonics originating from the waveforms of the electrical signals [45].

The way for taking the losses in the rotor iron core and permanent magnets into account is to use the same approach as for the iron core in the stator. Hence the amplitude and frequency, or alternatively the change rate $\frac{dB}{dt}$ of the flux variation are used to solve e.g. (5.29) or (5.36) – (5.38). In the prototype studied in this work, the rotor core shares the same material as the stator core. Using a high performing material in the rotor can be seen as superfluous since the losses are much lower than in the stator. This is however common practice when the stator lamination is manufactured in one piece. The material left inside the stator ID can just as well be used for the rotor. For machines built up by segmented stators a different steel grade can be used for the rotor. This could for example open up for a less expensive material, or a material with improved mechanical integrity to allow for higher rotational speeds [108]. Since the prototype studied here has the same material in the rotor and stator iron core, the parameters introduced in Table 5.1 can be re-used for the rotor core. The core loss model for rotor core also needs to take into account the field bias from the magnets.

The electric conductivity and relevant geometrical dimensions of the permanent magnets are used for estimating the magnet losses. Simulations performed in [109] indicate that a coarse axial segmentation is sufficient to reduce the magnet losses significantly. This is also supported by [110] where it is found effective to just partially segment the surface mounted magnets. The same paper also states that the eddy current density in the rotor decreases exponentially with distance from the airgap. For the interior permanent magnet machine with laminated electrical steel closest to the airgap, this should mean even lower losses in the magnets. The axial segmentation of the magnets in the prototype is therefore chosen in order to facilitate manufacturing rather than with consideration to the magnet losses [1].

The rotor losses are investigated at four different load cases according to Table 5.2. This means a square in the dq reference frame. The first load case is roughly representing the field weakening point. The second load case is at no load. The third case is in close connection

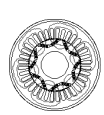

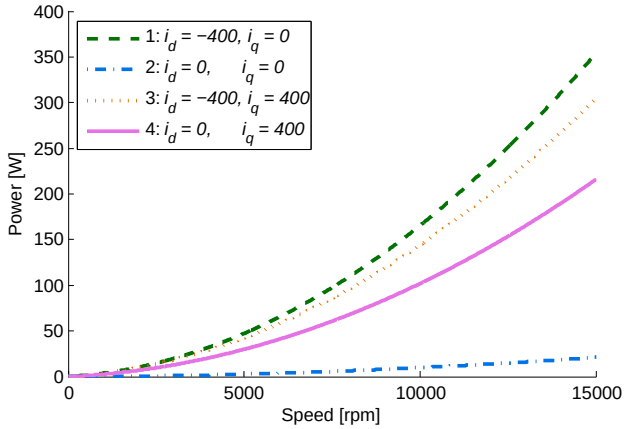

Figure 5.47: Rotor iron core power losses due to eddy current and hysteresis losses estimated from Ansys Maxwell 2D FE-simulations at four different load cases

with the maximum peak torque operation point. The forth case is in principle outside the normal operating region but is included as information.

Table 5.2: Definition of load cases when investigating the rotor losses

Load case	i_d [A]	i_q [A]	
1:	-400	0	*Short circuit*
2:	0	0	*Idling*
3:	-400	400	
4:	0	400	

The power losses in the rotor iron core estimated based on (5.36) – (5.38) being solved in Ansys Maxwell [96] 2D FE-simulations are presented in Figure 5.47. With no information availible on the loss coefficients (c_{hy} and c_{ec}) for the magnets, the PM power losses are instead estimated based on the electric conductivity and by considering the magnets as axially conducting rods in the rotor [105]. In combination with the B-field acting on the magnets, this gives induced eddy currents internally in the magnets. The resulting power losses in the magnets are presented in Figure 5.48. Here it should be noted that the losses in the magnets are estimated based on non segmented magnets, i.e., with magnets as long as the active length of the rotor. Since no end effects are included in the estimation of the eddy current losses, it is questionable whether 2D-simulations on a shorter machine (with the length of one magnet) would give an adequate result. If the rod becomes as long as it is wide, the neglected end effects should most likely have too much impact on the result.

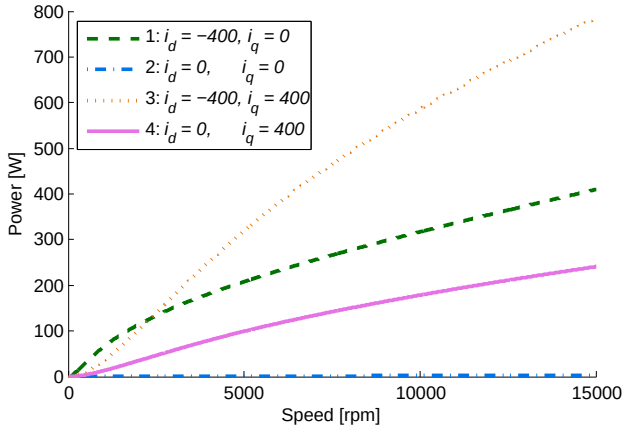

Figure 5.48: Induced eddy current power losses in 224 mm long magnets estimated from Ansys Maxwell 2D FE-simulations at four different load cases

As can be seen in Figure 5.47, the losses in the rotor iron core go up to around 350 W at top speed. It is also considerably higher during load compared to at no load. As the difference between load case 1 (lower left in the dq-map) and load case 3 (upper left in the dq-map) is small, the losses should be roughly the same as field weakening commences. This is provided that the relation between the four load cases are reasonably linear. This is however not investigated in this study. The result is instead used as indications on the order of magnitude of the losses in the rotor iron core

The seemingly high losses indicated by the results in Figure 5.48 are to a large extent misleading, partly since load case 3 (represented by the curve reaching up to almost 800 W at 15000 rpm) is not used above base speed. As the speed exceeds the base speed, the losses are gradually better represented by the curve related to load case 1. Hence with the prerequisites valid for Figure 5.48, the losses can be expected to be limited to around 400 W in accordance with load case 1. Even more significant to the result is that the simulations are done on non-segmented magnets. As the prototype holds 14 smaller magnets along the active length, the losses in the magnets should be considerably smaller. How much is not studied any deeper at this time. Instead the results presented in [109] are used to provide some indications. These results suggest a reduction in magnet losses with around 40% and 70% when the magnets are segmented into 4 and 8 pieces respectively. A coarse extrapolation of these results indicates a reduction of 80-85% or around 6 times, when using 14 segments. For the prototype studied here, this indicates losses in the permanent magnets staying well below 100 W in all possible operating points.

In combination with the rotor core losses, the total combined losses in the rotor iron core and permanent magnets are estimated to reach around 420 W during peak power operation

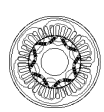

at top speed. Peak torque operation around base speed results in rotor losses of around 100 W. The uncertainties associated with these numbers are however limit the results to indications, rather than accurate predictions.

The indication from [111] is that the analytical approach to estimate the eddy current losses in the rotor magnets holds a limited accuracy compared to complete 3D electromagnetic FEM simulations. The study presented in [70] also indicates that the losses in the rotor can be significantly higher than predicted in ideal FE-simulations. This is due to the time harmonics introduced by the switching frequency and the DC-link voltage. Figures showing the loss distribution however indicates that the increased rotor losses are concentrated close to the airgap. Since that study is done on surface mounted magnets, the result is not directly transferable to the IPMSM design studied in this project. The laminated rotor core close to the airgap is better suited to limit the effect of the harmonics compared to the more coarsely segmented magnets.

An important reason for why the rotor losses need to be considered despite being comparably small, is the limitation in heat dissipation usually seen in the rotor. The way the oil cooling is implemented in the prototype studied here (introduced in section 2.2.2) however makes this issue less relevant. As one of the two oil circuits are passing through the rotor before being sprayed onto the windings, the heat generated in the rotor is removed, thus keeping the PM temperature down. Similar results are presented in [112]. It is also noticed in one of the continuous operation tests mentioned briefly in section 2.3. As the cooling circuit passing through the rotor is turned off, the PM temperature (estimated from induced voltage) is elevated with 20-30°C.

Since the intended normal condition for the machine under investigation is with coolant passing through the rotor, no more focus is directed towards the rotor losses. The heat arising in the rotor iron core and permanent magnets is handled and is hence not an issue when running the machine.

5.5 Winding losses

The losses in the windings consist of resistive DC-losses as well as AC-losses. The AC-losses are related to eddy currents due to proximity effects. This is a result of self flux leakage when alternating currents flow in the conductors, in combination with external flux leaking from the stator core, typically close to the air-gap [113–115]. At a certain ratio between frequency and conductor diameter, skin effects due to self inductance can occur as well.

The copper losses originally considered in this project are those related to the resistive DC copper losses. In addition to this, the AC-losses are investigated theoretically with consideration to proximity effects and by considering the skin depth.

5.5.1 DC copper losses

The DC copper losses in the stator windings are determined by looking at the resistive losses in the conductors. The DC-resistance, $R_{s,DC}$ is determined with (5.52) where ρ_{Cu} is the resistivity of copper and l_{cond} and A_{cond} are the total length and cross sectional area of the conductor respectively. The geometrical parameters are determined based on input from the FE-environment. The length is a combination of the active length l_{active} and end winding length l_{EW}, where the latter is estimated based on the distance between the relevant slots. The conductor area is the slot area A_{slot} times the copper fill factor k_{fill}. As the prototype is being built and the wire diameter and number of wires in each bundle is known, k_{fill} is adjusted accordingly. The resistance is also verified with measurements on each phase on the prototype machine at room temperature.

$$R_{s,DC} = \rho_{Cu} \cdot \frac{l_{cond}}{A_{cond}} = \rho_{Cu} \cdot \frac{l_{active} + l_{EW}}{A_{slot} \cdot k_{fill}} \tag{5.52}$$

The resistivity is temperature dependant according to (5.53) where tc_{Cu} is the temperature coefficient of copper and $\Delta\vartheta$ is the temperature difference to room temperature.

$$\rho_{Cu} = \rho_{Cu\{20°C\}} \cdot (1 + tc_{Cu} \cdot \Delta\vartheta) \tag{5.53}$$

In the simulations, the winding temperature is defined as a temperature difference to the permanent magnet temperature. The permanent magnet temperature is in turn defined when setting up the FE-simulations (see Chapter 3). When analysing the prototype the average copper temperature is assumed to be 20°C higher than the permanent magnet temperature. This is based on heat flow FE-simulations in [1] giving the preliminary heat distribution within the machine at an assumed continuous current density (presented in Figure 2.5). This is eventually also confirmed to be roughly adequate when performing measurements on the prototype.

The DC copper losses, P_{Cu}^{DC} are determined in the dq-reference frame according to (5.54) where i_d and i_q are the magnetizing and torque producing currents, respectively. Here, the dq-components are derived with power invariant transformation (see Appendix A).

$$P_{Cu}^{DC} = R_{s,DC} \cdot I_{rms}^2 = R_{s,DC} \cdot \left(i_d^2 + i_q^2\right) \tag{5.54}$$

The copper losses based on the DC-resistance at 130°C when utilizing MTPA in the control are presented in the torque speed map in Figure 5.49. Note that the losses here are presented in kW. As the DC-resistance has no speed dependency, the copper losses are constant for a given torque below base speed. As the machine reaches voltage limitation and field weakening starts, the copper losses are increased for the same torque. This is because the control leaves the MTPA and increase negative i_d to the expense of the torque producing i_q. Hence the current needed to produce the same torque is increased which consequently leads to higher copper losses.

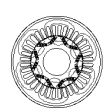

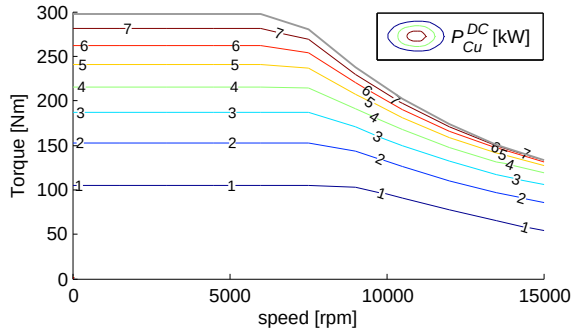

Figure 5.49: Estimated copper power losses, P_{Cu}^{DC} based on the DC-resistance at 130°C in the stator windings as function of torque and speed utilizing MTPA

5.5.2 AC copper losses

Estimating the resistance becomes more challenging when taking the AC-losses into account. The analysis is done on skin effects and proximity losses due to leakage inductance from the stator core. When relevant, the additional losses are added to the copper losses established based on the DC-resistance. Proximity losses due to self flux leakage is not included in the analysis done here.

Skin effect

The skin effect is a phenomenon caused by alternating currents creating a changing magnetic field which in turn generates opposing eddy currents. This results in that the center of the conductor can no longer be used to transport the current. Instead the current gets more concentrated around the periphery. The result is a reduced effective conductor area, hence increased resistance. The skin depth δ is established from the permeability μ and conductivity σ of the conductor together with the frequency f according to (5.55) [50, pg.209]. With copper being considered a non-magnetic material, the permeability of free space ($\mu_0 = 4\pi \cdot 10^{-7}$) can be used.

$$\delta = \frac{1}{\sqrt{\pi \cdot \mu \cdot \sigma \cdot f}} \tag{5.55}$$

A thicker skin depth means a longer distance into the conductor before the opposing eddy currents occur, hence is better from a conducting point of view. As can be noticed, the conductivity has a reverse relation to the skin depth, meaning that reduced conductivity leads to a thicker skin depth. This means that the skin effect in copper is reduced with increased temperature (compare to the resistivity in (5.53)). When solving(5.55) with relevant numbers for copper, the skin depth becomes around 2 mm at 1000 Hz. Lower frequency

means larger skin depth. With a wire diameter of 0.85 mm and a fundamental frequency of 750 Hz at maximum speed, the skin effect will not have any significant influence on the copper losses in the prototype. Also for the harmonics at higher frequencies, the increase in losses due to skin effects is negligible. In [116] a unitless parameter, X is defined as in (5.56) and used to evaluate the skin effect. Here, r is the conductor radius. The results presented from the FE-analysis confirms that the skin effect is negligible below a value of X =0.5.

$$X = \frac{r}{\delta} = \sqrt{f} \cdot r \cdot \sqrt{\pi \cdot \mu \cdot \sigma} \tag{5.56}$$

For the machine under investigation in this project, X is equal to 0.35 at maximum fundamental frequency (750 Hz at 15000 rpm). Meanwhile, 1% and 10% increase in impedance is reached approximately at X =0.7 and X =1.5 respectively. This corresponds to around 3 kHz and over 13 kHz respectively in the machine in question. The skin effects in the 0.85 mm diameter strands are therefore not considered any further in this analysis.

Proximity effects

The proximity effects in the windings are caused by magnetic fields affecting the conductors. This generates eddy currents in the same way as described previously for the iron core. The magnetic fields acting on the windings originate both externally through leakage from the surroundings and internally from the alternating currents in the neighbouring conductors [113–115]. The external fields in the PM machine originate both from the rotor magnets and from the stator armature field. Besides keeping the windings in place, the tooth tips also prevent the PM flux from reaching the windings. At the same time, a small airgap in an otherwise enclosed high permeability material leads to enhanced field near that airgap, which potentailly can give increased proximity losses [117]. In [118] it is shown that a homogenized approach can be used to approximate the proximity losses as long as the unitless parameter X (in (5.56)) is below 0.5. The homogenized approach means that the magnetic flux acting on the bundled wires are modelled as homogeneous, hence acting in one direction without being affected by the internal fields from the current running in the conductors. This is exemplified in Figure 5.50 where the magnetic flux B_{leak} leaking from the stator is drawn as homogeneous and evenly distributed.

This approach of a homogeneous field is used when investigating the proximity losses in the machine under investigation here. This work has been done based on the work in [119]. The derivation of the relevant equations is reproduced and explained more in detail in Appendix C. The study starts with the fundamental Maxwell-Faraday equation, here expressed as (5.57) [50, pg.208] with $\mathbf{E}$ and $\mathbf{B}$ as the electric and magnetic field vectors.

$$\nabla \times \mathbf{E} = -\frac{\partial \mathbf{B}}{\partial t} \tag{5.57}$$

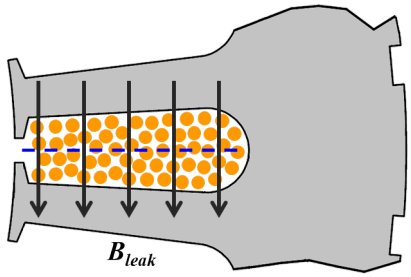

Figure 5.50: Homogeneously distributed magnetic flux (B_{leak}) leaking from the stator core through the windings

Since the diameter of the individual conductors in the bundle of wires is relatively small, it is assumed that the field passing through is unidirectional. Another assumption is that the current is evenly distributed in all wires within the slot. This should be fairly correct as long as there is transposition of the strands. This means that the exact location of each individual strand is different in the different slots as it passes through the machine. That should essentially be true for the prototype machine as all coils within each phase are connected in series. Further on, it is also assumed that the magnetic flux density varies sinusoidally and is evenly distributed, or uniform within the slot. With these assumptions, $\mathbf{B}$ within the slot can be expressed by the peak flux density, B_{peak} as a function of time, t and electrical angular frequency, ω_e as in (5.58).

$$\mathbf{B} = B_{peak} \cdot \sin(\omega_e t)\, \hat{y} \tag{5.58}$$

Here, $\hat{y}$ defines the direction of the magnetic field. Since it is unidirectional no $\hat{x}$ or $\hat{z}$ representing x- or z-components are needed. Solving (5.57) for the expression in (5.58), the electric field becomes as in (5.59).

$$\mathbf{E} = B_{peak} \cdot \omega_e \cdot x \cdot \cos(\omega_e t)\, \hat{z} \tag{5.59}$$

The power losses in a conductor due to resistance, R and current, i can be developed to instead consider resistivity, ρ and current density $\mathcal{J}$. With the conductivity σ being the resistivity inverse and current density being the conductivity multiplied by the electric field E in accordance with Ohm's law, the power loss due to an electric field becomes as in (5.60).

$$P = R \cdot i^2 = \rho \cdot \mathcal{J}^2 = \sigma \cdot E^2 \tag{5.60}$$

The losses in a round wire with radius r_{wire} due to the external magnetic field is obtained by integrating $\sigma \cdot E^2$ over a quarter of a circle and multiply by 4. Since it is the average power loss that is interesting, the squared cosine term can be replaced with a factor $1/2$.

This is done in (5.61).

$$P_{wire}^{avg} = 4 \cdot \sigma \cdot B_{peak}^2 \cdot \omega_e^2 \cdot \frac{1}{2} \int_{x=0}^{r_{wire}} \int_{y=0}^{\sqrt{r_{wire}^2 - x^2}} x^2 dy\, dx \tag{5.61}$$

When solving the integration in (5.61), the average power loss per unit conductor length in one conductor becomes as in (5.62).

$$P_{wire}^{avg} = \frac{1}{2} \cdot \sigma \cdot B_{peak}^2 \cdot \omega_e^2 \cdot \frac{\pi}{4} \cdot r_{wire}^4 \tag{5.62}$$

From (5.62) it can be concluded that the proximity losses depend on a square relation to the electrical angular frequency as well as the magnetic flux density passing through the wires. For electric machines, this means high speeds and typically large field weakening currents. This is because it suppresses the flux density in the teeth, making a larger part to find other paths. In the torque speed map of an electric machine, maximum influence on the losses should be seen when operating at high power and speed. Similarly to the skin effect, reduced conductivity means lower losses. Hence, as the temperature is increased, the proximity losses are reduced.

When reflecting a bit more on the expression in (5.62), the similarity to the equation used for proximity losses in [116] is evident. The difference except for the factor of $1/2$ due to the usage of peak flux density (as in (5.62)) instead of rms values (as in [116]), is a function of the previously used dimension less number X (defined earlier in (5.56)). This is to include what happens at higher frequencies. For X <0.5, this additional function included in [116] is equal to 1.

In order to get an estimation of the total proximity losses P_{Cu}^{prox} in the machine, the expression in (5.62) needs to be multiplied by the length of the conductors. Since the end windings are unaffected by the proximity effects due to slot leakage field [70, 120], the total length considered for the proximity losses, l_{prox} is the active length l_a multiplied by the number of conductors N_c in a slot and number of slots N_s in the machine according to (5.63). The number of conductors is the number of turns multiplied by the number of parallel strands in the wire bundle.

$$l_{prox} = l_a \cdot N_c \cdot N_s \tag{5.63}$$

This gives the total average proximity losses, P_{Cu}^{prox} in the entire machine with (5.64) where r_{wire} is the radius of a single strand.

$$P_{Cu}^{prox} = \frac{1}{2} \cdot \sigma \cdot B_{peak}^2 \cdot \omega_e^2 \cdot \frac{\pi}{4} \cdot r_{wire}^4 \cdot l_{prox} \tag{5.64}$$

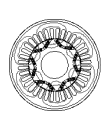

The flux density B_{peak} needed to solve (5.64) is established from FE-simulations with currents applied in the dq-reference frame (i_d from -500 to 0 and i_q from 0 to 500 in steps of 100 A). This is done by considering the integral of the square of the normal magnetic flux density along a line running from top to base in the middle of the slot (dashed line in Figure 5.50). This applies for the condition of the flux being equally distributed over the slot width, which of course not always is the case. Nevertheless, since the purpose of this study is to investigate the proximity losses, no more effort put on acquiring more accurate data. The peak magnetic flux density at each dq-current combination is determined by monitoring the average squared flux density in the slots for a number of different rotor positions. Repeating the procedure for a number of different temperatures indicates a marginal difference in B_{peak} only.

An alternative way to estimate the proximity losses would be to consider the flux density change instead of estimating the flux density as sinusoidal. In that case, the term $B_{peak}^2 \cdot \omega_e^2$ in (5.64) should be replaced by $\left(\frac{\partial B}{\partial t}\right)^2$. This requires a more accurate way to determine the flux density than just described. One way can be to again utilize the Maxwell-Faraday equation (expressed in (5.57)) and instead look at the electric field. Since the purpose of investigating the proximity losses here is to study the influence rather than absolute values, no more work is done on this alternative method.

The proximity losses determined with (5.64) are presented as a function of machine torque and speed in Figure 5.51. Note that the losses here are presented in W. Beside the assumptions stated above, the torque speed map is derived with MTPA and 130°C winding temperature. This is considered as average temperature during operation. With lower temperature, the conductivity is increased leading to higher proximity losses. It is also worth noticing that this is with the assumption that there are no circulating currents in the parallel strands in the wire bundle. Looking in the plot it is possible to confirm the predicted behaviour of proximity losses mainly impacting when operating at high power and high speeds. The temperature dependency is also mainly affecting that same operating region. At room temperature, the simulation model suggests reaching up to around 400 W as maximum at peak power and top speed. Looking at the rest of the torque speed map, the difference due to temperature is insignificantly small.

With the simulation model it is also possible to estimate the impact of changing the wire diameter. With double copper area in each strand and half the number of strands per wire bundle (to keep the same total copper area in each slot), the proximity losses are approximately doubled as well. The strand diameter is investigated also in [121], where a similar conclusion is reached. Increasing the strand diameter gives higher AC-losses in the windings.

Despite the assumptions made while deriving the proximity losses, the result is considered useful to indicate the approximate level and behaviour of proximity losses. Although it

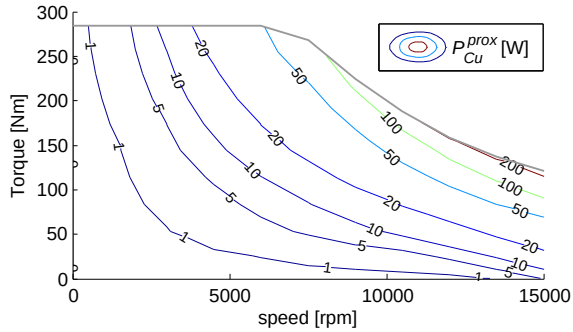

Figure 5.51: Estimated proximity losses, P_{Cu}^{prox} at 130°C in the stator windings as a function of torque and speed utilizing MTPA

is important to bare in mind that the uncertainty on the absolute values should be rather large, it is still possible to conclude that the impact is marginal on the overall copper losses in the prototype machine. Compared to the DC-losses, the proximity effect due to external magnetic flux leakage is close to negligible.

Something not considered in this analysis is the influence of the PWM-switching on the proximity losses, which might be visible already in Figure 5.43. Results presented in [122] indicate around twice the proximity losses with harmonics from the switching frequency superimposed on the applied fundamental phase currents, compared to if the fundamental current is applied only. Since the analytical evaluation on the proximity losses in the prototype indicates a marginal order of magnitude compared to the total copper losses, the part related to the switching frequency is not investigated further.

Another aspect, not investigated here is whether there are circulating currents in the windings. This could occur if the bundles of paralell strands in the wire are not twisted within the slot nor are displaced in the other slots connected in series. This means that the individual strands have approximately the same routing in all slots. This is the case in the study performed and presented in [70]. As magnetic flux leaks through the slot, electric fields are created. These fields generate opposing currents circulating through the conductors on each side of the stray flux (closer to the slot opening and closer to the stator back). This results in current imbalance, hence increased current in a number of strands and reduced current in others. Consequently this leads to increased losses in the windings.

A way to counteract the circulating currents is to introduce transposition of the conductors, hence to twist the wire bundles when winding the machine [77]. The effectiveness of this has been shown e.g. in [123], where the proximity losses are significantly reduced as transposition is implemented. Also a mutual displacement of the strands between different slots connected in series acts as countermeasure against circulating currents [124].

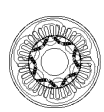

The impact on the winding losses due to any circulating currents in the prototype machine design is studied by simulations in [105]. The result indicates increased winding losses at base speed with a factor of 2 and 1.56 for currents applied in d and q direction respectively. This is with the precondition that no twisting or displacement of the strands is present. The uneven distribution is due to that current in d counteracts the PM flux from the rotor. This makes a larger proportion of the flux to leak through the slots.

The actual presence of this kind of rotating currents in the physical prototype is not investigated thoroughly. It is instead noted that all coils in each phase are connected in series. Hence the strands in the prototype are passing through the entire stator. This allows for some kind of stochastic distribution to be assumed and hence improved conditions for preventing current imbalance. This being said, there is still a possibility that the losses are affected to some extent. This is probably not as much as indicated in the simulations, but presumably more than nothing. How much is however not established within this analysis.

5.5.3 Copper losses from measurements

The copper losses are also verified by measurements on the prototype. The machine is mounted in the same back to back set-up as described earlier in section 5.3.5. The winding temperature is around 120°C (according to sensor #1, S_{HS} in Table 2.2) throughout the entire test. The rig-motor is controlled to 10 rpm, corresponding to 0.5 Hz in the 6 pole machine. The torque is controlled with MTPA and set torque is altered in steps up to peak torque. At this speed, the contribution from the iron losses as well as mechancial losses are assumed to be negligible. The power loss is derived by simply considering the difference between mechanical power at the shaft and electric power fed into the machine. The electric power is established with a Yokogawa WT3000 power analyser and mechanical power is obtained from torque measured with a HBM T12/1kNm torque transducer [28]. The resulting copper losses as a function of applied torque from measurements and simulations are presented in Figure 5.52. The match is seen as an indication that the simulation model, in which the DC-losses are dominating, is a good approximation of the case in the actual machine. It should be noted that the effects of circulating currents in terms of increased AC-resistance are according to [70] not visible at such low frequencies. The influence of the PWM switching should according to [122] be detectable also below base speed. There are however no results presented for speeds as low as 10 rpm. At these speeds it is assumed that the current controller can keep the set currents close to reference.

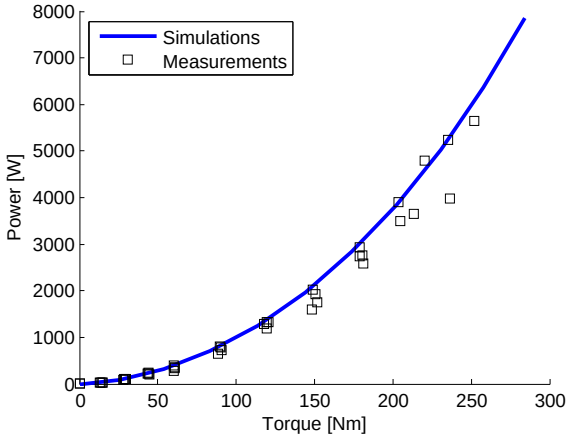

Figure 5.52: Copper power losses as a function of torque with MTPA-control from simulations and measurements on a warm machine with 120°C winding temperature at 10 rpm

5.6 Loss mapping summary and over all concluding remarks

The loss analysis chapter is summarized by looking at the combined losses from simulations compared to the measurements on the prototype machine. The results are also concluded in terms of where to put the effort when trying to predict the losses based on simulations and analytical models. The expectations on the accuracy in the machine loss predictions are discussed briefly, too.

5.6.1 Total losses from simulations

The losses derived throughout this chapter are combined into a loss map as a function of torque and speed in Figure 5.53 and as a function of power and speed in Figure 5.54. Included are the mechanical losses (P_{mech}) due to windage and friction from section 5.2, the revised iron core losses (P_{Fe}^{Corr}) from section 5.3, the rotor losses (P_{rotor}) from section 5.4 and the total combined DC- and proximity copper losses (P_{Cu}) considered in section 5.5. Maximum available DC-voltage in the simulations from which these loss maps are obtained is set to 600 V.

The losses in Figure 5.53 are used to derive the efficiency η according to (5.65). Here P_{in} is the power fed into the machine from the drive, P_{out} is the mechanical power on the shaft and P_{em} is the electromagnetic power that produces torque. The resulting efficiency map

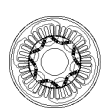

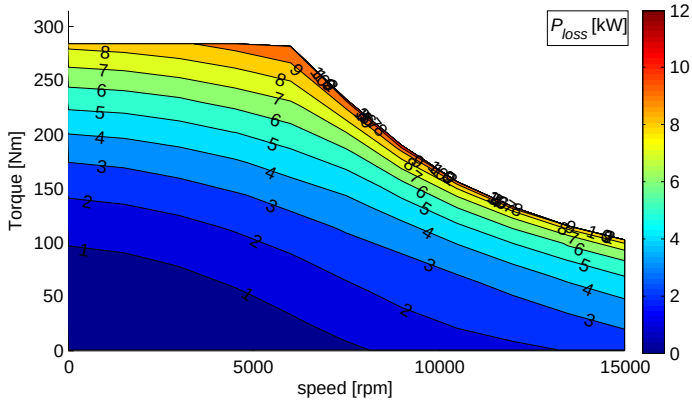

Figure 5.53: Total power losses, P_{loss} as a function of torque and speed from simulations on a warm machine with 100°C PM and 130°C winding temperature

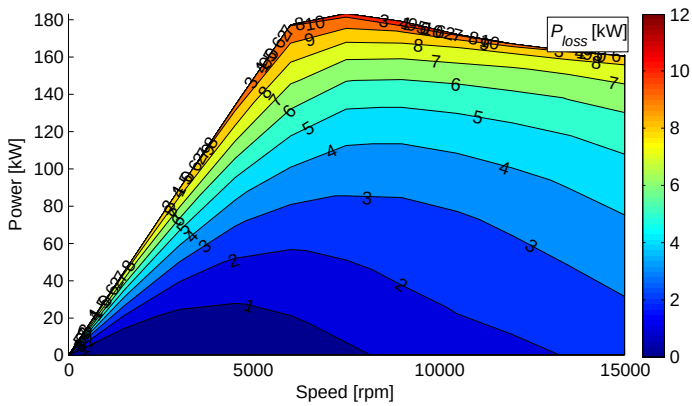

Figure 5.54: Total power losses, P_{loss} as a function of power and speed from simulations on a warm machine with 100°C PM and 130°C winding temperature

is presented in Figure 5.55.

$$\eta = \frac{P_{out}}{P_{in}} \cdot 100\% = \frac{P_{em} - P_{mech} - P_{Fe} - P_{rotor}}{P_{em} + P_{Cu}} \cdot 100\% \tag{5.65}$$

According to this prediction, the efficiency in the prototype machine should reach 96% in a large part of the operating region. When comparing to the efficiency map derived during the design phase, presented earlier in Figure 2.12 in Chapter 2, the maximum efficiency is dropped with around 2%. It is also established that the difference to the result in Figure 2.12 is especially pronounced at low torque, high speed operation. This makes sense since the

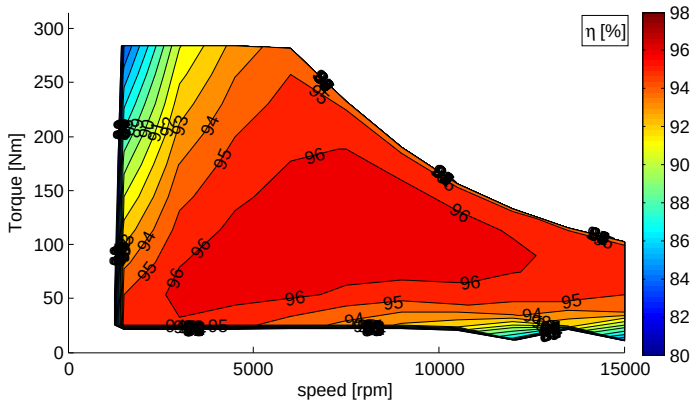

Figure 5.55: Efficiency η as a function of torque and speed from simulations of a warm machine with 100°C PM and 130°C winding temperature

revised speed dependant stator core losses differed rather much compared to the original prediction. At higher torque where the copper losses dominate, the difference is less obvious. This is also expected based on that the copper losses are not changed much in the analysis performed within the work presented here.

The difference in efficiency is especially affected by the increased losses above base speed. The amount of heat to be dissipated with the cooling is increased, hence the continuous power should be affected. If the initial cooling conditions are kept the same, the continuous power and torque are reduced compared to the original estimations. Since no deeper analysis is done on estimating the capacity of the cooling system, the influence on the continuous operation is not investigated any further.

5.6.2 Efficiency measurements

The simulated losses are compared to measurements on the prototype machine. The test procedure and result are presented here.

Test set-up

The efficiency of the prototype machine is measured by comparing power in and power out in the back to back test set-up described earlier in subsection 5.3.5. (Torque is recorded with a HBM T12/1kNm torque transducer [28] and electric power is established with a Yokogawa WT3000 power analyser). The used method makes it important to consider the uncertainties in the acquired data. This is because small differences are measured on large quantities.

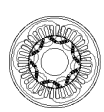

The closer to 100% efficiency, the larger the relative error will be in the final result. The uncertainties related to measured torque and measured power factor are identified as having a significant impact on the overall uncertainty in the efficiency measurements [107]. The efficiency can also be acquired by measuring the different losses separately and subtract them from the measured electric power as described in [125]. This is not done within the work presented here. A more accurate way to determine the efficiency is to perform calorimetric tests [126]. This is not possible within this work due to availability reasons.

The drive used to control the machine is a SKAI 2 inverter from Semicron [29]. The MTPA control is implemented with look up tables of i_d and i_q as function of speed and requested torque. The voltage is controlled with space vector modulation and has a voltage margin of 6% leaving a maximum phase voltage of 400 V. The switching frequency is 8 kHz. Limitations during the test are maximum 150 kW power due to the connected brake machine and 8000 rpm top speed due to resonance phenomena in the mechanical connection between the machines. Especially the top speed limitation is unfortunate since the impact of the iron losses is more distinguishable in the higher end of the speed range. The brake machine is controlled with speed references while the unit under test is controlled with torque references.

The test sequence automatically changes speed and torque in order to complete the entire torque speed map. The speed starts at 500 rpm, then 1000 rpm and further up in steps of 1000 rpm up to the largest tested speed. For each speed, the torque starts at zero and is increased in steps of 5% up to 20% (of peak torque at that speed), then in steps of 10% up to peak torque. The test sequence also includes negative torque, but that result is omitted here. Above base speed, peak power in the rig motor limits the torque from reaching 100%. Each test point is logged for 2.2 s to get an averaged result. Before commencing each test point, the machine is (electrically) heated or cooled down to maintain relatively constant temperature in all test points. Due to low accuracy when reading the motor temperature in the drive, the temperature sensor mounted in the hot spot of the windings (sensor #1, S_{HS} in Table 2.2) still indicates a temperature variation between 115-135°C. This is considered sufficiently constant for the purpose of the test. Immediately after each test point, the drive is disabled and the rig-motor is controlled to 1000 rpm. In this way, the magnet temperature can be estimated by recording the induced voltage of the test object. The estimated PM temperature indicates between 84-94°C for almost all test points. For both the windings and the magnets, the temperature in the higher range is recorded at higher speeds in the later part of the test sequence.

Test results

The test result is presented as losses in Figure 5.56 and as efficiency in Figure 5.57. Note the different speed scale compared to the simulation results presented previously. Peak effi-

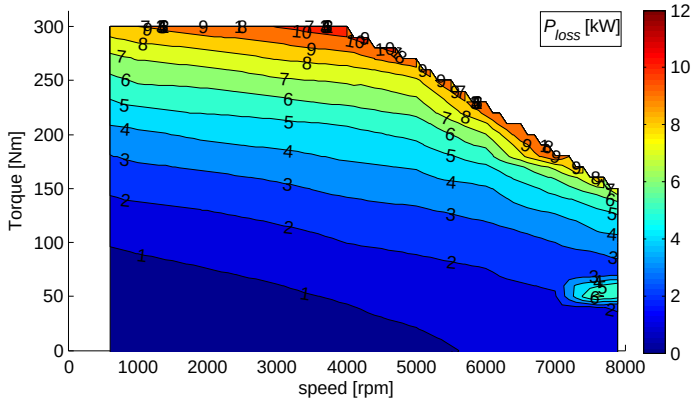

Figure 5.56: Measured power losses as a function of torque and speed on a warm machine with 84-94°C PM and 115-135°C winding temperature

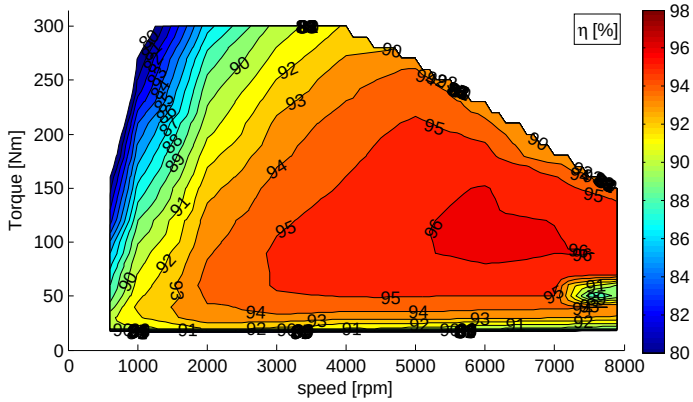

Figure 5.57: Measured efficiency as a function of torque and speed on a warm machine with 84-94°C PM and 115-135°C winding temperature

ciency in the test is above 96% in a limited area around 5500-7000 rpm and 100-150 Nm. The deviant readings at 8000 rpm, 50 Nm is caused by a faulty torque reading at that test point. In order to facilitate the comparison, the efficiency map from the simulations is presented again with the measured speed range in Figure 5.58. Here, the additional voltage margin of 6% used by the drive is considered as well.

When comparing to the simulation results in Figure 5.53 and 5.55 and with a more relevant speed range in Figure 5.58 it is concluded that the measured efficiency does not have the same wide area of above 96% efficiency predicted by the simulations. Although being closer to the measurements compared to the originally estimated efficiency map in Figure 2.12, the simulations still overestimate the efficiency. This is especially the case when entering

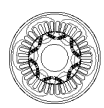

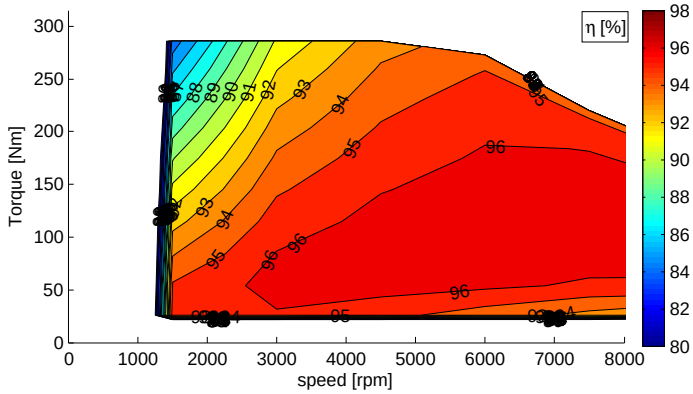

Figure 5.58: Efficiency η as function of torque and speed from simulations on a warm machine with 90°C PM and 120°C winding temperature

the field weakening region. The loss prediction at low speed and high torque follows the measurements better. This indicates that it is the speed dependant losses that still are underestimated in the simulations. Given the absolute values observed in the iron losses in the stator compared to the AC proximity losses in the windings, this deviation in speed dependency is more likely to be related to the iron core losses. The deviation in efficiency at low speed, low torque is considered less crucial since the losses generated in this region are small in relation to the cooling capability. The influence in terms of increased temperature in the machine or total energy efficiency in the system is marginal only.

An attempt to investigate the deviating result still noticed at higher speed, is done by manipulating the iron loss parameters even further. This time it is based on the roll out test result with the drive connected, presented previously in Figure 5.43. The difference between the two roll out tests in the figure is that higher losses are noticed when the drive still is connected and active with the current references set to zero. The influence on the core losses (or more generally in magnetization losses, if dividing all losses as DC-current and other losses) in the stator should be related to the switching frequency as well as the DC-voltage and is therefore dependant on the inverter. Since the roll out test is done with a different inverter as well as a different DC-voltage than that used in the efficiency measurements, the result can only provide a limited indication on how the results are affected by an inverter.

By adjusting the speed dependant eddy current term of the losses in (5.29) to match the roll out test with the drive connected, the iron losses are increased. This is accomplished by increasing the factor in front of the eddy current term in equation (5.43) from 4.9 to 8. This can be considered mathematically correct in terms of achieving a congruent result. It is however not necessarily physically correct since there is no evidence that all losses comes from the iron core. With all other loss contributors unchanged, the resulting simulated

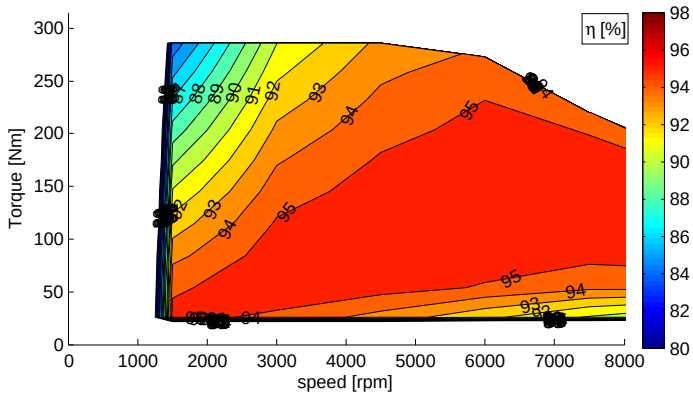

Figure 5.59: Efficiency η as a function of torque and speed from simulations on a warm machine (90°C PM and 120°C winding temperature) with modified speed dependant eddy current losses in the stator iron core

efficiency map is presented in Figure 5.59. As can be seen, the result is that the peak efficiency drops below 96%. On the other hand, when focusing on the surface representing an efficiency exceeding 95%, it is considered a better representation of that in the measured efficiency map. As already mentioned, the result from this simulation case is based on a different drive and should therefore be considered as an indicator only. It is nevertheless considered possible to conclude that the inverter is influencing the efficiency to a noticeable extent.

Any presence of circulating currents or current imbalance within the slots is not included in the simulations either. Studies performed and presented in [105] indicate that circulating currents could result in up to twice the copper losses in the prototype machine. This comes with the precondition that no twisting or displacement of the strands is present. As the machine has all coils connected in series, the circulating currents are assumed to be low. Omitting them entirely might however be a faulty assumption. A possible experimental investigation could be to perform a sequence of tests with opened and short circuited, or clamped bundle ends. Either during the manufacturing steps, or if it would be possible to access the winding terminals in the prototype. Since circulating currents have a dependency to frequency [70] and hence speed, it should be mentioned as a possible source for the deviation observed between the test result in Figure 5.57 and the simulation data in Figure 5.58.

Another thing that could be investigated when analysing the results is the harmonic content in the currents. A way to measure this is to look at the total harmonic distortion (THD) in the currents. High THD should result in both increased iron losses due to the high frequency components and also in higher copper losses due to the increased rms current.

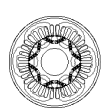

The THD measured by the power analyser (Yokogawa WT3000) during the test indicates 2–4% THD depending on load point and speed. The resulting influence on the loss map and hence efficiency is not pursued any further.

Additional reasons that to some extent can be used to explain the deviation between simulations and measurements are related to the hardware used during the test. One part is the test equipment. In addition to the inherited limitation in accuracy when comparing power in versus power out [126], there is a question mark on the torque transducer in the test set-up. As already mentioned, the maximum test speed is limited by resonance effects on the shaft connecting the test object with the rig-machine. This should influence the torque transducer readings to some extent. When studying the data sheet [28], external parasitic loads acting on the torque transducer are considered as one of the major contributor on the instrument accuracy. This is also explained a bit more in detail in Appendix B. How much the resonance influences the test data in this case is not investigated further, but the impact should be higher at higher rotational speed. Hence higher inaccuracy can be expected in the region where the higher deviation between test and simulation is observed.

In addition to this, the look up tables used to set up the control in the inverter do not have any field weakening scheme. Partly since the available test facilities hardly ever makes the machine to operate in field weakening. Field weakening is instead implemented by the drive by trying to maintain a desired voltage margin. The exact functionality of this part of the control has not been investigated in any deeper manner. Any influence on the measured data compared to the simulations due to this is therefore not established.

Finally, as touched upon previously in the thesis, temperature should influence the result as well, partly in terms of losses in the windings. Although being measured in a presumed hot spot, the temperature is not constant along the entire copper wires. Secondly, any influence on iron losses due to temperature variations is omitted in the analysis. How much this could affect the result is therefore not established.

The conclusion from studying the efficiency is that the simulations manage to provide a result that to a reasonable extent is comparable to the test. This is especially the case when the iron losses are corrected even further in Figure 5.59. It is however important to be aware of the limitations and uncertainties present in the analysis. This holds both from the simulations in terms of how well the models manage to represent reality and also from the measurements in terms of limitations and inaccuracies in the test equipment. The machine is only tested up to just over half its intended top speed and furthermore, with a limitation in maximum power. All in all, less than half the operating area is covered in the test. The result is however still considered as useful for verifying part of the loss analysis done throughout the chapter. High torque low speed operation indicates good agreement in the non speed dependant models. That adds credibility to the copper losses and to some extent the hysteresis part of the iron losses. As the speed reaches about half speed at 7000-

8000 rpm, the simulations could still be adjusted to agree well without being unrealistic. The limit in the result is obviously what is happening outside the tested speed range. This is unfortunate as it constrains the possibility to investigate and verify a major part of the field weakening region. This could on the other hand also have introduced further complications related to the control in the frequency converter.

The concluding remark on the efficiency measurements is therefore, in line with all tests performed throughout the thesis: It is a challenging task to combine and compare simulations and measurements. This goes for setting up the test as well as explaining the results. The outcome should therefore, as always mainly be considered as indications pointing in the right direction, rather than providing any definitive answers. Given the reasonable conformity between simulations and measurements, this is considered fulfilled.

5.6.3 Summary of the loss analysis

As stated already in the previous subsections, there are lots of challenges related to analysing the losses in an electric machine. This starts already in the modelling. The mechanical loss models implemented are analytical and based on empirical results in the works of others. The **bearing loss model** being based on the work of the manufacturer [49] is considered well proven. This is based both on the underlying data and on the measurements performed here. In combination with expressions for the friction from the oil seal and carbon brushes, the conformity to test is considered satisfying. The remaining part still interesting to have had done is related to the thermal aspects. A study on how well the model handles the changes in viscosity would have been interesting. On the other hand, the part of the total losses originating from the mechanical losses is marginal. The more interesting area of use is instead related to loss separation from the similarly behaving iron losses. An accurate model of the mechanical losses is an enabler for investigating the losses in the iron core in a better way.

The second part included in the mechanical loss model is the **air drag**. This part is considered as less proven compared to the friction losses. The main reason is the limited test speed. As there is no possibility to verify against measurements, the effort put on the model becomes less relevant. Also when studying the literature, the expressions are very much empirical with numerous variations depending on speed, temperature, relative air pressure, surface roughness and so on. No commonly used, general model seems to exist. The resulting losses obtained from the analytical model indicate a marginal effect on the total losses within the speed range of the machine.

The **iron loss model** originally considered is selected with focus on keeping the computational effort low. Focus is on the main power loss contributors to provide the vital input to cooling integration and thermal design. This model is hence known to be less accur-

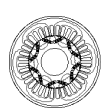

ate already from the start. This is partly due to the simplified way to acquire the relevant flux densities from the FEM simulations, but also since the models are known not to be based on the underlying physics, neither forseeing the impacts from practical realisation and manufacturing [63]. Although the model in use underestimates the losses rather much, the investigation indicates that other supposedly better models in principle are equally inaccurate (see Figure 5.36). The learning is instead the importance of knowing the limitations of the model that is in use and also which factors that have an impact on the losses in the physical machine. This includes the harmonics imposed by both geometry and applied currents and also the influences on the material parameters from manufacturing. During the no load roll out tests, global eddy currents caused by partial short circuits between laminations are the seemingly dominating explanation for the difference. These eddy current loops are introduced during the manufacturing process. Axially conducting paths at the lamination edges are created by e.g. damaged coating close to the edges and welding seams at the stator back. A factor of almost 5 is needed on the speed dependant eddy current loss torque to get the result to better agree with the test. When running the efficiency tests with a drive connected, this factor of 5 seems insufficient. Better conformity is achieved by increasing the eddy currents in the stator core with an additional factor of just over 1.6. This gives in total 8 times higher eddy current losses compared to those originally estimated. It is however not settled whether these additional losses are related to e.g. higher $\frac{dB}{dt}$ in the iron core only or if some parts also are related to AC-losses in the windings.

Less effort is directed towards the **rotor losses**. Although the models used share the same limitation in reliability as in the stator, the impact in absolute numbers are much smaller. The importance of still knowing the rotor losses is also somewhat mitigated by how the oil cooling is implemented. The usual problem of dissipating heat from the rotor is solved by the way the cooling system is implemented.

In addition to the straight forward DC **copper losses**, proximity losses due to external flux leakage in the slots and skin effects in the strands from the alternating currents are studied. Self flux leakage in strands is not included since it is not expected to give much influence with such small diameter on the copper (0.85 mm). The small copper wire diameter is also a sufficient precaution to prevent skin effects to occur, at least on the fundamental current components. The external flux leaking from the stator core through the slots is estimated from FE simulations. Together with a number of assumptions on for example the conformity and sinusoidal behaviour, this is used to estimate the proximity losses. Although being considered a rather blunt approach, the outcome should still be sufficient to give an indication on the order of magnitude. Compared to the DC-losses originally considered, the influence is limited. Also at high torque close to top speed where the proximity losses are most noticeable, the result according to the model used indicates less than 5% increase on the total winding losses. In the remaining part of the load map, the influence is much less than that. Other things not included in the analysis are any influence from harmonics

due to for example the switching frequency, or circulating currents due to strands not being sufficiently twisted or dislocated.

5.6.4 Conclusions from the loss analysis

The iron losses have the largest impact on the result based on the analysis performed here. This is to some extent expected since the iron losses are known to be hard to model correctly. This in combination with being one of the two major loss contributors in an electrical machine makes it relevant to study further. This is also why the majority of the work on mapping the losses is directed towards the stator core. All the more surprising is the order of magnitude with which the simulated iron losses must be increased in order to match the test results. The roll out test without the drive indicates a factor of 4.9 between simulations and measurements, while that with the drive still connected indicates a factor of 8. This brings the iron losses to about the same level as the copper losses in part of the load map. The stated explanations for having to scale up the iron losses are global eddy currents due to manufacturing in combination with harmonics from the frequency converter. Here, especially the first part is hard to predict. The important lesson must instead be to consider and if possible prevent this phenomenon during the machine assembly.

The short-cut in the analysis here is to adopt the model to the test data by implementing correction factors. This highlights the incomplete estimation of power losses and identifies different loss origins that are excluded in the design process. The correction factors are a seemingly straight forward method to improve the simulation model for fast prediction and machine sizing. Since lots of analysis work can be done more easily outside the test lab, the improved model is of use also when there is a physical prototype. The limitation with this approach found out during the study is the conformity between the prototype and a unit produced in higher volumes. The theoretical study on the iron losses concludes many of the impacting factors as being a result of the manufacturing method. As this can be quite different depending on the numbers produced, the verified and corrected simulation model will still have potential limitations in its accuracy. One example is the global eddy currents that to some extent are explained by the damaged coating on the iron sheets. This is in turn found to be a more likely event when cut with laser compared to when stamped. Hence the losses in the serially produced version might be different than that in the prototype.

The other part in the major loss contributor category is losses in the windings. Before commencing this work, the copper losses were believed to be dominating when making a loss separation. Unlike the iron losses, the copper losses originally considered are not affected much throughout the analysis done here. That is unexpected since already a small relative change in losses should result in a significant impact in absolute numbers. Here it must also be mentioned that these results are with some potential loss contributors being omitted. When consulting the literature, support can be found for AC-phenomena mainly

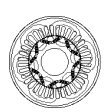

being an issue in larger machines or machines with solid windings [113, 121, 124, 127]. In randomly wound machines with wire bundles built up by several thin strands, the AC-losses seem less prominent. Going deeper into this area is an interesting topic for future work.

When the copper losses become speed dependent and hence start to resemble those in the stator core, things get more complicated. This is especially the case since the iron core losses also have a dependency to the applied load. The idea with the on load measurements in section 5.3.5 is to succeed in mapping the iron losses as a function of applied currents. This can provide a good starting position for isolating any speed dependency in the copper losses. Limitations in the test procedure in terms of requiring unrealistically high measurement accuracy, instead diminish the analysis to being a game of guessing. Is the load angle correct, or is the dq-map rotated a couple of degrees? Is the inaccuracy in the torque transducer deviating differently on opposite sides of zero torque? Does the data interpolation provide a decent representation of the data points? Hence more focus is directed to read out the test results instead of being able to try to make the line between iron losses and AC copper losses more visible.

This brings the next and also most important lesson learned, being the importance in knowing the limitations in the analysis. This holds for those introduced in the simulations as well as those imposed by the test set-up. Simulations are models trying to represent some kind of reality, while test results are blurry pictures of the same thing. Any discrepancy can therefore originate from either side of the table. The models are inaccurate, but it is hard to determine to what extent, since measurements not necessarily provides the full picture either.

One way to get around parts of the issues introduced during measurements is to run multiple tests. This way, the statistical basics get better. This could however be problematic if the tests are time consuming, both in terms of available resources and in getting similar conditions throughout all tests. The temperature can for example have an impact on both the test object and the test equipment.

Many of the tests in the work this thesis is based on are done during a limited time slot. The tests in the conventional test bench as well as in the back to back set-up are done during approximately two working weeks each. This includes time to install, debug and decommission the test object as well as setting up the motor control parameters and running the tests. In addition to the limited possibility to run multiple tests, the limited time also enforces intensive testing when the test window is open. This leaves little time to do deeper analysis work with the test object still in the test bench. Many questions regarding the data are therefore discovered after the test period and consequently often left unanswered.

Chapter 6

Discussion and Conclusions

As introduced in the Objectives section in Chapter 1, the work sets out to, to some extent close the knowledge gap between the automotive industry needs and the electric traction machine provisions. This should be done by providing a profound knowledge base concerning the design of an electric machine based on requirements from a heavy commercial vehicle. With the work presented here, some aspects important to consider in the borderline between the two disciplines are covered. This being said, many aspects are still to be pursued.

6.1 Conclusions

In addition to the conclusions given towards the end of each chapter, this section provides a shorter summary and some overall conclusions from the different parts of the project.

The first conclusion drawn from the PhD work is that there is no such thing as a perfect machine design. The constant flow of compromises that follow the work of designing an electric machine indicates the importance of having a good insight into the intended application. Corresponding insight and understanding are important also when ordering a machine for a specific application. A good understanding of the consequences of any specific requirement is the key to success. A potential consequence is the risk of getting what was ordered rather than what was actually wanted or needed.

The main conclusion from Chapter 3 is the importance of considering the thermal dependency of the magnet material. Since the material data provided by the suppliers in general is given at room temperature, the elevated temperatures during normal operating conditions have to be handled in the simulation model. It is also concluded that the fairly elemental

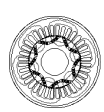

analytical expression describing the RTC of the permanent magnets, is sufficient for providing a functional thermal behaviour in the simulations. The flexibility of the simulation tool makes the implementation easily achievable in the pre- and post processing codes. With the rapid test procedure of the dynamic testing methodology, the thermal model is verified without time consuming tests.

The analysis in Chapter 4 provides conclusions on how much the torque production in an IPMSM actually is affected by skewing. This differs rather drastically from the expectations aquired when studying relevant text books, such as [8, 9, 16]. The simulation result indicates a load dependant influence on the torque production where some parts of the load map shows a considerable reduction. This influence is in the thesis defined as "the apparent skewing factor" of the machine. Since this apparent skewing factor is determined experimentally, the exact value needs to be settled individually for different machines. The overall trend should however be similar also for other IPMSM designs. Within the work on skewing, it is also shown that the part of the load map affected the most coincides with where the machine is operated during field weakening. This is an operating area frequently used by a traction machine in a vehicle application.

The concluding remarks from Chapter 5 are related to the difficulties in determining the iron losses. This is partly since it is hard to model correctly and partly since it also is hard to measure in an accurate way, at least at on-load conditions. Influences from the manufacturing process that are difficult to predict have a large influence on the iron losses in the machine. Ongoing activities in the research community focus on how the hysteresis and eddy current losses are affected on a local scale, e.g. in a single lamination. A more tricky aspect is the influence of eddy currents due to partial short circuit between the sheets. Since the conductivity in such a connection is hard to estimate, the resulting eddy current losses are hard to predict as well. The other of the two main loss contributors, namely the copper losses, instead turns out to agree better with the simplified original estimations than expected. The parallel strands in the wire bundles efficiently suppress the AC-components of the resistive losses. The conclusion from the mechanical loss study is first of all a sense for the order of magnitude, or rather lack of magnitude of the mechanical losses in the machine. This is valid at least at lower rotational speeds at which the dummy rotor used in the analysis seems to never come to a stop. The bearing loss model [49] developed by the bearing supplier is also found to provide a good representation of the actual case. Together with elementary analytical models for sliding friction, this provides a good base for estimating the mechanical losses.

The final overall conclusions are related to the machine designed and produced throughout the PhD work. Aspects identified as important prior to setting the actual requirements are the machine size and power density. In terms of size, the long and slender prototyped design is tailored to fit on the side of a high volume production heavy duty transmission. Installation in a rig set-up proves the fulfilment of the requirement. The long and slender

design also provides good conditions for handling high rotational speed with sufficient mechanical integrity in the rotor. This is in turn a prerequisite for the machine to provide sufficient power to propel a heavy hybrid electric or full electric vehicle in the limited space claim.

The power density of the machine is approximately 2.9 kW/kg or 12.9 kW/l considering 180 kW as peak power and 62 kg and 14 litres respectively. This is comparable with or higher than many of the competing machines intended for similar applications. Besides the increased speed, the other aspect identified as important to obtain a power dense machine is the implementation of direct cooling. With oil applied directly on the active parts, the housing can be made smaller and as the total machine weight goes down, the power density is increased.

6.2 Discussion

This section sets out to discuss some of the results and conclusions obtained from the work presented. The way of working throughout the project is mentioned. In addition to this, the discussion is somewhat extended beyond the scope of the thesis. This is in order to add a different aspect point on what to consider when designing a machine for a claimed environmental friendly application.

Regarding validation of the simulations The results presented in this thesis need to be discussed in terms of how the simulation results have been validated with measurements. A consistent theme with the test results presented, is the limitations imposed by the test facilities. This is either in terms of top speed or available power. Despite the limitations, the results are in most cases still considered sufficient to give indications on the credibility of the underlying simulations. The continuous performance test results (from Figure 2.20) can for example be plotted together with the simulated loss map to give a more accurate prediction of the continuous performance at higher rotational speeds. As can be seen in Figure 6.1, the continuous performance operation is when around 4 kW of losses are dissipated. This indicates around 80 kW at top speed.

Other test results that suffer from limitations are e.g. those performed on the dummy rotor. With the limited speed, the plateau at which the loss torque is expected to become stable is hardly reached. Furthermore, the windage cannot be considered to be validated at all. On the other hand, this opens for the possibility to instead focus more on the mechanical friction losses.

The results obtained in the torque ripple analysis are on the other hand considered more robust. The apparent skewing factor is indeed extracted from simulations. However, the

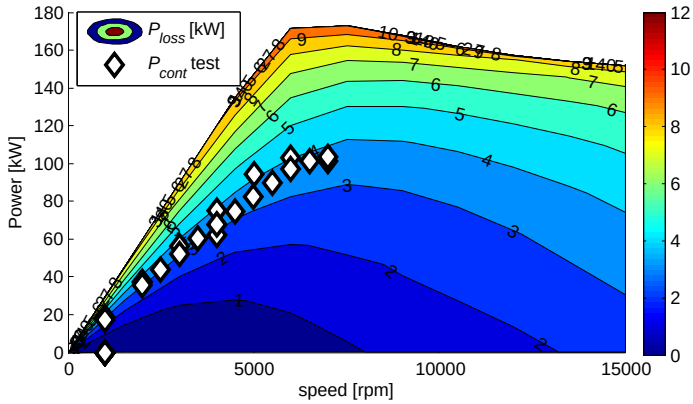

Figure 6.1: Loss map from simulations with measured continuous power

close conformity between expectations from simulations and the test result indicates credibility to the simulation model and hence the analysis. Also an unexpected torque variation is explained and eventually verified in complementary measurements. The implementation in the post-analysis model makes it possible to select and study any skewing angle. By comparing the results without skewing with the simulation results with a skewing of 1, 2, 3 and so on degrees, a smooth and continuous transition is seen. This adds further credibility to the simulation results.

The skewing analysis can also be discussed with regards to the actual results. The unexpectedly large impact on torque production in the usually occurring operation region might be a sufficient reason for not implementing skewing. This holds especially if it also affects the efficiency, as the reasoning towards the end of Chapter 4 indicates.

Regarding the way of working The way of working can be discussed in a couple of different aspects. One part is related to how the results are obtained. Here, a distinguishable difference can be noticed before and after licentiate. Pre-licentiate work is with a broader perspective with focus on fast and somewhat accurate results. With the help of the simulation environment, a prototype is designed and built rather early in the project. Post-licentiate work is more detailed, much slower and a bit more accurate. The extra effort spent is of course an important foundation for obtaining understanding, but gives a close to marginal result in terms of accuracy. Nevertheless, the understanding obtained here is a prerequisite for eventually finding an acceptable compromise between design speed and accuracy in the results.

An advantage of arranging the work as in this project is the access to something real to which the theoretical knowledge can be connected. This has been especially important for

the learning process of the author to this thesis. Real understanding is acquired when the test results are analysed and compared to the expectations.

Regarding the way of working as a PhD student with such close connection to the industry, some observations are made. As mentioned in the introduction, one major difference between industry and academia is the time aspect. This is partly in terms of the expectations on the results, but also related to the practical work in different lab environments. The experiments performed at the university have been set up and left for months. This way, test data analysis is made with the test object still being mounted in the rig. If needed, tests can be modified and re-made in order to answer any potentially question marks in the results. The test periods under the direction of industry is instead strictly limited. In order to maximize the valuable time in the rig, planning in advance is crucial and the deeper reflections have to wait until afterwards. Any confusion discovered afterwards is left to be solved with speculations. Something that in retrospective would have been considered valuable would have been a dedicated test lab for a longer part of the project. This way, the tests could have been performed with more focus on understanding the results, rather than just producing data.

Regarding the target applications The results in this thesis are presented with consideration to electric propulsion of a heavy commercial vehicle. Although many of the results are relevant also for other applications, some observations are made on the differences.

As mentioned several times, the most crucial aspect of a traction machine is to make it fit in the application. After that first requirement is fulfilled, cost and efficiency become the main focus. Another difference is related to how the machine is to be used. Rather than a constant operation, the load variations are large and ever-present. This way, the difference between peak and average operation can be fairly large.

Related to this, the definition of continuous and peak power is a topic necessary to discuss. The definitions considered in this thesis is operation at thermal equilibrium (hence similar to the S1 duty cycle[1]) for continuous operation and around 10 seconds of operation with maximum current for peak. Looking at the applications, continuous operation will never happen. Instead an average or possibly an rms-value needs to be considered.

The standard used within the automotive industry[2] is defining continuous power as 30 minutes of operation after at least 4 h of preconditioning at room temperature. Maximum, or Net Power is measured by preconditioning the machine at room temperature for atleast 2 h, followed by 3 minutes of operation at 80% of max power. Then the power is measured at full load at a sufficient number of motor speeds from standstill to top speed during

[1] "Duty type S1 - Continuous running duty" in IEC 60034

[2] UN ECE Regulation no.85

maximum 5 minutes.

When analysing the test procedures in the standard it is concluded that the tests in many aspects are adopted to passenger cars. The duration of a trip in a car can typically be 30 minutes or less. This is however not the case for a commercial vehicle, something that questions the usefulness of this definition for the given application. Another aspect is related to the size of the machine that is tested. For a smaller machine, 30 minutes might be sufficient for reaching stable temperature. The time this takes for a bigger machine with a larger thermal mass could very well be longer. The resulting 30 minutes power of a large electric machine can therefore be noticeably different from the continuous S1 performance. Also the rather long time window for operation at peak load can be debated. Again, the larger the machine, the longer the time before over-temperatures are reached.

Regarding environmental aspects The last part of the discussion is dedicated to environmental aspects. From this point of view, the decision to use rare earth material in the machine design can be discussed. The purpose with this part of the discussion is not to provide any answers on what would be the environmentally correct machine design. Instead the intention is to direct some focus to the issue of a potential shift from local to global emissions and pollution and that there is research focusing on these aspects. The discussion and conclusions here are all based on [128–130] where the results from the work on a life cycle assessment (LCA) analysis is presented. Included are three different types of PM machines designed for vehicle applications. The result is divided into carbon dioxide (CO_2)-emissions affecting the climate, along with health effects due to toxicity and toxic waste.

The material used in the three machines in question is approximately 45-48 kg of electric steel, around 5 kg of copper and 1.5-2.5 kg of magnets [129]. The amount of aluminium is not presented while the relatively large amount of steel is due to inefficient use of the steel sheets when stamping the laminations. More than 50% of the steel is not used in the actual machine, but lost in the stamping process. For the magnets, around 20% is lost in the manufacturing process. The mutual distribution between copper and magnets agrees well with that in the machine studied in this PhD work ($\approx$9 kg copper and $\approx$2 kg magnets).

In the LCA study, the CO_2-emissions are linked to the energy consumption during manufacturing together with that consumed during the use phase. The latter considers the energy needed to move the weight of the machine itself, along with the losses in the machine. This is hence highlighting the importance of designing a machine with a high efficiency over a large part of the intended operating region. That becomes even more important for a commercial vehicle, since the required and expected component life typically is up to 10 times longer than that of a passenger car. In the case of a vehicle being charged from the grid, the carbon intensity of the energy mix becomes an important factor. Depending on where

in the world the vehicle is charged, the CO_2-emissions related to the vehicle are different. The same goes for if the study considers an existing energy mix, or if assumptions are made regarding an improved future energy mix. During manufacturing, the major contributor to CO_2-emissions is the preparation of the iron core, followed by making the aluminium housing and the copper windings [130]. The CO_2-emission part of the LCA analysis is considered robust and well proven [128].

The other aspect covered in the LCA analysis in [128–130] is the toxicity. This part is especially distinctive during the material preparation and production phases. With the underlying assumptions to the study, the dominant contributor to toxicity is the copper. This is mainly connected to long term emissions of heavy metals to ground water. It is hence to some extent linked to the environmental legislation at the location of the mine and material processing facility. The toxicity part of the study is more uncertain and the results can differ considerably between different studies. This is because it is hard to quantify indirect toxicity and determine the true origin of contaminants where the effect is not directly noticeable [128].

Based on the results in the referenced study, some conclusions are drawn. One is that despite a rather large environmental impact per unit weight, the rare earth materials in the permanent magnets have a limited influence on the environmental impact of an IPMSM. This is due to the proportionally small amount mounted in the machine. Furthermore, since the study associates most toxicity to the copper, it is not obvious whether e.g. an electrically magnetized machine would be a better choice. This is especially since the mutual relation between copper and magnet weight in the machines in the study is around 2-3:1 only. Removing the magnets to the expense of more copper could perhaps even increase the environmental impact. As stated in [129], it would instead make more sense to consider e.g. concentrated windings and a segmented stator. This would mean less copper in the end windings and higher utilization of the electric steel.

The other conclusion from looking into the LCA-study is that both the CO_2-emissions and the toxicity to some extent are consequences of external factors. The climate impact is to a large extent related to the carbon intensity of the energy mix during the use phase. Hence a more clean energy production leads to a direct improvement on the environmental impact of the electric vehicle. Moreover, the toxicity from the production phase holds the potential to be improved. This is achieved by introducing tougher requirements regarding pollution from the mining and processing industries.

6.3 Future work

This section lists a number of studies identified as relevant and interesting to do as a continuation or complementation of the work and results presented throughout the thesis. Suggested topics are as follows:

- In connection to the thermal behaviour, a more thorough study is needed on the cooling of the machine. This should preferably include:
  - The creation of a thermal model capable of predicting the heat dissipation in the two oil circuits. The model should be used to tune the coolant flow distribution in order to either optimize the continuous performance or reduce the pumping power. Inspiration to the creation of the thermal model could potentially be found in [131] for the stator back and in [132] for the rotor and end winding cooling.
  - Operation at higher temperatures, both in terms of reducing the margin to the insulation class in the windings and the maximum operating temperature of the magnet grade. Also operation with a higher oil inlet temperature (up to 100-120°C) should be tested. This will investigate the potential to share oil with the gearbox without any additional oil cooler. Tests with higher oil inlet temperatures have not been possible to do due to safety restrictions on the oil temperature in the test cell.
  - Operation at lower temperatures to prove the usefulness of the oil cooling system at cold starts. Since the viscosity of oil is highly temperature dependent, too low temperatures could paradoxically lead to overheating the machine. The back pressure is then too large, leading to no oil circulation.
  - A deeper study of the cooling circuit routed via the rotor. Such a study could be partly related to centrifugal pumping effects and partly related to the results presented in [132]. In [132], tests of a similar rotor oil cooling solution reveal significantly higher mechanical looses in the upper speed range (7-10 krpm). This is a consequence of oil foam being created in the motor compartment that prevents proper oil drainage. Examples on what to study related to the pumping effect is the pumping power and whether it could be sufficient to run the rotor oil cooling.
- Some additional studies related to skewing and the torque ripple analysis could be carried out. Aspects to consider could be:
  - Experimental validation of the simulated apparent skewing factor. This would require building and testing a prototype without skewing. The study could

then also be extended to include a more thorough investigation on how the efficiency is affected by the implementation of skewing.

  - An alternative skewing angle to the 30 electrical degrees used in the prototype: A similar investigation is presented for a surface mounted PMSM in [34]. The implementation in the simulation model is easily done, while the subsequent analysis to find an optimum should prove less elementary. This holds both in terms of torque versus torque ripple and in terms of which part of the load map, the load dependant skewing factor should be optimized for.
  - Alternative means of reducing the torque ripple; this since one of the conclusions from the skewing chapter is how the fundamental torque is affected when operated in the field weakening, or constant power region. Examples on alternative means to reduce the torque ripple could be e.g. chamfered stator tooth-tips [133], rotor pole shaping [134], or shifting the magnets [24] or flux barriers [135] slightly between the poles. Torque ripple reduction can also be accomplished by manipulating the applied currents [136, 137]. The expense would be increased switching losses in the frequency converter [138].

- Repeating a number of the tests performed throughout the thesis. More specifically, the following is identified as relevant for improving the overall results:

  - Testing the continuous and peak performance and measuring the efficiency in the entire speed region of the machine.
  - Perform thermal dependency tests up to full speed and power.
  - Complement the dummy rotor tests with higher speeds and different temperatures to investigate the air friction as well as the thermal dependency of the bearing friction.
  - Perform no load iron loss tests at different temperatures to investigate any thermal dependency of the iron losses.
  - Investigate the possibility to map any circulating currents in the wire bundles inside the slots. This to determine if it would by possible to open the bundles in the winding terminals and compare to if the bundles are clamped and hence short circuited in the connection to the phase cables.
  - Consider re-testing the on-load iron losses with more effort to ensure as identical conditions as possible throughout all tests. In addition to this, a larger statistical basis should be collected. Before executing this test, consideration should be directed towards the influence of the accuracy in the instrumentation to determine the usefulness of the results.

- In the case of better test results being obtained from the on-load iron loss testing, the simulation model should be calibrated correspondingly. In this case, more con-

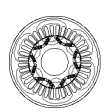

sideration needs to be made towards the control parameters of the drive as e.g. the switching frequency and DC voltage level should have an influence on the result.

Appendices

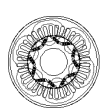

Appendix A

Park Clarke transformation

The transformation from a three phase system to the rotating dq coordinate system via the two-phase stator stationary $\alpha\beta$ coordinate system is described here. This transformation is done in order to facilitate the control of the electric machine. It is also a useful aid for understanding how torque is created in the electric machine. The transformation procedure is commonly known as the Park Clarke transformation.

The 3-phase AC-quantities (a, b & c) in an electric machine are generally expressed as vectors in a *stationary coordinate system* called $\alpha\beta$. The term "stationary" comes from that the axes are fixed to the stator. The idea is that the rotating magnetic field formed by the three alternating phase currents (i_{abc}) can be expressed as a vector that rotates in the $\alpha\beta$ reference frame. The α-axis is per definition aligned to the magnetic field created by a positive current in Phase A, or more simple; α is aligned to Phase A, with the β axis in orthogonal direction. Phase B and C are distributed with $\pm 120°$ respectively in the coordinate system.

Transformation from the three phase to the $\alpha\beta$ system with the so called Clarke transform, can be done with either *amplitude invariant* or *power invariant* transformation. As the name suggests, the amplitude invariant transformation keeps the same amplitude of the vectors throughout the transformation. The difference in power invariant transformation is a factor of $\sqrt{\frac{3}{2}}$ introduced to compensate for that the electrical power in a two-phase system gets lower than if multiplied in the three-phase system. In power invariant transformation, the power will be the same disregarding if it is calculated in the two-phase ($\alpha\beta$) or three-phase (abc) system. The assumption here is also that the three phases are symmetrical so that the sum of all phases are zero at all time. This means that the zero sequence term is neglected and left out. If the three phase system is not perfectly symmetrical, the zero sequence term, representing the sum of all phases should be included as well.

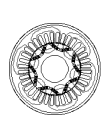

Power Invariant transformation from i_{abc} to $i_{\alpha\beta}$ is done according to:

$$i_\alpha = \sqrt{\frac{3}{2}} i_a \tag{A.1}$$

$$i_\beta = \frac{1}{\sqrt{2}} (i_b - i_c) \tag{A.2}$$

Amplitude Invariant transformation from i_{abc} to $i_{\alpha\beta}$ is done according to:

$$i_\alpha = i_a \tag{A.3}$$

$$i_\beta = \frac{1}{\sqrt{3}} (i_b - i_c) \tag{A.4}$$

Power Invariant transformation from $i_{\alpha\beta}$ to i_{abc} is done according to:

$$i_a = \sqrt{\frac{2}{3}} i_\alpha \tag{A.5}$$

$$i_b = \sqrt{\frac{2}{3}} \frac{-i_\alpha + \sqrt{3} i_\beta}{2} \tag{A.6}$$

$$i_c = \sqrt{\frac{2}{3}} \frac{-i_\alpha - \sqrt{3} i_\beta}{2} \tag{A.7}$$

Amplitude Invariant transformation from $i_{\alpha\beta}$ to i_{abc} is done according to:

$$i_a = i_\alpha \tag{A.8}$$

$$i_b = \frac{-i_\alpha + \sqrt{3} i_\beta}{2} \tag{A.9}$$

$$i_c = \frac{-i_\alpha - \sqrt{3} i_\beta}{2} \tag{A.10}$$

In order to further facilitate the control of the electric machine, one more coordinate system is introduced. Instead of being attached to the stator, the new coordinate system is attached to the rotor and is hence rotating with the same frequency as the electric machine. This *rotating coordinate system* is defined as the dq coordinate system. The big advantage is that the rotating flux vector in the stationary $\alpha\beta$ reference frame instead becomes stationary in the rotating dq coordinate system. The d-axis is per definition aligned to the permanent magnet flux in the rotor. Orthogonally directed is the q-axis. In its most basic set-up, with a magnetic bar in the rotor, maximum torque in a machine is obtained if the current is applied in q-direction. This means that the electromagnetic south pole in the stator is kept 90 degrees ahead of the permanent magnet north pole in the rotor. Since the coordinate

system is rotating with the rotor, the torque is preserved for as long as i_q is kept constant. With iron present in the rotor as well, things are getting more complicated as the reluctance torque starts to have an impact as well. Even though this is utilized in the machine designed in the PhD work, the theory behind the reluctance torque is out of the scope here.

Transformation from $\alpha\beta$– to dq coordinates is done with the Park transform. In order to complete the transformation, knowledge of the rotor position angle Θ is required. Transformation from $i_{\alpha\beta}$ to i_{dq} is done according to:

$$i_d = i_\alpha \cos\Theta + i_\beta \sin\Theta \tag{A.11}$$

$$i_q = i_\beta \cos\Theta - i_\alpha \sin\Theta \tag{A.12}$$

Transformation from i_{dq} to $i_{\alpha\beta}$ is done according to:

$$i_\alpha = i_d \cos\Theta - i_q \sin\Theta \tag{A.13}$$

$$i_\beta = i_d \sin\Theta + i_q \cos\Theta \tag{A.14}$$

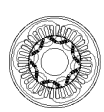

Appendix B

Torque transducer measurement uncertainties

This appendix describes how to establish the uncertainties from the HBM torque transducer used for part of the measurements. All parameters from the data sheet are specified as maximum, or worst case values. The information is mainly acquired from the HBM webpage[1] together the data sheet of the torque transducer in question [28].

Parameters specified as maximum values in the data sheet have a rectangular distribution. This means that a distribution factor of $\frac{1}{\sqrt{3}}$ shall be used to obtain the typical values.

This gives the measurement uncertainty u_{dC} from the sensitivity tolerance d_C and maximum torque of the application T_{max} according to

$$u_{dC} = \frac{1}{\sqrt{3}} \cdot d_C \cdot T_{max} \tag{B.1}$$

The measurement uncertainty u_{dlh} due to linear deviation including hysteresis effects is determined from the linearity and hysteresis deviation d_{lh} according to

$$u_{dlh} = \frac{1}{\sqrt{3}} \cdot d_{lh} \cdot T_{nom} \cdot k_{mr} \tag{B.2}$$

Additional input is the measuring range of the transducer T_{nom} and a factor for the mechanical remanence k_{mr} of the material in the transducer. A mechanical remanence factor of

[1] https://www.hbm.com/se/3941/the-calculation-of-the-measurement-uncertainty-for-torque-applications/ Accessed on 2018-12-02

2 needs to be considered when both positive and negative torque is recorded. The torque transducer have a nominal measuring range of 1 kNm.

The measurements uncertainty u_{dTKC} due to the temperature impact on the sensitivity d_{TKC} is determined according to

$$u_{dTKC} = \frac{1}{\sqrt{3}} \cdot d_{TKC} \cdot T_{max} \cdot \frac{\vartheta_{max} - \vartheta_{nom}}{10} \tag{B.3}$$

where $\vartheta_{max} - \vartheta_{nom}$ is the deviation in temperature ϑ from nominal (room temperature).

The measurement uncertainty u_{dTK0} due to the temperature influence on the zero signal d_{TK0} is determined according to

$$u_{dTK0} = \frac{1}{\sqrt{3}} \cdot d_{TK0} \cdot T_{nom} \cdot \frac{\vartheta_{max} - \vartheta_{nom}}{10} \tag{B.4}$$

The measurement uncertainty $u_{d\sigma}$ from the standard deviation of the repeatability d_σ is determined based on the difference between maximum and minimum measured torque according to

$$u_{d\sigma} = d_\sigma \cdot (T_{max} - T_{min}) \tag{B.5}$$

Since d_σ is given as typical value, the distribution factor is not included here.

The measurement uncertainty u_{par} due to any parasitic loads acting on the torque transducer is determined according to

$$u_{par} = \frac{1}{\sqrt{3}} \cdot \frac{L_{par}}{L_{par,ref}} T_{nom} \cdot d_{par} \tag{B.6}$$

Here the sum of the relation between the different parasitic loads and each relevant maximum permissible load, is denoted $\frac{L_{par}}{L_{par,ref}}$. Maximum acceptable value of $\frac{L_{par}}{L_{par,ref}}$ is 100%. The deviation factor d_{par} indicates how much the parasitic loads affect the result.

The total measurement uncertainty is obtained by considering the rms value of all individual contributors. This gives a confidence interval of 68%. For a higher confidence interval, the resulting total uncertainty is multiplied with a factor 1.645 for 90%, 1.96 for 95% and 2.576 for 99% confidence interval.

A sensitivity analysis is done by using relevant numbers from the data sheet to solve B.1-B.6. The results are obtained by considering torque measured between ±300 Nm. Hence T_{max} is 300 Nm in this specific case. The temperature at the torque transducer is varied from nominal temperature used during calibration, to a temperature difference of 20°C. The parasitic loads are varied from 0-100%. The result is presented in Table B.1 where the

Table B.1: Sensitivity analysis on measurement uncertainties when measuring between between ±300 Nm with a temperature difference $\Delta\vartheta$ ranging from 0°C to 20°C from calibration temperature and a parasitic load variation ranging from 0% to 100%

u_{dC}	0.09	Nm	
u_{dlh}	0.06	Nm	
u_{dTKC}	0-0.12	Nm	*depending on temperature*
u_{dTK0}	0-0.11	Nm	*depending on temperature*
$u_{d\sigma}$	0.06	Nm	
u_{par}	0-0.17	Nm	*depending on parasitic load*

variation on u_{dTKC} and u_{dTK0} is due to the temperature variation and the variation in u_{par} is due to the order of the parasitic loads.

As can be seen in the table, the largest potential uncertainties come from the temperature effect together with any parasitic loads on the transducer. These are also the two contributors that are affected more by ambient conditions rather than the torque transducer itself. It is therefore not considered when calibrating the sensor and can hence easily be missed when performing the analysis.

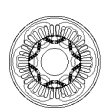

Appendix C

Proximity loss derivation

The derivation of the AC losses in the wires due to proximity effects based on the work in [119] is presented here. The underlying assumption is that the magnetic field, $\mathbf{B}$ is uniform and unidirectional, hence that it is evenly distributed and has one direction only. The magnetic field is defined as

$$\mathbf{B} = B \cdot \sin(\omega t)\, \hat{y} \tag{C.1}$$

with the derivative

$$\frac{\partial \mathbf{B}}{\partial t} = B \cdot \omega \cdot \cos(\omega t)\, \hat{y} \tag{C.2}$$

Maxwell's third equation states that:

$$\nabla \times \mathbf{E} = -\frac{\partial \mathbf{B}}{\partial t} \tag{C.3}$$

where $\mathbf{E}$ is the electric field. The curl of $\mathbf{E}$ is developed to

$$\begin{aligned} \nabla \times \mathbf{E} &= \begin{pmatrix} \hat{x} & \hat{y} & \hat{z} \\ \frac{\partial}{\partial x} & \frac{\partial}{\partial y} & \frac{\partial}{\partial z} \\ E_x & E_y & E_z \end{pmatrix} \\ &= \left[\hat{x} \left(\frac{\partial E_z}{\partial y} - \frac{\partial E_y}{\partial z} \right), \hat{y} \left(\frac{\partial E_x}{\partial z} - \frac{\partial E_z}{\partial x} \right), \hat{z} \left(\frac{\partial E_y}{\partial x} - \frac{\partial E_x}{\partial y} \right) \right] \end{aligned} \tag{C.4}$$

With current running only in the direction of the wires, the electric field is reduced to a $\hat{z}$-component, hence E_x and E_y are equal to zero. From C.2 it is also assumed that the B-field only has a $\hat{y}$-component, hence $\hat{x}$ and $\hat{z}$ are equal to zero as well. This leaves

$$\nabla \times \mathbf{E} = -\hat{y} \frac{\partial E_z}{\partial x} \tag{C.5}$$

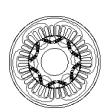

Insertion of this into Maxwell's third equation gives

$$-\hat{y}\frac{\partial E_z}{\partial x} = -\hat{y}B \cdot \omega \cdot \cos(\omega t) \tag{C.6}$$

When solved for $\mathbf{E}$ this becomes

$$\mathbf{E} = \int \frac{\partial E_z}{\partial x}\hat{z}dx = \int B \cdot \omega \cdot \cos(\omega t)\,\hat{z}dx = B \cdot \omega \cdot x \cdot \cos(\omega t)\,\hat{z} \tag{C.7}$$

Power losses in a conductor due to resistance, R and current i can be developed to a function of resistivity ρ and current density $\mathcal{J}$ according to

$$P = R \cdot i^2 = \rho \cdot \mathcal{J}^2 \tag{C.8}$$

With the conductivity being the resistivity inverse and current density being the electric field E times the conductivity σ, the power loss can be re-written to

$$\rho \cdot \mathcal{J}^2 = \frac{1}{\sigma} \cdot (\sigma \cdot E)^2 = \sigma \cdot E^2 \tag{C.9}$$

By replacing E with the previously derived expression (C.7), the average power loss can be determined with (C.10) where the average loss density is integrated over a quarter of a circle and multiplied by 4. With the average value of $\cos^2(\omega t)$ being equal to the average value of $\sin^2(\omega t)$, the Pythagorean trigonometric identity gives that the average of $\cos^2(\omega t) = \frac{1}{2}$.

$$\begin{aligned} P_{wire}^{avg} &= 4 \cdot \int_{x=0}^{r} \int_{y=0}^{\sqrt{r^2-x^2}} \sigma \cdot E^2 dy\,dx \\ &= \frac{1}{2} \cdot \sigma \cdot B^2 \cdot \omega^2 \cdot 4 \int_{x=0}^{r} \int_{y=0}^{\sqrt{r^2-x^2}} x^2 dy\,dx \\ &= \frac{1}{2} \cdot \sigma \cdot B^2 \cdot \omega^2 \cdot 4 \int_{x=0}^{r} x^2 \cdot \sqrt{r^2 - x^2} dx \end{aligned} \tag{C.10}$$

The solution to the standard integral

$$\int x^2 \cdot \sqrt{c^2 - a^2x^2} dx \tag{C.11}$$

is [139, pg.162]

$$\left[-\frac{x\left(c^2 - a^2x^2\right)^{3/2}}{4a^2} + \frac{c^2 x\sqrt{c^2 - a^2x^2}}{8a^2} + \frac{c^4}{8a^3}\arcsin\left(\frac{ax}{c}\right) \right] \tag{C.12}$$

where the two first terms are equal to zero if $a = 1$, $c = r$ and the limit goes from $x = 0 \rightarrow r$. This leaves

$$\left[\frac{r^4}{8}\arcsin\left(\frac{x}{r}\right)\right]_{x=0}^{r} = \frac{r^4}{8}\arcsin\left(\frac{r}{r}\right) - \frac{r^4}{8}\arcsin\left(\frac{0}{r}\right) \tag{C.13}$$

where $\arcsin(1) = \frac{\pi}{2}$ and $\arcsin(0) = 0$. Hence the integration in the last step of C.10 becomes $\frac{r^4}{8} \cdot \frac{\pi}{2} = \frac{\pi}{16} \cdot r^4$. Inserting this into (C.10) finally gives

$$P_{wire}^{avg} = \frac{1}{2} \cdot \sigma \cdot B^2 \cdot \omega^2 \cdot \frac{\pi}{4} \cdot r^4 \tag{C.14}$$

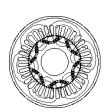

Appendix D

Nomenclature

α_{sh}	Skewing angle [rad]
γ	Loss correction factor for iron core losses with rotational flux [-]
δ	Skin depth [m]
$\Delta\vartheta$	Temperature difference [°C]
ΔB	Magnetic flux density difference [T]
ΔT	Average torque ripple [Nm]
ΔT_{EM}	Peak to peak torque ripple in the electric machine [Nm]
$\Delta T_{Reduction}$	Reduction in torque ripple due to skewing [%]
η	Efficiency [%]
Θ	Rotor position angle [rad]
Θ_{EL}	Electric rotor position angle [rad]
ϑ	Temperature [°C]
ϑ_K	Temperature [K]
λ	Ratio between major and minor flux components [-]
λ_{I}	Relative distance from bearing I to CoG [-]
λ_{II}	Relative distance from bearing II to CoG [-]
μ	Magnetic permeability [H/m]
μ_0	Magnetic permeability of free space [H/m]
μ_r	Relative magnetic permeability [H/m]
μ_{Fe}	Relative magnetic permeability of iron [H/m]
μ_{brush}	Carbon brush friction coefficient [-]

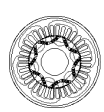

μ_{fb}	Bearing friction coefficient [-]
μ_{sl}	Sliding friction coefficient [-]
μ_{sc}	Sliding friction coefficient at standstill [-]
μ_{FF}	Sliding friction coefficient at full-film conditions [-]
μ_{seal}	Friction coefficient of the oil seal lip to shaft contact [-]
ν_{air}	Dynamic viscosity of air [Pa·s]
ν_g	Operating viscosity of the bearing grease [Pa·s]
ρ	Electrical resistivity [Ω·m]
ρ_{Cu}	Resistivity of copper [Ω·m]
ρ_{air}	Density of air [kg/m^3]
σ	Electrical conductivity [S/m]
σ_{rel}	Relative standard deviation [-]
σ_{yield}	Yield strength [Pa]
τ	Sheer stress [Pa]
ϕ	Angle between voltage and current [rad]
ΦA, B & C	Phase A, B & C
ψ	Magnetic flux linkage [Wb]
ψ_{dq}	Magnetic flux linkage in the rotating reference frame [Wb]
ψ_{dq}^{meas}	Measured magnetic flux linkage in the rotating reference frame [Wb]
ψ_{dq}^{sim}	Simulated magnetic flux linkage in the rotating reference frame [Wb]
ω	Angular frequency [rad/s]
ω_{crit}	Critical resonance rotational speed [rad/s]
ω_e	Electrical angular frequency [rad/s]
ω_m	Mechanical rotational speed [rad/s]
ω_{max}	Maximum rotational speed [rad/s]
∇	Vector differential operator
$\varnothing$	Diameter [m]
A	Area [m^2]
A_{cond}	Cross sectional area of a conductor [m^2]
A_d	Area of the magnetic path through the air(gap) [m^2]
A_{Fe}	Area of the magnetic path through iron [m^2]
A_{PM}	Area of the magnetic path through magnets [m^2]
A_{slot}	Stator slot area [m^2]
$\mathbf{B}$	Magnetic field vector [T]

B	Magnetic flux density [T]
B_d	Magnetic flux density in the air(gap) [T]
B_r	Magnetic remanence (residual magnetism) [T]
B_{Fe}	Magnetic flux density in iron [T]
B_{leak}	Magnetic flux density leaking through a stator slot [T]
B_m	Instantaneous value of the magnetic flux density [T]
B_{Maj}	Major flux density component [T]
B_{max}	Maximum magnetic flux density [T]
B_{Min}	Minor flux density component [T]
B_{min}	Minimum magnetic flux density [T]
B_{peak}	Peak value of the magnetic flux density [T]
B_{0PM}	Magnetic flux density in a magnet due to the permanent magnetization [T]
B_{PM}	Magnetic flux density in magnets [T]
c_{an}	Anomalous loss coefficient[1]
c_{ec}	Eddy current loss coefficient[1]
c_{hy}	Hysteresis loss coefficient[1]
$\cos\phi$	Power factor [-]
C_{an}	Coefficient associated to anomalous power losses [-]
C_F	Correction factor for the rolling resistance [-]
C_f^{env}	Viscous drag coefficient for the envelope surface [-]
C_f^{gab}	Viscous drag coefficient for the gables [-]
d_σ	Standard deviation in the torque transducer [-]
d_b	Width of the iron bridge between two adjacent magnets [m]
d_{brush}	Carbon brush contact diameter [mm]
d_B	Bearing bore diameter [mm]
d_C	Deviation in the torque transducer due to sensitivity tolerances [-]
d_g	Radial airgap distance [m]
d_{lam}	Lamination thickness [mm]
d_{lh}	Deviation in the torque transducer due to linearity and hysteresis [-]
d_{seal}	Inner diameter of the oil seal [mm]
d_{TK0}	Deviation of the zero signal in the torque transducer due to temperature [-]
d_{TKC}	Deviation in the torque transducer due to temperature [-]

[1] No units are allocated to these coefficients since they represent empirical observations rather than underlying physics [21, 61]

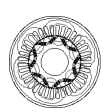

e_{hy}	Hysteresis loss exponent [-]
e_r	Rotor eccentricity (rotor imbalance) [μm]
$\mathbf{E}$	Electric field vector [V/m]
E	Electric field [V/m]
E_{Fe}	Young's modulus for steel [MPa]
f	Frequency [Hz]
f_{eq}	Equivalent frequency [Hz]
f_m	Factor for the relation between static and dynamic bearing forces [-]
F	Force [N]
F_b	Bearing force [N]
F_{brush}	Force applied by the carbon brush [N]
F_D	Dynamic centrifugal force [N]
F_E	Externally applied force [N]
F_G	Gravitational force [N]
F_{seal}	Force applied by the oil sealing [N]
F_{seal}^{line}	Line force in oil sealing [N/m]
g	Gravitational acceleration [m/s^2]
G_{sl}	Sliding frictional variable [-]
G_{rr}	Rolling frictional variable [-]
h_a	Harmonic order [-]
h_m	Machine height (active length) [m]
H_c	Magnetic coercivity [kA/m]
H_cB	Normal magnetic coercivity [kA/m]
H_cI	Intrinsic magnetic coercivity [kA/m]
H_{irr}	Irreversible hysteresis losses [W/kg]
i	Alternating current [A]
$i_{\alpha\beta}$	Currents in the stationary reference frame [A]
i_{abc}	Currents in the 3-phase system [A]
i_{dq}	Currents in the rotating reference frame [A]
i_{max}	Maximum current [A]
I	Direct current [A]
I_{rms}	Rms current [Arms]
$\mathcal{J}$	Current density [A/m^2]
J	Moment of inertia [kg·m^2]

J_{ext}	Moment of inertia of an external flywheel [kg·m^2]
J_{rotor}	Moment of inertia of the rotor [kg·m^2]
J_{tot}	Total moment of inertia [kg·m^2]
k_{fill}	Stator slot fill factor [-]
$k_{m,Fe}$	Factor considering iron the core mass and number of poles [kg]
k_{mr}	Factor for the mechanical remanence in the torque transducer [-]
k_{sh}	Skewing factor [-]
k_{sh}^{ap}	Apparent skewing factor acting on the torque [-]
$k_{sh}^{\lvert\psi\rvert}$	Apparent skewing factor acting on the linked magnetic flux [-]
k_{sr}	Surface roughness coefficient [-]
l	Length [m]
l_a	Active electric machine length [m]
l_{active}	Total active conductor length [m]
l_b	Distance between the bearings [m]
l_{cond}	Total conductor length [m]
l_d	Airgap distance [m]
l_{EW}	Total endwinding conductor length [m]
l_{Fe}	Length of the magnetic path through iron [m]
l_{PM}	Lenght of the magnetic path through magnets [m]
l_{prox}	Total conductor length when considering proximity losses [m]
l_R	Rotor length [m]
l_{tot}	Total (overall) machine length [m]
L_{par}	Parasitic load acting on the torque transducer [N]
$L_{par,ref}$	Maximum permissible parasitic load on the torque transducer [N]
m	Mass [kg]
m_{act}	Mass acting on the iron bridge between two adjacent magnets during rotation [kg]
m_{Fe}	Iron core mass [kg]
$m_{Fe,th}$	Stator teeth iron core mass [kg]
$m_{Fe,yk}$	Stator yoke iron core mass [kg]
m_r	Rotor mass [kg]
M_{Area}	Area moment of inertia [m^4]
n_{base}	Base speed [rpm]
n_{burst}	Burst speed [rpm]
n_{max}	Maximum operational speed [rpm]

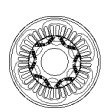

N	Number of turns in a coil [-]
N_{brush}	Number of carbon brushes [-]
N_c	Number of conductors in a stator slot [-]
N_p	Number of poles [-]
N_s	Number of slots in the stator [-]
p	Absolute pressure [Pa]
p_{an}	Anomalous power losses [W/kg]
p_{ec}	Eddy current power losses [W/kg]
p_{hy}	Hysteresis power losses [W/kg]
p_{Fe}	Iron core power losses [W/kg]
$p_{Fe,th}$	Stator teeth iron core power losses [W/kg]
$p_{Fe,yk}$	Stator yoke iron core power losses [W/kg]
P_{air}	Air friction, or windage power losses [W]
P_{air}^{env}	Air friction, or windage power losses at the rotor envelope surface [W]
P_{air}^{gab}	Air friction, or windage power losses at the rotor gables [W]
P_B	Bearing power losses [W]
$P_{Bearing}$	Bearing power losses [W]
P_{brush}	Carbon brush power losses [W]
P_{cont}	Continuous power [W]
P_{Cu}	Copper power losses in the stator windings [W]
P_{Cu}^{DC}	DC copper power losses in the stator windings [W]
P_{Cu}^{prox}	Total average proximity power losses [W]
P_{el}	Electric power to/from the machine [W]
P_{Fe}	Iron core power losses in the stator [W]
$P_{Fe}^{0\,\mathrm{deg}}$	Iron core power losses in the stator in the major flux density direction [W]
$P_{Fe}^{90\,\mathrm{deg}}$	Iron core power losses in the stator in the minor flux density direction [W]
P_{Fe}^{Corr}	Power losses in the iron core from simulations corrected based on measurements [Nm]
$P_{Fe,FEMM}$	Iron core power loss estimation from simulations in FEMM [14] [W]
$P_{Fe,Maxwell}$	Iron core power loss estimation from simulations in Ansys Maxwell [96] [W]
$P_{Fe}^{Orginal}$	Iron core power losses in the stator estimated during the design stage [W]
P_{Fe}^{rot}	Iron core power losses with consideration to rotational flux density variation [W]
P_{in}	Power going in to the electric machine [W]
P_{Loss}	Overall power losses in the electric machine [W]
P_{Loss}^{Corr}	Total mechanical and iron core power losses from corrected simulation model [W]

P_{Loss}^{sim}	Total mechanical and iron core power losses from original simulation model [W]
P_{mech}	Mechanical power losses [W]
P_{out}	Power going out from the electric machine [W]
P_{peak}	Peak power [W]
$P_{peak\ sim}$	Peak Power according to simulations [W]
P_{rotor}	Power losses in the rotor [W]
P_{seal}	Oil seal power losses [W]
P_{shaft}	Mechanical power measured on the electric machine shaft [W]
P_{wire}^{avg}	Average power losses per unit length in a wire due to proximity effects [W/m]
r	Radius [m]
r_A	Airgap radius [m]
r_{act}	Radius to CoG of the mass m_{act} [m]
r_{in}	Inner rotor radius [m]
r_{ish}	Reduction factor for inlet shear heating in bearings [-]
r_{rs}	Reduction factor for kinematic replenishment in bearings [-]
r_w	Weighting factor for the sliding friction [-]
r_{wire}	Radius of a conducing wire [m]
R	Resistance [Ω]
R_1	Rolling frictional constant [-]
R_A	Specific gas constant of air [-]
R_s	Stator resistance [Ω]
$R_{s,DC}$	DC stator resistance [Ω]
Re_δ	Couette Reynolds number [-]
Re_a	Reynolds number for axial airflow in the airgap[-]
Re_r	The tip Reynolds number [-]
RTC	Reversible temperature coefficient of the permanent magnets [%/°C]
s	Axial distance from a rotor gable to the opposing stationary housing gable [m]
S_1	Sliding frictional constant [-]
S_{EW}	Temperature sensor located in the end windings of phase A
S_{DE}	Temperature sensor located at the driving end bearing
S_{HS}	Temperature sensor located at hotspot of phase A
S_{NDE}	Temperature sensor located at the non driving end bearing
S_{SB}	Temperature sensor located at the stator back outside of phase A
t	Time [s]

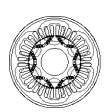

tc_{Cu}	Temperature coefficient of copper [K^{-1}]
T	Torque [Nm]
T_B^{Loss}	Loss torque in the bearings [Nmm]
$T_{B,drag}$	Bearing loss torque due to drag losses [Nmm]
$T_{B,rr}$	Bearing loss torque due to rolling resistance [Nmm]
$T_{B,seal}$	Bearing loss torque due to friction in the bearing seal [Nmm]
$T_{B,sl}$	Bearing loss torque due to sliding friction [Nmm]
T_{brush}	Loss torque in the carbon brushes [Nmm]
T_{cont}	Continuous torque [Nm]
T_{em}	Electromagnetic torque [Nm]
T_{EM}	Electric machine torque [Nm]
T_{Loss}	Loss torque [Nm]
T_{Loss}^{Corr}	Loss torque from simulations, corrected based on measurements [Nm]
T_{Loss}^{sim}	Loss torque from simulations due to mechanical- and iron losses [Nm]
$T_{Loss,Fe}$	Loss torque due to iron losses [Nm]
$T_{Loss,Fe}^{sim}$	Loss torque due to iron losses from simulations in FEMM [14] [Nm]
$T_{Loss,Fe}^{sim,Maxwell}$	Loss torque due to iron losses from simulations in Ansys Maxwell [96] [Nm]
T_{max}	Maximum torque of the application [Nm]
T_{mech}	Loss torque due to mechanical losses [Nm]
T_{meas}	Measured Torque [Nm]
T_{meas}^{+}	Measured positive Torque [Nm]
T_{meas}^{-}	Measured negative Torque [Nm]
T_{min}	Minimum torque of the application [Nm]
T_{nom}	Measuring range of the torque transducer [Nm]
T_{peak}	Peak Torque [Nm]
T_{seal}	Loss torque in the oil seal [Nmm]
TK_0	Temperature effects on the torque transducer zero signal [-]
TK_C	Temperature effects on the torque transducer reading [-]
u_{dq}	Voltages in the rotating reference frame [V]
$u_{d\sigma}$	Measurement uncertainty due to the standard deviation [Nm]
u_{dC}	Measurement uncertainty due to the sensitivity tolerance deviation [Nm]
u_{dlh}	Measurement uncertainty due to the linear deviation [Nm]
u_{dTK0}	Measurement uncertainty due to the torque transducer zero signal deviaiton [Nm]
u_{dTKC}	Measurement uncertainty due to the torque transducer temperature deviation [Nm]

u_n	Measurement uncertainty on negative torque readings [Nm]
u_p	Measurement uncertainty on positive torque readings [Nm]
u_{par}	Measurement uncertainty due to parasitic loads on the torque transducer [Nm]
v_1	Peripheral rotor speed [m/s]
v_{axial}	Axial air flow in the air-gap [m^3/s]
$\hat{x}$	Unit vector in x-direction
X	Unitless parameter for evaluating the skin depth [-]
$\hat{y}$	Unit vector in y-direction
$\hat{z}$	Unit vector in z-direction

2D	Two Dimensional
3D	Three Dimensional
AC	Alternating Current
AMT	Automatic Mechanically engaged Transmission
AP	Axial field die Pressed
CAD	Computer-Aided Design
CFD	Computational Fluid Dynamics
CO_2	Carbon Dioxide
CoG	Center of Gravity
CPSR	Constant Power Speed Range
DC	Direct Current
DE	Driving End
EM	Electric Machine
Emf	Electro-motive force
ESS	Energy Storage System
EV	Electric Vehicle
EW	End Windings
FE	Finite Element
FEA	Finite Element Analysis
FEM	Finite Element Modelling
FFT	Fast Fourier Transform
FPGA	Field-Programmable Gate Array
HEV	Hybrid Electric Vehicle
HS	Hot Spot

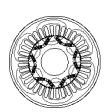

IEA	Division of Industrial Electrical Engineering and Automation
ICE	Internal Combustion Engine
ID	Inner Diameter
IPMSM	Interior Permanent Magnet Synchronous Machine
LCA	Life Cycle Assessment
LTH	Faculty of Engineering at Lund University
MTPA	Maximum Torque Per Ampere
MFPT	Minimum Flux Per Torque
MMF	Magnetomotive Force
MSE	Modified Steinmetz Equation
NdFeB	Neodymium-Iron-Boron
NDE	Non-Driving End
OD	Outer Diameter
ppm	parts per million
PEC	Power Electronic Converter
PM	Permanent Magnet(s)
PMSM	Permanent Magnet Synchronous Machine
PTO	Power Take Off
PWM	Pulse Width Modulation
rms	root mean square
RTC	Reversible Temperature Coefficient
RTD	Resistance Temperature Detector
SAE	Society of Automotive Engineers
SB	Stator Back
THD	Total Harmonic Distortion
TP	Transverse field die Pressed
WEG	Water/Ethylene/Glycol

Bibliography

[1] Rasmus Andersson. *Electric Traction Machine Design for Heavy Hybrid Vehicles*. Licentiate thesis, Lund University, Lund, Sweden, 2014.

[2] Avo Reinap, Dan Hagstedt, Francisco Márquez, Yury Loayza, and Mats Alaküla. Development of a radial flux machine design environment. *Proceedings of the 2008 International Conference on Electrical Machines, ICEM'08*, 2008.

[3] Malin Reinholds and Steve Andreasson. *Dynamic gear shifting of an automated manual transmission*. Master thesis, Lund University, 2013.

[4] Erik Hoevenaars. *Integrated charging systems for heavy hybrid vehicles*. Master thesis, Eindhoven University of Technology, 2013.

[5] Johanna Aspenberg. *Integrerad laddning - design av komponenter*. Master thesis, Lund University, 2013.

[6] E. Andersson and J. Schöld. *Integrated Charging - Concept Evaluation*. Master thesis, Lund University, 2014.

[7] SAE. Engine Flywheel Housing and Mating Transmission Housing Flanges J617_201404, 2014.

[8] T. A. Lipo. *Introduction to AC Machine Design*. University of Wisconsin, Madison, WI, 2000.

[9] T. J. E. Miller. *Brushless Permanent-Magnet and Reluctance Motor Drives*. Oxford: Clarendon, Oxford, 1989.

[10] Karin Jonasson. *Control of Hybrid Electric Vehicles with Diesel Engines*. PhD thesis, Lund University, Lund, Sweden, 2005.

[11] Mats Alaküla, Karin Jonasson, Christian Andersson, Bengt Simonsson, and S. Marksell. Hybrid drive systems for vehicles, part 1 Course material, 2010.

[12] Zhe Huang, Shafigh Nategh, Viktor Lassila, Mats Alaküla, and Jinliang Yuan. Direct oil cooling of traction motors in hybrid drives. *2012 IEEE International Electric Vehicle Conference, IEVC 2012*, 2012.

[13] Alfredo Vagati, Gianmario Pellegrino, and Paolo Guglielmi. Comparison between SPM and IPM motor drives for EV application. *19th International Conference on Electrical Machines, ICEM 2010*, 2010.

[14] D. C. Meeker. Finite Element Method Magnetics Version 4.0.1, 2006.

[15] Francisco J. Márquez-Fernández. *Electric Traction Machine Design for an E-RWD Unit*. PhD thesis, Lund University, Lund, Sweden, 2014.

[16] Juha Pyrhonen, Tapani Jokinen, and Valeria Hrabovcova. *Design of Rotating Electrical Machines*. John Wiley & Sons, Ltd, 2008.

[17] Conny Högmark. *Moulded Electrical Machines and Laminated Windings*. Licentiate thesis, Lund University, Lund, 2013.

[18] Conny Högmark, Rasmus Andersson, Avo Reinap, and Mats Alaküla. Electrical Machines with Laminated Winding for Hybrid Vehicle Applications. *Electric Drives Production Conference (EDPC), 2012 2nd International*, 2:1–6, 2012.

[19] Rasmus Andersson, Conny Högmark, Avo Reinap, and Mats Alaküla. Electrical Machines with Laminated Winding for Hybrid Vehicle Applications. In *Electric Drives Production Conference (EDPC), 2012 2nd International*, volume 2, pages 1–7, Nuremberg, 2012.

[20] Avo Reinap, Francisco J Márquez-Fernández, Rasmus Andersson, Conny Högmark, Mats Alaküla, and Anders Göransson. Heat Transfer Analysis of a Traction Machine with Directly Cooled Laminated Windings. *Electric Drives Production Conference (EDPC), 2014 4th International*, (4):1–7, 2014.

[21] K.H.J. Buschow. *Concise encyclopedia of magnetic & superconducting materials*. ELSEVIER, Oxford, 2 edition, 2005.

[22] VACUUMSCHMELZE GmbH & Co. KG. Vacodym 863 TP Data sheet. `www.vacuumschmelze.com/en/products/permanent-magnets-assemblies/permanent-magnets/nd-fe-b/vacodym/vacodym-863-tp.html`, 2015. [Online; Last accessed on 2018-12-04].

[23] Niels Saabye Ottosen, Matti Ristinmaa, and Christer Ljung. *Hållfasthetslära Allmänna tillstånd*. Studentlitteratur, 1 edition, 2007.

[24] Yury Alcides Loayza Vargas. *Highly Dynamic Drives for Electric Hybrid Vehicles*. PhD thesis, Lund University, Lund, Sweden, 2017.

[25] Yury Loayza, Avo Reinap, and Mats Alaküla. Performance and efficiency evaluation of FPGA controlled IPMSM under dynamic loading. *Diagnostics for Electric Machines, Power Electronics & Drives (SDEMPED), 2011 IEEE International Symposium on*, pages 550–555, 2011.

[26] Sebastian Hall, Yury Loayza, Avo Reinap, and Mats Alakula. Consistency analysis of torque measurements performed on a PMSM using dynamic testing. *Proceedings - 2014 International Conference on Electrical Machines, ICEM 2014*, pages 1529–1535, 2014.

[27] Francisco J. Márquez-Fernández, Sebastian Hall, and Mats Alaküla. Dynamic Testing Characterization of a HEV Traction Motor. *Proceedings - 2014 International Conference on Electrical Machines, ICEM 2014*, pages 1569–1575, 2014.

[28] HBM. *T12 Digital Torque Transducer Data Sheet, B1941-5.1 en*. Hottinger Baldwin Messtechnik GmbH, Darmstadt, Germany.

[29] SEMIKRON International GmbH. SKAI® 2 power electronic system. `www.semikron.com/products/product-lines/skai.html`, 2018. [Online; Last accessed on 2018-12-04].

[30] Greg Stone, Edward A. Boulter, Ian Culbert, and Hussein Dhirani. *Electric Insulation for rotating machines, Design, Evaluation, Aging, Testing and Repair*. John Wiley & Sons, 2004.

[31] Andreas Krings, Seyed Ali Mousavi, Oskar Wallmark, and Juliette Soulard. Temperature Influence of NiFe Steel Laminations on the Characteristics of Small Slotless Permanent Magnet Machines. *IEEE Transactions on Magnetics*, 49(7):4064–4067, 2013.

[32] Norio Takahashi, Masayuki Morishita, Daisuke Miyagi, and Masanori Nakano. Comparison of Magnetic Properties of Magnetic Materials at High Temperature. *IEEE Transactions on Magnetics*, 47(10):4352–4355, 2011.

[33] R Andersson and S Hall. Evaluation of a Temperature Model for an Interior Permanent Magnet Synchronous Machine for Parallel Hybrid Electric Heavy Vehicles. *Power Electronics, Electrical Drives, Automation and Motion (SPEEDAM), 2016 International Symposium on*, pages 419–424, 2016.

[34] W. Q. Chu and Z. Q. Zhu. Investigation of Torque Ripples in Permanent Magnet Synchronous Machines With Skewing. *IEEE Transactions on Magnetics*, 49(3):1211–1220, 2013.

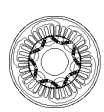

[35] Rajesh P. Deodhar, David A. Staton, and Timothy J E Miller. Modeling of Skew Using the Flux-MMF Diagram. *IEEE Transactions on Industry Applications*, 32(6):1339–1347, 1996.

[36] G. Y. Sizov, P. Zhang, D. M. Ionel, N. A O Demerdash, I. P. Brown, A. O. Smith, and M. G. Solveson. Modeling and Analysis of Effects of Skew on Torque Ripple and Stator Tooth Forces in Permanent Magnet AC Machines. *2012 IEEE Energy Conversion Congress and Exposition, ECCE 2012*, pages 3055–3061, 2012.

[37] Oskar Wallmark. *AC Machine Analysis – Fundamental Theory*. KTH, Stockholm Sweden, Stockholm, 2017.

[38] Yongheng Yang, Keliang Zhou, Huai Wang, and Frede Blaabjer. Harmonics Mitigation of Dead Time Effects in PWM Converters Using a Repetitive Controller. *Applied Power Electronics Conference and Exposition (APEC), 2015 IEEE*, pages 1479–1486, 2015.

[39] Raja Ramakrishnan, Abraham Gebregergis, Mohammad Islam, and Tomy Sebastian. Effect of position sensor error on the performance of PMSM drives for low torque ripple applications. *Proceedings of the 2013 IEEE International Electric Machines and Drives Conference, IEMDC 2013*, pages 1166–1173, 2013.

[40] Andreas Bünte and Stephan Beineke. High-Performance Speed Measurement by Suppression of Systematic Resolver and Encoder Errors. *IEEE Transactions on Industrial Electronics*, 51(1):49–53, 2004.

[41] H. S. Mok, S. H. Kim, and Y. H. Cho. Reduction of PMSM torque ripple caused by resolver position error. *Electronics Letters*, 43(11):646–647, 2007.

[42] Jorge Lara, Jianhong Xu, and Ambrish Chandra. Effects of Rotor Position Error in the Performance of Field Oriented Controlled PMSM Drives for Electric Vehicle Traction Applications. *IEEE Transactions on Industrial Electronics*, 0046(c):1–1, 2016.

[43] Fang Deng. An improved iron loss estimation for permanent magnet brushless machines. *IEEE Transactions on Energy Conversion*, 14(4):1391 – 1395, 1999.

[44] Dianhai Zhang, Fengxiang Wang, and Xiaoguang Kong. Air friction loss calculation of high speed permanent magnet machines. *2008 International Conference on Electrical Machines and Systems*, pages 320–323, 2008.

[45] Wang Jiqiang, Wang Fengxiang, and Yu Tao. Analysis of rotor losses for a high speed PM generator. *2005 International Conference on Electrical Machines and Systems*, 2, 2005.

[46] John C. Dixon. *The Shock Absorber Handbook: Second Edition*. John Wiley & Sons, Ltd, 2007.

[47] Juha Saari. *Thermal analysis of High speed Induction Machines*. PhD thesis, Helsinki University of Technology, Helsinki, 1998.

[48] Heinz Heisler. *Advanced vehicle technology*. Butterworth-Heinemann, Oxford, 2 edition, 2002.

[49] SKF Group. Rolling bearings. PUB BU/P1 10000/2 EN, 2013.

[50] Carl Norling and Jonny Österman. *Physics Handbook for Science and Engineering*. Studentlitteratur, Lund, Sweden, Lund, 6 edition, 2002.

[51] ISO - International Organization for Standardization. ISO 1940-1 - Mechanical vibration – Balance quality requirements for rotors in a constant (rigid) state – Part 1: Specification and verification of balance tolerances, 2003.

[52] Papa Diouf and Walt Herbert. Understanding rotor balance for electric motors. In *Conference Record of 2014 Annual Pulp and Paper Industry Technical Conference*, pages 7–17, Atlanta, GA, USA, 2014. IEEE.

[53] Shaotang Chen, Thomas A. Lipo, and Dennis Fitzgerald. Modeling of motor bearing currents in PWM inverter drives. *IEEE Transactions on Industry Applications*, 32(6):1365–1370, 1996.

[54] Morgan AM&T. *Book 1 How to Select Carbon Brushes for Motors and Generators*. Greenville, SC.

[55] F Magnussen, E Nordlund, S Châtelet, and C Sadarangani. Measurements on Slip Ring Units for Characterization of Performance. *IPEC 2003 - 6th International Power Engineering Conference*, (6), 2013.

[56] Martin Schuster and Andreas Binder. Comparison of different inverter-fed AC motor types regarding common-mode bearing currents. *2015 IEEE Energy Conversion Congress and Exposition (ECCE)*, pages 2762–2768, 2015.

[57] M. Schuster, D. Masendorf, and A. Binder. Two PMSMs and the influence of their geometry on common-mode bearing currents. *Proceedings - 2016 22nd International Conference on Electrical Machines, ICEM 2016*, pages 2126–2132, 2016.

[58] DIN 3760. Rotary Shaft Lip Type Seals. Technical report, Deutsches Institut für Normung e.V., Berlin, 1996.

[59] Daniel Frölich, Balázs Magyar, and Bernd Sauer. Semi-Analytical Model for the Contact Temperature Calculation in Radial Shaft. In *STLE Annual Meeting*, pages 1–5, Lake Buena Vista, Florida, 2014.

[60] Simon Plath, Stefan Meyer, and V. M. Wollesen. Friction torque of a rotary shaft lip type seal - A comparison between test results and finite element simulation. *Mechanika*, 4:55–59, 2005.

[61] Giorgio Bertotti. General Properties of Power Losses in Soft Ferromagnetic Materials. *IEEE Transactions on Magnetics*, 24(1):621–630, 1988.

[62] Jürgen Reinert, Ansgar Brockmeyer, and Rik W A A De Doncker. Calculation of Losses in Ferro- and Ferrimagnetic Materials Based on the Modified Steinmetz Equation. *IEEE Transactions on Industry Applications*, 37(4):1055–1061, 2001.

[63] Giorgio Bertotti. Magnetic Losses. In K. H. J. Buschow, editor, *Concise encyclopedia of magnetic & superconducting materials*, pages 463–469. Elsevier, Oxford, 2 edition, 2005.

[64] D. Lin, P. Zhou, W. N. Fu, Z. Badics, and Z. J. Cendes. A dynamic core loss model for soft ferromagnetic and power ferrite materials in transient finite element analysis. *IEEE Transactions on Magnetics*, 40(2 II):1318–1321, 2004.

[65] Yujing Liu, S. K. Kashif, and A. M. Sohail. Engineering considerations on additional iron losses due to rotational fields and sheet cutting. *Proceedings of the 2008 International Conference on Electrical Machines, ICEM'08*, pages 1–4, 2008.

[66] Andreas Krings and Juliette Soulard. Overview and Comparison of Iron Loss Models for Electrical Machines. *Journal of Electrical Engineering*, 10:162–169, 2010.

[67] Erik Lamprecht, Martin Homme, and Thomas Albrecht. Investigations of eddy current losses in laminated cores due to the impact of various stacking processes. *2012 2nd International Electric Drives Production Conference, EDPC 2012 - Proceedings*, pages 1–8, 2012.

[68] Lode Vandenbossche, Sigrid Jacobs, Xavier Jannot, Mike McClelland, Jacques Saint-Michel, and Emmanuel Attrazic. Iron loss modelling which includes the impact of punching, applied to high-efficiency induction machines. *2013 3rd International Electric Drives Production Conference, EDPC 2013 - Proceedings*, 2013.

[69] M Reinlein, T Hubert, A Hoffmann, and A Kremser. Optimization of analytical iron loss approaches for electrical machines. *Electric Drives Production Conference (EDPC), 2013 3rd International*, pages 1–7, 2013.

[70] M. Van Der Geest, H. Polinder, and J. A. Ferreira. Influence of PWM switching frequency on the losses in PM machines. *Proceedings - 2014 International Conference on Electrical Machines, ICEM 2014*, pages 1243–1247, 2014.

[71] G von Pfingsten, S Steentjes, A Thul, T Herold, K Hameyer, and Senior Member Ieee. Soft Magnetic Material Degradation due to Manufacturing Process : A Comparison of Measurements and Numerical Simulations. *Electrical Machines and Systems (ICEMS), 2014 17th International Conference on*, pages 2018–2024, 2014.

[72] Chao Chien Chiang, Andrew M. Knight, Min Fu Hsieh, Mu Gong Tsai, Bernard Haochih Liu, In Gann Chen, Zwe Lee Gaing, and Mi Ching Tsai. Effects of annealing on magnetic properties of electrical steel and performances of SRM after punching. *IEEE Transactions on Magnetics*, 50(11), 2014.

[73] Anouar Belahcen, Paavo Rasilo, Thu-Trang Nguyen, and Stephane Clénet. Uncertainty propagation of iron loss from characterization measurements to computation of electrical machines. *COMPEL: The International Journal for Computation and Mathematics in Electrical and Electronic Engineering*, 34(3):624–636, 2014.

[74] Steve Sprague. Examining magnetic property variation: A look at specification-acceptable electrical steel. *IEEE Industry Applications Magazine*, 20(1):33–40, 2014.

[75] Greg Heins, Dan M Ionel, Dean Patterson, and Steve Stretz. Combined Experimental and Numerical Method for Loss Separation in Permanent Magnet Brushless Machines. *IEEE Transactions on Industry Applications*, 52(2):1791–1798, 2014.

[76] Rafael K. Jardan, Zoltan Varga, Peter Stumpf, Istvan Nagy, Christian Endisch, Peter Sipos, and Miklos Simon. Development of a dedicated laboratory system for measurement of iron losses in high speed PMSM. In *Proceedings of the IEEE International Conference on Industrial Technology*, number June, pages 708–713, 2015.

[77] Rafal Wrobel, Phil Mellor, Mircea Popescu, and Dave Staton. Power Loss Analysis in Thermal Design of Permanent Magnet Machines – A Review. *IEEE Transactions on Industry Applications*, PP(99):1–1, 2015.

[78] Chao Chien Chiang, Min Fu Hsieh, Yu Hsien Li, and Mi Ching Tsai. Impact of Electrical Steel Punching Process on the Performance of Switched Reluctance Motors. *IEEE Transactions on Magnetics*, 51(11):2474, 2015.

[79] Hristian Naumoski, Andreas Maucher, and Ulrich Herr. Investigation of the influence of global stresses and strains on the magnetic properties of electrical steels with varying alloying content and grain size. *2015 5th International Conference on Electric Drives Production, EDPC 2015 - Proceedings*, pages 1–8, 2015.

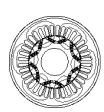

[80] Damian Kowal, Peter Sergeant, Luc Dupre, and Lode Vandenbossche. Comparison of iron loss models for electrical machines with different frequency domain and time domain methods for excess loss prediction. *IEEE Transactions on Magnetics*, 51(1), 2015.

[81] Markus Hofmann, Hristian Naumoski, Ulrich Herr, and Hans Georg Herzog. Magnetic Properties of Electrical Steel Sheets in Respect of Cutting: Micromagnetic Analysis and Macromagnetic Modeling. *IEEE Transactions on Magnetics*, 52(2), 2016.

[82] Marc Veigel, Alexandra Kramer, Gisela Lanza, and Martin Doppelbauer. Investigation of the impact of production processes on iron losses of laminated stator cores for electric machines. *ECCE 2016 - IEEE Energy Conversion Congress and Exposition, Proceedings*, pages 1–5, 2016.

[83] K Bourchas, A Stening, J Soulard, A Broddefalk, M Lindenmo, M Dahlén, and F Gyllensten. Quantifying Effects of Cutting and Welding on Magnetic Properties of Electrical Steels. *IEEE Transactions on Industry Applications*, 53(5):4269 – 4278, 2016.

[84] T. Kochmann. Relationship between rotational and alternating losses in electrical steel sheets. *Journal of Magnetism and Magnetic Materials*, 160:145–146, 1996.

[85] Carlos A. Hernandez-Aramburo, Tim C. Green, and Alexander C. Smith. Estimating Rotational Iron Losses in an Induction Machine. *IEEE Transactions on Magnetics*, 39(6):3527–3533, 2003.

[86] Aroba Saleem, Natheer Alatawneh, Richard R Chromik, and David A Lowther. Effect of Shear Cutting on Microstructure and Magnetic Properties of Non-Oriented Electrical Steel. *IEEE Transactions on Magnetics*, 52(5):1–4, 2016.

[87] A.C. Smith and K Edey. Influence of manufacturing processes on iron losses. In *1995 Seventh International Conference on Electrical Machines and Drives (Conf. Publ. No. 412)*, number 412, pages 77–81, Durham, UK, 1995. IET.

[88] Madeleine Bali and Annette Muetze. The degradation depth of non-grain oriented electrical steel sheets of electric machines due to mechanical and laser cutting : A state-of-the-art review. *IEEE Transactions on Industry Applications*, PP(c):1, 2018.

[89] Chas. Proteus Steinmetz. American Institute of Electrical Engineers. *Transactions of the American Institute of Electrical Engineers*, IX(1):1–64, 1892.

[90] A. Hernando, P. Crespo, P. Marín, and A. González. Magnetic Hysteresis. In K. H. J. Buschow, editor, *Concise encyclopedia of magnetic & superconducting materials*, pages 444–451. Elsevier, Oxford, 2 edition, 2005.

[91] Eddie van Halen, Alex van Halen, Michael Anthony, and David Lee Roth. Jump, 1983.

[92] Methods of Measurement of the Magnetic Properties of the Electrical Steel Strip and Sheet by Means of Epstein Frame. International Standard, IEC 60404-2, 2008.

[93] Shaoshen Xue, Jianghua Feng, Shuying Guo, Jun Peng, W Q Chu, and Z Q Zhu. A New Iron Loss Model for Temperature Dependencies of Hysteresis and Eddy Current Losses in Electrical Machines. *IEEE Transactions on Magnetics*, 54(1):1–10, 2018.

[94] Edoardo Barbisio, Fausto Fiorillo, and Carlo Ragusa. Predicting Loss in Magnetic Steels Under Arbitrary Induction Waveform and With Minor Hysteresis Loops. *IEEE Transactions on Magnetics*, 40(4):1810–1819, 2004.

[95] Shaoshen Xue, Jianghua Feng, Shuying Guo, Zhichu Chen, Jun Peng, W Q Chu, P L Xu, and Z Q Zhu. Iron Loss Model for Electrical Machine Fed by Low Switching Frequency Inverter. *IEEE Transactions on Magnetics*, 53(11):2–5, 2017.

[96] Ansys®, Electromagnetics Suite, Release 16.2.

[97] S. Steentjes, D. Franck, K. Hameyer, S. Vogt, M. Bednarz, W. Volk, J. Dierdorf, G. Hirt, V. Schnabel, H. N. Mathur, and S. Korte-Kerzel. On the effect of material processing: microstructural and magnetic properties of electrical steel sheets. *2014 4th International Electric Drives Production Conference (EDPC)*, pages 1–7, 2014.

[98] Ravi Sundaria, D G Nair, A Lehikoinen, A Arkkio, and A Belahcen. Loss Model for The Effects of Steel Cutting in Electrical Machines. In *2018 XIII International Conference on Electrical Machines (ICEM)*, pages 1260–1266, Alexandroupoli, Greece, 2018. IEEE.

[99] Cogent Power Limited. Non-Oriented Electrical Steel - Technical Properties Coatings. `www.cogent-power.com/products/non-oriented-electrical-steel/technical-specifications/technical-properties-coatings`, 2018. [Online; Last accessed on 2018-12-04].

[100] Daisuke Miyagi, Noriko Maeda, Yuki Ozeki, Kouhei Miki, and Norio Takahashi. Estimation of Iron Loss in Motor Core With Shrink Fitting Using FEM Analysis. *IEEE Transactions on Magnetics*, 45(3):1704–1707, 2009.

[101] K. Ali, K. Atallah, and D. Howe. Predictions of mechanical stress effects on the iron loss in electrical machines. *Journal of Applied Physics*, 81(8):4119–4121, 1997.

[102] Ikram Junaid, Junaid Qudsia, and Byung-il Kwon. Improved Model of the Iron Loss for the Permanent Magnet Synchronous Motors. *Electrical Machines and Systems (ICEMS), 2010 International Conference on*, pages 1246–1251, 2010.

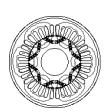

[103] Qi Li, Tao Fan, and Xuhui Wen. Characterization of Iron Loss for Integral-Slot Interior. *IEEE Transactions on Magnetics*, 53(5), 2017.

[104] Aldo Boglietti. A First Approach for the Iron Losses Building Factor Determination. In *34th IAS Annual Meeting IEEE Industry Applications Conference*, pages 489–493, Phoenix, AZ, USA, 1999. IEEE.

[105] R. Andersson and A. Reinap. Loss mapping of an Insert Permanent Magnets Synchronous Machine for parallel hybrid electric heavy vehicles. *Proceedings - 2016 22nd International Conference on Electrical Machines, ICEM 2016*, pages 1847–1853, 2016.

[106] Seok Hee Han, Thomas M. Jahns, and Z. Q. Zhu. Design tradeoffs between stator core loss and torque ripple in IPM machines. *IEEE Transactions on Industry Applications*, 46(1):187–195, 2010.

[107] N Yogal, C Lehrmann, and M Henke. Determination of the Measurement Uncertainty of Direct and Indirect Efficiency Measurement Methods in Permanent Magnet Synchronous Machines. In *2018 XIII International Conference on Electrical Machines (ICEM)*, pages 1149–1156, Alexandroupoli, Greece, 2018. IEEE.

[108] Sigrid Jacobs, Jan Rens, Lode Vandenbossche, and Emmanuel Attrazic. Effect of stator segmentation and manufacturing degradation on the performance of IPM machines, using iCARe® electrical steels. *World Electric Vehicle Journal Vol. 8*, 8(2):450–460, 2016.

[109] Phil Mellor, Rafal Wrobel, Adrian Mlot, Tony Horseman, Dave Staton, and Lloyds Bank Chambers. Influence of Winding Design on Losses in Brushless AC IPM Propulsion Motors. *Energy Conversion Congress and Exposition (ECCE)*, pages 2782–2789, 2011.

[110] Dominic A. Wills and Maarten J. Kamper. Reducing PM eddy current rotor losses by partial magnet and rotor yoke segmentation. *19th International Conference on Electrical Machines, ICEM 2010*, 2010.

[111] Shafigh Nategh. *Thermal Analysis and Management of High-Performance Electrical Machines*. PhD thesis, KTH Royal Institute of Technology, School of Electrical Engineering (EES), 2013.

[112] Kea-ho Lee, Hyun-rok Cha, and Young-bae Kim. Development of an interior permanent magnet motor through rotor cooling for electric vehicles. *Applied Thermal Engineering*, 95:348–356, 2016.

[113] Wenliang Chen, Yujing Liu, Jahirul Islam, and Dmitry Svechkarenko. Strand-level finite element model of stator AC copper losses in the high speed machines. *Proceedings - 2012 20th International Conference on Electrical Machines, ICEM 2012*, pages 477–482, 2012.

[114] Mircea Popescu and David G Dorrell. Skin effect and Proximity Losses in High Speed Brushless Permanent Magnet Motors. *Energy Conversion Congress and Exposition (ECCE), 2013 IEEE*, pages 3520–3527, 2013.

[115] Alexander D Podoltsev, Irina N Kucheryavaya, and Boris B Lebedev. Analysis of Effective Resistance and Eddy-Current Losses in Multiturn Winding of High-Frequency Magnetic Components. *IEEE Transactions on Magnetics*, 39(1):539–548, 2003.

[116] Johan Gyselinck and Patrick Dular. Frequency-Domain Homogenization of Bundles of Wires in 2-D Magnetodynamic FE Calculations. *IEEE Transactions on Magnetics*, 41(5):1416–1419, 2005.

[117] Martin Van Der Geest, Henk Polinder, Jan A Ferreira, and Dennis Zeilstra. Stator winding proximity loss reduction techniques in high speed electrical machines. *Electric Machines & Drives Conference (IEMDC), 2013 IEEE International*, pages 340–346, 2013.

[118] Johan Gyselinck, Patrick Dular, Christophe Geuzaine, and Ruth V Sabariego. Direct Inclusion of Proximity-Effect Losses in Two-Dimensional Time-Domain Finite-Element Simulation of Electrical Machines. *Proceedings of the 8th International Symposium on Electric and Magnetic Fields (EMF2009)*, pages 4–5, 2009.

[119] Pär Ingelström. Thermal measurements and simulations of the VCE wheel hub electrical motor. Volvo Internal Report; ER-659628 , Göteborg, 2014.

[120] Milind Paradkar and Joachim Böcker. Analysis of eddy current losses in the stator windings of IPM machines in electric and hybrid electric vehicle applications. *Power Electronics, Machines and Drives (PEMD 2016), 8th IET International Conference on*, pages 1–5, 2016.

[121] Kai Liu, Xin He Fu, Ming Yao Lin, and Da Xu. AC Copper Losses Calculation of the Ironless BLDCM Used in a Flywheel Energy Storage System. In *2015 IEEE International Conference on Applied Superconductivity and Electromagnetic Devices (ASEMD)*, pages 280–281, Shanghai, China, 2015. IEEE.

[122] S Iwasaki, Rajesh P Deodhar, Yong Liu, Adam Pride, Z Q Zhu, and Jonathan James Bremner. Influence of PWM on the Proximity Loss in Permanent-Magnet Brushless AC Machines. *IEEE Transactions on Industry Applications*, 45(4):1359–1367, 2009.

[123] Patel B Reddy, Thomas M Jahns, and Theodore P Bohn. Transposition Effects on Bundle Proximity Losses in High-Speed PM Machines. In *Energy Conversion Congress and Exposition, 2009. ECCE 2009. IEEE*, number 1, pages 1919–1926. IEEE, 2009.

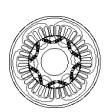

[124] Mario Vetuschi and Francesco Cupertino. Minimization of Proximity Losses in Electrical Machines With Tooth-Wound Coils. *IEEE Transactions on Industry Applications*, 51(4):3068–3076, 2015.

[125] Björn Deusinger, Marcel Lehr, and Andreas Binder. Determination of efficiency of permanent magnet synchronous machines from summation of losses. In *2014 International Symposium on Power Electronics, Electrical Drives, Automation and Motion*, pages 619–624. IEEE, 2014.

[126] Barna Szabados and Adrian Mihalcea. Design and Implementation of a Calorimetric Measurement Facility for Determining Losses in Electrical Machines. *IEEE Transactions on Instrumentation and Measurement*, 51(5):902–907, 2002.

[127] Christian Du-bar and Oskar Wallmark. Eddy Current Losses in a Hairpin Winding for an Automotive Application. In *2018 XIII International Conference on Electrical Machines (ICEM)*, pages 710–716, Alexandroupoli, Greece, 2018. IEEE.

[128] Anders Nordelöf. *Using life cycle assessment to support the development of electrified road vehicles*. PhD thesis, Chalmers University of Technology, 2017.

[129] Emma Arfa Grunditz, Sonja Tidblad Lundmark, and Anders Nordelöf. Three Traction Motors with Different Magnet Materials - Influence on Cost , Losses , Vehicle Performance , Energy Use and Environmental Impact. In *Ecological Vehicles and Renewable Energies (EVER), 2018 Thirteenth International Conference on*, Monaco, 2018.

[130] Anders Nordelöf, Emma Grunditz, Sonja Lundmark, Anne-Marie Tillman, Mikael Alatalo, and Torbjörn Thiringer. Life cycle assessment of permanent magnet electric traction motors. *Manuscript undergoing peer-review for journal publication*, pages 1–21, 2017.

[131] Shafigh Nategh, Zhe Huang, Andreas Krings, Oskar Wallmark, and Mats Leksell. Thermal Modeling of Directly Cooled Electric Machines Using Lumped Parameter and Limited CFD Analysis. *IEEE Transactions on Energy Conversion*, 28(4):979–990, 2013.

[132] B Assaad, K Mikati, T V Tran, and E Negre. Experimental study of oil cooled induction motor for hybrid and electric vehicles. In *2018 XIII International Conference on Electrical Machines (ICEM)*, pages 1195–1200, Alexandroupoli, Greece, 2018. IEEE.

[133] Naoya Soda and Masato Enokizono. Relation Between Stator Core Shape and Torque Ripple for SPM Motor. In *2018 XIII International Conference on Electrical Machines (ICEM)*, pages 955–960, Alexandroupoli, Greece, 2018. IEEE.

[134] Seok-myeong Jang, Hyung-il Park, Jang-young Choi, Kyoung-jin Ko, and Sung-ho Lee. Magnet Pole Shape Design of Permanent Magnet Machine for Minimization

of Torque Ripple Based on Electromagnetic Field Theory. *IEEE Transactions on Magnetics*, 47(10):3586–3589, 2011.

[135] Simone Ferrari, Gianmario Pellegrino, Matteo Davoli, and Claudio Bianchini. Reduction of Torque Ripple in Synchronous Reluctance Machines through Flux Barrier Shift. In *2018 XIII International Conference on Electrical Machines (ICEM)*, pages 2290–2296, Alexandroupoli, Greece, 2018. IEEE.

[136] E Favre, L Cardoletti, and M Jufer. Permanent-Magnet Synchronous Motors : A Comprehensive Approach to Cogging Torque Suppression. *IEEE Transactions on Industry Applications*, 29(6):1141–1149, 1993.

[137] Y Ito and K Akatsu. Minimization of torque ripple in an Inset type Magnet Reluctance Motor with square wave current. In *2018 XIII International Conference on Electrical Machines (ICEM)*, pages 1593–1597, Alexandroupoli, Greece, 2018. IEEE.

[138] Cristian A Lopez and Elias G Strangas. Optimization of PMSM Performance with Torque Ripple Reduction and Loss Considerations. In *2018 XIII International Conference on Electrical Machines (ICEM)*, pages 899–905, Alexandroupoli, Greece, 2018. IEEE.

[139] Lennart Råde and Bertil Westergren. *Mathematics Handbook for Science and Engineering*. Studentlitteratur, Lund, Sweden, 5 edition, 2004.

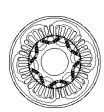

Printed by Media-Tryck, Lund 2019 NORDIC SWAN ECOLABEL 3041 0903

Lund University
Faculty of Engineering
Department of Biomedical Engineering
Division of Industrial Electrical Engineering and Automation
ISBN 978-91-88934-97-0
CODEN: LUTEDX/(TEIE-1091)/1-233/(2019)